

Improvement and Characterisation of pixelated Cadmium-Zinc-Telluride detectors for use in neutrino-less double-beta decay searches

by

Simeon James Matthew Spencer

A thesis submitted to
The University of Birmingham
for the degree of
DOCTOR OF PHILOSOPHY

School of Physics and Astronomy
The University of Birmingham

September 2011

**UNIVERSITY OF
BIRMINGHAM**

University of Birmingham Research Archive

e-theses repository

This unpublished thesis/dissertation is copyright of the author and/or third parties. The intellectual property rights of the author or third parties in respect of this work are as defined by The Copyright Designs and Patents Act 1988 or as modified by any successor legislation.

Any use made of information contained in this thesis/dissertation must be in accordance with that legislation and must be properly acknowledged. Further distribution or reproduction in any format is prohibited without the permission of the copyright holder.

Synopsis

Cadmium-Zinc-Telluride (CZT) detectors are seen as an ideal material for constructing intrinsic detectors for neutrino-less double-beta decay. However, the poor mobility of the charge carriers (specifically the holes) is known to result in poor resolution and decreased photo-efficiency. Simulations of this effect show that the resolution is a function of the detector width/depth ratio, suggesting pixelation as a solution. Pixelation of the detector also allows background sources, and even single-beta events to be selectively vetoed. However, this technique alone cannot completely remove the effect of the reduced resolution.

A technique which combines ‘Gain Matching’ and removal of the low energy tail is outlined and qualified for the resulting improvements in resolution and efficiency. The sharing of events between multiple pixels is also studied and the quality of reconstructed events is established.

The pixelated nature of the detector also opens the door to operation of the detectors as a ‘Compton Camera’. Accordingly, Geant4 simulations are compared with real-world measurements, to establish the benefits of pixelation upon the operation of the detectors as a ‘Compton Camera’.

Finally, comparisons are performed between Geant4 simulations and real-world measurements of intrinsic photopeak efficiency calculations.

For my mother, a token of my appreciation for 20 years of education.

Acknowledgements

This work would never have been possible without the assistance and support of everyone in the department, especially my supervisor Prof. Martin Freer. His willingness to address any problems has been invaluable. In addition, Nick Ashwood, Neil Curtis, Lee Barnby, Garry Tungate, Peter Jones, Tom Leadbeater and Carl Wheldon all deserve my thanks for their assistance at one time or another. My thanks also to everyone in E320, past and present, for being a sounding board, for providing useful insights and, when needed, for being a distraction.

Finally, my apologies to all those who helped proof-read the various drafts: Ben and Joel, my brothers, both my parents and Dr Mervyn Taylor. Their insights have ranged from the confusing (“Is a neutron a nucleon?”) to the random (“Gap... or River Island?”) and to the deeply philosophical (“Will we ever find a scenario where Energy is not conserved?”), for all of those comments, and especially the grammatical ones, I thank you all.

There is one other person who deserves my appreciation and respect; my fiancée Stephanie, who has been patient, understanding and insightful throughout my studies. She has provided everything, from comments on the grammar, to dinner, and deserves my appreciation for all of that.

Table of Contents

Table of Contents.....	i
List of Figures.....	iv
List of Tables	xix
Introduction	1
1. The Neutrino and Neutrino-less Double-beta Decay.....	3
1.1 Double-beta Decay	8
1.2 Double-beta Decay Processes.....	12
1.3 The Solar Neutrino Problem.....	13
1.4 Neutrino-less Double-beta Decays in Neutrino-mass searches	19
1.5 An Ideal $0\nu2\beta$ Experiment.....	22
2. Semi-conductor Detectors and CdZnTe.....	25
2.1 Semi-conductor Materials.....	25
2.2 Semi-conductor Detectors	27
2.3 Cadmium Zinc Telluride as a Semi-Conductor Detector	28
2.4 Simulating the Shockley-Ramo Theorem and the Small Pixel Effect	35
3. Improving the Energy Resolution and Sensitivity of CZT Detectors for use in Neutrino-less Double-beta Decay Measurements.	45
3.1 Reducing Background and False Positives.....	45
3.2 Determination of the Optimal Pixel Size of a Pixelated CZT Detector	54
3.3 Improving the Energy Resolution by ‘Gain Matching’ and Removing the Energy Tail.....	57
4. Quantifying the Improvement in Energy Resolution and Efficiency	70
4.1 Increase in the Efficiency for the Entire Detector	72
4.2 Energy Resolution Improvement for the Entire Detector.....	75

4.3 Discussion of Improvements across the Entire Detector.....	76
4.4 Increase in the Efficiency for Individual Pixels	77
4.5 Energy Resolution Improvement for the Individual Pixels	79
4.6 Comparison of Efficiency Increase in Individual Pixels Compared to Efficiency Increase within the Entire Detector	81
4.7 Confirmation of the Absence of a Dependence upon the Source Location of the Energy Resolution and Efficiency Improvements.....	83
4.8 Dependence of the Energy Resolution and Efficiency Improvements as a Function of Source Energy	85
4.9 Conclusion	88
5. Signal Sharing between Pixels	89
5.1 The Effect of Signal Sharing	92
5.2 Recombining the Signals	100
6. Compton Camera Techniques.....	106
6.1 Pixelated CZT Detectors as a Compton Camera.....	110
6.2 Pixelation and Improvement to Scattering Angle Calculations.....	129
7. Efficiency Calculations and Measurements	136
Conclusion	143
Outlook and Future Work.....	144
Appendices	146
Appendix A – Measurements and Source Locations	146
Appendix B – MathCAD Analysis	148
Appendix C – Pixel maps for improvements	151
Appendix D – C++ Simulation of Compton Scattering	154
Appendix E – Geant4 Simulation of Compton Scattering	161
Additional Bibliography	204

Journal Articles.....	204
Conference Proceedings	205
Websites	206
Presentations.....	206
Books	206
References.....	207

List of Figures

- Figure 1 - Figure from work by G Csikai and S Szalay showing the decay of a ${}^6\text{He}$ at rest into a ${}^6\text{Li} + e^-$ within a cloud chamber. The track of the lithium and electron are clearly shown, with the lithium ion travelling a short distance and the electron a much longer distance. The electron path is seen to curve due to the magnetic field in the cloud chamber. The two particles fail to conserve momentum in the decay. 4
- Figure 2 - Diagram showing the beta decay of a neutron (${}_0^1n$) into a proton (${}_1^1p$) and electron (e^-). The spin of all three particles are $\frac{1}{2}$. In order to conserve momentum, energy and spin, a third decay product of spin $\frac{1}{2}$ must be present in the final state. 5
- Figure 3 – Example of the continuous beta decay energy spectrum of ${}^{210}\text{Bi}$. The energy of the electron produced by the decay will be at any value up to that of the Q-value of the decay (1.16 MeV)..... 5
- Figure 4- Mass chain of nuclei of $A=125$ and 128. The most stable isotopes lie at the bottom with proton number increasing from left to right. The right hand mass chain ($A=128$) shows the mass chains for the two possible cases; the lower line represents those nuclei where all the nucleons are paired, while the upper line represents those nuclei with two unpaired nucleons. 10
- Figure 5 – Diagram of 4-Proton to ${}^4\text{He}$ Fusion in the Sun. two pairs of protons fuse and decay into deuterium, releasing two positrons and two neutrinos. These each then fuse with another proton producing ${}^3\text{He}$ and releasing energy in a photon. Finally the two ${}^3\text{He}$ nuclei fuse to produce a ${}^4\text{He}$ nucleus and release 2 protons. 14
- Figure 6 - Regions in which effective double-beta decay masses may lie as a function of neutrino mass – the inverted region is where the heaviest neutrino mass contributes most to the mixing, the normal where the heaviest neutrino mass contributes least to the mixing and the degenerate region lies where all three masses contribute evenly. The plot was created using $\theta_{sol} (\theta_{12}) = 33.9^\circ$, $\theta_{atm} (\theta_{23}) = 45^\circ$, $\theta_{13} = 0^\circ$, $\Delta m^2_{21} = 8.0 \times 10^{-5} \text{ eV}^2$ and $\Delta m^2_{32} = 2.4 \times 10^{-3} \text{ eV}^2$ 18

- Figure 7 - Separation of conduction and valence bands in insulators, semiconductors and conductors. In an insulator there is a large energy gap between the two bands which prevents electrons from being excited into the conduction band. In a conductor there is no gap and so electrons can move freely from one band into the other. Finally in a semi-conductor a band-gap exists but is relatively small, as a result, electrons can be excited by thermal interactions into the conduction band. The Fermi level is the upper limit of the occupied electron energy levels at absolute zero.....25
- Figure 8 - Diagram of a 'Frisch grid' in operation. Ion pairs are formed in the lower part of the detector (between the cathode and the grid), where the positive ions are attracted to the cathode and the electrons travel through the grid and then to the anode. The ions cannot induce any signal upon the anode, and the extra distance travelled by the electrons accounts for the different mobilities.32
- Figure 9 - Weighting potential as a function of depth of interaction while varying pixel-width to pixel-depth ratio (W/L). The weighting potential indicates the fraction of the carrier's charge that is induced upon the electrode as a function of distance from the electrode. At W/L ratios of 1, the induced charge decreases almost linearly with distance, but as the ratio decreases, the induced signal falls off rapidly away from the electrode.34
- Figure 10 - Signal induced on the anode as a function of the depth of interaction. At events near the anode (Depth=0) the holes are still near the anode when the electrons are collected, accordingly they induce a large signal cancelling the electrons. As the depth increases, the holes are further away, reducing the induced signal until, the holes induce no signal upon the anode when the electrons are collected.37
- Figure 11 - Signal induced on the cathode as a function of the depth of interaction. At events near the cathode (Depth=1) the electrons lie near the cathode as the holes are collected, cancelling the signal, however, as the depth from the anode decreases (Depth=0.9) the electrons move away from the cathode, reducing the cancelling effect. At Depth=0.77, the electrons start to reach the anode before the holes reach the cathode, leading to incomplete collection of

the holes; as the depth continues to decrease, the number of holes collected reduces and so does the signal.....38

Figure 12 - Simulation of the spectrum produced by plotting the signal on the cathode against the signal on the anode at the time the electrons strike the anode. Events which lie near the anode show a small signal on both the anode and cathode, as the signal is collected when the electrons reach the anode, no holes are collected on the cathode, and there is a strong cancelling signal from the holes which still lie close to the cathode. This forms the long energy tail. As the interactions move away from the anode, the anode signal rises rapidly, due to the reduced induction from the holes but the cathode signal increases slowly due to induced signal from the holes. As the interactions approach the cathode, holes begin to be collected, leading to a sharp rise in the cathode signal, however, this then falls away in this simulation as the electrons induce a strong cancelling effect, leading to the events which lie below the peak at an anode signal of 2500 keV and cathode signals of 0 to 500 keV.....39

Figure 13 - Figure showing the number of counts deposited at varying depths within the photopeak (the right hand side indicating the top of the photopeak). The photopeak measured was a 1332 keV gamma ray peak from a ^{60}Co source situated above the anode face.40

Figure 14 - Simulation of 20,000 2 MeV gamma rays interacting at random depths within the detector and at random positions from half a pixel-width outside the detector in both the x and y planes. As in Figure 12 the energy tail and sharply rising cathode signal are caused by events near the anode and cathode respectively. The broad photopeak is due to the sinusoidal nature of the simulation causing perturbations near the edge of the pixels. The strong peak near an anode signal of 0 keV is due to events which lie outside the pixel but which are collected on the non-pixelated cathode. Finally, events which lie outside the pixel, but whose charge carriers induce signal inside the pixel lie in the spread between the two strong peaks.....41

- Figure 15 - Simulation showing the sinusoidal fluctuation seen at the edges of the pixel. For events located near the sides of the pixel, a strong sinusoidal perturbation is seen due to the fitting of sinusoidal waves to a square wave.....42
- Figure 16 - Example spectrum of a $6.4 \times 6.4 \times 7$ mm³ 4x4 pixelated detector (corresponding to a W/L ratio of 0.23) showing the 1173 and 1332 keV peaks from a ⁶⁰Co source situated to the side of the detectors. As in Figure 14, low energy tails are seen extending from near the origin with rapidly rising anode signal, and then rising sharply with cathode signal. These are the photopeaks for events lying near the centre of the pixel and which are fully collected on the pixel. Events whose energy is fully collected on both electrodes form a diagonal line from the origin to the apex of the photopeaks. Events which are incompletely collected on the pixels form the continuum of peaks which lie below this diagonal, while events which are shared between pixels form the distribution above the diagonal.....43
- Figure 17 - Reproduction of Figure 4 from Bloxham et al showing the 3 differences between single and double-beta decay tracks with energy of 2800 keV, double-beta events are shown in filled circles or with solid lines. Bloxham et al show that double-beta events will normally trigger fewer pixels, which are separated by a greater distance, and deposit energy with a more even distribution.....47
- Figure 18 – Diagram of the simulated detector - 16 × 16 × 1 array of 200 micron² × 7 mm pixels. The left hand side shows the top view down onto the pixelated anode, the right side shows a side view of detector.....49
- Figure 19 - Simulated reproduction of the left-hand graph from Figure 17. This simulation shows the distribution of the number of active pixels for single and double-beta events. The red line corresponds to the double-beta events while the black line is for the single-beta events. As with Bloxham et al, double-beta events trigger fewer pixels.....49
- Figure 20 - Simulated reproduction of the central graph from Figure 17. This simulation shows the ratio of the standard deviation of energy deposited in active pixels to the average energy deposited for single and double-beta events. The red line indicates double-beta events while the black line

indicates single-beta events. As with Bloxham et al, double-beta events deposit their energy more evenly.....50

Figure 21 - Simulated reproduction of the right hand graph from Figure 17. This simulation shows the maximum separation of the two pixels with the highest energy deposition. The red circles indicate double-beta events while the black diamonds indicate single-beta events. Unlike Bloxham et al, this work suggests that double-beta events have a smaller maximum separation than single-beta events.51

Figure 22 - Simulated reproduction of Figure 17. This simulation shows the number of pixels active (top left), the ratio of the standard deviation of energy deposited in active pixels to the average energy deposited for single and double-beta events (top right) and the maximum separation of the two pixels with the most deposition (bottom). The black lines and circles indicate single-beta events, the red lines and squares are indicative of $0\nu2\beta^-$ events. The green lines and plus markers show $0\nu2\beta^+$ events and finally the blue lines and crosses indicate right handed $0\nu2\beta$ events. The techniques used to calculate these methods are taken from *Atomic Data and Nuclear Data Tables* 61 (1995) p43.'53

Figure 23 - Number of pixels of different sizes triggered at different threshold energy values (cut energy) for different source energies. The black line indicates a 1500 keV beta-particle, the red line shows a 1750 keV beta-particle, the green line corresponds to a 2000 keV beta-particle, the blue line shows a 2250 keV beta-particle and the brown line indicates a 2500 keV beta-particle. The 6 graphs indicate 100 micron pixels (top left), 200 micron (top right), 400 micron (middle left), 600 micron (middle right), 800 micron (bottom left) and 1000 micron (bottom right).56

Figure 24 - Photograph of the connectors on the master-board showing the two sizes of detector. In the upper middle position is the smaller detector; consisting of sixteen $1\times1\times5$ mm³ pixels. In the central position is the larger detector consisting of sixteen $1.6\times1.6\times7$ mm³ pixels. The pixelated anodes are facing the master-board and the un-pixelated cathodes face the camera.58

Figure 25 - Example spectrum from the $1.6 \times 1.6 \times 7$ mm ³ pixel detector showing the 662 keV peak from a ^{137}Cs source located above the detectors. The dashed line indicates complete and equal collection of deposited charge on both electrodes.....	59
Figure 26 - 1-dimensional projections of Figure 25, the left figure shows the anode signal, while the right figure shows the cathode signal.....	60
Figure 27 - Figure showing CZT spectrum following 'correction'. This spectrum is from the $1.6 \times 1.6 \times 7$ mm ³ pixel detector and shows the photopeak from a ^{137}Cs sources located above the detector. The peaks have been aligned and calibrated before being 'straightened'. A high energy tail is now present on the anode signal due to over-correction at low cathode signal values.....	62
Figure 28 - Example of 'corrected' spectrum showing varying curvature of peaks with anode signal. This spectrum is from the $1.6 \times 1.6 \times 7$ mm ³ pixel detector and shows photopeaks from ^{137}Cs and ^{152}Eu sources located above the detector. The 'correction' only works for the 662 keV peak from the ^{137}Cs , showing an 'over-correction' for lower energies and an 'under-correction' for higher energies.....	63
Figure 29 - Figure showing a spectrum without 'straightening' after the 'flattening' of the complete collection line. The figure shows a ^{137}Cs source, located above the $1.6 \times 1.6 \times 7$ mm ³ pixel detector, showing the 662 keV photopeak with the peaks un-straightened. The cathode lies along the line of 1000 on the y-axis (indicated by the dashed line) while the anode lies at around 350 on the same axis (indicated by the dotted line).....	64
Figure 30 - Final 'straightened' and 'flattened' spectrum showing a ^{137}Cs source located above a $1.6 \times 1.6 \times 7$ mm ³ pixel detector. The photopeak shows a discontinuity at a height of 1000 as this is the cut-off for the 'correction' process.....	65
Figure 31 - Final 'straightened' and 'flattened' spectrum showing ^{152}Eu and ^{137}Cs sources located above a $1.6 \times 1.6 \times 7$ mm ³ pixel detector. Once again a discontinuity is seen at a height of 1000; unlike in Figure 28, the 'correction' technique applies to all the photopeaks seen in the ^{152}Eu source as well as the 662 keV peak in the ^{137}Cs source.	66

Figure 32 – Spectra showing the entire process of improvement for a 1.6×1.6×7 mm³ pixel detector measuring a ¹³⁷Cs 662 keV gamma-ray source located above the detector. The top left spectrum shows the initial data, top right the data following the alignment of the photopeaks in the 16 individual pixels. The bottom left spectrum shows the result of the ‘flattening’ of the cathode signal, while the bottom right spectrum shows the final result when the photopeaks have been ‘straightened’67

Figure 33 - Spectra showing the signal on the anode, the figure on the left shows the signal after alignment of gains, the figure on the right shows the signal after the ‘straightening’ of the photopeaks as seen in Figure 32. It is apparent that the width of the peak (FWHM) has increased, and that the relative height of the photopeak to the ‘trough’ at 525 keV has greatly increased.68

Figure 34 - Figure showing the corrected spectra for both the source to the side (left) and the source above (right). If the source location affected deposition within the tail significantly then the right spectrum might be expected to demonstrate even deposition along the vertical direction while the left should be more intense at the top of the pixel (Height=100). Both spectra show similar distributions suggesting that source location does not significantly affect the deposition height within the pixel.74

Figure 35 - Ratio of area under the peak after correction to before - shown for 16 pixels for ¹³⁷Cs 662 keV and ⁶⁰Co 1332 keV gamma ray sources. The Caesium source analysis is performed for both detectors with the source situated above the detectors. The Cobalt analysis is performed with the larger detector and with the source both to the right-hand side of the detector and above. Ratios greater than 1 indicate an increase in efficiency after correction. Pixel maps for this data showing the area under the photopeak in each pixel before and after correction are seen in Appendix C.....78

Figure 36 - Ratio of Full-Width Half Maximum of the peak after correction to before - shown for 16 pixels for a ¹³⁷Cs source (662 keV gamma-rays) and a ⁶⁰Co source (1332 keV gamma-rays). The Caesium source analysis is performed for both detectors with the source situated above the detectors. The Cobalt analysis is performed with the larger detector with the source to the right-

hand side of the detector and also above the detector. Pixel maps for this data showing the FWHM in keV in each pixel before and after correction are seen in Appendix C	80
Figure 37 – Ratio of the peak to trough ratio after correction to before - shown for 16 pixels for a ^{137}Cs source (662 keV gamma-rays) and a ^{60}Co source (1332 keV gamma-rays). The Caesium source analysis is performed for both detectors with the source situated above the detectors. The Cobalt analysis is performed with the larger detector and with the source both to the right-hand side of the detector and above. Pixel maps for this data showing the peak to trough ratio in each pixel before and after correction are seen in Appendix C.....	81
Figure 38 - Location of pixels within the detector.	83
Figure 39 - Ratio of the area under the peak and the Full-Width Half Maximum of the peak after correction to before. The analysis was performed for a ^{60}Co source (1332 keV gamma) situated to the right-hand side of the detector and with the source situated above the detector. Ratios less than 1 indicate a decrease in FWHM after correction and thus an improvement in energy resolution.	84
Figure 40 - Plot of detector energy resolution (%) against Source energy (keV) both after alignment and after the photopeaks were straightened. Measurements are shown for 344.27 keV (^{152}Eu), 511 keV (^{22}Na), 662 keV (^{137}Cs), 1173 keV (^{60}Co), 1274 keV (^{22}Na) and 1332 keV (^{60}Co). Measurements were taken for all data points with sources both to the side and above the detectors.....	85
Figure 41 - Ratio of the FWHM after peak straightening to after alignment. Measurements are shown for 344.27 keV (^{152}Eu), 511 keV (^{22}Na), 662 keV (^{137}Cs), 1173 keV (^{60}Co), 1274 keV (^{22}Na) and 1332 keV (^{60}Co). Measurements were taken for all data points with sources both to the side and above the detectors.....	86
Figure 42 - Ratio of the area under the peak after peak straightening to after alignment. Measurements are shown for 344.27 keV (^{152}Eu), 511 keV (^{22}Na), 662 keV (^{137}Cs), 1173 keV (^{60}Co), 1274 keV (^{22}Na) and 1332 keV (^{60}Co). Measurements were taken for all data points with sources both to the	

side and above the detectors. The trend line is based upon a weighted fit, the weightings for each data point being the reciprocal of the errors squared. A trend is shown suggesting that the improvement in the area under the peak is indeed energy dependent and that this improvement increases at around 40% per MeV. Ratios greater than 1 indicate an increase in the area under the peak after correction and thus an increase in efficiency.....	87
Figure 43 – CZT spectrum where proposed signal sharing can be seen to the left of the line of maximum collection on the cathode (as indicated by the solid line) – the spectrum corresponds to a ^{60}Co source located to the side of the $1.6 \times 1.6 \times 7 \text{ mm}^3$ pixel detector. Note the vertical pile-up present in this spectrum due to high detector counting rate.....	89
Figure 44 - Spectrum for ^{60}Co source located to the side of the $1.6 \times 1.6 \times 7 \text{ mm}^3$ pixel detector for multiplicity 1 events - within a central pixel (pixel 6). Events lying above the diagonal of complete collection are reduced, in addition, the single pixel and single event nature of this spectrum leads to significantly improved resolution of the two photopeaks.	90
Figure 45 - Spectrum for ^{60}Co source located to the side of the $1.6 \times 1.6 \times 7 \text{ mm}^3$ pixel detector for multiplicity 1 events - within a pixel situated on the side of the detector (pixel 5). While the two photopeaks remain clear, the events above the diagonal of complete collection have increased.	91
Figure 46 - Spectrum for ^{60}Co source located to the side of the $1.6 \times 1.6 \times 7 \text{ mm}^3$ pixel detector - within a pixel situated on the corner of the detector (pixel 4). The events above the diagonal of complete collection have increased substantially over pixel 6, and even over pixel 5.	92
Figure 47 – Two-dimensional spectrum of multiplicity 1 events measured in the central pixel (pixel 6) plotted against the cathode energy of the large ($1.6 \times 1.6 \times 7 \text{ mm}^3$ pixel) detector showing the cathode energy window of $1065.6 \pm 133.2 \text{ keV}$ used to produce the spectra in Figure 48.	93
Figure 48 – One-dimensional spectra of energy deposited in pixels 4, 5 and 6, for multiplicity 1 events, within a cathode energy range of $1065.6 \pm 133.2 \text{ keV}$ for the larger ($1.6 \times 1.6 \times 7 \text{ mm}^3$ pixel) detector.....	94

Figure 49 – Sample spectra from corner and central pixels (left and right respectively) in the small and large detectors (top and bottom respectively). It is apparent that the central pixels have reduced signal above the line of complete collection, but that while this reduction is very large in the larger detector, it is minimal in the small detector. All four measurements were performed with the ^{60}Co source located to the side of the detectors.....	96
Figure 50 - Spectrum for central pixel of a $1.6 \times 1.6 \times 7 \text{ mm}^3$ pixel detector with a ^{60}Co source, located to the side of the detector, where only two pixels (one of which is the central pixel) are triggered.	98
Figure 51 - Plot of signal in the central pixel against signal in the second active pixel for a $1.6 \times 1.6 \times 7 \text{ mm}^3$ pixel detector with a ^{60}Co source located to the side of the detector. Events which are completely collected between the two pixels lie within a diagonal line of that energy. Events which lie below these diagonals are due to incomplete collection, either due to loss of energy outside the detector, or loss to adjacent pixels which are not triggered. Those events which lie above the diagonal suggest events where two independent gamma-ray's were collected, to some extent, upon the two pixels, these events will also contribute to the spectrum within the diagonals.	99
Figure 52 - Example of spectra of multiplicity two events where pixel 6 and one other pixel (E1) were active. The measurement was taken using a $1.6 \times 1.6 \times 7 \text{ mm}^3$ pixel detector and a ^{60}Co source located to the side of the detector. A threshold of 70 keV was used to select active pixels. The diagonal line of complete collection is seen, along with events which are apparently still due to sharing/loss of signal to adjacent pixels. In addition, the 1332 keV photopeak is seen to be constructed of 2 components. In addition, there are also components of events where two separate gamma-rays have been collected, seen at anode signals of greater than 1332 keV and of pile-up of signals upon the cathode (seen at cathode signals of greater than 1332 keV).....	100
Figure 53 - Multiplicity 2 events where pixel 6 and one other pixel (E1) were active. The measurement was taken using a $1.6 \times 1.6 \times 7 \text{ mm}^3$ pixel detector and a ^{60}Co source located to the side of the detector. A threshold of 205 keV was used. The number of events which are incompletely collected upon the two	

pixels is reduced, but still significant, however, the 1332 keV photopeak is now comprised of one component, and the energy resolution is greatly improved.....	102
Figure 54 - Multiplicity 2 events where pixel 6 and one other pixel (E1) were active. The measurement was taken using a $1.6 \times 1.6 \times 7$ mm ³ pixel detector and a ^{60}Co source located to the side of the detector. A threshold of 345 keV was used. The incompletely collected events are again reduced, with some further gain in energy resolution to the photopeaks. However, the efficiency of the peaks is greatly reduced.	103
Figure 55 – The energy deposited during the Compton scatter in the first detector is a function of the angle through which the gamma-ray scattered. By establishing a vector from the point of the scatter to the point of deposition in the second detector, it is possible to find a cone of vectors along which the gamma-ray must have travelled prior to the scatter.	107
Figure 56 – By examining events in multiple pairs of detectors, it is possible to find cones along which the gamma-rays must have travelled within several planes. The source is located as indicated at the crossing point of the 3 cones created from interactions in detectors situated at each of the points marked X.	107
Figure 57 - Intensity of scattered radiation as a function of scattering angle for Compton scattering at various incident energies α ($E_{\text{gamma}}/511$), as predicted by Equation 6.3.....	109
Figure 58 - Photo of lower master board showing a small detector in position 8 (top middle) and the larger detector in position 5 (central).	111
Figure 59 - Diagram showing relative location of detectors in the Compton Camera measurements. Detectors one and three are $4 \times 5 \times 4$ mm ³ and detector two is $6.4 \times 7 \times 6.4$ mm ³ . The centre of detector three's base was chosen as the origin, meaning that the detectors are centred at (0,37.5,0), (17,3.5,0) and (0,2.5,0) respectively. All units are given in mm. The z-axis is into the plane of the paper.	112
Figure 60 – Signal sharing between detectors two and three where both detectors only see one pixel active from a ^{137}Cs 662 keV gamma-ray source.....	113

Figure 61 - Signal sharing between detectors two and three where both detectors only have one pixel active from a ^{137}Cs 662 keV gamma-ray. A 170 keV gate has been taken around the full gamma energy of 662 keV.....	114
Figure 62 - Signal sharing between two pixels in detector one with a ^{137}Cs 662 keV source.....	115
Figure 63 - Signal sharing between two pixels in detector one with a 170 keV gate around the 662 keV gamma line from a ^{137}Cs gamma source.....	115
Figure 64 - Energy collected in detector two (left) and three (right) from events extending into the window shown in Figure 61 - showing the original data in black, the fitted function in green, the background in blue and the function and background in red. The peaks in detector two lie at 251.6 ± 2.2 keV and 379.9 ± 5.4 keV while the peaks in detector three lie at 326.2 ± 7.2 keV and 446.2 ± 2.1 keV.	117
Figure 65 - Diagram showing layout of the detectors and source. The detectors are centred at $(x,y,z) = (0,37.5,0)$, $(17,3.5,0)$ and $(0,2.5,0)$. The source was located at $(5,50,20)$. All units are given in mm. The z-axis is into the paper.....	118
Figure 66 - Energy collected in detector one (left) and detector two (right) from events shared between detectors one and two (top), in detector two (left) and detector three (right) from events shared between detectors two and three (middle) and in detector one (left) and detector three (right) from events shared between detectors one and three (bottom). Events shown are those extending into the 170 keV window around the 1332 keV gamma line from a Co-60 gamma source. Black shows the real data, red shows the simulated fit folded with a 40 keV energy resolution. Note that the lack of the Klein-Nishina formula in the simulation means that the intensities of the simulated peaks are identical.	121
Figure 67 - Diagram showing the relative location of the detectors to the source and each other for the Geant4 simulation. The detectors and source are located as outlined in Table 12.....	126
Figure 68 - Geant4 simulation of events where a 662 keV gamma-ray interacts in a single detector (black) and where the gamma-ray scatters in the first detector (red) and then interacts in the second detector (green) depositing its full	

energy in the two detectors. The single detector spectrum shows the photopeak and Compton edge clearly, while the double detector spectrum shows the symmetrical nature of such plots. The detectors and source locations are given in Table 12 and Figure 67.	126
Figure 69 – Geant4 simulation of a 662 keV gamma-ray showing events where the gamma-ray interacts only in a single detector (black) showing the photopeak and Compton edge, and events where the gamma-ray scatters in the first detector (red) and then interacts in the second detector (green) depositing its full energy in the two detectors. An energy resolution of 40 keV has been convoluted with the simulations. The detector and source locations are given in Table 12 and Figure 67.....	127
Figure 70 - Simulations of measurement 3, from Table 11, compared to the measurement with a gate of 170 keV. The peaks are seen to lie at the same energies in both simulation and measurement although significant reduction is energy resolution is seen in the measurements.....	128
Figure 71 - Diagram showing location of two detectors relative to one another. Photons enter from the left, aimed to hit the upper detector. The second detector is situated at the lower edge of the first detector (situated 6.4 mm downstream (z) and 7 mm vertically displaced (y)).	129
Figure 72 - Plot showing the actual angles between interaction points in black, the angles measured by using the centre of pixels as interactions points in red and the angle measured when using the centre of the detectors as the interaction points in green. This plot matches the setup shown in Figure 71. The angles shown are the angle of scatter within detector 1.....	130
Figure 73 - Plot showing the curves for three types of interactions overlaid on the plot for the simulated interactions. The green curve shows events where the photon has scattered through some angle in detector one and deposited the remnant in detector two. The red curve indicates events where a photon has passed through detector one and undergone a $(180 - \text{angle})^\circ$ scatter in detector two to return to the first. Finally the blue line shows events where the photon scattered in detector one to enter detector two before undergoing a near 180° scatter to return to detector one. This plot matches the setup	

described in Figure 71. The angles shown are the angle of scatter within detector 1.	131
Figure 74 - Diagram showing the paths of photons described by the three loci seen in Figure 73.....	132
Figure 75 - Diagram showing location of two detectors relative to one another. Photons enter from the left, aimed to hit the nearer detector. The second detector is situated at the side edge of the first detector (situated 6.4 mm downstream (z) and 6.4 mm horizontally displaced (x)).	134
Figure 76 - Plot of energy against angle showing the real angle calculated from the interaction positions in black, the angle assuming the interactions occurred in the centre of the pixels in red and the angle assuming the interactions occurred in the centre of the detectors in green. This plot matches the setup described in Figure 75. The angles shown are the angle of scatter within detector 1.	134
Figure 77 – Scale diagram showing the relative locations of the three detectors to the sources in the efficiency measurements. The detectors lie at (0,37.5,0), (0,3.5,0) and 17,2.5,0) respectively. The circular ^{22}Na source lies at (0,29.5,-2.5) and the rectangular ^{137}Cs and ^{60}Co sources both lie at (0,22,-2.5). All measurements are in mm and the z-axis is into the plane of the paper.	137
Figure 78 – Plots of efficiency values in the three detectors. ‘Before correction’ indicates the efficiency measured before the peaks were aligned, ‘flattened’ and ‘straightened’ as described in Section 3. ‘After correction’ indicates the efficiency measurement after those processes. ‘M1&2 events’ indicates where the efficiency after correction has been combined with the recovered efficiency due to multiplicity two events.	138
Figure 79 - Measured efficiency against Geant4 simulations for a $6.4 \times 6.4 \times 6.4 \text{ mm}^3$ detector. The red line shows the efficiency for the 16 pixels, while the black line shows the efficiency for the entire detector. The green circle denotes the efficiency for the initial data, the blue square the efficiency for the data after the peaks were aligned (as in Section 3), the purple diamond the efficiency after the spectrum was ‘flattened’ and the brown triangle shows the efficiency for the vertically straightened data.	140

Figure 80 - Efficiency plot for the newer simulations, the green line denotes simulations for the entire large detector, the blue line is the simulations for the single pixels of the large detector. The black line is the entire small detector and the red line is the pixels of the small detector. The single markers show the calculated efficiencies within the large detector. The yellow circle shows the initial measurement, the brown square shows the measurement after the photopeaks were 'aligned', the grey diamond shows the efficiency after the spectra were 'flattened' and, finally, the purple triangle shows the efficiency after the peaks were 'straightened'. These points should lie around the same values as the blue line.	141
Figure 81 - MathCAD sheet showing the detector locations, variable source location and the resulting energies deposited for scatters within the three detectors.....	148
Figure 82 -Two-dimensional plot of the detector and source positions in the simulation. Also shown is the table of data-points for the peak centroids in the measured data, with a value of 1 associated to the detector 1 and 2 pairing, 0.75 to the detector 1 and 3 pairing and 0.5 to the detector 2 and 3 pairing.	149
Figure 83 - Plot showing the real peak locations (marked as X) and the peak locations with the current fitted source location. Y-axis values of 1 relate to the detector 1 and 2 pairing, 0.75 to the detector 1 and 3 pairing and 0.5 to the detector 2 and 3 pairing.	150
Figure 84 - Sum of the squared difference between the fitted and the measured peak locations, as a function of the source location.	150
Figure 85 - Pixel map showing the area in the photopeak prior to 'correction'.	151
Figure 86 - Pixel map showing the area in the photopeak after 'correction'....	151
Figure 87 - Pixel map showing the FWHM in keV prior to 'correction'.	152
Figure 88 - Pixel map showing the FWHM in keV after 'correction'....	152
Figure 89 - Pixel map showing the Peak to Trough ratio prior to 'correction'.	153
Figure 90 - Pixel map showing the Peak to Trough ratio after 'correction'.	153

List of Tables

Table 1 - Table of double-beta decay candidates and the Q-values associated with the decays, including the 9 candidates in CdZnTe. ¹ Natural abundance refers to percentage of the isotope present in the naturally occurring element.	24
Table 2 - Table of Semi-conductor material properties showing atomic number, density, size of the Bandgap between the conduction and valence bands, ionisation energy (the energy required to produce each electron/hole pair) and the percentage energy resolution at 122 and 662 keV.....	30
Table 3 - Table showing the ratios of the peak areas after steps in the correction to before, for measurements taken with ^{137}Cs 662 keV and ^{60}Co 1332 keV gamma-ray sources measured with the $1\times 1\times 5\text{ mm}^3$ pixel detector and the $1.6\times 1.6\times 7\text{ mm}^3$ pixel detector.	73
Table 4 - Table showing the ratios of the FWHM after steps in the correction process to before, for measurements with ^{137}Cs 662 keV and ^{60}Co 1332 keV gamma-rays, using the $1\times 1\times 5\text{ mm}^3$ pixel detector and the $1.6\times 1.6\times 7\text{ mm}^3$ pixel detector.	75
Table 5 - Table of ratios of ‘peak to trough’ ratios after steps in the correction to before for measurements with ^{137}Cs 662 keV and ^{60}Co 1332 keV gamma-rays; using the $1\times 1\times 5\text{ mm}^3$ pixel detector and the $1.6\times 1.6\times 7\text{ mm}^3$ pixel detector.	76
Table 6 - Table showing the ratios of efficiency and energy resolution after correction to the initial values. The average improvement for individual pixels is shown in addition to the measured values for the entire detectors. Measurements were performed using ^{137}Cs 662 keV and ^{60}Co 1332 keV sources with both detector sizes.....	82
Table 7 – Change in the ratio of photopeak intensity to component intensity with the source located to the side of the detector. The ratio changes as signal sharing is suppressed for events where only one pixel is triggered.	94
Table 8 – Change in the ratio of peak intensity to component intensity as signal sharing between pixels is suppressed for events where two pixels are triggered.....	97

Table 9 - Table showing the area under the ^{60}Co 1332 keV photopeak and the FWHM of the section of the peak that lies within a window on the Cathode energy of 1267 ± 79.5 keV while increasing the threshold energy on the pixel anodes. All the values are calculated for multiplicity two events where pixel 6 and one other pixel are active, except for the multiplicity one value, which is calculated for events within pixel 6. All are software threshold values and are applied after hardware thresholds.....	104
Table 10 - Table showing the detector locations along with the expected and fitted location of the source. Detector three's location is defined as the origin for all other points. The fit is a good match for the actual source location.....	119
Table 11 - Table showing the calculated source locations for a series of measurements. Locations were fitted by using a predicted location (noted in Appendix A) and finding the local minimum of the average of the differences given as the ‘Sum of the residuals’. The ‘Sum of the residuals’ measure is given by the average of the differences between the real peak energies and the peak energies, as predicted by the Compton scatter equation, when the source is in the fitted location. As a result, this is a measure of the accuracy of the fitted location. Finally, the fit vs. the prediction is the sum of the difference between the fitted location and the initially estimated location. As such it is an estimate of how close the fitted location lay in relation to the estimated location of the source. The detectors are located by their positions in the boards. Detector three was designated as the origin and the other source locations were measured from that point.....	123
Table 12 - Table showing the location of the source and detectors in the Geant4 simulation	125
Table 13 - Table of results of efficiency simulations of a $6.4 \times 6.4 \times 6.4$ mm ³ detector. Entire detector indicates events where the photon deposited its energy within the detector, possibly across several pixels. ‘16 pixels’ indicates events where the photon deposited its energy within a single pixel.....	136
Table 14 – Table showing the ratio of the efficiency for multiplicity one and two events against the efficiency for multiplicity one events only. In addition a	

Geant4 prediction is given of the ratio of events of any multiplicity to events of multiplicity one within a 16 pixel $6.4 \times 6.4 \times 6.4$ mm ³ detector.	139
Table 15 - Table showing the connector locations on the Masterboard.....	146
Table 16 - example of output file from Geant4 simulation measured using a 662 keV photon within a $1.6 \times 1.6 \times 7$ mm ³ detector.	181

Introduction

“Absence of evidence is not evidence of absence”
The Demon-Haunted World: Science as a Candle in the Dark
Carl Sagan

The Standard Model of particle physics has been a tried and tested mainstay of physics for over 50 years. However, the model relies upon a series of relatively simple assumptions: that each particle has an anti-particle associated with it, and that this anti-particle is identical to the particle in mass, but opposite in many of the other fundamental attributes (most noticeably charge). A second, equally important, basis of the model is that for any interaction, certain conservation laws must be followed. The most fundamental of these is the well known energy conservation, but equally important are momentum, and, albeit at a more complicated level, Charge-Parity-Time. A second set of laws also applies, described as ‘baryon’ and ‘lepton’ conservation; these cover the conservation of the number of baryons (particles composed of quarks) within a system and, similarly, of the number of leptons (describing the electrons and neutrinos). However, this second conservation is found not to hold unilaterally across ‘generations’ⁱ of leptons. Instead, it is found that each generation is bound to a separate conservation rule.

During the last 30 years this assertion has been increasingly challenged, suggesting instead that one class of particle, the neutrino, may be capable of ‘oscillating’ between these generations. Furthermore, the neutrino is suggested to be capable of becoming its own anti-particle. These theories hold the power to weaken the Standard Model, requiring that the ‘Dirac’ formalism for particles is not universally true, that the apparently mass-less neutrino has mass and, perhaps most remarkably of all, that many of the long held conservation rules do not in fact apply to neutrinos.

The presence of a massive neutrino also opens the door to decay processes such as neutrino-less double-beta decay, an observation of which would provide a value for the mass eigenstates of the neutrino as well as confirming that the neutrino and its anti-particle are one and the same.

ⁱ Where the electron generation contains the electron, anti-electron (positron), electron-neutrino and electron-anti-neutrino.

This work aims to study the viability of Cadmium-Zinc-Telluride (CZT), a material which has been suggested to be suitable for performing measurements of neutrino-less double-beta decay half-lives. CZT contains 9 potential double-beta decay isotopes, several of which have significant natural abundances. However, detectors made with CZT are well known to have poor energy resolution due to significantly lower values of mobility for the holes, which lead to an asymmetric peak shape for more energetic particles.

During this work, this ‘energy tail’, and the resultant decrease in photopeak efficiency and energy resolution, will be assessed and a possible solution implemented. In addition, comparisons will be made between simulations and experimental measurements in order to assess the viability of ‘Compton Camera’ measurements to locate sources. The increasing need for precise measurements of radio-isotopes within security operations, as well as the ability to operate CZT detectors at room temperature, makes this an area of study that is increasingly important. Finally, the efficiency of three detectors will be measured and compared to simulations performed within Geant4, a package that has made significant steps in recent years to improve its reliability in the low energy domain.

1. The Neutrino and Neutrino-less Double-beta Decay

The field of Nuclear Physics evolved rapidly at the beginning of the 20th century, from the discovery of the nucleus,¹ and subsequent suggestion of the shell model by Bohr,^{2,3,4} to the discovery of the proton within the nucleus by Rutherford.^{5,6} As understanding of the nucleus grew, the processes by which it could decay, and the resultant products, became the targets of much research.

Following the discovery of radioactivity by Becquerel in 1896 and of the electron by Thompson in 1897, Rutherford and both Marie and Pierre Curie undertook substantial work to understand radioactivity and identified three distinct decay processes. The corresponding three decay products were studied extensively, especially by Rutherford, and, by 1919, were understood well enough to be used as probes of the nucleus itself.

While alpha and gamma decays could be understood in terms of the concept of restructuring of the nucleus, beta decay could not be and involved the decay of a constituent ‘nucleon’ (a proton or a neutron). This decay would stabilise the nucleus by redressing the balance of the strong nuclear and electromagnetic forces, and would lead to the emission of an electron and some energy (gained from the increased stability of the nucleus). It was expected that the electron would be emitted with an energy consistent with that released by the nucleus itself, and thus be constant for a particular nuclear decay. In fact, the nature of the beta decay spectrum was determined to be continuous by independent studies by Ellis and Chadwick^{7,8} in the 1920’s which led to a more precise examination of the true nature of beta decay.

By the start of the 1930’s the theory of beta decay suggested that a neutron (a theoretical particle only, until its discovery in 1932^{9,10}) would decay into a proton, emitting an electron. This presented several problems, notably that the spin and energy carried by the proton and the electron were imbalanced. In the example of a neutron decaying into a proton, it was observed that the initially stationary atom was given momentum during the decay, but that this momentum was not correspondingly balanced by the momentum given to the electron (see the work by Leipunski¹¹). This point was proven most dramatically by Gyula Csikai and Sándor Szalay in 1955 with experiments performed on ⁶He. The photograph of their

successful demonstration of the non-conservation of linear momentum by a ${}^6\text{He}$ nucleus decaying at rest is shown in Figure 1.

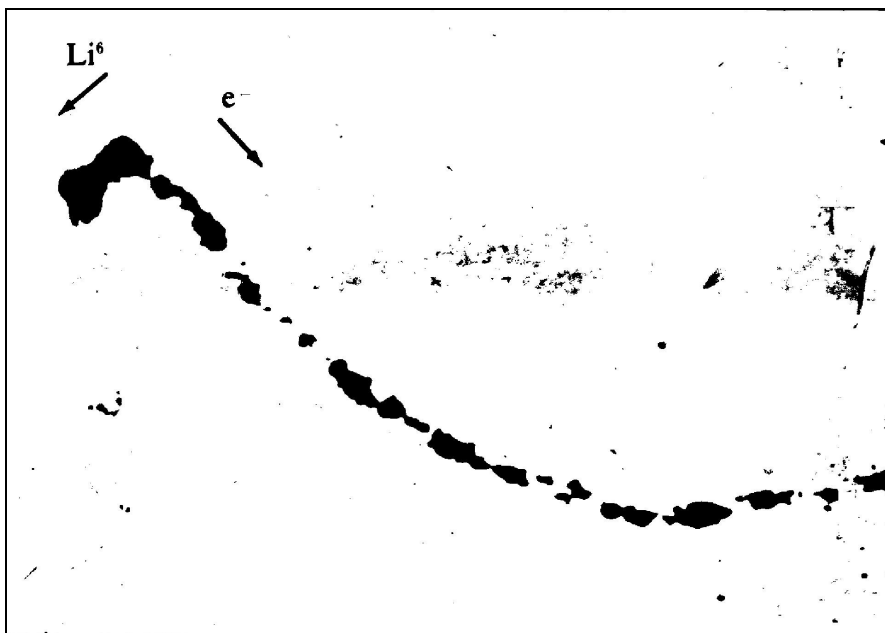


Figure 1 - Figure from work by G Csikai and S Szalay¹² showing the decay of a ${}^6\text{He}$ at rest into a ${}^6\text{Li} + \text{e}^-$ within a cloud chamber. The track of the lithium and electron are clearly shown, with the lithium ion travelling a short distance and the electron a much longer distance. The electron path is seen to curve due to the magnetic field in the cloud chamber. The two particles fail to conserve momentum in the decay.

The decay can be simplified to the example of the decay of a single nucleon, either bound or otherwise. In Figure 2, a 2-dimensional representation of a free neutron decaying into a proton and electron is shown. The neutron decays into a proton and emits an electron, but, in order for linear momentum to be conserved, there must be a third decay product (denoted by the '?'). Without this additional product, neither vertical nor horizontal momentum is conserved.

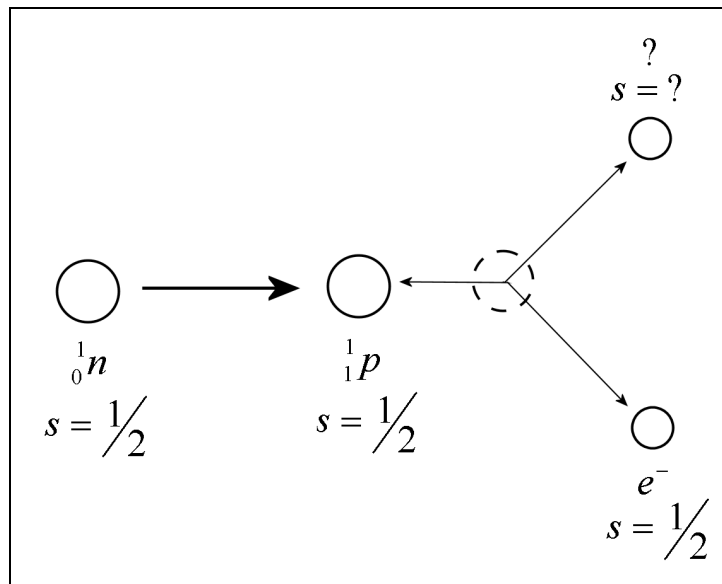


Figure 2 - Diagram showing the beta decay of a neutron (${}_0^1n$) into a proton (${}_1^1p$) and electron (e^-). The spin of all three particles are $\frac{1}{2}$. In order to conserve momentum, energy and spin, a third decay product of spin $\frac{1}{2}$ must be present in the final state.

In addition, the energy of the emitted electron was found not to be fixed to the Q-value (the difference in energy between the initial and final states) of the decay, but was produced in a continuous distribution (Figure 3). This could not be attributed to the electron losing energy before detection¹³ and, instead, suggested that another particle carried some fraction of the decay energy.

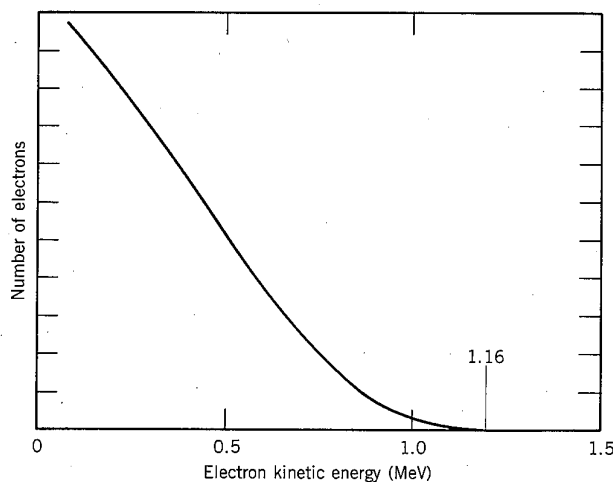


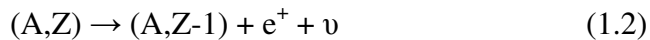
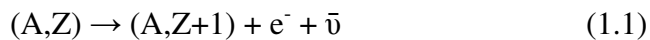
Figure 3 – Example of the continuous beta decay energy spectrum of ${}^{210}\text{Bi}$. The energy of the electron produced by the decay will be at any value up to that of the Q-value of the decay (1.16 MeV).¹⁴

One final piece of evidence for the existence of the neutrino was that the spin of the neutron had been determined to be $\hbar/2$. Similarly, the spin of the proton and electron had also been measured to be $\hbar/2$. In order for spin to be conserved, there must be another particle with spin $\hbar/2$ present in the decay.

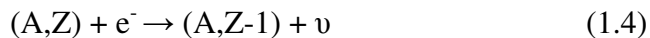
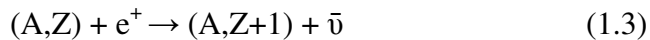
In 1930 Wolfgang Pauli^{15,16} suggested a ‘neutron’ (later renamed ‘neutrino’ by Fermi), to explain the conservation of energy, spin and momentum in beta decays. The existence of the neutrino precisely explained the missing components of the decay. However, such a particle had never been observed experimentally. In order to explain this failure, the neutrino’s properties had to be such that the particle was nearly impossible to detect. When, in 1934, Fermi produced a theory of beta decay introducing a hypothetical unobserved particle,¹⁷ the neutrino and its properties, although still undetected until 1956,¹⁸ became an integral part of nuclear and particle physics theory.

The theory of beta decay provided the neutrino with several simple interactions, which formed a key element in our understanding of radioactivity, and furnished Cowan and Reines¹⁸ with the means by which to detect the neutrino. These interactions fall into four distinct groups for both neutron-proton and proton-neutron beta decays (so called β^- and β^+ decays).

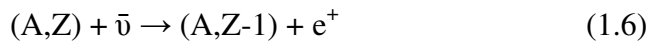
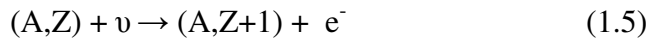
Beta Decay



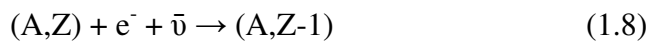
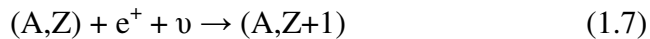
Electron Capture



Stimulated Beta Decay



Stimulated Electron Capture



In equations 1.1 to 1.8, (A,Z) refers to a nucleus of atomic mass A and atomic number Z, e^- and e^+ refer to the electron and the positron, respectively, while ν and $\bar{\nu}$ refer to the neutrino and the anti-neutrino.

The neutrino's properties, as given by Fermi's theory, are as follows: it is a light (mass-less) particle which, having no charge, interacts extremely weakly with other particles. It is a fermion and thus, having a non integer spin, must obey the Pauli Exclusion Principle (which dictates that no two fermions can reside in the same quantum state). Traditionally, this was all that was required to complete the neutrino's properties. The ratification of this picture came in 1960, when Frederick Reines and Clyde Cowan¹⁹ discovered the electron anti-neutrino ($\bar{\nu}_e$) by use of the stimulated beta decay (Equation 1.6).ⁱⁱ The electron's heavier cousin the muon, discovered in 1937²⁰ also has an accompanying neutrino, discovered in 1962²¹ by studying pion and kaon decays with energies in the GeV range by use of the $\pi \rightarrow \mu + \nu_\mu$ decay processes. Finally, the tau was discovered in 1975.²² The discovery of the tau led to the conclusion that a tau-neutrino must exist, but also led to work to determine precisely how many lepton generations exist.

The number of generations was established in 1989 by measurements of the decay of the Z boson;²³ the width measurements of the decay dictated that the number of neutrinos was $N_\nu = 2.8 \pm 0.6$. The work was confirmed at the LEP (Large Electron–Positron Collider) experiment at CERNⁱⁱⁱ in 1990, where all four collaborations published measurements of the neutrino number based on Z width measurements.^{24,25,26,27} Combined, these measurements give a neutrino number of $N_\nu = 2.89 \pm 0.10$.²⁸ The final neutrino, the tau neutrino, was eventually discovered in 2001 by the Fermilab DONUT experiment.²⁹

These ‘heavier’ neutrinos present serious problems: while the heavier quarks and electrons carry the same properties as the original particles, but with more mass, the neutrino had no mass and thus, logically, could not have ‘heavier’ cousins. Aside from this challenge, it is

ⁱⁱ These experimental proofs all rely on the requirement that not just the number of leptons (electrons and neutrinos) is conserved, but that also the generation (electron, muon or tau) is conserved.

ⁱⁱⁱ *Organisation Européenne pour la Recherche Nucléaire*

likely that this model of three mass-less neutrinos would still be the way the neutrino was regarded if it were not for two things: the discovery of Double-beta Decay by Maria Goeppert-Mayer in 1935³⁰ and the Solar Neutrino Problem.³¹

1.1 Double-beta Decay

Nuclear stability can be described by the ‘semi-empirical mass formula’ an expression which describes the binding energy of the nucleus in terms of 5 factors.

$$B = a_V A - a_S A^{2/3} - a_C Z(Z-1)A^{-1/3} - a_{\text{sym}} \frac{(A-2Z)^2}{A} + \delta \quad (1.1.1)$$

Where:

- B is the binding energy of the nucleus;
- A is the mass of the nucleus (mass number);
- Z is the number of protons (atomic number);
- a_i is a constant relevant to a particular term;
- $a_V A$ is the volume term;
- $a_S A^{2/3}$ is the surface term;
- $a_C Z (Z-1) A^{-1/3}$ is the Coulomb term;
- $a_{\text{sym}} \frac{(A-2Z)^2}{A}$ is the symmetry term;
- δ is the spin pairing term.

The specifics of the constants ‘ a ’ are not relevant here. As a simple approximation, it might be assumed that each nucleon is bound to all other nucleons, giving a volume term related to $A(A-1)$. In fact, the linear variance of B upon A suggests that the strong nuclear force has a very small range and that individual nucleons only interact with their closest neighbours (saturation). This statement must be modified at the surface; since nucleons at the surface have fewer neighbours, they are less tightly bound than those nucleons at the centre. A second modification must be made to account for the reduction in the binding energy due to the electromagnetic repulsion of the protons, described by the Coulomb term. Thirdly is the deviation in this balance of nuclear force and electromagnetic force in the nucleus due to the

symmetry in numbers of protons and neutrons. The final term increases the binding of the nucleus in the event that all the nucleons are paired in anti-aligned spin pairs.

Due to spin pairing in the nucleus; pairs of nucleons of the same type - for instance two protons or two neutrons - will pair up with spins anti-aligned. Protons and neutrons must obey the Pauli Exclusion Principle and so two protons are forbidden from existing in the same quantum state as one another. However, the direction of the spin allows two nucleons of the same type to reside in states with the same spatial wave-function. Thus, paired nucleons are more stable than unpaired nucleons and this maximises the binding energy (the energy required to separate the nucleons). In a nucleus with an odd number of nucleons, the nucleons will pair up leaving one un-paired nucleon (either a neutron or a proton). In a nucleus with an even number of nucleons, the nucleons will also pair up, and either, leave one unpaired neutron and one unpaired proton (if odd numbers of protons and neutrons are present), or, all the nucleons will pair giving a total angular momentum of zero.

It follows that the mass of a stable nucleus is governed by the binding energy, and that for otherwise identical isobars (nuclei with the same atomic mass, but differing numbers of protons and neutrons) the only relevant factors in the mass formula are the Coulomb, symmetry and pairing terms. Thus, it is possible to plot a figure (such as that seen in Figure 4) which shows the ‘mass chains’ – plots of isobars with increasing proton number against the mass of the isobar - for nuclei of mass 125 and 128 atomic units. The vertical axis on these plots indicates the mass of the nuclei.

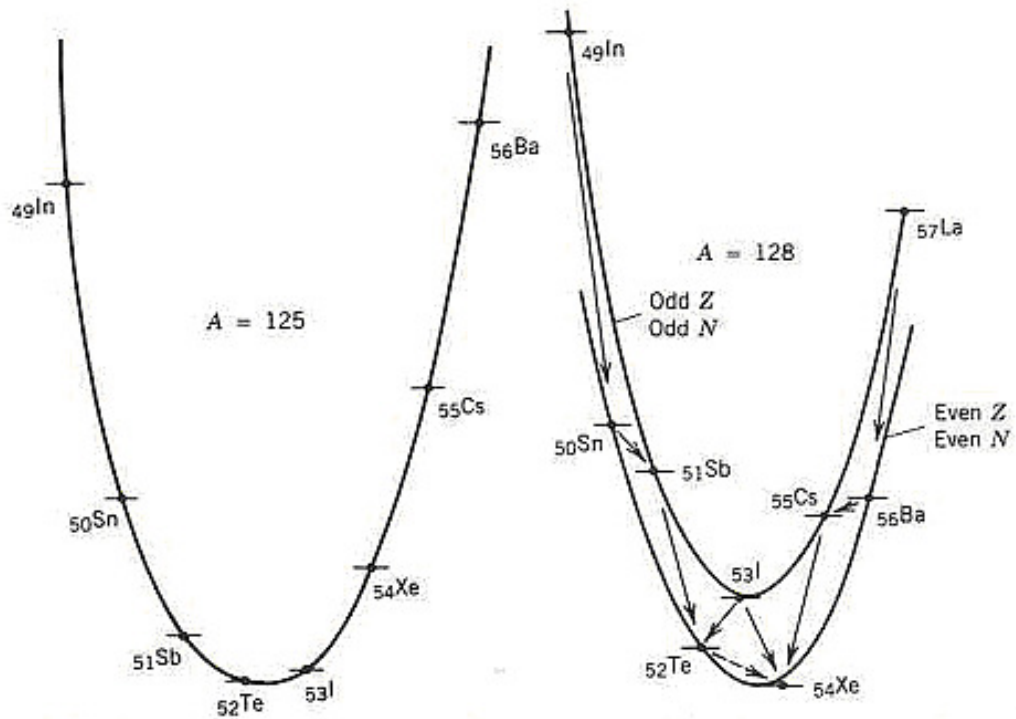


Figure 4- Mass chain of nuclei of $A=125$ and 128 .³² The most stable isotopes lie at the bottom with proton number increasing from left to right. The right hand mass chain ($A=128$) shows the mass chains for the two possible cases; the lower line represents those nuclei where all the nucleons are paired, while the upper line represents those nuclei with two unpaired nucleons.

In a nucleus with an odd atomic mass (such as $A=125$ in Figure 4), there are always 62 pairs of nucleons and one unpaired nucleon. As there is no significant distinction in the binding energy if this unpaired nucleon is a neutron or a proton, the masses of the isobars can be shown as a single line, which forms a distinctive parabola. Nuclei beta decay to move towards the centre of the ‘valley’; which is the result of the symmetry and Coulomb terms seen in equation 1.1.1 – The Coulomb term favours large ratios of neutrons to protons, while the symmetry term favours equal numbers of neutrons and protons. As a result, in nuclei where there are fewer neutrons than protons, the proton repulsion modelled by the Coulomb term leads to instability, while in nuclei with more neutrons than protons, the unbalanced numbers of neutrons and protons in the same orbit also reduces the binding energy. However, in the case of a nucleus with an even number of nucleons ($A=128$ in Figure 4), there is an additional effect.

In such a nucleon there are two possible combinations of nucleons:

- a nucleus with 63 pairs of nucleons and two unpaired nucleons (so called odd-odd nuclei for the odd number of protons and odd number of neutrons);
- a nucleus with 64 pairs of nucleons.

For the odd-odd nucleus there is no spin-pairing between the final two nucleons and thus the nucleus is less stable than an even-even nucleus of the same mass. As a result, two parabolas are seen, displaced by 2δ , with the upper parabola formed by the odd-odd, less stable, nuclei and the lower by the even-even, more stable, nuclei.

Beta decays can only ‘convert’ one nucleon at a time from proton into neutron or vice-versa and thus a nucleus must move between isobars with a difference in proton number (and neutron number) of only one. For some isobars, such as $^{128}_{52}Te$ (shown in Figure 4), it is obvious that there is a more stable nuclear configuration ($^{128}_{54}Xe$). However, in order to decay, the nucleus must do so through the less stable intermediary isobar $^{128}_{53}I$. This decay process ($^{128}_{52}Te$ to $^{128}_{53}I$) is energetically forbidden; accordingly, the nucleus beta decays twice in quick succession (constrained by the Uncertainty Principle) to $^{128}_{54}Xe$. The energy required to decay to the intermediary $^{128}_{53}I$ needs to be ‘borrowed’ from the Heisenberg Uncertainty Principle. Thus the time within which the process is constrained is given by:

$$\Delta t \geq \frac{\hbar}{\Delta E} \quad (1.1.2)$$

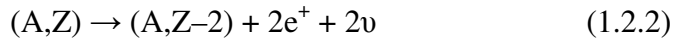
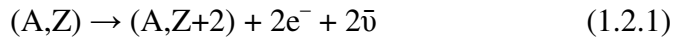
where Δt is the constraining time, ΔE the energy ‘borrowed’ and \hbar is the reduced Planck constant. The constraining time is small compared to the typical beta decay half-life of the order of one second and so the probability of double-beta decay is correspondingly very small.

M. Goepport-Mayer’s work³⁰ (focused on the stability of even-even nuclei) provided the background for subsequent work in the field of double-beta decay. These decays not only include the double-beta decay process (Equations 1.2.1 and 1.2.2), but also, in theory, all the double decay versions of stimulated and electron capture decays (Equations 1.2.3 to 1.2.8).

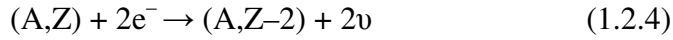
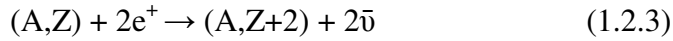
1.2 Double-beta Decay Processes

Equations 1.2.1 to 1.2.8 show the decay processes of double-beta decay. In each of these, the nucleus decays virtually through an intermediate nucleus in decaying to the stable isobar. In both the stimulated and electron capture events it is possible that the stimulating neutrino, or captured electron, may provide enough energy to overcome the energy barrier to the first decay. This makes both decays more probable than double-beta decay, but requires strong fluxes of the stimulating particles. Double stimulated electron capture requires that the initial nucleus captures both the electron and neutrino required for the first decay before capturing another electron and neutrino to stimulate the second. As a result, this decay process is extremely unlikely.

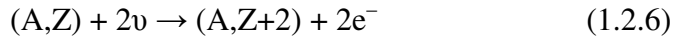
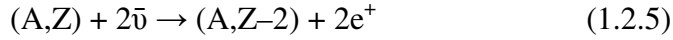
Double-beta Decay



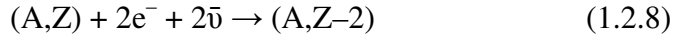
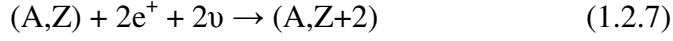
Double Electron Capture



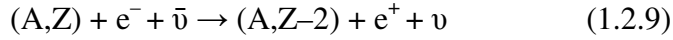
Stimulated Double-beta Decay



Stimulated Double Electron Capture



Electron-Capture and Single-beta Decay



Neutrino-less Double-beta Decay



It is also possible to have double-beta decays combining two different forms of the single decay processes. Equation 1.2.9 shows such a decay, where the initial nucleus captures an electron and an anti-neutrino prior to undergoing the decay.

In 1939 W.H. Furry showed that the theory of symmetry between particles and their antiparticles, suggested by E. Majorana,³³ could allow for the process of ‘neutrino-less’ double-beta decay.³⁴ This process would require a decay where, instead of the emission of two electrons (or positrons) and two anti-neutrinos (or neutrinos), the decay would produce just the two electrons (or positrons), but no anti-neutrinos (or neutrinos). In the decay shown in Equation 1.2.10, the first β^- decay produces a ‘virtual’ neutrino, which then becomes an anti-neutrino and stimulates the second decay. In this case, the lepton number is not conserved by the decay process, being violated by two units. This non-conservation is inconsistent with the ‘Standard Model’.

The half-life can be related to the mass of the neutrino by the equation (See Section 1.4):

$$\frac{1}{T_{1/2}^{0\nu}} = G^{0\nu} |M_{GT}^{0\nu}|^2 \left(\frac{\langle m_\nu \rangle^2}{m_e^2} \right) \quad (1.2.11)$$

In equation 1.2.11, ³⁵ $G^{0\nu}$ is the phase-space of the decay, $\langle m_\nu \rangle^2$ is the squared, time averaged, mass of the neutrino, m_e^2 is the squared mass of the electron and $M_{GT}^{0\nu}$ is the matrix element describing the overlap of the wave-functions of the initial nucleus in its 0^+ ground state and the final nucleus (commonly in its 0^+ ground state).³⁶

1.3 The Solar Neutrino Problem

The second major challenge to the understanding of the neutrino’s properties was that of the ‘Solar Neutrino Problem’.³⁷ The sun is a massive source of neutrinos, since the fusion cycle that powers it leads to an enormous number of beta decays per second. In the hydrogen fusion process, first suggested by Bethe and Critchfield,³⁸ four protons combine to make ${}^4\text{He}$ by the process outlined in Figure 5.

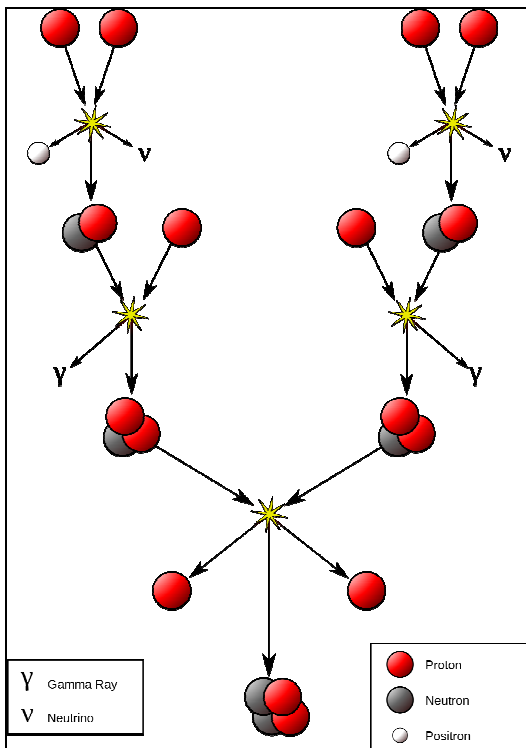
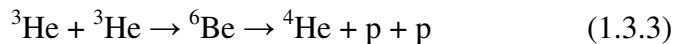
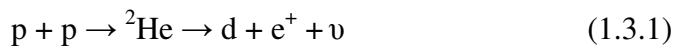


Figure 5 – Diagram of 4-Proton to ${}^4\text{He}$ Fusion in the Sun.³⁹ Two pairs of protons fuse and decay into deuterium, releasing two positrons and two neutrinos. These each then fuse with another proton producing ${}^3\text{He}$ and releasing energy in a photon. Finally the two ${}^3\text{He}$ nuclei fuse to produce a ${}^4\text{He}$ nucleus and release 2 protons.

The various steps shown in Figure 5 for the proton to ${}^4\text{He}$ process are outlined in Equations 1.3.1, 1.3.2 and 1.3.3:



While proton to helium fusion is the simplest process in the Sun, it is not the only one. Other processes include the fusion of ${}^3\text{He}$ and ${}^4\text{He}$ to form ${}^7\text{Be}$ (which can then decay to ${}^7\text{Li}$); subsequently, ${}^7\text{Be}$ and a proton to form ${}^8\text{Be}$ which decays to two ${}^4\text{He}$. In addition, the Carbon-Nitrogen-Oxygen (CNO) cycle involves a series of fusions of nuclei and protons followed by beta decays with corresponding neutrino emission.

Experiments performed to study the constant neutrino flux from the sun (using neutrino capture by ${}^{37}\text{Cl}$ to form ${}^{37}\text{Ar}$) showed distinct differences to the theoretical estimates for neutrino production.^{40,41} The measured solar (electron) neutrino flux was determined by Ray

Davis^{47,42} to be $2.56 \pm 0.16_{\text{stat}} \pm 0.16_{\text{syst}}$ SNU, while the predicted flux was proposed to be $7.6^{+1.3}_{-1.1}$ SNU (where one SNU is 10^{-36}s^{-1} interactions per nucleus). Furthermore, the ‘double ratio’ of atmospheric neutrinos, which is given by equation 1.3.4, was shown to be less than unity; implying that the total number of electron neutrinos is fewer than expected.⁴⁷

$$R_{\text{atm}} = \frac{(\bar{\nu}_\mu - \bar{\nu}_e) / (\bar{\nu}_e - \bar{\nu}_e)}{(\bar{\nu}_\mu - \bar{\nu}_e) / (\bar{\nu}_e - \bar{\nu}_e)}_{\text{Experimental}} \quad (1.3.4)$$

Three possible solutions were suggested:

- the ‘heavy’ neutrino half-lives had been incorrectly measured – possibly there were some terrestrial effects that modified this;
- the theories of fusion and radioactive decay were incorrect;
- something was happening between the sun and the earth that was modifying the number of neutrinos of each generation.

These solutions suggested that the theories underpinning neutrino physics or nuclear fusion were incorrect. The result of the Solar Neutrino Problem was to re-open the examination into the neutrino and its properties, most importantly the possibility of the neutrino having mass. If the neutrinos were to have mass then it was predicted that they may oscillate between the weak eigenstates; i.e. an electron neutrino may change into a muon neutrino.

Further evidence for the oscillation of neutrinos was observed in measurements of the total (all three generations) neutrino flux compared to the electron-neutrino flux.³⁷ The measured electron neutrino flux was found to be a third of the predicted flux, while the measured total neutrino flux was the same as the predicted flux. Pions produced by atmospheric cosmic ray reactions decay into muons and muon-neutrinos.⁴³ However, measurements of neutrinos produced by these decays show that fewer muon-neutrinos are measured as coming from above the detector than are measured as having travelled first through the earth. The ratio of muon-neutrinos from above to muon-neutrinos from below is $0.551 \pm 0.035_{\text{stat}} \pm 0.004_{\text{syst}}$ and confirms that oscillations are taking place for those neutrinos which must travel the far greater distance through the earth.⁴⁴

Neutrino oscillations allow one type (generation) of neutrino to oscillate into another. In order for this to occur, the neutrino must be a superposition of ‘flavour’^{iv} and mass eigenstates; accordingly the neutrinos themselves must be massive.⁴⁵ The mass is dictated by a mass eigenstate⁴⁶ meaning that, theoretically, an electron-neutrino could have the mass of a muon-neutrino. This has led to experiments to find the various parameters which govern these oscillations.

In the simplified scenario of neutrino oscillations, within a vacuum, between two neutrino flavours, it can be shown⁴⁷ that the probability of a neutrino of type l oscillating into a neutrino of type k is given by equation 1.3.5.

$$P(v_l \rightarrow v_k) = \sin^2 2\theta \sin^2 \left(1.27 \Delta m^2 \frac{L}{E_\nu} \right) \quad (1.3.5)$$

$$\Delta m^2 = |m_l^2 - m_k^2| \quad (1.3.6)$$

Where the squared masses (m_i^2) and mass squared differences (Δm^2) are given in eV², θ dictates the amplitude of the mixing, L is the distance between source and detection in km and E_ν is the energy of the neutrino in GeV. As such, the mass difference (the difference in mass between mass eigenstates l and k) can be probed by examining the ratio of the two neutrino flavours at various values of L/E_ν .

For a system comprising three neutrinos, there are thus six unique parameters of importance: two mass differences Δm_{12}^2 and Δm_{23}^2 , three mixing angles θ_{12} , θ_{23} and θ_{13} and one CP phase δ .⁴⁴ The mixing angles and CP phase, along with two majorana phases α_1 and α_2 which cannot be calculated from oscillations, are present in the mixing matrix^{48,49} U (the Pontecorvo-Maki-Nakagawa-Sakata lepton mixing matrix), which in turn can be used, as in equation 1.3.7, to calculate the effective double-beta decay neutrino mass.⁴⁶

$$\langle m_{ee} \rangle = \left| \sum_k m_k U_{ek}^2 e^{i\phi(k)} \right| = \left| \sum_k \sqrt{m_L^2 + \Delta m_{kL}^2} U_{ek}^2 e^{i\phi(k)} \right| \quad (1.3.7)$$

Where m_{ee} indicates the effective mass of the majorana electron-neutrino, m_k indicates the mass of the k 'th eigenstate, m_L the mass of the lightest neutrino, Δm_{kL} the mass difference between the lightest neutrino and the k 'th eigenstate and U_{ek} indicates the mixing matrix

^{iv} Where, flavour indicates whether the neutrino is an electron, muon or tau neutrino.

values for an oscillation between the electron neutrino and the k 'th neutrino state. Finally $\phi(k)$ is the phase of the k 'th eigenvalue. Although neutrino oscillation experiments can provide the mixing angles and the phases found in the mixing matrix, without an absolute value of the mass of the neutrino (and hence Δm_{kL}) the mass information available from these experiments is of limited use.

The introduction of mass to the neutrino has forced a re-examination of earlier works that had assumed that the neutrino was mass-less. This has led to suggestions that neutrino-less double-beta decay and other such exotic processes could exist, and thus, work has begun to try to understand fully both the oscillations (with experiments such as SNO⁵⁰ and MINOS⁵¹) and the properties of the neutrino. Various measurements of solar neutrinos and atmospheric neutrinos (especially at KamLAND and SNO) have set limits on four of the neutrino oscillation parameters:⁴⁴

$$\Delta m_{12}^2 = 8.0_{-0.4}^{+0.6} \times 10^{-5} \text{ eV}^2$$

$$\Delta m_{23}^2 = (3.05_{-0.55}^{+0.60} \pm 0.12) \times 10^{-3} \text{ eV}^2$$

$$\tan^2 \theta_{12} = 0.45_{-0.07}^{+0.09}$$

$$\sin^2 2\theta_{23} = 0.88_{-0.15}^{+0.12} \pm 0.06$$

While new experiments would provide limits on $\sin^2 \theta_{13}$ and greater sensitivity to the mass differences, oscillation experiments cannot provide a determination of the absolute mass of the neutrino.

These oscillation data support four hypotheses which are formed from a combination of the possibilities that the neutrino is a Dirac particle (the particle and its anti-particle are not the same) or a Majorana particle (the particle is its own anti-particle) and the possibilities that the mass regime is either ‘inverted’ or ‘normal’. If the three mass differences are all similar then the regime is said to be quasi-degenerate, if the largest mass has the smallest probability ($m_1 < m_2 < m_3, \Delta m_{12}^2 \ll \Delta m_{23}^2$) then the regime is said to be ‘normal’ while if the largest mass has the largest probability ($m_3 < m_1 < m_2, \Delta m_{12}^2 \ll |\Delta m_{13}^2|$) then the regime is said to be inverted. A plot of the effective double-beta decay mass as a function of the minimum neutrino mass (the lightest neutrino mass eigenstate) is shown in Figure 6. The effective double-beta decay mass (the neutrino mass calculated from double-beta decay measurements)

is defined as $\langle m_{\beta\beta} \rangle = \left| \sum_i U_{ei}^2 m_{\nu_i} \right|^2$ (where i is the neutrino flavour, U_{ei} is the mixing matrix for oscillation from flavour i into electron neutrinos and m_{ν_i} is the mass of the i 'th neutrino flavour).

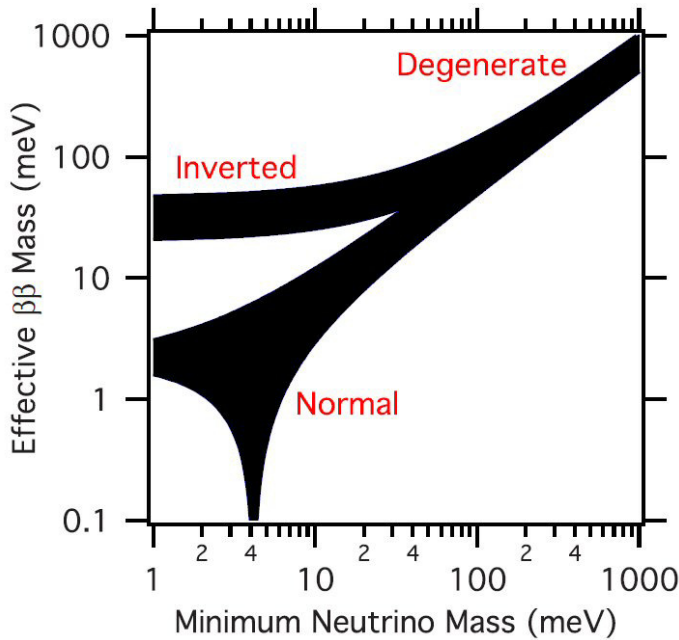


Figure 6 - Regions in which effective double-beta decay masses may lie as a function of neutrino mass – the inverted region is where the heaviest neutrino mass contributes most to the mixing, the normal where the heaviest neutrino mass contributes least to the mixing and the degenerate region lies where all three masses contribute evenly. The plot was created using $\theta_{sol}(\theta_{12}) = 33.9^\circ$, $\theta_{atm}(\theta_{23}) = 45^\circ$, $\theta_{13} = 0^\circ$, $\Delta m^2_{21} = 8.0 \times 10^{-3} \text{ eV}^2$ and $\Delta m^2_{32} = 2.4 \times 10^{-3} \text{ eV}^2$.⁴⁸

Current generation experiments have the ability to probe effective double-beta decay masses in the range of 0.1 to 1 eV, while proposed next generation experiments hope to examine the 10 to 100 meV range. These experiments will be able to measure the ‘degenerate’ and ‘inverted’ regions, but will not be able to study the ‘normal’ domain. However, successfully finding an effective double-beta mass would prove the majorana nature of the neutrino, irrespective of the ability to differentiate between the three regions.

Direct measurements of neutrino masses are possible however, and have provided a limit of $m_{\nu_e} < 4.35 \text{ eV}$ using tritium β decays.⁵² These measurements were performed by pumping tritium through a closed loop, passing the tritium by a Si(Li) detector which detected only

those electrons produced within the magnetic field of the system (i.e. those from the tritium decay), and examining the deviation of the apparent endpoint of the spectrum from the predicted endpoint. This deviation is then compared to a prediction of the spectrum assuming certain values for the mass of the neutrino.

The limit on the muon-neutrino mass of $m_{\nu_\mu} < 170$ keV was determined using pion decays at rest⁴³ by measuring the momentum (p_{μ^+}) of the muon produced ($\pi^+ \rightarrow \mu^+ \nu_\mu$) and by knowing the masses of the negative pion (the mass of the positive pion is assumed to be identical to that of the negative pion⁵³) and the anti-muon. Together they can be used to find the mass of the muon-neutrino from equation 1.3.8.

$$m_{\nu_\mu}^2 = m_{\pi^-}^2 + m_{\mu^+}^2 - 2m_{\pi^-} \left(m_{\mu^+}^2 + p_{\mu^+}^2 \right)^{\frac{1}{2}} \quad (1.3.8)$$

Finally, the tau-neutrino mass limit of $m_{\nu_\tau} < 24$ MeV was found using decays of tau-electrons by the ALEPH collaboration.⁵⁴

1.4 Neutrino-less Double-beta Decays in Neutrino-mass searches

The advantage of neutrino-less double-beta decay measurements is the ability to determine the absolute mass of the neutrino, rather than the mass differences that oscillation experiments measure. The sensitivity of any experiment is dictated by the half-life that can be measured. For neutrino-less double-beta decay this limit is dictated by:

$$T_{1/2} \propto A\varepsilon \left(\frac{Mt}{B\Delta E} \right)^{\frac{1}{2}} \quad (1.4.1)$$

The half-life limit is a function of the relative isotopic abundance of the isotope being studied (A), the efficiency of the detector (ε), the overall mass of the detector (M), the running time of the experiment (t), the background (B) and the energy resolution (ΔE).

The half-life measured is then related to the mass of the neutrino by:

$$\frac{1}{T_{1/2}^{0\nu}} = G^{0\nu} |M_{GT}^{0\nu}|^2 \left(\frac{\langle m_\nu \rangle^2}{m_e^2} \right) \quad (1.4.2)$$

$G^{0\nu}$ is the phase-space of the decay process, $M_{GT}^{0\nu}$ is the matrix element, m_ν is the effective mass of the neutrino and m_e is the mass of the electron.³⁵

It is important to note that the peak corresponding to $0\nu 2\beta$ events sits at the end point of a distribution of $2\nu 2\beta$ events. For a system with perfect energy resolution, these two distributions would be differentiable, but in a real-world system this is not the case. Accordingly, the fraction (F) of $0\nu 2\beta$ events that actually correspond to unresolved $2\nu 2\beta$ events is given by:^{55,56,v}

$$F = \frac{8Q\left(\frac{\Delta E}{Q}\right)^6}{m_e} \quad (1.4.3)$$

where Q is the Q-value of the decay. From this, the ratio of the $0\nu 2\beta$ signal within the peak (S) to $2\nu 2\beta$ background under the peak (B) can be shown to be that seen in equation 1.4.4.

$$\frac{S}{B} = \frac{m_e}{8Q\left(\frac{\Delta E}{Q}\right)^6} \frac{T_{1/2}^{2\nu}}{T_{1/2}^{0\nu}} \quad (1.4.4)$$

Initial work in the field of neutrino-less double-beta decay includes experiments such as the NEMO-3 work on ^{48}Ca , ^{96}Zr and ^{150}Nd , which has given half-life limits of $1.3 \times 10^{22}\text{y}$, $8.6 \times 10^{21}\text{y}$ and $1.8 \times 10^{22}\text{y}$ respectively⁵⁷. In addition, semiconductor experiments, such as the Heidelberg-Moscow experiment, have given a half-life limit of around 10^{25}y for ^{76}Ge and a resulting mass limit of 0.38 eV. The proposed new generation of experiments are split into two camps; those which utilise ^{76}Ge as the source material, usually to take advantage of the benefits of an intrinsic detector^{vi} and the energy resolution of Germanium detectors, and those which utilise other materials, either as intrinsic systems, for example CUORE, or extrinsic such as Super-NEMO.

The GERDA experiment, aims to operate 15 kg of segmented Germanium detectors inside a cryostat of liquid argon, shielded by a water bath. It is hoped in future phases to upgrade this system to 35 kg and subsequently to a 500 kg system.^{58,59} The Majorana Project⁶⁰ aims to utilise an array of detectors consisting of 500 kg of germanium enriched to 86% ^{76}Ge . The

^v The factor 8 given here, and by Zuber, and 7 given by Vogel dictates the resolution of the Detector system. 5 equates to a resolution of 10%, 7 to a resolution of 5% and 8.5 to a resolution of 1%. Knoll⁶⁹ gives a value of 1.75% at 662 keV for $\text{Cd}_{0.8}\text{Zn}_{0.2}\text{Te}$.

^{vi} A detector constructed of the source material.

current plans are to use cryogenically cooled detectors stored in a cylindrical container – each container holding 57 crystals, each separately shielded by low background copper. However, the experiment remains in the preliminary phase.

The CUORE⁶¹ system will use 988 TeO₂ bolometers in a cylindrical configuration of 19 towers, each containing 53 crystals of 5 cm side. This equates to a 741 kg system. The detectors work by measuring the temperature rise resulting from the release of energy during the decay. The detectors are intrinsic and therefore should have good efficiency and an expected energy resolution of around 5 keV at 2615 keV.⁶² Finally, the NEMO experiment,⁶³ whose upgrade ‘SuperNEMO’ is in the design phase, is a large gas detector whose sources are provided by large ‘foils’ inserted into the detector chamber. The decay interacts within the gas detectors and can be tracked through the chamber. Unlike the other experiments, NEMO has the ability to measure several isotopes at the same time, as well as providing measurements of materials which cannot be used in intrinsic detector experiments. However, due to the extrinsic nature of the experiment, the efficiency is significantly lower than in the other experiments.

The COBRA^{vii} project⁶⁴, aims to use intrinsic Cadmium-Zinc-Telluride detectors to study several isotopes. A proof-of-principle detector was constructed using 4, 1 cm³ detectors with an active mass of 26.12 g which only read out the electron signal. As a result, the detector had no tracking or depth sensitivity capabilities. The detector was shielded by copper and situated within a 7 cm thick, boron-loaded polyethylene, neutron shield. The proof-of-principle detector was operated from 2003 to 2006 in the ‘Gran Sasso’ national laboratory with an accumulated exposure of 3.82 kg days. During this time, world best half-lives were achieved for both ⁶⁴Zn and ¹²⁰Te. The prototype is being upgraded to a 4 × 4 × 4 array of 1 cm³ detectors which would constitute an active mass of 418 g.

^{vii} Cadmium-Zinc-Telluride *O*-neutrino double-Beta Research Apparatus

1.5 An Ideal $0\nu2\beta$ Experiment

The proposed nature of the neutrino has changed substantially since its inception. It is now a massive (if not greatly so) particle that exists as a combination of two probability distributions of flavour (electron, muon or tau neutrino) and mass ($m_{\nu_e}, m_{\nu_\mu}, m_{\nu_\tau}$). It interacts weakly with matter, but can do so in a variety of ways. It is a fermion, but is suggested to be also a majoran (a particle that can become its own anti-particle); such particles are not included in the ‘Standard Model’.

Much research is being undertaken to establish the true nature of the neutrino: studying whether it is truly a majoran and attempting to establish the masses of the three neutrinos themselves. The most common method of research into this field, oscillation experiments, only provides the difference in mass between any two neutrinos. Experimental techniques such as direct measurements of the mass with tritium are challenging,⁵² while techniques such as magnetic moment studies⁶⁵ are still in their infancy. For this reason, neutrino-less double-beta decay is a field which has the potential to provide unique answers. By studying a source capable of neutrino-less double-beta decay, it is possible to use the count-rate to establish the half-life of the decay process and thus determine the mass of the majorana neutrino.⁶⁶ In addition, a confirmed neutrino-less double-beta decay event would prove that the process can occur, as well as demonstrating that the neutrino could be capable of becoming its own anti-particle. In the eventuality that such an experiment provided a null result, the measurements taken of $2\nu2\beta$ decays would be useful, and the half-lives studied would provide mass limits on the neutrino in $0\nu2\beta$ experiments.

Double-beta decaying isotopes are very rare, requiring an isotope where two even-even isobars, one of which is more stable than the other, are both more stable than the intermediary odd-odd isobar. The half-life of the decay is determined by the energy difference between the two even-even states. The addition of the neutrino-less element requires the neutrino to become an anti-neutrino in the limited time granted by the uncertainty principle which allowed the decay. This time is dictated by the energy difference between the first even-even state and the odd-odd state. Thus the half-life of the neutrino-less double-beta decay is a

combination of the probability of neutrino to anti-neutrino decay in the time allowed and the probability of double-beta decay initially.

For these reasons, any experiment must have excellent energy resolution, good tracking (to eliminate background single-beta decays) and would preferably be an intrinsic detector using isotopes that are abundant, cheap and work well as a detector material. The detector itself must be designed to minimise background and, ideally, will operate stably for extended running periods and at room temperature.

Table 1 shows a list of double-beta decay candidates, both $\beta^- \beta^-$ and $\beta^+ \beta^+$. High Q values are essential to move outside the restricting range of background from natural radiation. They are especially important for $\beta^+ \beta^+$ decays, as these are mostly electron capture processes which reduce the detectable energy. Due to the large number of suitable isotopes of Cadmium, including ^{114}Cd with its natural abundance of 28.7% and ^{116}Cd (7.5%) with its characteristic energy lying above the highest background source energy of 2.614 MeV (^{228}Th), it is considered to be a good candidate for study. Combined with the three suitable isotopes in tellurium, which make up close to two thirds of naturally occurring tellurium and the two isotopes of zinc, CdZnTe promises to be an excellent material for study of double-beta decays of both the $\beta^- \beta^-$ and the $\beta^+ \beta^+$ forms.

Transition	Q-Value (keV)	Natural Abundance %
$^{48}_{20}Ca \rightarrow ^{48}_{22}Ti (\beta^- \beta^-)$	4271	0.187
$^{70}_{30}Zn \rightarrow ^{70}_{32}Ge (\beta^- \beta^-)$	1001	0.62
$^{76}_{32}Ge \rightarrow ^{76}_{34}Se (\beta^- \beta^-)$	2039	7.8
$^{82}_{34}Se \rightarrow ^{82}_{36}Kr (\beta^- \beta^-)$	2995	9.2
$^{96}_{40}Zr \rightarrow ^{96}_{42}Mo (\beta^- \beta^-)$	3350	2.8
$^{100}_{42}Mo \rightarrow ^{100}_{44}Ru (\beta^- \beta^-)$	3034	9.6
$^{110}_{46}Pd \rightarrow ^{110}_{48}Cd (\beta^- \beta^-)$	2013	11.8
$^{114}_{48}Cd \rightarrow ^{114}_{50}Sn (\beta^- \beta^-)$	534	28.7
$^{116}_{48}Cd \rightarrow ^{116}_{50}Sn (\beta^- \beta^-)$	2802	7.5
$^{124}_{50}Sn \rightarrow ^{124}_{52}Te (\beta^- \beta^-)$	2288	5.64
$^{128}_{52}Te \rightarrow ^{128}_{54}Xe (\beta^- \beta^-)$	868	31.7
$^{130}_{52}Te \rightarrow ^{130}_{54}Xe (\beta^- \beta^-)$	2533	34.5
$^{136}_{54}Xe \rightarrow ^{136}_{56}Ba (\beta^- \beta^-)$	2479	8.9
$^{150}_{60}Nd \rightarrow ^{150}_{62}Sm (\beta^- \beta^-)$	3367	5.6
$^{64}_{30}Zn \rightarrow ^{64}_{28}Ni (\beta^+ \beta^+)$	1096.3	48.6
$^{78}_{36}Kr \rightarrow ^{78}_{34}Se (\beta^+ \beta^+)$	2882	0.35
$^{96}_{44}Ru \rightarrow ^{96}_{42}Mo (\beta^+ \beta^+)$	2720	5.5
$^{106}_{48}Cd \rightarrow ^{106}_{46}Pd (\beta^+ \beta^+)$	2771	1.25
$^{108}_{48}Cd \rightarrow ^{108}_{46}Pd (\beta^+ \beta^+)$	231	0.9
$^{120}_{52}Te \rightarrow ^{120}_{50}Sn (\beta^+ \beta^+)$	1722	0.10
$^{124}_{54}Xe \rightarrow ^{124}_{52}Te (\beta^+ \beta^+)$	2866	0.10
$^{130}_{56}Ba \rightarrow ^{130}_{54}Xe (\beta^+ \beta^+)$	2578	0.11
$^{136}_{58}Ce \rightarrow ^{136}_{56}Ba (\beta^+ \beta^+)$	2406	0.19

Table 1 - Table of double-beta decay candidates and the Q-values associated with the decays, including the 9 candidates in CdZnTe.^{67,73} Natural abundance refers to percentage of the isotope present in the naturally occurring element.

2. Semi-conductor Detectors and CdZnTe

The requirements that an ideal detector be intrinsic, have high efficiency and be capable of high energy resolution measurements, in the energy domains of interest (as discussed in Section 1.5), point to a segmented semi-conductor detector as being the ideal solution. Cadmium-Zinc-Telluride (CZT) has proven itself as a semi-conductor detector material; however, the material exhibits several problems which require an understanding of the operation of semi-conductor detectors.

2.1 Semi-conductor Materials

Materials are split into three standard electrical groups: insulators, conductors and semi-conductors.

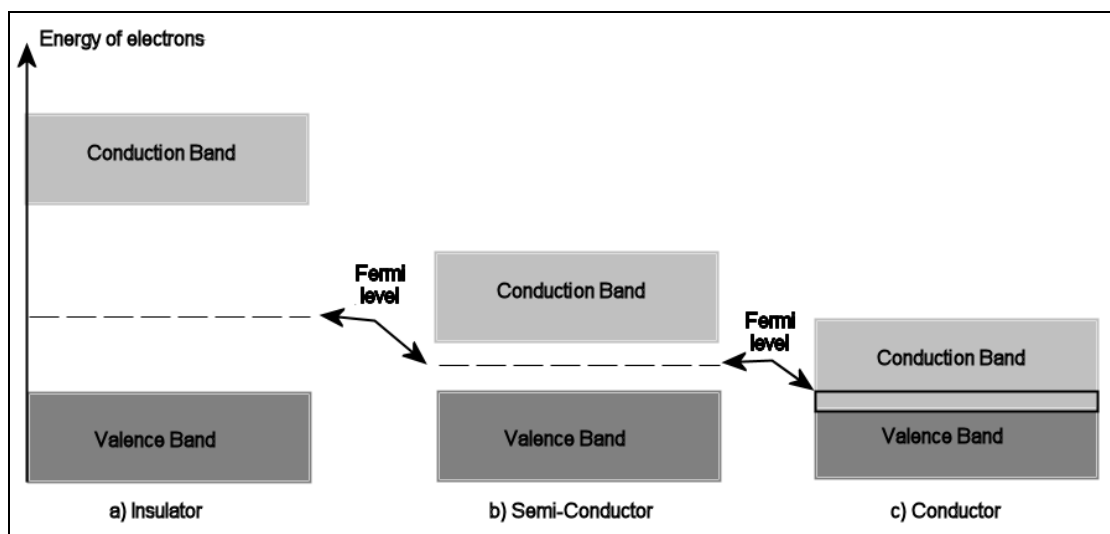


Figure 7 - Separation of conduction and valence bands in insulators, semiconductors and conductors. In an insulator there is a large energy gap between the two bands which prevents electrons from being excited into the conduction band. In a conductor there is no gap and so electrons can move freely from one band into the other. Finally in a semi-conductor a band-gap exists but is relatively small, as a result, electrons can be excited by thermal interactions into the conduction band. The Fermi level is the upper limit of the occupied electron energy levels at absolute zero.

The three groups are defined by the separation of the conduction and valence bands as shown in Figure 7. In the atom, electrons are situated in shells; the valence shell being the highest energy shell containing electrons, while the conduction shell is the first empty shell. When the atoms are bonded into a lattice the shells degenerate into energy bands. The energy of these shells depends upon the nucleus, but, when filled, the interaction of the electrons between one another and with the nucleus lowers the energy of the shell, increasing the gap between that shell and the next. The result is that atoms with unfilled valence shells are more reactive (and conductive) than those with filled valence shells – for example Lithium is more reactive than its closed-shell neighbour Beryllium.

The energy gap between the valence and conduction bands is the factor that defines a material's electronic classification. If the bands overlap, as in a conductor, then electrons can easily move from the valence band to the conduction band. However, if the gap is large (over several kT),^{viii} as in an insulator, the electrons cannot move between the bands without substantial energy input. In a semi-conductor the band gap is small (e.g. 1.11 eV in Silicon and 0.67eV in Germanium)⁶⁸ and electrons can move from the valence band to the conduction band by thermal excitation, or by external influences (intrinsic or extrinsic interactions).

When an electron moves from the valence band into the conduction band, it leaves a ‘hole’ behind. This hole behaves as the opposite of an electron: having a negative effective mass, equal to that of the electron, and a positive effective charge.

Intrinsic interactions, such as thermal excitation, can be promoted by ‘doping’: the process of putting elements with one more (or one less) electron into the semi-conductor lattice to provide a point with more (or fewer) electrons. Doped materials are called ‘n doped’ to imply extra electrons and ‘p doped’ to imply fewer electrons. Extrinsic interactions can be caused by particle interactions within the material exciting electrons into the conduction band – for example gamma-rays or other particles interacting within the material. Once the electron and hole have been created (or the pre-created electron/holes made by doping), these charge carriers can move freely through the lattice. If an electric field is applied the electrons move to the anode and the holes to the cathode. In a pure semi-conductor this is the complete picture; in a doped or alloyed material, however, extra effects are seen. The different relative

^{viii} Where k is the Boltzmann constant and T is the temperature.

intensities of charge carriers mean that one type can move faster than another; furthermore, the mixture of atoms within the lattice increases the likelihood of one of the carrier types becoming ‘trapped’.^{ix} The specifics of these effects depend on the material being studied and the quality of the crystal growth.

By combining positively and negatively doped semi-conductors, it is possible to form a ‘p-n junction’. In the p-n junction the electrons from the n-type semi-conductor diffuse into the p-type semi-conductor, and vice-versa, forming a neutral ‘depletion zone’, leaving fixed donor sites in the p-doped region and fixed acceptor sites in the n-doped region. Particles entering the depletion zone can still create electron and hole pairs, which now diffuse through the depletion zone towards the n and p doped regions respectively.

2.2 Semi-conductor Detectors

Semi-conductor junctions form the basis of the semi-conductor detector. The n and p doped materials form a depleted region with ideally no free vacancies or electrons. When the junction is reverse-biased (the p-doped material is given a negative potential difference with respect to the n-doped material) the holes from the electron-rich n-doped material and the electrons from the hole-rich p-doped material become the charge carriers. Radiation moving through the detector medium will displace an electron from the lattice in the depleted region, leading to the formation of a hole, and the two charge carriers are free to move towards their respective electrodes.

The number of electrons and holes produced by an interaction is dependent upon the ionization energy; Knoll⁶⁹ gives values of 3.61 eV per electron/hole pair in silicon and 2.98 eV per pair for Germanium. The number of pairs varies statistically, and is thus significantly larger than the band-gap. Electrons can be excited into any state; if the energy level is below the band-gap then either the electron will rest in one of the donor atom’s intermediary levels

^{ix} An electron or hole is said to be trapped when the charge carrier enters an energy level from which it cannot easily escape. These are commonly formed by impurities which provide levels within the band-gap. Lattice defects such as vacancies and interstitials can also act as traps by acting as acceptor and donor atoms respectively.

(statistically unlikely), or the electron will relax back to the initial state. If the electron is excited to a much higher state then it may either relax back down to the lowest level in the conduction band – releasing energy or continue in the higher energy state. In both scenarios, the extra energy is lost to the system as kinetic energy. This loss leads to a decrease in resolving accuracy of the system, especially given that the loss of energy varies with events. This variation is less than would be expected if the formation of charge carriers were a Poisson process. Accordingly, the Fano factor is introduced to relate the observed variance to the Poisson predicted variance.

Traditional semi-conductors such as Silicon and Germanium have many advantages over other detectors. The energy resolution of semi-conductor detectors is far better than that of (for example) scintillation detectors (a factor of 10 better than that of a Sodium-Iodide crystal⁷⁰), while the sensitivity to high doses is better than that of photo-multiplier tubes and dead time is significantly lower, being of the order of 10ns, rather than micro-seconds for (for example) proportional counters⁷¹. However, despite their many advantages, traditional semi-conductors suffer from a need to be either extremely pure (HPGe detectors), or doped and cooled to temperatures of around 77 K (Ge(Li) detectors). In addition, Germanium and Silicon are both relatively light atoms, and, as a result, the efficiency of these detectors is a factor of two below that of scintillator detectors,⁷² since photoelectric absorption varies as Z^4 . These requirements make semi-conductor detectors very expensive, and, in Hyper-Pure detectors, highly susceptible to radiation damage. However, they are the detector of choice in most circumstances, due to their excellent energy resolution and time response.

2.3 Cadmium Zinc Telluride as a Semi-Conductor Detector

For several years Cadmium Telluride (CdTe) has been used in large scale experiments, mostly due to the possibility of operating the material at room temperature and also its relatively good photo-efficiency (in CdTe the photon absorption is four times larger than in Ge and 100 times larger than in Si⁶⁹). Over the last few years, however, significant research effort has been devoted to studying Cadmium Zinc Telluride (CZT) as a semi-conductor material. CZT is of interest to researchers studying double-beta decay as it contains several double-beta decay candidates.⁷³ In addition to its suitability as a source, and thus as an intrinsic detector,

CZT detectors can also operate effectively at room temperatures and can be manufactured relatively cheaply, making them excellent choices for large detector systems (intrinsic or otherwise). Furthermore, as with CdTe, the high atomic number (Z) of the atoms comprising CZT results in high photon sensitivity compared to traditional semi-conductor detectors; this leads to an increased photo-efficiency.

When grown, pure Cadmium Telluride crystals are not ‘active’ to gamma rays; this means that the material cannot absorb gamma rays. In addition, the resistivity of the material is quite low. The value depends upon the dominant material; Tellurium leads to resistivities of 10^3 to $10^5 \Omega\text{cm}^{-1}$ with a dominance of vacancies (p-type) while Cadmium leads to resistivities of 10^5 to $10^6 \Omega\text{cm}^{-1}$ and an n-type semi-conductor. To promote γ -activity the crystals are doped, with Indium and Aluminium in the Cadmium, and Chlorine and other Halides in the Tellurium. However, these further reduce the resistivity (increasing the conductivity). The resistivity can be increased by annealing. Zinc increases the band-gap and thus the electrical resistivity further, reducing the ‘dark current’ noise – noise caused by thermal excitation of electrons. The presence of donor materials leads to levels which lie in the band-gap. These levels are the source of ‘trapping’ where charge carriers become trapped in the energy wells provided by these levels. Those levels which lie below the Fermi level trap holes, while those which lie above the Fermi level trap electrons. Trapping can be modified by increasing the number of donors of one type; by increasing the number of free electrons, the traps for electrons can be filled, raising the Fermi level. This process then increases the lifetime of the electrons. However, the converse is also true, the lifetime of the holes is decreased, in addition, the conductivity is increased due to the increase in electrons and the thermal noise is also increased.

Table 2 shows the band-gap and ionization energy for several major semi-conductor materials. It is clear that, while CZT suffers from a significantly worse energy resolution than either Silicon or Germanium, the 3-fold increase in the density relative to Silicon, and factor of 2 increase in atomic number, leads to substantially better photo-efficiency.

Material	Atomic Number (Z)	Density (g/cm ³)	Bandgap (eV)	Ionisation Energy (eV per e/h pair)	% Energy Resolution at 122 keV	% Energy resolution at 662 keV
Si (77K)	14	2.33	1.16	3.76	0.451 %	
Ge (77K)	32	5.33	0.72	2.98	0.328 %	
CdTe (300K)	48/52	6.06	1.52	4.43	2.869 %	
HgI ₂ (300K)	80/53	6.4	2.13	4.3	2.623 %	0.900 %
Cd _{0.8} Zn _{0.2} Te (300K)	48/30/52	6	1.64	5.0		1.752 %

Table 2 - Table of Semi-conductor material properties showing atomic number, density, size of the Bandgap between the conduction and valence bands, ionisation energy (the energy required to produce each electron/hole pair) and the percentage energy resolution at 122 and 662 keV.⁶⁹

Impure semi-conductors demonstrate different qualities for electrons and holes. In Silicon the mobility at 77 K (standard operating temperature for a pure Silicon detector) is $2.1 \times 10^4 \text{ cm}^2 \text{V}^{-1} \text{s}^{-1}$ (electrons) and $1.1 \times 10^4 \text{ cm}^2 \text{V}^{-1} \text{s}^{-1}$ (holes).⁷⁴ In CZT however, the difference is substantially larger: Zumbiehl⁷⁵ puts it at the order of a factor of ten, while Knoll⁷⁶ gives values of $1350 \text{ cm}^2 \text{V}^{-1} \text{s}^{-1}$ for electrons and $120 \text{ cm}^2 \text{V}^{-1} \text{s}^{-1}$ for holes.

This difference in mobility means that CZT detectors show a markedly slower response at the cathode than at the anode. In most semiconductors the relatively small difference in collection time means that the energy resolution on the anode and cathode is comparable. In addition, if an interaction occurs in the middle of the detector, the signal on the cathode and anode will be formed simultaneously. Thus a time delay between collections on the two electrodes gives depth information about the source of the interaction.

In CZT, since the average life-time of the holes before they become ‘trapped’ is less than that of the electrons, and can be substantially less than the time taken for the holes to traverse the detector (Knoll gives lifetime before trapping values of 50-300 ns for holes and 0.1-10 μs for electrons⁷⁶), then the holes may not reach the cathode before the electrons reach the anode. This fact, combined with the significant difference in mobility of the two charge carriers, means that not only is it not possible to use the time delay to determine the depth of the

interaction, but also, that the energy resolution on the cathode is extremely poor. However, it is possible that this defect could be used to calculate the depth of the interaction; if the signal is generated when the electrons reach the anode, then the signal collected upon the cathode is a function of the depth of the interaction from the anode.

Signal collection at the electrode is a combination of two components: first, the collected charge from the carrier reaching the electrode and, second, the charge induced by the carrier which is a function of the distance from the electrode (see Figure 9). This induction means that a nearby electron can induce a signal, and the hole (which is further away) induces a slightly smaller signal of the opposite sign. As the electron approaches the anode the hole moves away and the combined signal increases until the electrons reach the anode and are collected. The collected electrons are drawn away and the holes continue to move towards the cathode where they are collected. This effect can cause significant problems for events near the anode; when the electrons are collected, the holes still induce a significant cancelling signal. This decreases the energy resolution of the detectors near the anode, and, in a 2-dimensional spectrum of the cathode against the anode, a significant energy ‘tail’ can be seen. This problem is commonly redressed with CZT detectors by matching the shaping time on the anode signal to the time required to collect across the detector⁷⁷. Thus it is possible to disregard the contribution of the holes on the anode. However, this method also removes the ability to measure the signal collected on the cathode, and thus removes any possibility of locating the depth of the interaction.

Similar problems, arising from ion mobility, have been corrected in ion chambers by the use of a ‘Frisch grid’: ⁷⁸ in this case the anode is moved away from the interaction chamber and a grid put in its place to correct the reduced electric field (see Figure 8). The grid shields the anode from the slow moving ions and stops them inducing a current upon the anode. As a result, the electrons also only induce a signal upon the anode as they pass through the grid. A similar solution can be implemented in semiconductor detectors by the separation of the anode structure into a Co-Planar Grid.

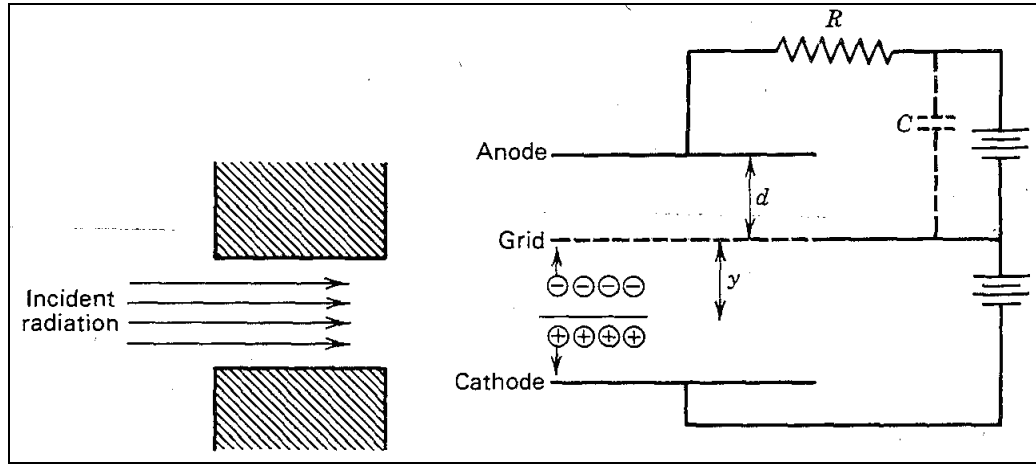


Figure 8 - Diagram of a 'Frisch grid' in operation. Ion pairs are formed in the lower part of the detector (between the cathode and the grid), where the positive ions are attracted to the cathode and the electrons travel through the grid and then to the anode. The ions cannot induce any signal upon the anode, and the extra distance travelled by the electrons accounts for the different mobilities.⁷⁸

An alternative technique is to use the ‘small pixel effect’ (a product of having small pixel width to pixel depth ratios) to reduce the induction effect at ‘large’ distances from the electrode. To understand this effect, it is necessary to consider the process by which a signal is induced upon an electrode within the pixel.

The signal induction on the electrodes can be described by the Shockley-Ramo theorem,⁷⁹ as encapsulated in equation 2.3.1.

$$S = -q^{n,p} \sum_{j=1}^m (\phi_{jF}^{n,p} - \phi_{jI}^{n,p}) \quad (2.3.1)$$

where $\phi_{jI}^{n,p}$ corresponds to the initial ‘weighting potential’ (the fraction of the charge carrier’s charge induced at that distance from the electrode) for charge carrier j of type n or p (electrons or holes) at its starting point, while $\phi_{jF}^{n,p}$ is the ‘weighting potential’ at the final point and q is the charge of the charge carrier of type n or p . These ‘weighting potentials’ for a moving charge at position x , y and z can be defined as being a combination of three distinct functions, each limited to one dimension.

$$\phi(x, y, z) = X(x)Y(y)Z(z) \quad (2.3.2)$$

For a detector which has a pixelated anode in the x-y plane, this linear combination can be shown^{75,80} to be a summation of a sinusoidal distribution in the x and y dimensions (the pixelated plane of the detector) and a hyperbolic sine in the z dimension (the depth of the pixel);

$$\phi(x, y, z) = \sum_{m=1}^{\infty} \sum_{n=1}^{\infty} A_{mn} \sin\left(\frac{m\pi}{a}x\right) \sin\left(\frac{n\pi}{a}y\right) \sinh\left(\frac{\pi\sqrt{m^2 + n^2}}{a}z\right) \quad (2.3.3)$$

where m and n are the limits of the summation, W is the width of the pixel, a is the width of the detector array and L is the depth of the pixel. The coefficient A_{mn} is given by;

$$A_{mn} = \frac{4}{mn\pi^2 \sinh\left(\left(\frac{\pi\sqrt{m^2 + n^2}}{a}\right)L\right)} f_m f_n \quad (2.3.4)$$

where f_m and f_n are defined in terms of the functions:

$$f_m = \left(\cos \frac{m\pi(a+W)}{2a} - \cos \frac{m\pi(a-W)}{2a} \right) \quad (2.3.5)$$

$$f_n = \left(\cos \frac{n\pi(a+W)}{2a} - \cos \frac{n\pi(a-W)}{2a} \right) \quad (2.3.6)$$

The final signal induced is then given as a combination of the positions of the hole and the electron as shown in equation 2.3.1. Since m and n are the limits of the summation, their infinite nature present the largest challenge with utilising the Shockley-Ramo theorem and some reasonable compromise has to be sought. Typically values of ~ 100 provide reasonable convergence. It can be seen that the multiplier A_{mn} , which has a dependence on f_m and f_n , requires the weighting potential $\phi(x, y, z)$ to be a function of the ratio W/L – the ratio of the pixel width to depth.

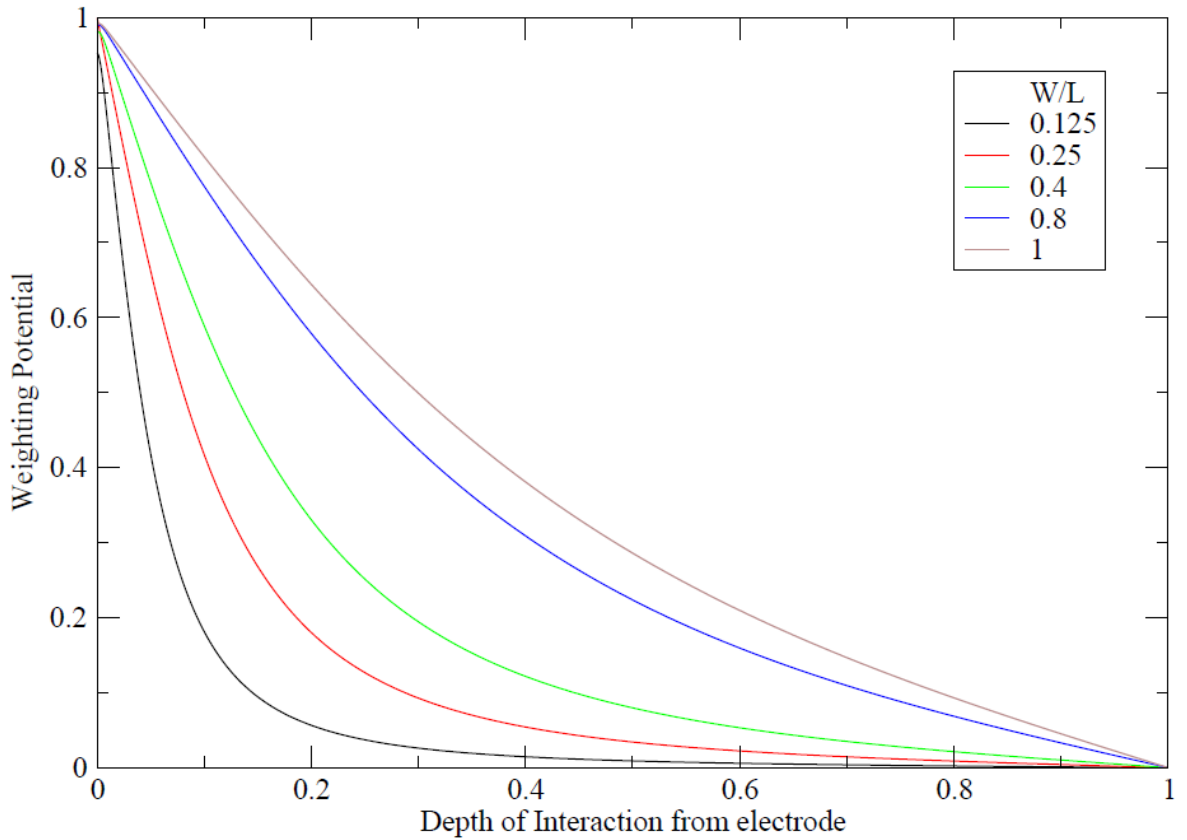


Figure 9 - Weighting potential as a function of depth of interaction while varying pixel-width to pixel-depth ratio (W/L). The weighting potential indicates the fraction of the carrier's charge that is induced upon the electrode as a function of distance from the electrode. At W/L ratios of 1, the induced charge decreases almost linearly with distance, but as the ratio decreases, the induced signal falls off rapidly away from the electrode.

Figure 9 shows this weighting potential $\phi(x, y, z)$, for electrons at varying distances through the detector from the anode, for pixels of various ratios of W/L . It can be seen that in a planar detector (W/L ratio equal to 1) the induction effect is roughly linear. However, as the ratio of the detector's width to depth reduces, the induction effect approaches an exponential drop as a function of distance. For such extreme ratios it can be seen that a charge will not be observed unless it is rather close to the electrode (at depth ≈ 0) in Figure 9. This is what is known as the small pixel effect.

2.4 Simulating the Shockley-Ramo Theorem and the Small Pixel Effect

In order to understand the charge collection properties of a pixelated detector, a FORTRAN code was written to simulate the behaviour of a CZT detector using Equation 2.2.1.⁸¹ The simulation operates by modelling the interaction process within the detector. As a gamma ray or particle travels through the detector it has an exponentially varying probability of interacting, the variation of which is given by $\exp(-\mu z)$, where μ is the linear attenuation coefficient and z is the distance travelled through the detector medium. Upon interaction a number of electron/hole pairs are produced; this number is characterised by:

$$\left(\frac{F \cdot E}{WE} \right)^{\frac{1}{2}} \quad (2.4.1)$$

where F is the Fano factor, E the energy deposited during the interaction and WE is the average pair production energy. These particles will then move through the detector to a distance from the interaction point governed by:

$$D = \mu_c t \frac{V}{L} \quad (2.4.2)$$

where μ_c is the mobility of the charge carrier, V is the applied voltage, L is the thickness of the detector and t is the lifetime of that individual particle before trapping, the probability distribution of which is given by $\exp(-t/\tau)$, where τ is the mean life-time of the carrier before trapping. These particles then diffuse through the x and y planes in a manner described by a Gaussian distribution, as seen in equation 2.4.3:

$$\varphi(r) = \frac{e^{-\left(\frac{r^2}{2\sigma^2}\right)}}{2\pi\sigma^2} \quad (2.4.3)$$

where

$$r = \sqrt{x^2 + y^2} \quad (2.4.4)$$

$$\sigma = \sqrt{2D_c t} \quad (2.4.5)$$

$$D_c = \frac{kT}{q} \mu_c \quad (2.4.6)$$

$\phi(r)$ is the probability of a particle being at distance r from the interaction point, D_c is the diffusion coefficient, k is the Boltzmann constant, T is the temperature and q is the charge of the charge carrier.

The Shockley-Ramo theorem (described by equation 2.3.1) can then be used to calculate the induced signal from the particles at these positions. In order to model the response of the detector, a lattice of interaction points was studied and a fixed number of charge carriers were created. The response was then calculated at regular time steps as the charge moved through the detector material, until the holes reached the cathode. The trapping was simulated by reducing the number of charge carriers by the number whose lifetimes have expired. At each time-step, the induced signal was re-calculated.

Consideration of the number of lattice points to be studied, as well as the number of time steps, was important in order to limit the computation time. These both have significant impact upon the quality of the resulting data, with larger values producing more accurate results. Also of interest are the values of the m and n limits in the Shockley-Ramo theorem. These are the summation limits and, while theoretically infinite, Zumbiehl et al⁸⁰ suggest that a value of 1000 should be adequate provided that sufficient interactions are studied. In practice, observation showed that a value of 100 led to usable results but showed a far greater dependence on the other factors in the weighting equation (specifically the value of W) than exhibited at higher values of m and n . These constraints notwithstanding; the major limiting factor on the choice of m and n was that of execution time; a factor of 10 increase in both values would lead to a hundred-fold increase in the calculation time.

This simulation was then used to show the signal collected on the anode and cathode for events at different depths within the detector and finally to reveal the complete spectrum of cathode signals plotted against anode signals for events at different interaction depths. These simulations use a pixel width to depth ratio of 0.1. Figure 10 shows the signal induced on the anode, when the electrons reach the anode, for varying depths of interaction: an interaction depth of 0 is for interactions occurring on the anode, while a depth of 1 is for interactions occurring on the cathode. This figure shows that for events near the anode, the holes are insufficiently distant from the electrode and thus induce a significant cancelling signal. For interactions at greater distance from the anode, this cancelling effect is minimal.

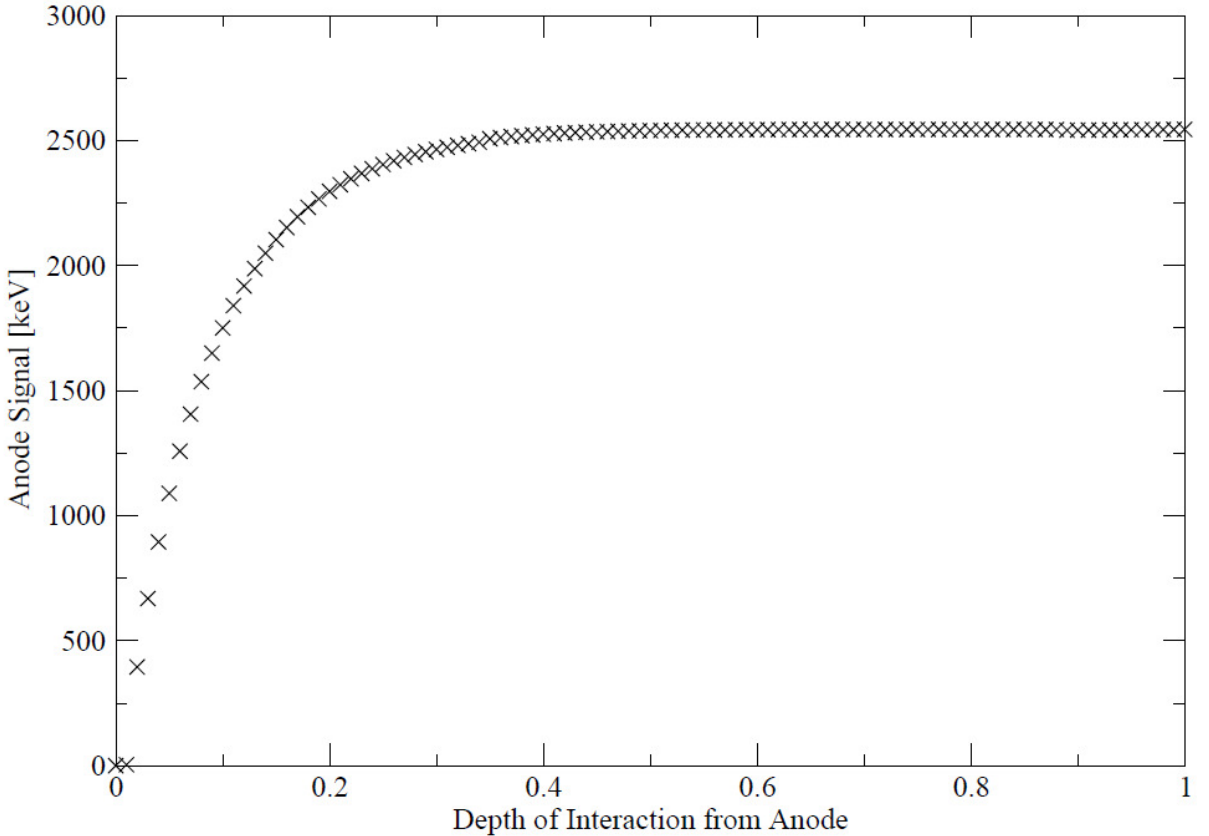


Figure 10 - Signal induced on the anode as a function of the depth of interaction. At events near the anode (Depth=0) the holes are still near the anode when the electrons are collected, accordingly they induce a large signal cancelling the electrons. As the depth increases, the holes are further away, reducing the induced signal until, the holes induce no signal upon the anode when the electrons are collected.

Figure 11 shows the signal induced on the cathode at the time when the electrons reach the anode. For interactions near the cathode (at a depth of 1), the signal induced on the cathode is

near zero as the holes have been fully collected. As the interaction depth decreases the number of holes left uncollected, and thus able to induce signal, increases until a critical point is reached, where the electrons start to reach the anode before the holes can reach the cathode. As the depth decreases beyond this point, the distance from the holes to the anode increases and the induced signal reduces accordingly.

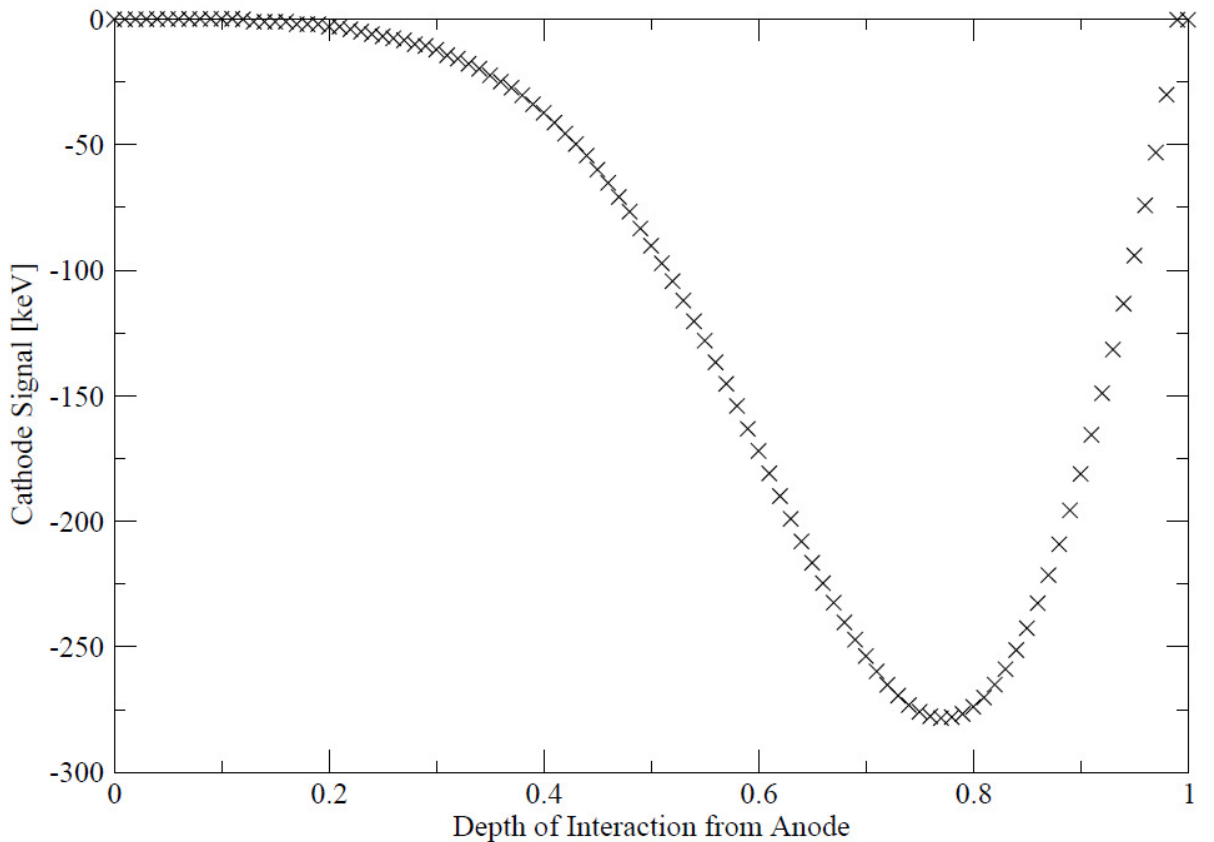


Figure 11 - Signal induced on the cathode as a function of the depth of interaction. At events near the cathode (Depth=1) the electrons lie near the cathode as the holes are collected, cancelling the signal, however, as the depth from the anode decreases (Depth=0.9) the electrons move away from the cathode, reducing the cancelling effect. At Depth=0.77, the electrons start to reach the anode before the holes reach the cathode, leading to incomplete collection of the holes; as the depth continues to decrease, the number of holes collected reduces and so does the signal.

Finally, a plot of the signal on the anode against the signal on the cathode is shown in Figure 12. The distinctive energy tail and extended cathode signal can be seen. In addition, the varying deposition in the cathode, at full collection in the anode, shows the incomplete collection of holes due to trapping within the detector material. This effect can be used as a depth marker for interactions, as the distance a hole will travel before trapping is dictated by

the probability distribution seen in Equation 2.4.2. The final feature of interest is those events which appear to be fully collected on the anode, but seem to be incompletely collected on the cathode and lie below the events which are due to poor hole mobility. These are an artefact of the simulation, appearing as a result of events occurring on the cathode – having reached the cathode within the simulation, the holes are then removed and cease to play any part in the simulation. In the real world, these points would lie at higher cathode signal values as the collected signal is also important.

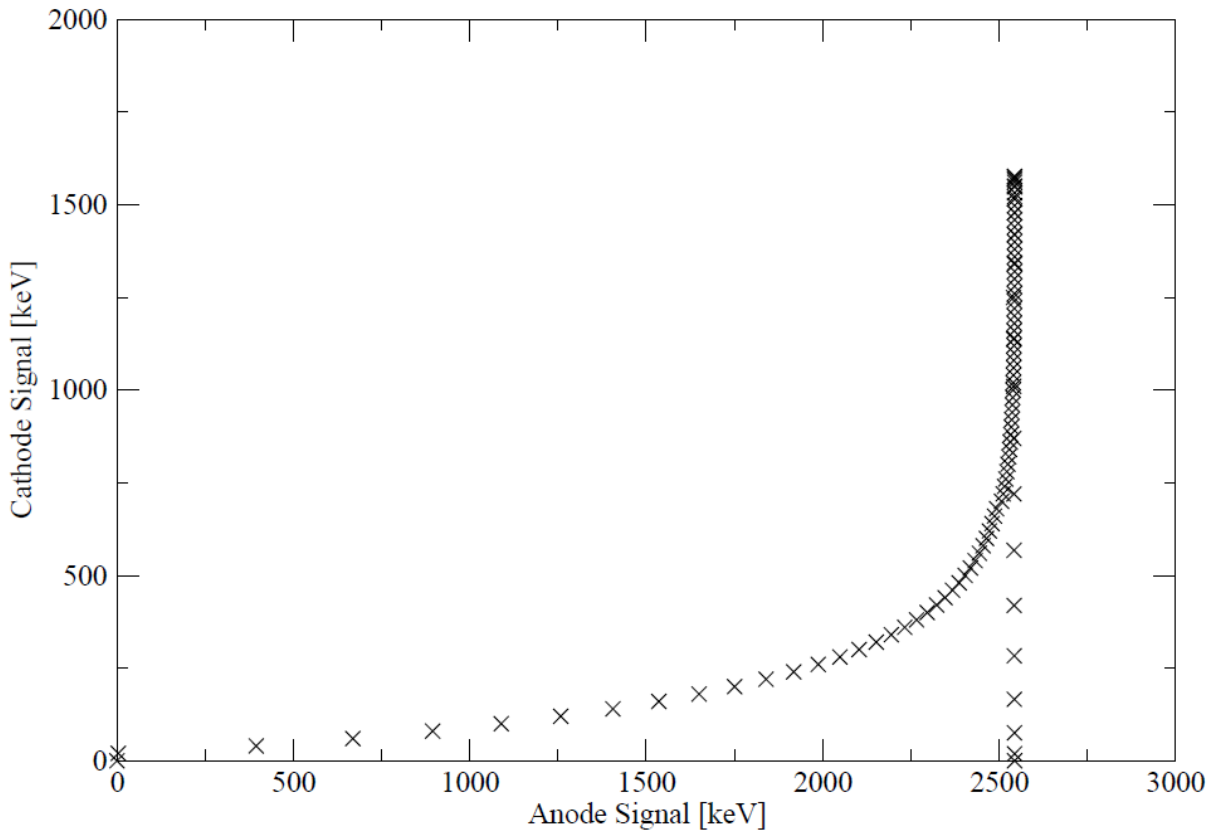


Figure 12 - Simulation of the spectrum produced by plotting the signal on the cathode against the signal on the anode at the time the electrons strike the anode. Events which lie near the anode show a small signal on both the anode and cathode, as the signal is collected when the electrons reach the anode, no holes are collected on the cathode, and there is a strong cancelling signal from the holes which still lie close to the cathode. This forms the long energy tail. As the interactions move away from the anode, the anode signal rises rapidly, due to the reduced induction from the holes but the cathode signal increases slowly due to induced signal from the holes. As the interactions approach the cathode, holes begin to be collected, leading to a sharp rise in the cathode signal, however, this then falls away in this simulation as the electrons induce a strong cancelling effect, leading to the events which lie below the peak at an anode signal of 2500 keV and cathode signals of 0 to 500 keV.

Measurements were performed, with real detectors, of the anode signal intensity at varying cathode signal values and are plotted in Figure 13. The left side of the figure indicates those events which are fully collected on the anode but minimally collected upon the cathode, while the right side shows those events which are fully collected on both electrodes. It is apparent that the two detectors behave very differently. The smaller pixel detector shows an almost flat distribution, suggesting that the events are evenly distributed; however, the larger pixel detector shows a dramatic increase in counts near the cathode suggesting a non-linear response, or that those events which interact in the middle of the detector are fully collected on both electrodes and thus appear to occur near the cathode.

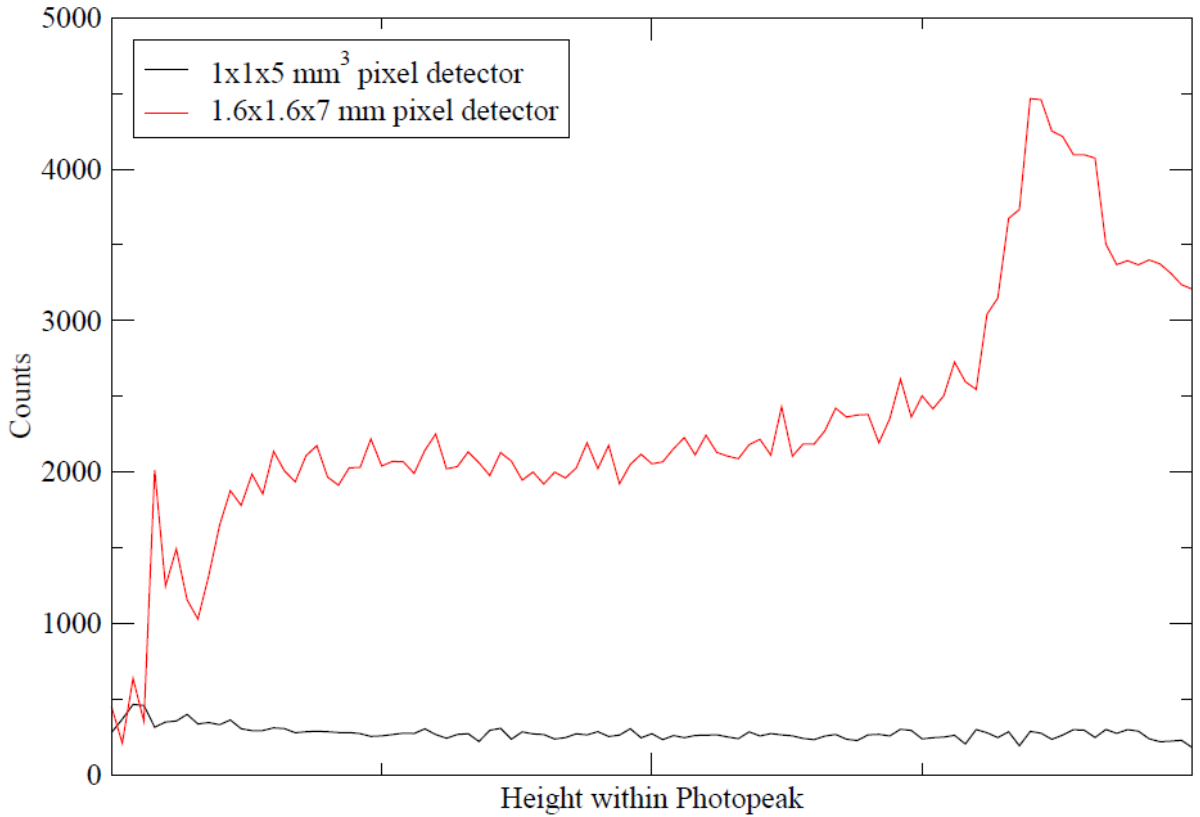


Figure 13 - Figure showing the number of counts deposited at varying depths within the photopeak (the right hand side indicating the top of the photopeak). The photopeak measured was a 1332 keV gamma ray peak from a ^{60}Co source situated above the anode face.

A simulation was made of 20,000 interactions for a 2000 keV gamma ray at randomised depths within the detector and at randomised positions, laterally both within the detectors and also up to half a pixel-width outside the detector in both the x and y planes (Figure 14).

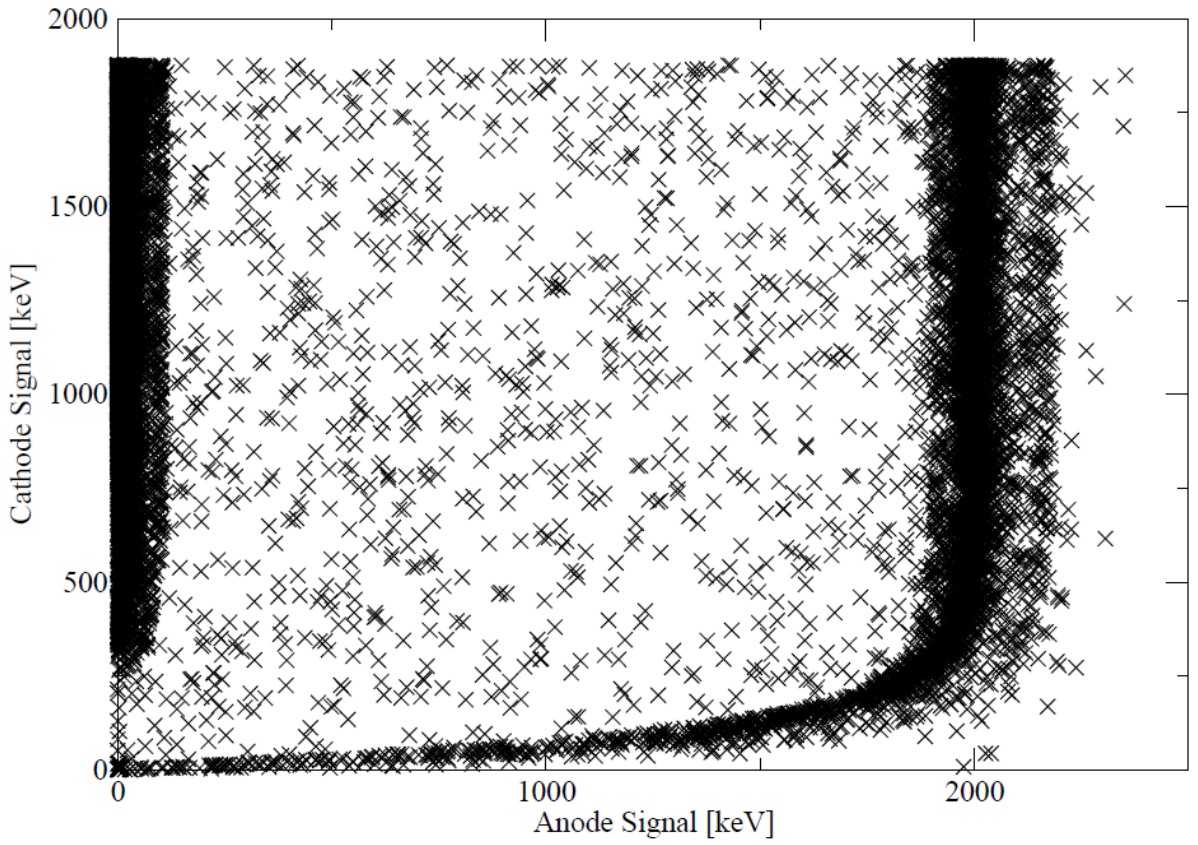


Figure 14 - Simulation of 20,000 2 MeV gamma rays interacting at random depths within the detector and at random positions from half a pixel-width outside the detector in both the x and y planes. As in Figure 12 the energy tail and sharply rising cathode signal are caused by events near the anode and cathode respectively. The broad photopeak is due to the sinusoidal nature of the simulation causing perturbations near the edge of the pixels. The strong peak near an anode signal of 0 keV is due to events which lie outside the pixel but which are collected on the non-pixelated cathode. Finally, events which lie outside the pixel, but whose charge carriers induce signal inside the pixel lie in the spread between the two strong peaks.

This final simulation shows a signal peak at about 2000 keV, with a few points beyond this; these points are due to the fitting mechanism, which uses a combination of sine waves to match the distribution in the x and y dimensions. As a result, when the lateral position within the pixel is plotted against the signal collected on the anode, a sinusoidal fluctuation is seen (shown in Figure 15), with a strong deformation near the edges of the pixel. Higher summation limits would constrain these points; however, they are limited by the size of the array of pixels and the summation limits – these constraints are discussed by Zumbiehl et al⁸⁰.

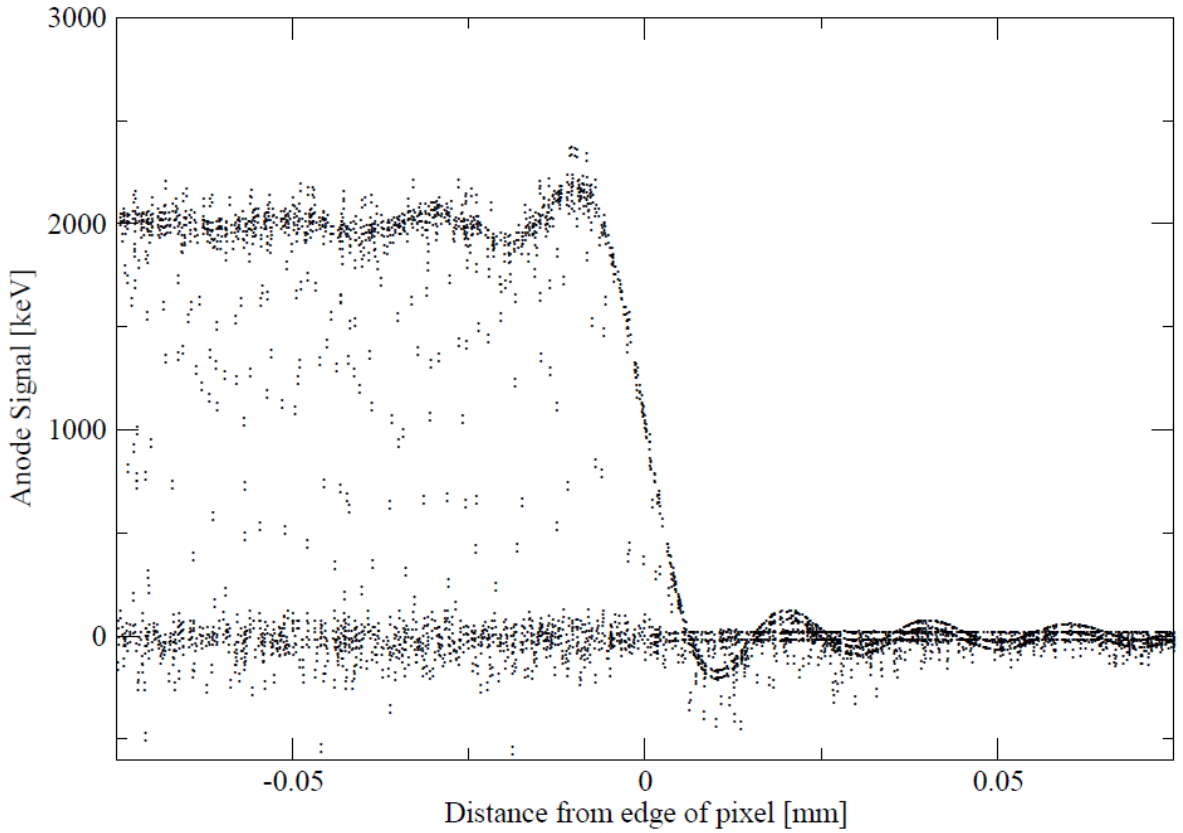


Figure 15 - Simulation showing the sinusoidal fluctuation seen at the edges of the pixel. For events located near the sides of the pixel, a strong sinusoidal perturbation is seen due to the fitting of sinusoidal waves to a square wave.

The apogee of the photopeak in Figure 14, seen at around 1900 keV on the cathode, is due to a signal fully collected on electrodes (i.e. from events near the cathode). The cathode signal is not maximal, however, as some electrons will remain near the cathode and will induce a negative charge. As the cathode signal reduces, the apparent depth of interaction from the anode increases, this reduction in cathode signal is due to ‘trapping’ of the holes. The curvature at low cathode signal is due to events near the anode, where the holes induce a significant positive signal onto the anode. In addition, events can be seen at mid-range anode signal values; these are caused by interactions just outside the pixel, which induce signal in the simulated pixel. Finally, a large peak at about an anode signal of zero shows interactions some distance outside pixel, which induced only a very small amount of signal - or none at all - in the anode of the active pixel, while still inducing signal in the un-pixelated cathode. In a real measurement, other features would also be present; a Compton edge and associated Compton scatter events would be present, causing significant numbers of events to lie between the photopeak and zero anode signal. In addition, low energy noise and events where

the gamma-rays were incompletely collected would further add to the spectrum. The simulation seen in Figure 14 can be compared to the response of an actual detector, shown in Figure 16.

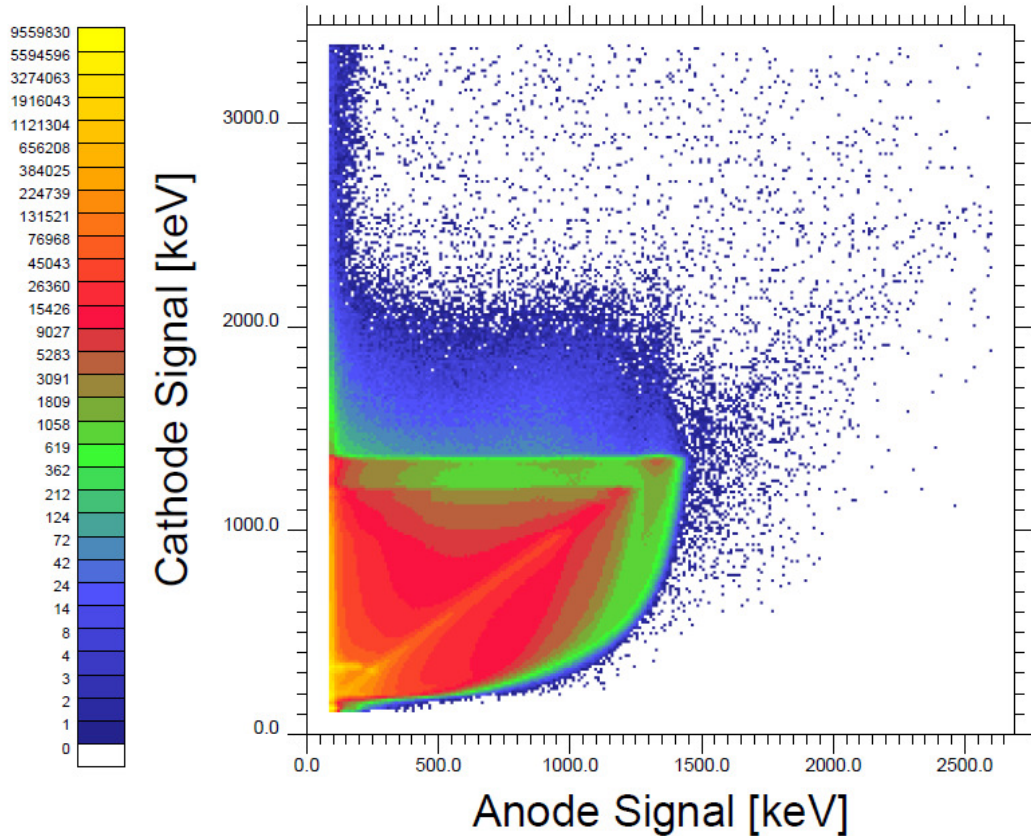


Figure 16 - Example spectrum of a $6.4 \times 6.4 \times 7$ mm 3 4×4 pixelated detector (corresponding to a W/L ratio of 0.23) showing the 1173 and 1332 keV peaks from a ^{60}Co source situated to the side of the detectors. As in Figure 14, low energy tails are seen extending from near the origin with rapidly rising anode signal, and then rising sharply with cathode signal. These are the photopeaks for events lying near the centre of the pixel and which are fully collected on the pixel. Events whose energy is fully collected on both electrodes form a diagonal line from the origin to the apex of the photopeaks. Events which are incompletely collected on the pixels form the continuum of peaks which lie below this diagonal, while events which are shared between pixels form the distribution above the diagonal.

Figure 16 shows a spectrum for a CZT detector with a 0.23 width/depth ratio measuring a ^{60}Co gamma-ray source. As with the simulation, the photopeak can be clearly seen, exhibiting events which are completely collected in both electrodes (i.e. near the cathode), where holes are trapped and the cathode signal is reduced (at varying depth of interaction) and finally where the energy tail becomes a prominent feature (events near the anode). The Compton

edge (and associated incompletely collected events), along with events which are incompletely collected without undergoing Compton scatter both provide significant intensity of events at lower energies than the photopeak. Finally, a distribution of low electrical energy noise and events inducing limited signal into adjacent pixels (while still collecting large signal on the cathode) can be seen near the origin. It is clear that while the cathode signal is potentially useful for depth measurements, the corresponding tail greatly decreases the energy resolution. For the 1332 keV peak seen here, an energy resolution of about 235 keV is observed when including the entire peak, while an energy resolution of only 80 keV is seen if a limited range of cathode signals are considered close to the maximum value. It is clear that there is a potential for significantly improving the energy resolution of the detectors if this tail can be removed.

Many of the challenges presented by CZT are a result of the poor hole mobility. Accordingly, it is important to balance the pixel width to depth ratio to maximise energy resolution and efficiency while maintaining the depth sensitivity of the cathode signal. As much work has already been done to study such pixelated detectors,⁸² the details of the detectors currently available are fixed. As described earlier, the COBRA proof of principle detector consists of four 1cm³ detectors. However, the studies into pixelated detectors at Birmingham have utilized two different detectors, both made by eV Products:⁸³

- 4×4×5 mm³ detector with the anode divided into 16 pixels of 1×1 mm²;
- 6.4×6.4×7 mm³ detector with the anode divided into 16 pixels of 1.6×1.6 mm².

The differences in dimensions (and accordingly pixel width to depth ratios) have meant that comparisons can be made between the two designs.

3. Improving the Energy Resolution and Sensitivity of CZT Detectors for use in Neutrino-less Double-beta Decay Measurements.

When collecting signals from both electrodes, the depth sensitivity of Cadmium-Zinc-Telluride (CZT) permits a pixelated CZT detector to be used as a 3-dimensional position sensitive detector. In order to track events with high resolution and sensitivity, and obtain the required energy resolution, CZT detectors must be designed carefully to ensure minimisation of the energy tail caused by poor hole mobility in the semi-conductor. Software processing must be used to improve this response. Background reduction is essential as the long half-lives of double-beta decay processes mean that, even in a large detector, very few events will be measured each year. Reduction of background ensures that all events that take place can be measured accurately without distortion of the signal. Thus, backgrounds produced by high-energy gamma rays undergoing Compton scattering, and the high energy sources themselves, must be suppressed. In addition, events which resemble double-beta events must be vetoed. In principle, the pixelated detector permits event characterisation, and hence backgrounds, to be suppressed.

3.1 Reducing Background and False Positives

In order to reduce background levels, it is necessary to select suitable operational environments, such as situating the experiment under several kilometres of rock to suppress cosmic ray interactions, and optimise the experimental design for low background, such as keeping the detector in a nitrogen environment to reduce radon gas exposure. In addition, detailed veto and trigger mechanisms may be used to remove events that do not represent double-beta decay events.

In order to eliminate gamma-ray interactions, their characteristic interactions must be understood; gamma rays interact in three ways:

- Photoelectric interactions produce electrons of nearly the same energy as the gamma itself. These cannot be easily distinguished from beta decay tracks (but can be reduced by the same mechanism as those used to reduce single-beta events).
- Pair production occurs when a gamma ray with energy exceeding 1022 keV is converted into an electron/positron pair. The electron is again difficult to distinguish from beta decay tracks, but the positron will undergo annihilation with another electron producing two gamma rays of energy greater than 511 keV, which can be tagged in coincidence with the electron to identify the pair-production event.
- Compton scattering is an event where the gamma ray scatters from an electron and loses some energy. In the event of a second interaction by the gamma ray, the event can be vetoed by requiring the active pixels not to be adjacent. If the gamma ray does not interact a second time within the detector, the event can be removed as a normal beta decay event.

In addition to gamma-rays, there are characteristic alpha particles and beta particles which arise from natural decay chains. These alpha particles are often released coincidentally with a gamma ray, which provides a simple veto method. Furthermore, the high energy deposition over a short distance (and, assuming no sources within the detector itself, the focus of the deposition near the edge of the detector) can be easily distinguished from other decay types.

There is also significant background from Cosmic-ray interaction products, which are often high energy and can range from neutrons and protons to the more exotic (muons, pions, etc). Cosmic-ray sources are most easily reduced by situating the source deep underground, with a large neutron shield to remove neutrons and a veto shield (such as a calorimeter) to remove other sources. This veto is also suitable for removing other external sources.

It is clear then, that the most significant challenge comes in reducing single-beta decay signatures; from other isotopes within the detector material, from gamma ray interactions within the detector or from other external sources. The similarity between single and double-beta events makes it difficult to distinguish between them, which must be done in order to reduce the background sufficiently for double-beta decay measurements. Previous work⁸⁴ has shown that it is possible to distinguish between single and double-beta decay tracks with an efficiency of 70% by using a trio of event-characterisation tests.

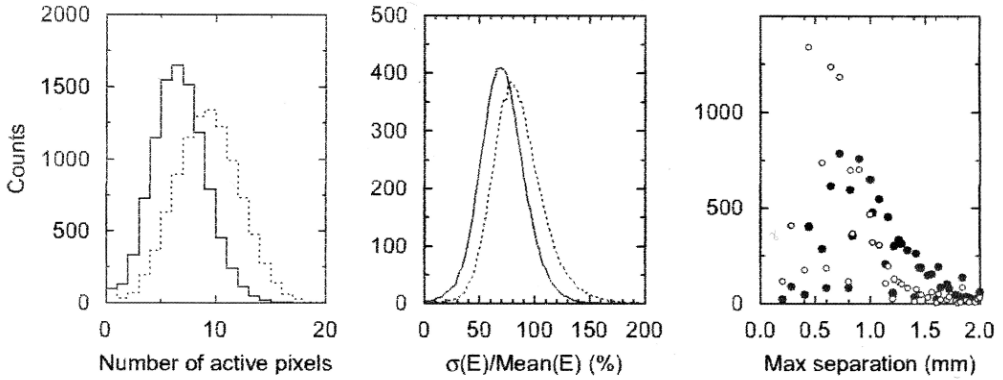


Figure 17 - Reproduction of Figure 4 from Bloxham et al⁸⁴ showing the 3 differences between single and double-beta decay tracks with energy of 2800 keV, double-beta events are shown in filled circles or with solid lines. Bloxham et al show that double-beta events will normally trigger fewer pixels, which are separated by a greater distance, and deposit energy with a more even distribution.

In order to evaluate the degree to which event types may be characterised; a series of simulations were performed by Bloxham et al.⁸⁴ using the Geant4 simulation framework. These simulations were performed for 2.8 MeV single-beta and double-beta events. Figure 17 shows the three tests devised by Bloxham et al. to distinguish between single and double-beta decay events:

- The number of pixels triggered (indicative of the mean free path) by a single-beta source and a double-beta source have different distributions. It has been shown that double-beta events activate fewer pixels. This is due to the energy deposition pattern of beta decay events, whose range scale quasi-exponentially with the energy of the particle. Thus, two electrons with 1.4 MeV of kinetic energy will travel less distance than a single electron with 2.8 MeV of kinetic energy, and will deposit energy in fewer pixels.
- The standard deviation of the energies, deposited in the separate pixels, as a ratio with the average energy deposited ($\sigma(E)/\text{Mean}(E)$) is the second measure. Since the energy deposition of a beta particle is largest at the end of the track, two particles with

1.4 MeV will deposit more uniformly than a single particle of 2.8 MeV and thus will have a lower standard deviation to average energy deposition.^x

- The maximum separation of the pixels with most energy deposited within them is the final test in this technique. Ideally, the separation would be between the end points for the two electron tracks in double-beta decay or between the two pixels of most intense deposition, which would commonly be close to the endpoint of the path for single electron tracks. However, double-beta decay events can have any angle of emission and could have minimal separation between the endpoints. This test is then the hardest to demonstrate explicitly and is strongly dependent upon the method of calculating the separation.

The necessity of these characterisation tests is to reduce the single-beta background (for instance ^{214}Bi , which beta decays with an energy of 3.272 MeV⁸⁵) and thus increase the sensitivity of the detector to double-beta decays. By using this trio of tests, Bloxham et al. suggested that it should be possible to distinguish between the two types of events with a success level of around 70%. An attempt was made to reproduce these results in order to verify the simulation software developed for the COBRA collaboration.

A series of Monte Carlo simulations was performed; these simulations were run using the POISON-0.9.2 front-end for GEANT4.⁸⁶ POISON is a front-end developed for the COBRA collaboration by Henning Kiel at the University of Dortmund, which allows the user to build a COBRA style detector array and simulate the generation and behaviour of several of the key radiation sources relevant in neutrino-less double-beta decay searches. For these simulations, POISON-0.9.2 was run on Geant4.7.1. The detectors were simulated as a 16 by 16 array of 200 micron², 7 mm deep pixels as shown in Figure 18. As with the simulations of Bloxham et al. the total source energy was 2.8 MeV for both single and double-beta events.

^x From http://www.kayelaby.npl.co.uk/atomic_and_nuclear_physics/4_5/4_5_3.html (retrieved 23 Jun 2010) it can be estimated that an electron of 1400 keV will have a range of around 1 mm and a 2800 keV electron will have a range of some 2.3 mm.

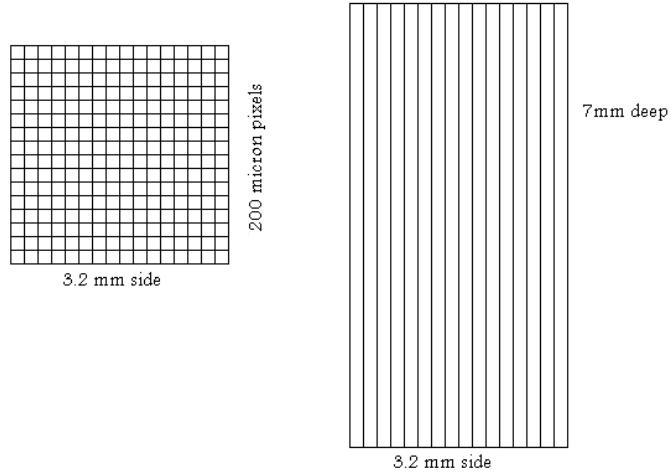


Figure 18 – Diagram of the simulated detector - $16 \times 16 \times 1$ array of $200 \text{ micron}^2 \times 7 \text{ mm}$ pixels. The left hand side shows the top view down onto the pixelated anode, the right side shows a side view of detector.

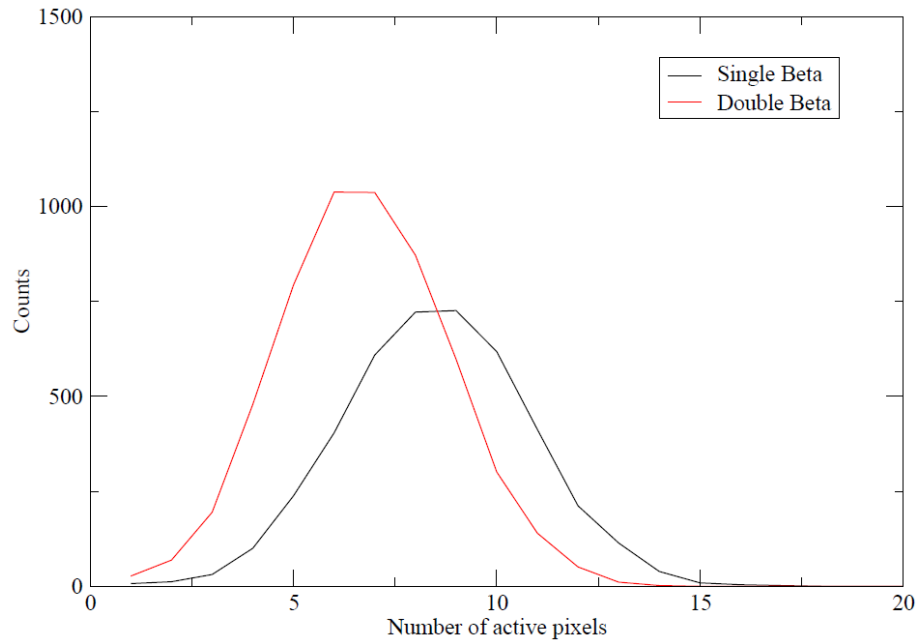


Figure 19 - Simulated reproduction of the left-hand graph from Figure 17. This simulation shows the distribution of the number of active pixels for single and double-beta events. The red line corresponds to the double-beta events while the black line is for the single-beta events. As with Bloxham et al, double-beta events trigger fewer pixels.

Figure 19 shows a simulation of the calculation performed in part one of Figure 17; the figure closely matches the results given by Bloxham et al. The centroid for single-beta events is found to be 8.5 pixels with a standard deviation of 2.3 pixels. Double-beta events show a

centroid of 6.7 pixels and a standard deviation of 2.0 pixels. These numbers appear to be quite close to those which would be extracted from Figure 17.

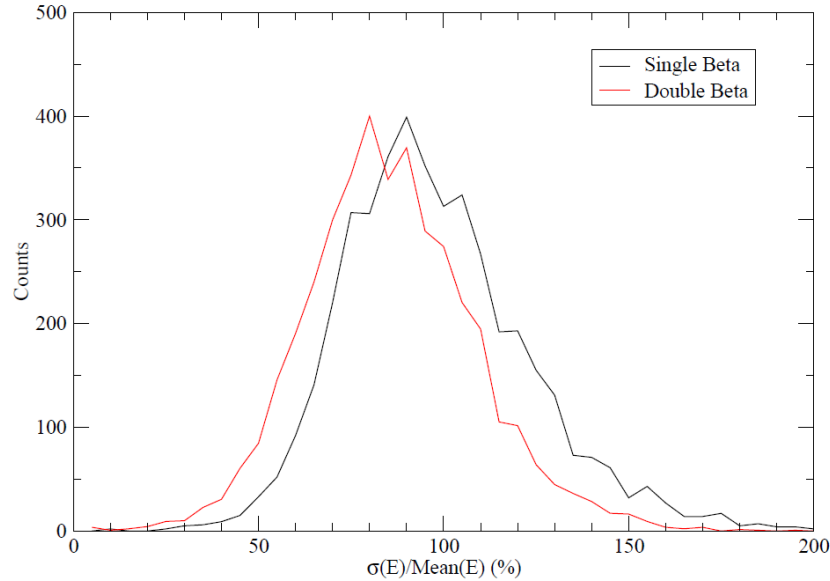


Figure 20 - Simulated reproduction of the central graph from Figure 17. This simulation shows the ratio of the standard deviation of energy deposited in active pixels to the average energy deposited for single and double-beta events. The red line indicates double-beta events while the black line indicates single-beta events. As with Bloxham et al, double-beta events deposit their energy more evenly.

Figure 20 shows a similar simulation of part two of Figure 17. Once again this figure resembles that shown in Bloxham et al's work (Figure 17). The single-beta events have a centroid of 97.9% with a standard deviation of 25.1%, while the double-beta events centre at 85.7% with a standard deviation of 22.8%.

Finally, Figure 21 shows the simulation of the final part of the analysis by Bloxham et al. shown in Figure 17; those separations which show no counts are due to separations that are not possible given the pixel size. The single-beta events are found to have a centroid of 0.98 mm and a standard deviation of 0.36 mm, while the double-beta events show a centroid of 0.78 mm and a standard deviation of 0.35 mm.

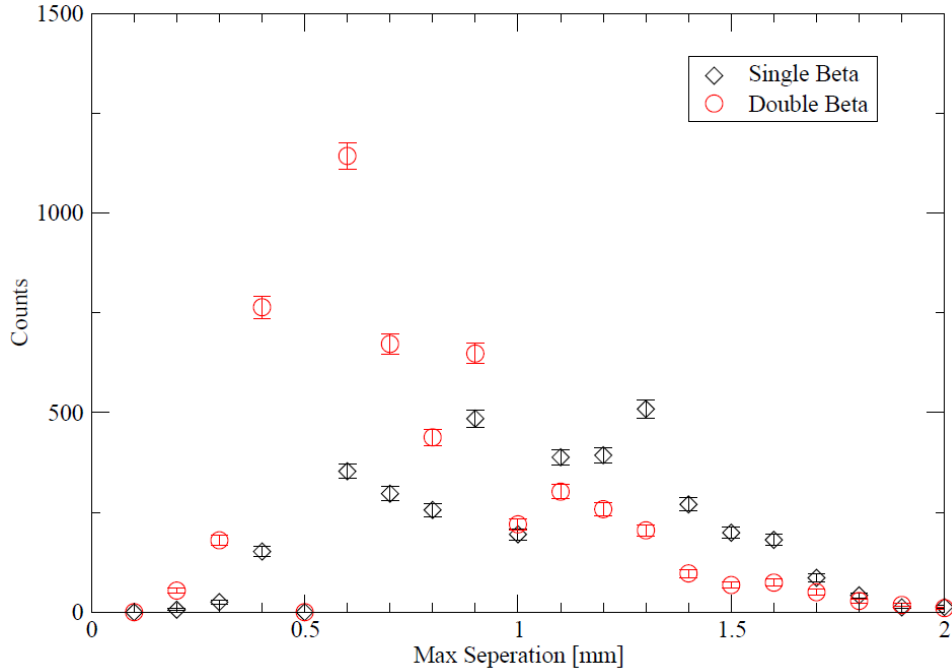


Figure 21 - Simulated reproduction of the right hand graph from Figure 17. This simulation shows the maximum separation of the two pixels with the highest energy deposition. The red circles indicate double-beta events while the black diamonds indicate single-beta events. Unlike Bloxham et al, this work suggests that double-beta events have a smaller maximum separation than single-beta events.

The simulation seen in Figure 21 shows a different distribution of maximum separation from that seen by Bloxham, whose work demonstrated that the maximum separation of deposition for two beta particles is around 0.25 mm greater than that for a single beta particle. The present analysis suggests that the opposite is true, that single-beta events have a greater separation (by almost 0.2 mm) than double-beta events. This difference is almost certainly due to analysis differences. This work assumed a 50 keV threshold energy, for a pixel to be considered in the distance calculation. Subsequent analysis has demonstrated that modifying this threshold could have a strong effect upon the distributions. This is due to beta particles depositing most of their energy at the end of the track; as such, a single-beta event will have a path which is marked by one end with small deposition, near the beginning of the path, and one end with large deposition. As the threshold energy increases, the pixels near the beginning of the track will be removed from the calculation, reducing the apparent distance travelled. Conversely, double-beta events will deposit significantly at the end points of both tracks, meaning that (excepting the limited range of angles where the separation of end points is less than the lengths of the individual beta tracks) the threshold will have minimal effect.

The increase in threshold energies reduces the centroid position of the single-beta-particle distribution without substantially changing the double-beta distribution, but this does not, even in the extreme case of 500 keV thresholds, move the distribution to lie at lower distances than the double-beta distribution.

A second possibility for the discrepancy is the method used to calculate the distance. Since the simulated pixels lie in an array of 16×16 pixels, they are addressed in rows from the bottom left of the array. Initially, the distance was then calculated between the first pixel found to be ‘active’ and the last, but this could mean that a distance was calculated along one face of the detector when a longer, diagonal, path was more suitable. Subsequently, a second technique was utilised, which calculated the distance between all available pair combinations of the active pixels. However, it was found that this made minimal difference to the spectra produced. It is not known which technique Bloxham et al. used to calculate the distance, or indeed whether they utilised an energy threshold or not.

There is a further factor which may play an important role. Within the POISON framework there is support for 3 different varieties of $0\nu2\beta$ decay,^{87,88} each of which will give unique signals. The logic for their inclusion within the POISON package, and indeed, one of the key justifications for detectors which can track particles, is that the angle of emission of the two electrons in these different decay processes will vary; this is an important test for which decay process has occurred and thus the ability to differentiate between the 3 processes is essential. The three varieties of $0\nu2\beta$ decay are demonstrated in Figure 22. The red lines and markers indicate double electron emission, while the green lines indicate double positron emission. The third method (blue) indicates the possibility of ‘right handed’ neutrinos. Measurements of neutrinos properties have thus far suggested that all neutrinos have left handed ‘helicities’ (the ‘helicity’ of a particle is said to be left handed if the direction of spin is opposite to that of the particle’s momentum) and that all anti-neutrinos are right-handed. This suggests that either right-handed neutrinos do not exist, or that their properties differ from those of left handed neutrinos. As such, they are suggested to be either very heavy (the ‘Seesaw mechanism’) or unable to interact via the weak force (‘Sterile’ neutrinos).⁴⁵ In the ‘Sterile’ case, these right-handed neutrinos could simulate neutrino-less double-beta decay without requiring the neutrino itself to be a majoran.

Figure 19 to Figure 21 are reproduced below (Figure 22) using all three different neutrino-less double-beta decay scenarios.

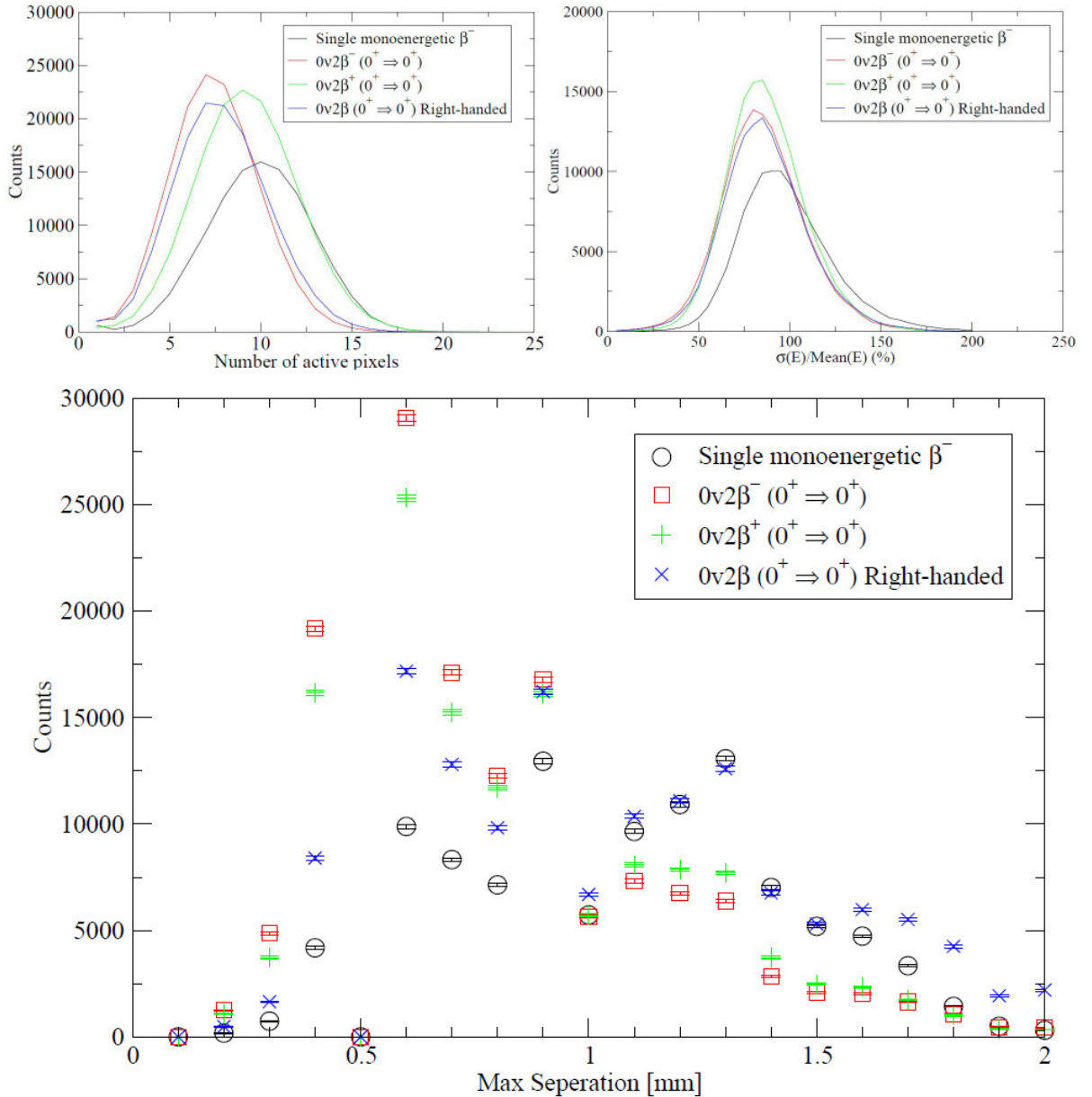


Figure 22 - Simulated reproduction of Figure 17. This simulation shows the number of pixels active (top left), the ratio of the standard deviation of energy deposited in active pixels to the average energy deposited for single and double-beta events (top right) and the maximum separation of the two pixels with the most deposition (bottom). The black lines and circles indicate single-beta events, the red lines and squares are indicative of 0v2 β^- events. The green lines and plus markers show 0v2 β^+ events and finally the blue lines and crosses indicate right handed 0v2 β events. The techniques used to calculate these methods are taken from *Atomic Data and Nuclear Data Tables* **61** (1995) p43.^{89,90}

Despite the difference between this work and Bloxham, it is still possible to identify a difference in the distributions for single and double-beta events and thus support Bloxham et al's claim that it is possible to remove 70% of single-beta events by combining the three characterisation tests to determine which events are single-beta and which are double-beta. However, without more details regarding the work undertaken by Bloxham, it is not possible to fully explain the difference between these two analyses. The work undertaken to examine the different processes that POISON simulates did not reveal which method Bloxham et al. utilised. The simulations do show that both left and right handed $0\nu2\beta^-$ events exhibit similar patterns of behaviour, noticeably different from $0\nu2\beta^+$ events. Unfortunately, this means that it may be harder to differentiate single electron and $0\nu2\beta^+$ events (although they may be easily distinguished by the 4×511 keV gamma-rays produced by the $0\nu2\beta^+$ decay) and that the method outlined by Bloxham et al. cannot easily be used to differentiate between left and right handed double-beta events.

3.2 Determination of the Optimal Pixel Size of a Pixelated CZT Detector

As discussed in Section 3.1, it is essential to reduce the background, particularly in any experiment searching for neutrino-less double-beta decay. While the method described in Section 3.1 has been shown to be successful in reducing the signature of single-beta decays, it must also be able to distinguish the neutrino-less double-beta decay ($0\nu2\beta$) peak from the spectrum produced by ‘normal’ double-beta decay ($2\nu2\beta$) processes. Much as the neutrino was originally introduced because of the continuous nature of the beta spectrum (Section 1), where a peak was expected to lie at the end point instead of the observed continuum, $2\nu2\beta$ events, when measured, display a spectrum of energies, at the end-point of which the $0\nu2\beta$ peak is expected to lie. To confirm the existence of the $0\nu2\beta$ peak, it is necessary to study sufficient events to distinguish the peak over the background produced by the high end of the $2\nu2\beta$ energy spectrum. To do this the detector must have sufficient energy resolution to resolve the two features of the spectrum. For CZT detectors it has been seen that there is a low energy tail on the peak response function which degrades the experimental energy resolution.

The ratio of the width of the detector to the depth of the detector (see Section 2) has a large impact upon the signal induced on an electrode, as a function of the charged particle distance from the electrode (Figure 9). One solution is to develop a detector with an optimal width/depth ratio. However, even at ratios of $W/L=0.125$, a significant portion (roughly ten percent) of the depth leads to degraded events. To minimise the width/depth ratio, the depth can be simply increased; however, thicker detectors require a higher operating voltage and, eventually, the increased voltage will cause surface breakdown (discharge across the detector). The width is also variable, but the variation is subject to a balance between electronics cost (higher number of electronics channels required per unit area), positional sensitivity, pixel efficiency and energy resolution.

For the same size of detector, smaller pixels will require a greater number of electronics channels: indeed, the number of channels rises as the square of the ratio of the change in pixel size. This increase in channels leads to a proportionate increase in readout electronics, and similarly the costs related to acquisition, operation and cooling also increase. In addition, the increase in electronics will lead to increased background. This same change in pixel size would, however, also quadruple the positional sensitivity to the interaction, as well as halving the width/depth ratio and thus improving the energy resolution. As a result, the determination of the optimal pixelation is an important question.

Some of these challenges can be constrained; the ‘passivation’ paint, which is applied to the outside of the detectors in order to reduce surface conductivity, can be removed to reduce the heavy elements such as thorium present within it. Similarly, the electronic noise could be reduced (as well as the electronic cost) by the use of integrated circuitry close to the detector itself, in the form of an ASIC^{xi}. The balance of pixel efficiency and energy resolution is also a challenge to resolve. As we have seen, the smaller the pixels (relative to the depth), the better the energy resolution, as the energy tail is unimportant for a greater portion of the cathode signal range. Unfortunately, the reduction in pixel size increases the probability of events depositing small amounts of energy in many pixels – this increases the likelihood of events being rejected for depositing less energy than the energy threshold, which is determined by the limiting electronic noise.

^{xi} Application-Specific Integrated Circuit

Hence, an examination of the effects of changing pixel size with different source energies and different trigger threshold values was performed in order to determine the optimal pixel size.

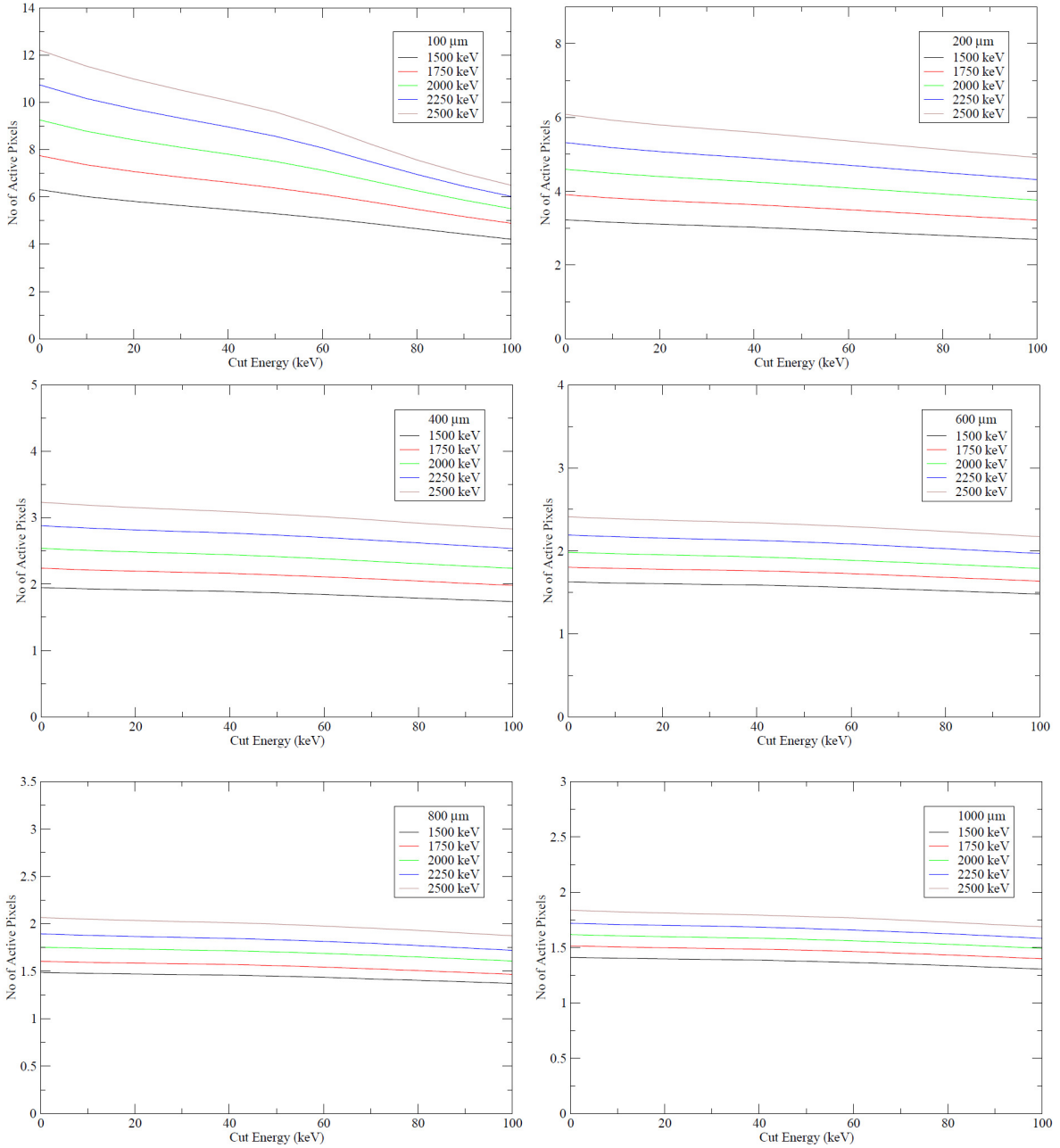


Figure 23 - Number of pixels of different sizes triggered at different threshold energy values (cut energy) for different source energies. The black line indicates a 1500 keV beta-particle, the red line shows a 1750 keV beta-particle, the green line corresponds to a 2000 keV beta-particle, the blue line shows a 2250 keV beta-particle and the brown line indicates a 2500 keV beta-particle. The 6 graphs indicate 100 micron pixels (top left), 200 micron (top right), 400 micron (middle left), 600 micron (middle right), 800 micron (bottom left) and 1000 micron (bottom right).

Figure 23 shows how the average number of pixels triggered by different energy beta-particles varies as a function of the cut energy – this energy is the minimum energy for which a pixel is said to be ‘active’ and is imposed by the requirement to set a threshold (‘cut’) level above the electronic noise. The larger pixels show reasonable stability in number of pixels triggered with increasing cut energy, while the smallest pixels show a large reduction in active pixels as the cut energy increases. However, the smaller pixels show many more pixels to be triggered, providing better characterisation of the path of the radiation through the detector. In addition, as the distance travelled by the beta particle is a function of the energy of the source, it is desirable to have a large variation in the number of pixels triggered for different energy sources. A balance must then be chosen between the higher tracking precision, and energy determination properties of smaller pixels and the stability of efficiency, at higher cut energies (which is useful for cutting out background radiation and noise), of the larger pixels.

It follows that 200 micron pixels provide the optimal balance, showing reasonable stability as the cut energy increases and a large difference between the number of pixels active for a 1500 keV and a 2500 keV beta-particle. In addition, pixels of this size provide tracking over 3 pixels for a 1500 keV beta-particle and as many as 6 pixels for a 2500 keV beta-particle.

3.3 Improving the Energy Resolution by ‘Gain Matching’ and Removing the Energy Tail

In a traditional experiment, it is customary to perform ‘gain matching’ (e.g. the alignment of the photopeaks to the same channel in all the relevant detectors). However, in large scale experiments, and especially when many thousands or even millions of channels are involved, as in any pixelated multi-ton $0\nu2\beta$ experiment, this process would be both long and laborious. As a result, during the analysis that follows, the benefits of this ‘gain matching’ as well as other techniques will be discussed.

In order to compare the idealised response of the simulated system to actual detectors a number of measurements were performed. Two types of pixel detectors were examined, both sixteen pixel arrays, one consisting of sixteen $1\times1\times5$ mm³ pixels (referred to hereafter as the

small detector) and one consisting of sixteen $1.6 \times 1.6 \times 7$ mm³ pixels (the large detector) – these values equate to a 0.20 and a 0.23 width to depth ratio, respectively, and, thus, can be expected to show weighting potentials similar to those seen for a width to depth ratio of $W/L = 0.25$ in Figure 9.

The differences between the two detectors are limited: the smaller detector has a lower efficiency (due to the smaller mass of the detector), while the larger detector shows a slightly larger energy tail. The operating voltages are slightly different (to avoid sparking across the pixels in the small detector it was operated at 500 V while the larger detector was initially operated at 700 V but was subsequently lowered to 500V), but in most respects the detectors are identical. A photograph of the two detectors mounted on the master board fabricated especially for these measurements is shown in Figure 24.

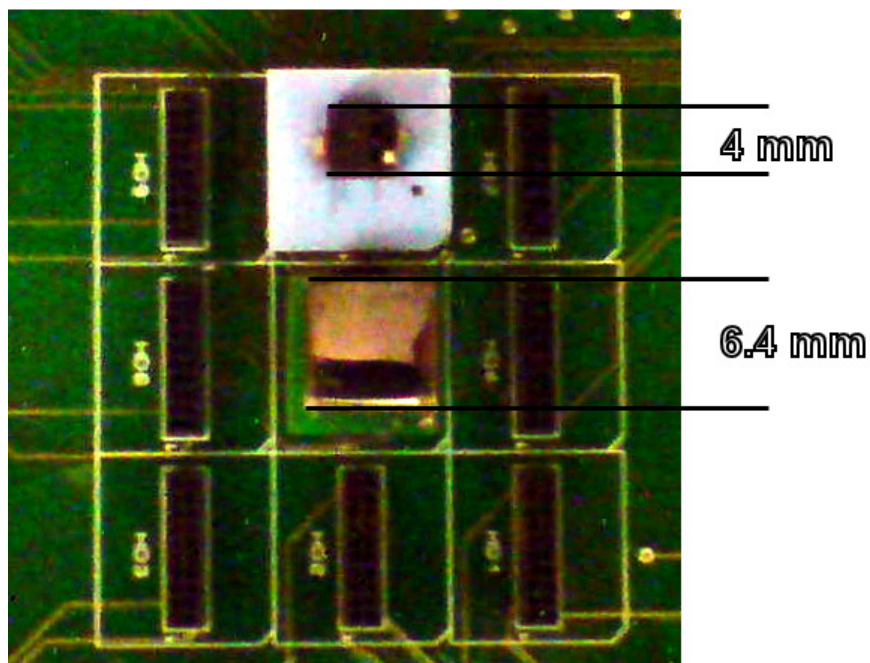


Figure 24 - Photograph of the connectors on the master-board showing the two sizes of detector. In the upper middle position is the smaller detector; consisting of sixteen $1 \times 1 \times 5$ mm³ pixels. In the central position is the larger detector consisting of sixteen $1.6 \times 1.6 \times 7$ mm³ pixels. The pixelated anodes are facing the master-board and the un-pixelated cathodes face the camera.

The two detectors were provided with a voltage applied across the cathodes, pre-amplifiers were then attached to each of the 16 pixels and one cathode terminal on the two detectors. These pre-amplifier signals were then sent to three 16-channel amplifiers which dictated the

gains and shaping times used for the channels. The signals were then sent to two Analogue to Digital Converters (ADC) which provided thresholds for triggering. If an event triggered any one of the 34 channels then all 34 channels were read out by the Digital Acquisition system (DAQ). The threshold levels were set by trying to reduce the low anode-signal noise by raising the thresholds in order to reduce the dead-time.

If the shaping time is less than the time taken to collect the charge carriers, then the pulse height measured will be reduced and there will be ‘ballistic deficit’. The collection can be calculated from the mobilities, the applied voltage on the terminal and the distance between the electrodes. For applied voltages of 500V, the electron collection times for the large and small detectors are found to be 0.73 μ s and 0.37 μ s respectively, the hole collection times are found to be 8.2 μ s and 4.2 μ s respectively. The amplifiers used allowed the shaping time to be set to 0.3, 1 or 3 μ s only. Previous work⁸¹ had found the shaping time for the anodes to lie between 0.2 and 1 μ s and so values of 1 μ s were thus used for all channels. The result is the presence of some ballistic deficit on the cathode, with the effect being greater in the larger detector, but not on the anode.

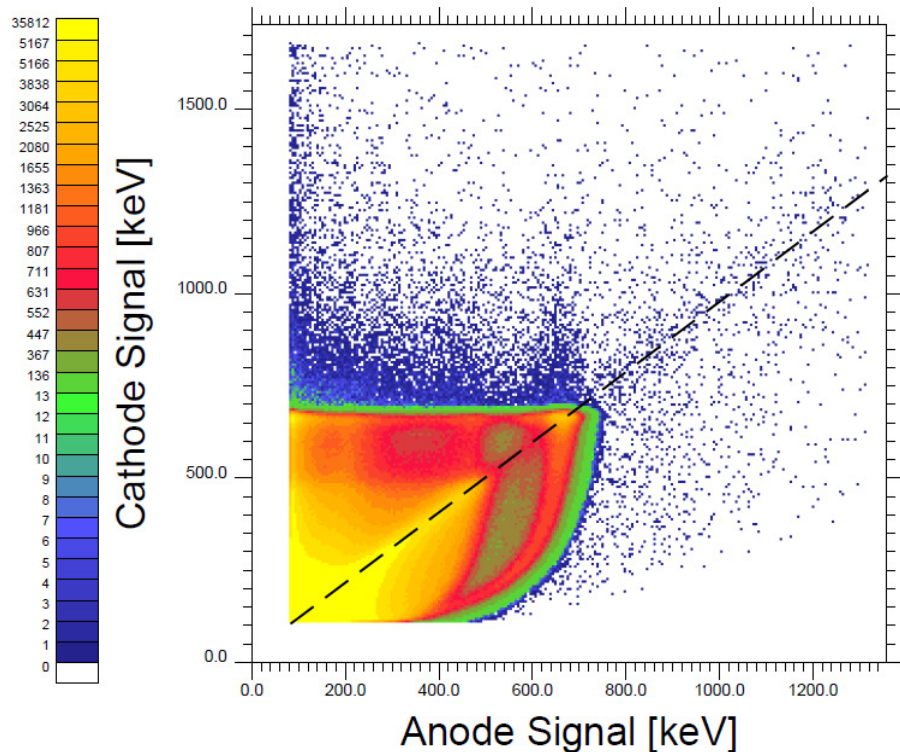


Figure 25 - Example spectrum from the 1.6×1.6×7 mm³ pixel detector showing the 662 keV peak from a ¹³⁷Cs source located above the detectors. The dashed line indicates complete and equal collection of deposited charge on both electrodes.

Figure 25 shows the variation of the un-pixelated cathode signal against the pixelated anode signal. The data corresponds to a ^{137}Cs 662 keV gamma-ray source. There are four key components which must be considered:

- The first component is the 662 keV photopeak, which lies to the right of the spectrum; the photopeak is broadly distributed in the cathode signal due to trapping of holes. There is also an energy tail in the anode signal due to induced signal by holes for events near the anode.
- Second the Compton edge, which lies at around 460 keV, caused by Compton backscattering of the incident radiation within the detector.
- Third, the points of equal collection of energy in both electrodes lie on a diagonal line (marked with a dashed line in Figure 25), with the points below this line being caused by incomplete collection on the cathode. The complete charge collection points (for both electrodes) for the peak, and the Compton edge, are significantly more intense than the points of incomplete collection, which indicates a non-linear response in this region. This suggests that either the depth response is non-linear, or that the efficiency varies strongly with depth.
- The final feature of interest is the region to the left of the line of complete collection – this is believed to be due to incomplete collection on the anode (the pixelated side) and is due (shown later in Section 5) to sharing of signal between two pixels, while the un-pixelated cathode completes collection.

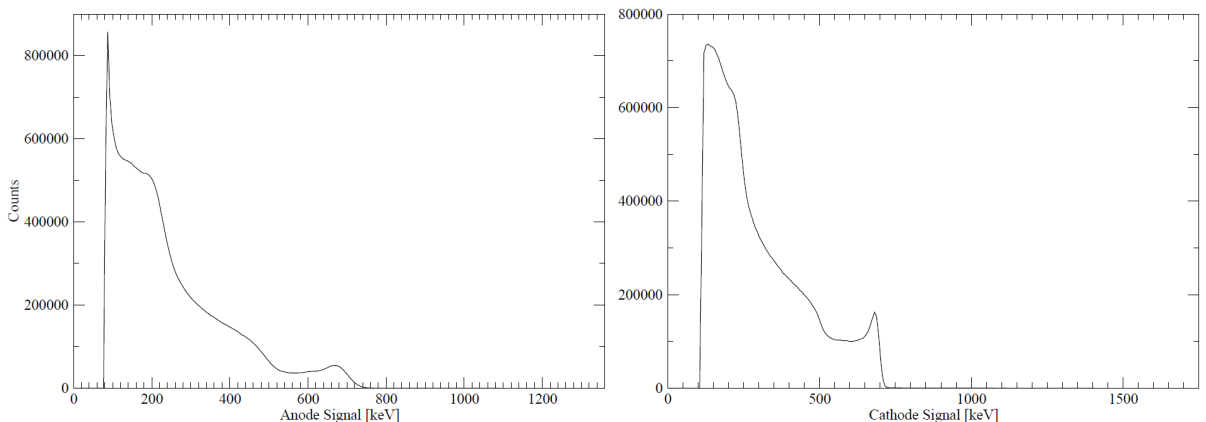


Figure 26 -1-dimensional projections of Figure 25, the left figure shows the anode signal, while the right figure shows the cathode signal.

Figure 26 shows the two 1-dimensional projections of Figure 25. There are several components of interest:

- The photopeak on the anode has a greater Full-Width Half-Maximum than the photopeak on the cathode, this is due to x-ray fluorescence, which occurs when an event occurs within a pixel, the electrons relaxing back to their ground state produce x-rays which are collected in adjacent pixels;
- The anode spectrum displays a sharp spike of events at very low energy - this is the collection in adjacent pixels of the x-ray fluorescence;
- There are fewer events at lower energies in the anode compared to the cathode. This is due to the poor mobility of the holes: for events near the cathode, collection of the holes is probable, with no signal lost due to electrons inducing counter signal, however, for events further away from the cathode, fewer holes are collected due to trapping and hence the signal at lower energies is greater.

A spectrum such as that shown in Figure 25, demonstrates that the first step in increasing the energy resolution would be to match the detector and electronic response of the pixels. Secondly, a significant improvement could be gained from ‘straightening’ the photopeak energy tail. In essence this can be done by multiplying the anode signal by a function of the cathode signal. This function can be determined in one of two ways, either by simulation using the Shockley-Ramo theorem suggested by Zumbiehl,⁷⁵ or by empirical analysis. Since both methods involve finding a fit to the curvature of the spectrum, finding its inverse, and using it to correct the spectrum, there is little to suggest one over the other. However, the simulation method is both long, and imperfect – the simulation summation limits^{xii} are theoretically required to be infinite, simulations must be done at many points within the detector and accordingly only an approximation is available – while using experimental observations is potentially less accurate, but significantly less time-consuming. The method used for the empirical approach is:

- i. Fit the centroid of the anode peak as a function of the cathode signal;
- ii. Calculate the reciprocal of the anode signal values;
- iii. Plot a graph of deduced cathode signal against the reciprocal of the anode signal;
- iv. Fit a polynomial function to these data.

^{xii} See Equation 2.3.3.

This gives a high order (10^{th} order) polynomial distribution which provides the function of the cathode signal by which the anode signal must be multiplied for ‘correction’. An example of this ‘correction’ can be seen in Figure 27 – in this figure, the photopeaks have been aligned, calibrated and then the tail has been removed.

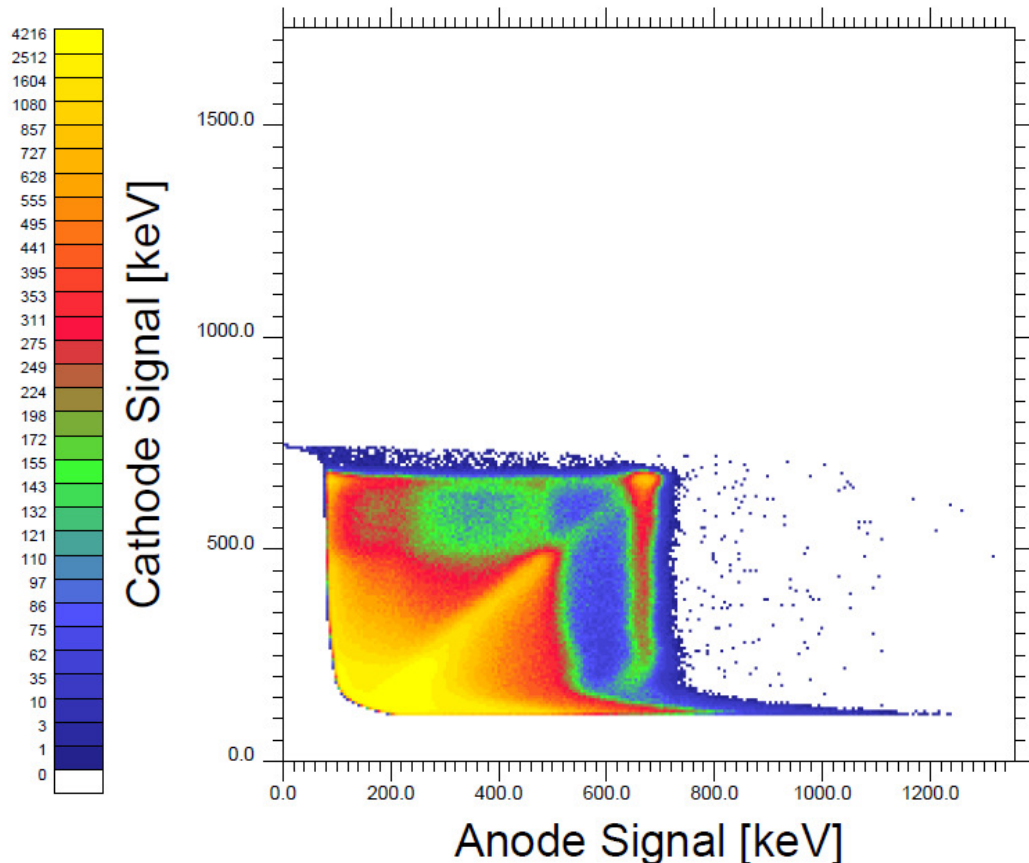


Figure 27 - Figure showing CZT spectrum following ‘correction’. This spectrum is from the $1.6 \times 1.6 \times 7\text{mm}^3$ pixel detector and shows the photopeak from a ^{137}Cs sources located above the detector. The peaks have been aligned and calibrated before being ‘straightened’. A high energy tail is now present on the anode signal due to over-correction at low cathode signal values.

This method is not perfect, as it requires that the curvature is energy independent. This is not so (see Figure 28) and, in fact, the curvature is dependent on the cathode signal. Accordingly, if the fit seen in Figure 27 is applied to several different energies, the curvature is still visible. Consequently, an additional step must be taken prior to the ‘correction’ to eliminate this dependence.

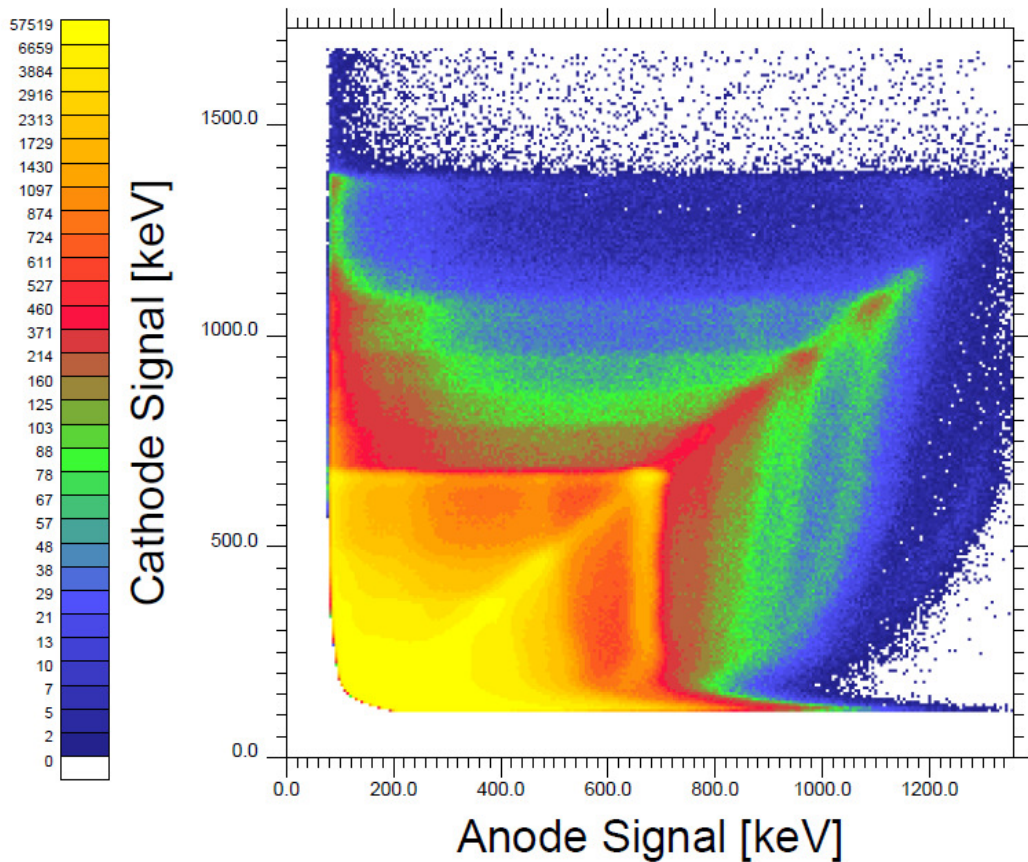


Figure 28 - Example of 'corrected' spectrum showing varying curvature of peaks with anode signal. This spectrum is from the $1.6 \times 1.6 \times 7\text{mm}^3$ pixel detector and shows photopeaks from ^{137}Cs and ^{152}Eu sources located above the detector. The 'correction' only works for the 662 keV peak from the ^{137}Cs , showing an 'over-correction' for lower energies and an 'under-correction' for higher energies.

Since the correction is dependent upon the cathode signal, the simplest method of removing this dependency is to calculate depth, which is independent of energy. Since the full collection cathode signal is dependent upon the energy of the source, as is the anode signal, the two should be constant relative to one another for events fully collected on both electrodes. By calculating the ratio of the anode signal to the cathode signal, and plotting this ratio against the anode signal, a horizontal line of equal collection of the deposited charge can be seen. The result is a spectrum similar to that seen in Figure 29; the 'flattening' of the complete collection results in a 'teardrop' shape, which exhibits all the same features as before: the peak, Compton edge and their associated incomplete cathode collection energy tails are all apparent. The cathode now lies along the line of deposition around 1000 (indicated by the dashed line) while the anode lies at around 350 (indicated by the dotted line). The depth of the

interaction can be determined from the point between these two lines where the specific interaction lies.

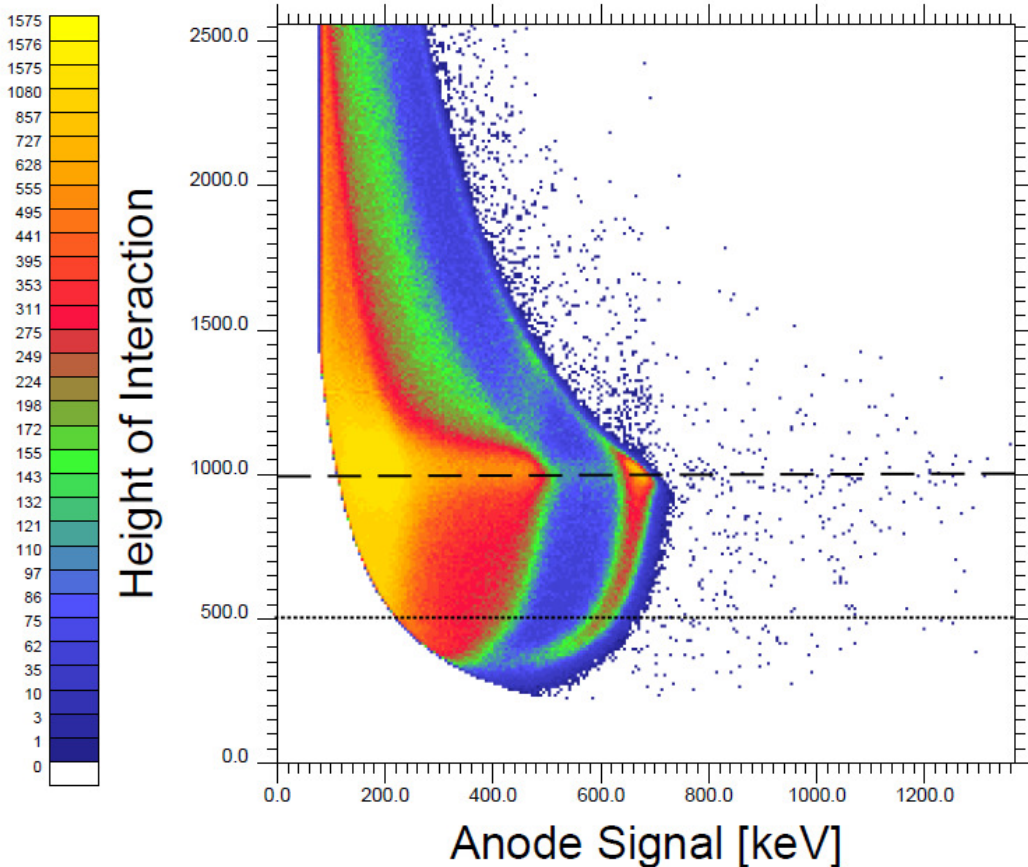


Figure 29 - Figure showing a spectrum without ‘straightening’ after the ‘flattening’ of the complete collection line. The figure shows a ^{137}Cs source, located above the $1.6 \times 1.6 \times 7 \text{ mm}^3$ pixel detector, showing the 662 keV photopeak with the peaks un-straightened. The cathode lies along the line of 1000 on the y-axis (indicated by the dashed line) while the anode lies at around 350 on the same axis (indicated by the dotted line).

This ‘flattening’ requires that the ‘correction’ process outlined above be performed again as the process changes the coefficients required. The final spectrum from this correction process can be seen in Figure 30.

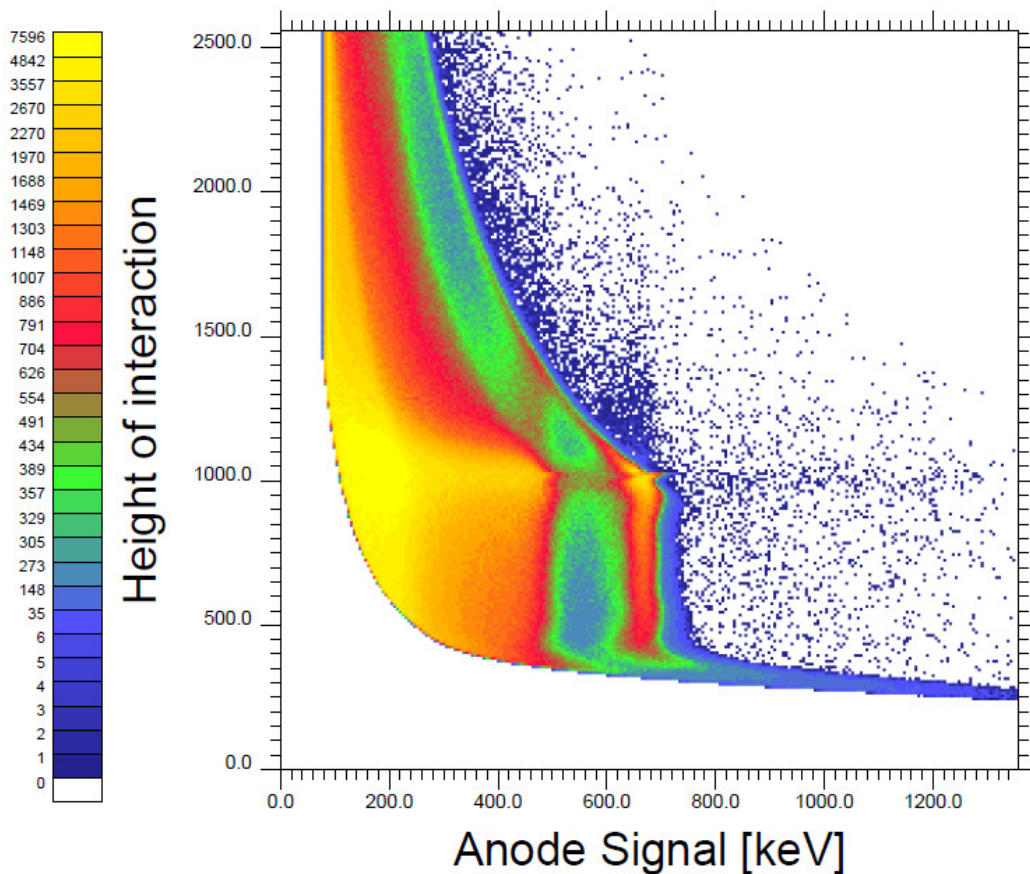


Figure 30 - Final ‘straightened’ and ‘flattened’ spectrum showing a ^{137}Cs source located above a $1.6 \times 1.6 \times 7 \text{ mm}^3$ pixel detector. The photopeak shows a discontinuity at a height of 1000 as this is the cut-off for the ‘correction’ process.

The process of ‘straightening’ the peak requires that anode signal values be plotted against the cathode signal values at various depths of the photopeak. This cannot be done above the line of equal collection on both anode and cathode (at a y-axis value of 1000) and so the formula must be constrained. The events which lie above the line of equal collection are incompletely collected upon the anode and so cannot be added to the events which now lie below them. This leads to the discontinuity seen at this value. In addition, for events very near the anode it is extremely difficult to determine the peak centroids. As a result, the formula must be constrained, or a small intensity, high energy tail, as seen at y-axis values of 250 in Figure 30, will result.

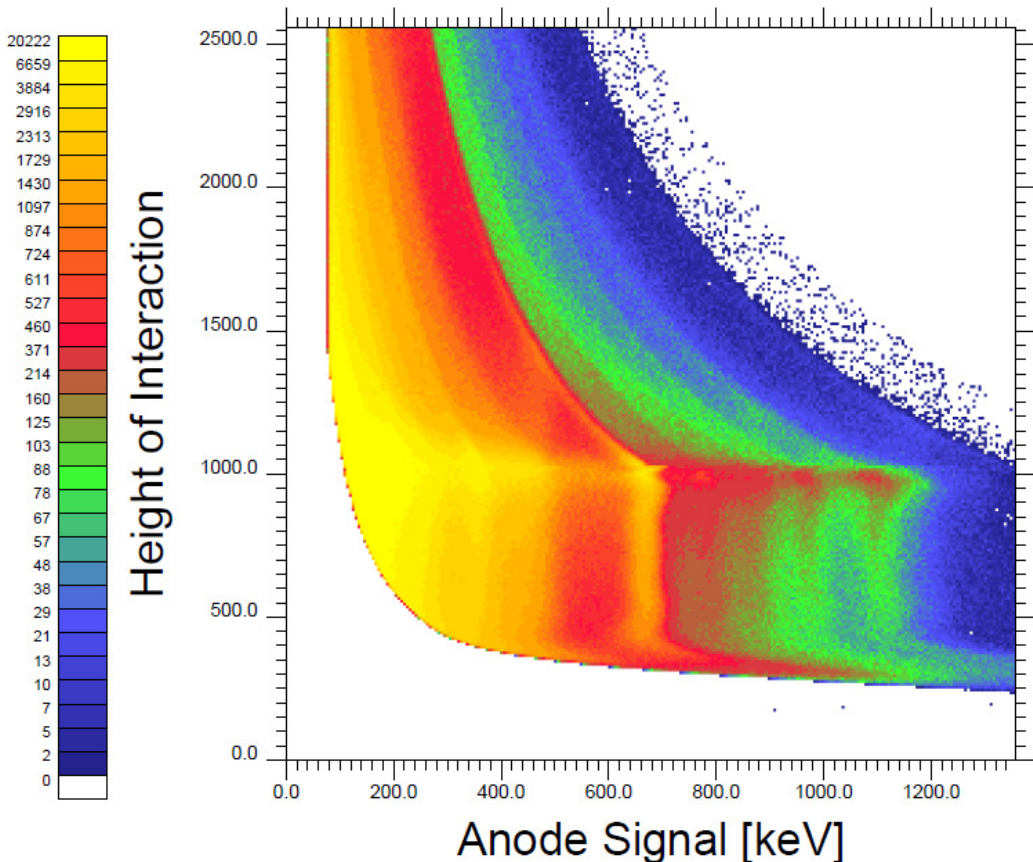


Figure 31 - Final ‘straightened’ and ‘flattened’ spectrum showing ^{152}Eu and ^{137}Cs sources located above a $1.6 \times 1.6 \times 7 \text{ mm}^3$ pixel detector. Once again a discontinuity is seen at a height of 1000; unlike in Figure 28, the ‘correction’ technique applies to all the photopeaks seen in the ^{152}Eu source as well as the 662 keV peak in the ^{137}Cs source.

Figure 31 shows the flattened and straightened spectrum for a combination of Europium and Caesium sources. The flattening process means that the straightening technique is now energy independent. The discontinuity and low level tail can again be seen but again, these can be removed with better constraint of the straightening formula.

The above corrections were performed on a ‘detector by detector’ basis, i.e. each detector was ‘corrected’ separately but not each pixel. While each pixel in a detector should show the same response, it is probable that individual pixels will respond differently. The correction method is not however especially complex and could be performed on a pixel by pixel basis (as the

calibration must be).^{xiii} It is, however, impractical to consider manual correction on the scale of detector that the COBRA experiment would need in its final configuration (using $1.6 \times 1.6 \times 7 \text{ mm}^3$ pixels, the current final state COBRA experiment would have around 2.5 million pixels scaling up to 160 million pixels for 200 micron pixels) and so software automation for the correction method must be considered.

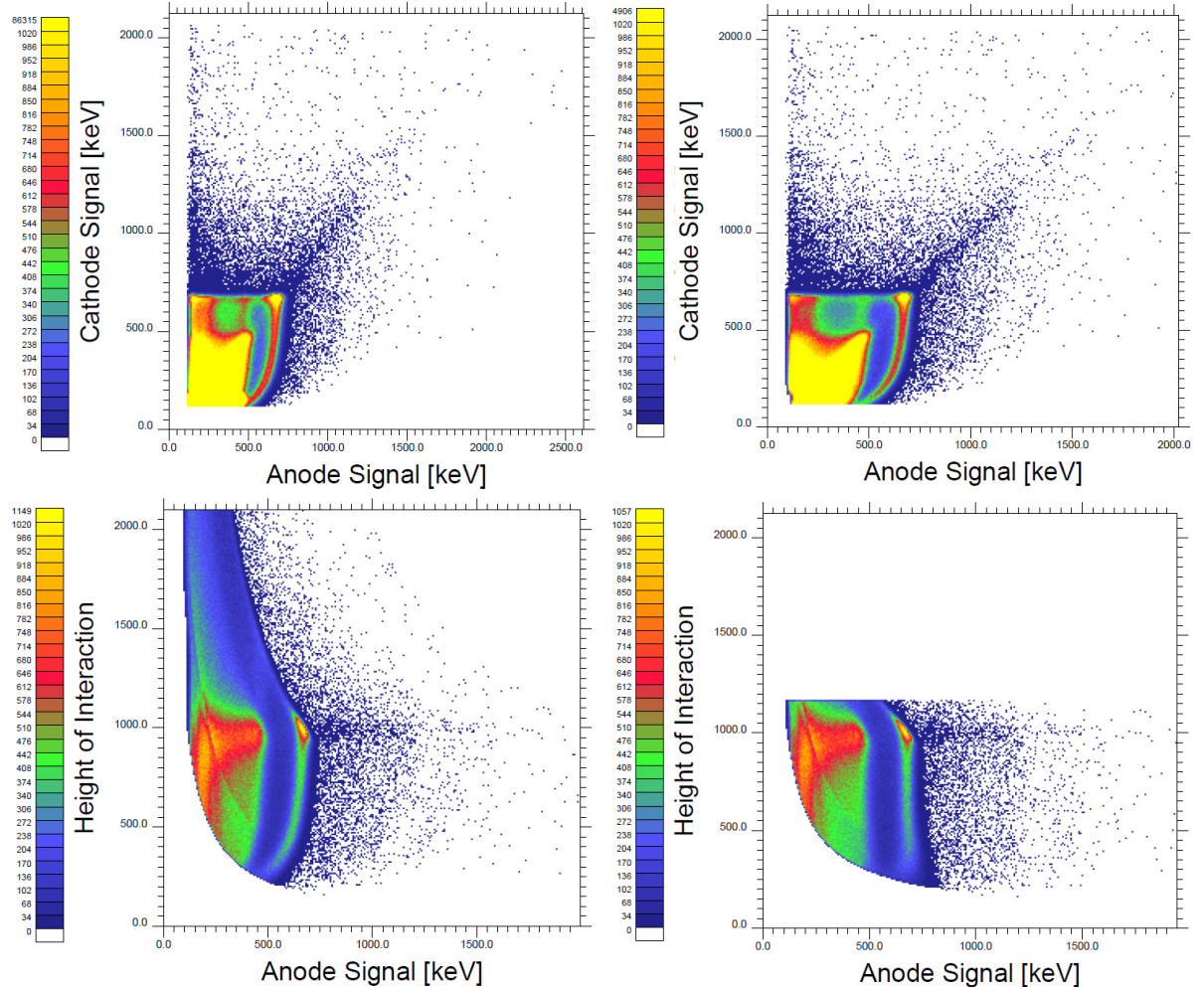


Figure 32 – Spectra showing the entire process of improvement for a $1.6 \times 1.6 \times 7 \text{ mm}^3$ pixel detector measuring a ^{137}Cs 662 keV gamma-ray source located above the detector. The top left spectrum shows the initial data, top right the data following the alignment of the photopeaks in the 16 individual pixels. The bottom left spectrum shows the result of the ‘flattening’ of the cathode signal, while the bottom right spectrum shows the final result when the photopeaks have been ‘straightened’.

^{xiii} Indeed, since the calibration requires the detectors to be run with a test source anyway – with a correspondence between operation time and calibration accuracy – the addition of single pixel correction would not require the detectors to operate for any extra length of time.

Finally, it is preferable to remove the events which lie above the complete collection line for both the anode and cathode – as these events are those which are shared between multiple pixels. With suitable constraints at low energy a plot such as that seen in Figure 32 can be produced. Figure 32 also shows the steps taken in improving the energy resolution, highlighting the intermediary steps.

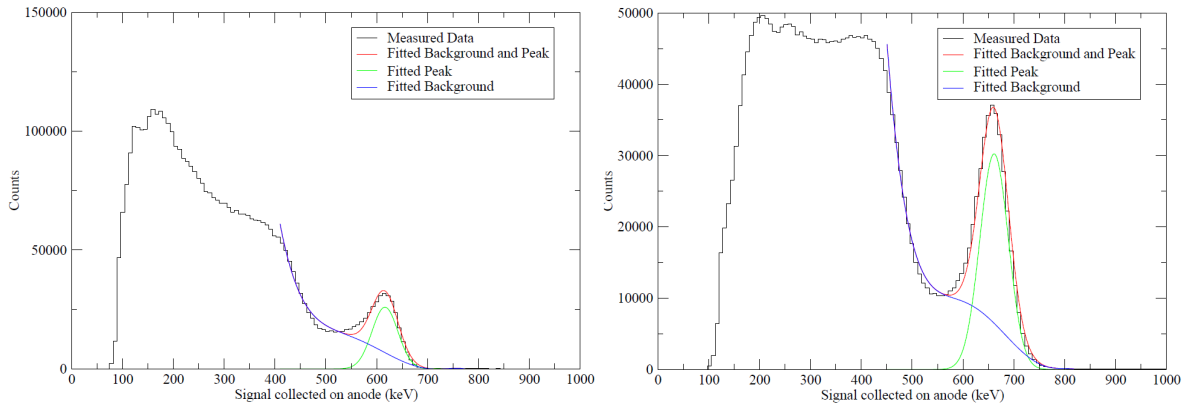


Figure 33 - Spectra showing the signal on the anode, the figure on the left shows the signal after alignment of gains, the figure on the right shows the signal after the ‘straightening’ of the photopeaks as seen in Figure 32. It is apparent that the width of the peak (FWHM) has increased, and that the relative height of the photopeak to the ‘trough’ at 525 keV has greatly increased.

Figure 33 shows the improvement in the anode signal seen due to the correction from the aligned stage to the corrected stage seen in Figure 32. The aligned stage is shown rather than the initial data due to the presence in the initial spectra of several strong points of noise due to sparking over the detector. The Full-Width Half-Maximum (FWHM) of the photopeak worsens slightly (from 60.5 ± 0.3 keV to 66.0 ± 0.2 keV), while the number of counts in the peak increases (from 232852 ± 1846 to 282571 ± 1258). A second measure of improvement is the increase in the ratio of the centroid height to the height at the bottom of the ‘trough’ adjacent to the photopeak; for the measurements shown in Figure 33 this ratio increases from $1.98^{+0.07}_{-0.07}$, prior to correction, to $3.47^{+0.14}_{-0.13}$. This equates to a 75% increase in the ratio, as compared to around a 20 percent change in the number of counts in the photopeak. This measure is not applicable to measurements with multiple gamma-ray sources, where the incompletely collected events from higher energy sources compound the apparent background within the valley between photopeak and Compton edge.

The correction technique outlined in this Section can be used to remove the energy tail from the detectors across all energies. It can be performed relatively swiftly and empirically once all the individual pixels have been calibrated and can produce a visible improvement in the spectra. The technique could be improved by correcting each pixel uniquely or by utilizing simulations to provide the polynomial used in correction, rather than the empirical solution used here. These methods would however require significant time input (especially to fit each individual pixel) and extremely detailed information (the simulation method is only applicable if the exact dimensions of each pixel are known).

In order for future work examining the improvements to this correction technique to be worthwhile, it is necessary to quantify the increase in efficiency and energy resolution due to the technique in its current form. As seen above the FWHM does not improve noticeably between the aligned stage and the corrected stage, while the number of counts in the peak does increase by around 20%; however, this improvement is mainly to reduce the contribution to the background below the peak, and, consequently, the peak to background ratio improves by 75%. These improvements will be quantified more clearly in the next Section.

4. Quantifying the Improvement in Energy Resolution and Efficiency

The correction methods outlined above (Section 3) are suggested to improve the efficiency, and perhaps energy resolution, of the detectors. However, in order to qualify these improvements, it is necessary to assess several steps of the process. The key markers of the improvement are commonly the Full-Width Half-Maximum (FWHM) for energy resolution and the area under the photopeak for efficiency. However, these tests are only representative of the energy resolution and the efficiency and are not absolute values.

The efficiency of the detector can be defined as the number of photons emitted by the source which interact within the detector (the geometric efficiency); this can be further constrained to those photons emitted by the source in the solid angle subtended by the detector (the intrinsic efficiency) and further to cover only those events where the photon is fully collected within the detector (intrinsic photopeak efficiency). This efficiency is dependent upon several factors, not least the energy of the source, the source activity and the dimensions of the detector. However, it follows that the area under the photopeak is a measure of this efficiency, and that when comparing two efficiency measurements, the ratio is identical to the ratio of the photopeak areas.

The second measure is that of the energy resolution, Energy resolution is commonly defined as:

$$R = \frac{FWHM}{Centroid - Energy} = \frac{2.35}{\sqrt{N}} \quad (4.1)$$

where N is the number of charge carriers collected, *Centroid* is the centroid energy of the photopeak and *FWHM* is the Full-Width Half-Maximum, the width of the peak at half the maximum intensity of the peak. This *FWHM* is commonly used as a measure of the energy resolution. The Full-Width Tenth-Maximum, where the width of the peak at a tenth of the maximum intensity is measured, was also considered, however, it was found that this measure provided no extra information and was difficult to calculate.

A second test of the energy resolution is also examined, the ratio of the peak intensity, as discussed in Section 3.3, provides a measure of the quality of the photopeak shape relative to the background.

The process outlined earlier comprises several steps of data processing:

- ‘Initial’ - the data prior to any correction being performed;
- ‘Aligned’ - the data after the photopeaks have been calibrated;
- ‘Flattened’ - the data after the cathode signal has been ‘flattened’;
- ‘Straightened’ - the data after the photopeaks have been straightened to remove the low energy tail.

In addition, the response of the entire detector and individual pixels may be quantified. The best statistics are available when examining all the pixels combined, but the improvements may differ from those seen in individual pixels. The simplest example of this would be during the aligning process. There should be minimal effect on the individual pixels at this stage as the photopeak is calibrated – this may reduce or increase the width in channels of the photopeak, but not by any significant amount. However, when examining the entire detector, it is possible that the spectrum for a single pixel could lie substantially out of line with the others prior to calibration and thus not be counted in the area under the photopeak. In addition, the different positions of the photopeaks in the separate pixels mean that the FWHM prior to correction is likely to be substantially greater than after the correction process. As a result, while individual pixels should show minimal improvement at this stage, the overall detector response may show substantial improvements in efficiency and energy resolution.

During this analysis, peaks were fitted using the BUFFIT^{xiv} fitting routine. This routine allows users to specify limits (start and end) of a background fit, along with parameters such as the order of polynomial to use as a fitting function. In addition, the user may specify estimates for the locations of the photopeaks within the data. The fitting program then calculates a polynomial background and Gaussian peak combination to fit to the data being analysed. Finally, the user is presented with the centroid locations, area under the photopeaks and the FWHM of the peaks (along with associated statistical errors). Since these fits vary depending on these parameters, the measurements were all fitted several times with different parameters.

^{xiv} Birmingham University Fast FITting routine – written by N. M. Clarke, version 4.8 8/6/1998

The errors in the calculated areas for these values were then used to provide a weighting of the quality of the fits, and a weighted average was calculated from these.

Tests were performed using both the smaller ($1 \times 1 \times 5$ mm 3 pixel detector) and the larger ($1.6 \times 1.6 \times 7$ mm 3 pixel detector) and initially using two sources: a ^{137}Cs 662 keV gamma-ray source and a ^{60}Co 1173 and 1332 keV gamma-ray source. The measurements undertaken with the Cobalt source were performed with the source situated in two locations; initially to the right side of the detector (measurement R3) and then above the detector (measurement R4). The measurements with the Caesium source were performed with the source to the right side of the detector. The aim of these three measurements was to determine if there was any indication of a positional dependence to the improvements, as well as providing an initial measure of any energy dependence.

4.1 Increase in the Efficiency for the Entire Detector

The evaluation of the increase in the area under the peak is separated into three steps: the ratio of the area under the peak after ‘aligning’ the photopeaks to before (Aligned/Initial), the ratio of the area after ‘straightening’ to before (Straightened/Initial) and finally the ratio of the area after ‘straightening’ to after ‘aligning’ (Straightened/Aligned). These three ratios allow an appreciation of the effect of ‘aligning’ the photopeaks, and of straightening the photopeaks both independently and together. Poor statistics and high background from the 1332 keV Compton edge prohibited the use of the lower energy 1173 keV gamma ray in the ^{60}Co source. In addition, it was not possible to accurately calculate the initial area under the 1332 keV peak for the ^{60}Co source when measured with the smaller detector due to the low efficiency of the detector at this energy, however, the aligned and straightened peaks were identifiable. The ratios are seen in Table 3, where values of greater than 1 imply an increase in the efficiency.

$1 \times 1 \times 5 \text{ mm}^3$ pixel detector	Aligned /Initial	Straightened /Initial	Straightened /Aligned
^{137}Cs Above	1.43 ± 0.04	1.32 ± 0.04	0.92 ± 0.01
^{60}Co Side			1.32 ± 0.03
^{60}Co Above			2.02 ± 0.03

$1.6 \times 1.6 \times 7 \text{ mm}^3$ pixel detector	Aligned /Initial	Straightened /Initial	Straightened /Aligned
^{137}Cs Above	1.37 ± 0.01	1.49 ± 0.01	1.08 ± 0.01
^{60}Co Side	1.35 ± 0.01	2.14 ± 0.02	1.59 ± 0.01
^{60}Co Above	1.36 ± 0.02	2.01 ± 0.03	1.48 ± 0.01

Table 3 - Table showing the ratios of the peak areas after steps in the correction to before, for measurements taken with ^{137}Cs 662 keV and ^{60}Co 1332 keV gamma-ray sources measured with the $1 \times 1 \times 5 \text{ mm}^3$ pixel detector and the $1.6 \times 1.6 \times 7 \text{ mm}^3$ pixel detector.

It can be seen from the third column in Table 3, which shows the change in photopeak efficiency over the entire process, that there is a substantial increase in the area under the photopeak. However, the second column, which shows the change due to the process of aligning the photopeaks, reveals that much of the improvement is due to this step. The fourth column shows the improvement as a result of straightening the photopeaks. It can be seen that the effect is small for the 662 keV photopeaks, and even indicates a reduction in efficiency in the smaller detector. However, at 1332 keV there is a substantial improvement. It is apparent (see Figure 28) that prior to the 2-dimensional spectra being ‘flattened’ and the peaks ‘straightened’, the curvature of the tail is a function of energy. As a result, the correction technique will have a greater effect upon the ‘straightness’ of the tail at higher energies. An alternative explanation is that sources located above the detector (especially lower energy sources) might be expected to deposit preferentially near the anode (in the unaffected portion of the peak). This would not be true in events where the source is located to the side where the distribution would be even throughout the detector. However, this is not the case in Figure 34 where the distributions are similar for both cases. In addition, the gamma-ray linear

attenuation at high energies is quite small, which means, for the present case, there is an almost uniform probability of interaction throughout the detector.

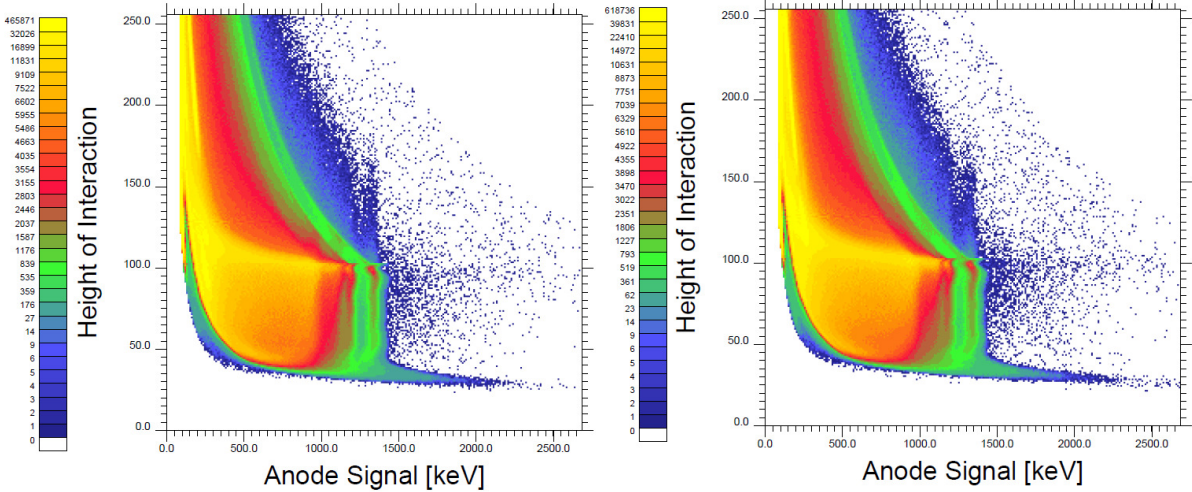


Figure 34 - Figure showing the corrected spectra for both the source to the side (left) and the source above (right). If the source location affected deposition within the tail significantly then the right spectrum might be expected to demonstrate even deposition along the vertical direction while the left should be more intense at the top of the pixel (Height=100). Both spectra show similar distributions suggesting that source location does not significantly affect the deposition height within the pixel.

The alignment stage was expected to improve efficiency and energy resolution as this step corrects for gain mismatches between pixels; as well as accounting for differing charge collection efficiency in the pixels. As a result, it is not surprising to see increases in efficiency where individual pixel photopeaks, formerly lying outside the composite photopeak in the detector, are moved into the composite photopeak. In addition, this same process would improve the energy resolution. It is surprising however, that the process of straightening the photopeaks shows almost no effect on efficiency of the detectors at 662 keV, while simultaneously, an increase of over 50% was observed at 1332 keV. This suggests a strong energy dependence, which will be discussed later (Section 4.8).

4.2 Energy Resolution Improvement for the Entire Detector

The Full-Width Half-Maximum (FWHM) was calculated for the same data sets as presented in Section 4.1. These values were converted into ratios to give a measure of the improvement in energy resolution due to the different steps. A ratio of less than unity indicates a decrease in FWHM and, thus, an improvement in the energy resolution.

$1 \times 1 \times 5 \text{ mm}^3$ pixel detector	Aligned /Initial	Straightened /Initial	Straightened /Aligned
^{137}Cs Above	0.77 ± 0.01	0.66 ± 0.01	0.85 ± 0.01
^{60}Co Side			1.03 ± 0.02
^{60}Co Above			1.29 ± 0.02

$1.6 \times 1.6 \times 7 \text{ mm}^3$ pixel detector	Aligned /Initial	Straightened /Initial	Straightened /Aligned
^{137}Cs Above	0.852 ± 0.004	0.781 ± 0.003	0.916 ± 0.002
^{60}Co Side	0.720 ± 0.004	0.750 ± 0.004	1.041 ± 0.003
^{60}Co Above	0.746 ± 0.003	0.738 ± 0.003	0.989 ± 0.002

Table 4 - Table showing the ratios of the FWHM after steps in the correction process to before, for measurements with ^{137}Cs 662 keV and ^{60}Co 1332 keV gamma-rays, using the $1 \times 1 \times 5 \text{ mm}^3$ pixel detector and the $1.6 \times 1.6 \times 7 \text{ mm}^3$ pixel detector.

Again, the third column indicates the improvement in energy resolution due to the entire correction process; this suggests an improvement in the energy resolution of around 25%, however, the second column indicates that much of this improvement is due to the process of aligning the pixel gains, and that the improvement in energy resolution due to the straightening of the peaks – which was expected to be the major factor, is minimal; in some cases the FWHM is actually slightly larger after the peaks are straightened. This is likely to be due to the predominance of events that are apparently fully collected on both electrodes - the intense distribution at the fully collected end of the peak (Figure 34) - which mean that the low energy tail contributes little to the FWHM.

The analysis of the ratio of the peak centroid intensity to the intensity in the ‘trough’ adjacent to the peak can also be taken as a measure of the energy resolution. This analysis is presented in Table 5.

$1 \times 1 \times 5 \text{ mm}^3$ pixel detector	Aligned /Initial	Straightened /Initial	Straightened /Aligned
^{137}Cs Above	1.26 ± 0.03	1.88 ± 0.05	1.50 ± 0.04
^{60}Co Side			1.34 ± 0.05
^{60}Co Above			1.35 ± 0.04

$1.6 \times 1.6 \times 7 \text{ mm}^3$ pixel detector	Aligned /Initial	Straightened /Initial	Straightened /Aligned
^{137}Cs Above	1.34 ± 0.01	2.08 ± 0.02	1.55 ± 0.02
^{60}Co Side	1.46 ± 0.01	2.33 ± 0.02	1.59 ± 0.02
^{60}Co Above	1.51 ± 0.01	2.40 ± 0.02	1.60 ± 0.01

Table 5 - Table of ratios of ‘peak to trough’ ratios after steps in the correction to before for measurements with ^{137}Cs 662 keV and ^{60}Co 1332 keV gamma-rays; using the $1 \times 1 \times 5 \text{ mm}^3$ pixel detector and the $1.6 \times 1.6 \times 7 \text{ mm}^3$ pixel detector.

Table 5 demonstrates the improvement in the ‘peak to trough’ ratio and suggests that this effect is not energy dependent as the FWHM appears to be and that most of the improvement arises as a result of the straightening of the photopeaks. These data support the suggestion that the straightening of the tail increases the number of events within the photopeak by reducing the number within the tail, and improves the overall peak shape.

4.3 Discussion of Improvements across the Entire Detector

The tests described in Sections 4.1 and 4.2 indicate that (for the large detector) there is no variation in the response between measurements which used the ^{60}Co source positioned at the right hand side of the detectors, or when the source was located above the detectors. The smaller detector does show an apparent difference in performance with a greater improvement

in efficiency and an increase in FWHM (the energy resolution is worse) when the source was above the detector.

Most of the improvement is seen during the initial alignment, a step that aligns the photopeaks within the various pixels – this process corrects for variations in gains within individual pre-amplifiers and charge collection efficiency. Those pixels where the photopeak initially lay out of line, relative to the photopeaks in their counterparts, will be reintroduced and will thus increase the observed efficiency. The alignment stage was thus found to provide the main contribution to the efficiency improvements. In addition, substantial improvements in the energy resolution are seen for the same reasons. However, while the efficiency of the detectors was again found to increase with the straightening of the photopeaks, especially at higher energy, the energy resolution is found to be changed very little. This was unexpected, but suggests that the presence of the tail has a minimal effect upon the energy resolution of the detector initially. As stated earlier this is possibly due to the statistical dominance of events which are fully collected on both electrodes.

4.4 Increase in the Efficiency for Individual Pixels

The improvement in the efficiency for individual pixels was examined. Figure 35 shows the ratio of the area under the peak after correction to before. As before, a value greater than 1 indicates an improvement in the efficiency. The figure shows that all 16 pixels exhibit a roughly similar improvement of around 50% at 1332 keV and 20% for the larger detector at 662 keV and 8% for the smaller detector at 662 keV.

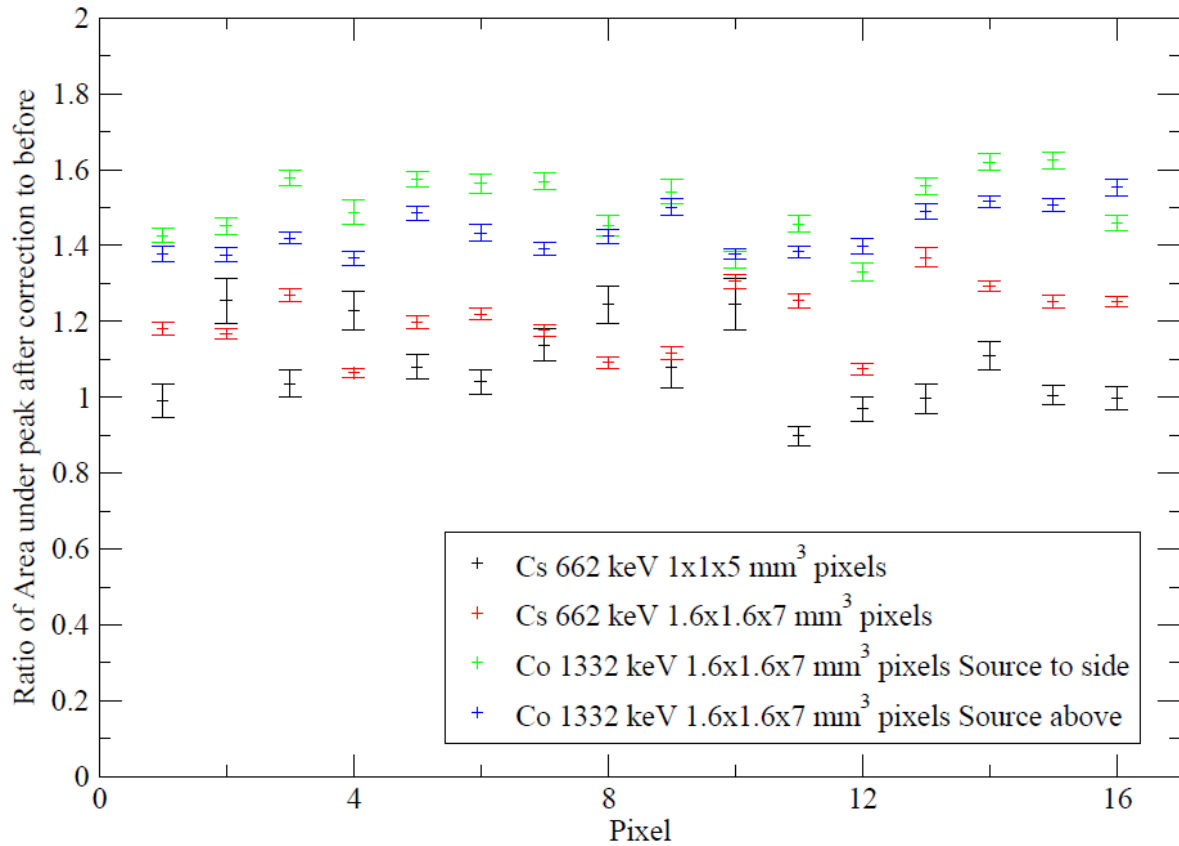


Figure 35 - Ratio of area under the peak after correction to before - shown for 16 pixels for ^{137}Cs 662 keV and ^{60}Co 1332 keV gamma ray sources. The Caesium source analysis is performed for both detectors with the source situated above the detectors. The Cobalt analysis is performed with the larger detector and with the source both to the right-hand side of the detector and above. Ratios greater than 1 indicate an increase in efficiency after correction. Pixel maps for this data showing the area under the photopeak in each pixel before and after correction are seen in Appendix C.

The larger detector, due to the greater width/depth ratio should have a more prominent energy tail, and thus regain more of the peak due to the correction, as seen in this figure. In addition, the apparent energy dependence is seen when comparing the improvement for 662 keV and 1332 keV photons. It can be seen, by comparing the pixels here with the pixel maps shown in Appendix C, that those pixels which initially show more events, exhibit a smaller improvement than those pixels which initially exhibit fewer events. This suggests that the correction process has a greater effect for those pixels within an array which are initially less efficient.

4.5 Energy Resolution Improvement for the Individual Pixels

As with the efficiency, the calculation of the FWHM change is plotted in Figure 36. This ratio appears to be relatively consistent with all four measurements, suggesting that the improvement is not dependent on source energy, position or pixel size. Furthermore, while the ratio appears to be consistent with unity, there is some spread of the data points. This spread, combined with the initially highly variable FWHM values (seen in Appendix C), suggests that the individual pixels exhibit different responses, perhaps dependent upon size or electronics. The apparent consistency with unity is surprising, as it was expected that the straightening of the peaks would improve the energy resolution substantially; as it was envisioned that the energy tail would be a major factor in the energy resolution of the photopeak. It is possible that the dominance of events lying on the full charge collection line (see Figure 25), means that the energy tail contributes significantly less than half the full-height and thus is not a factor in the calculation of the FWHM.

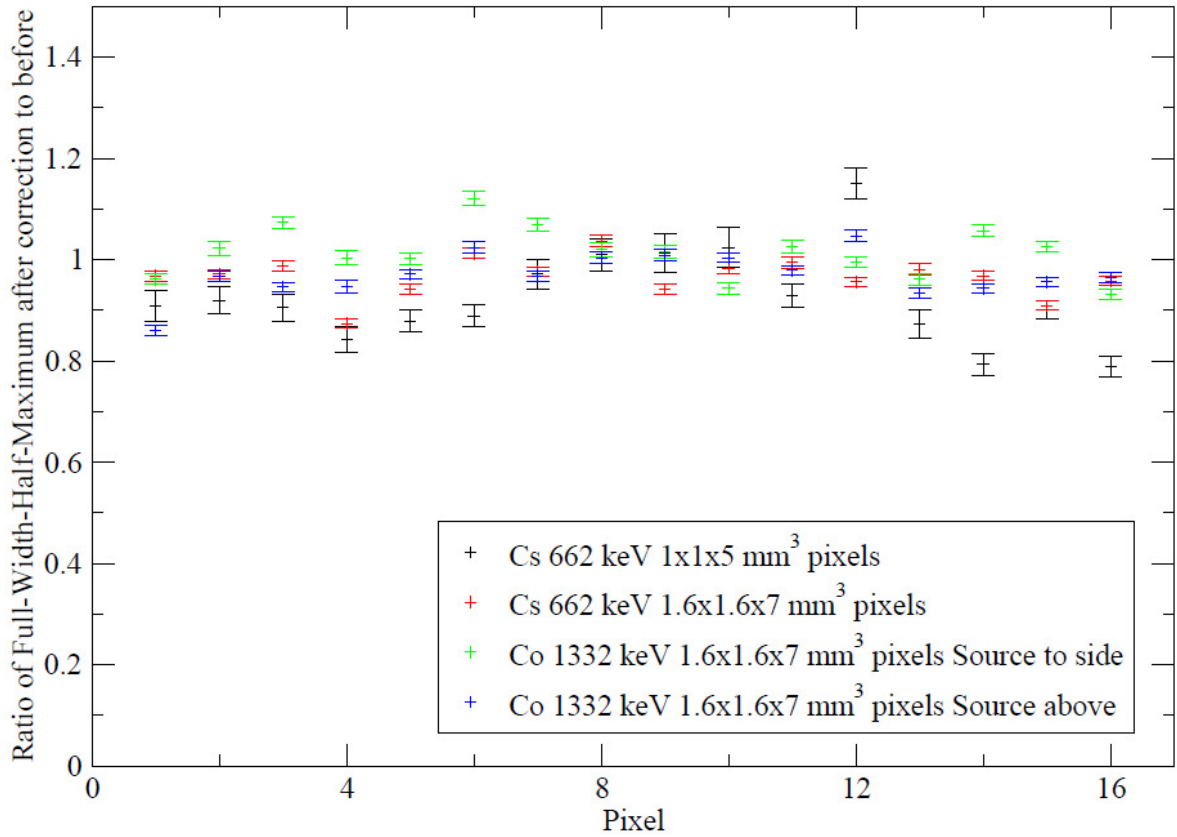


Figure 36 - Ratio of Full-Width Half Maximum of the peak after correction to before - shown for 16 pixels for a ^{137}Cs source (662 keV gamma-rays) and a ^{60}Co source (1332 keV gamma-rays). The Caesium source analysis is performed for both detectors with the source situated above the detectors. The Cobalt analysis is performed with the larger detector with the source to the right-hand side of the detector and also above the detector. Pixel maps for this data showing the FWHM in keV in each pixel before and after correction are seen in Appendix C.

In addition, the ratio of the photopeak intensity to the signal in the trough adjacent to the photopeak was also plotted and is presented here, in Figure 37. As with the FWHM, these values appear consistent with all four measurements, with the smaller detector exhibiting slightly worse ratios, which is in agreement with the expectation that the improvement should be smaller for the smaller detector (where the curvature of the tail is less than that for the larger detector).

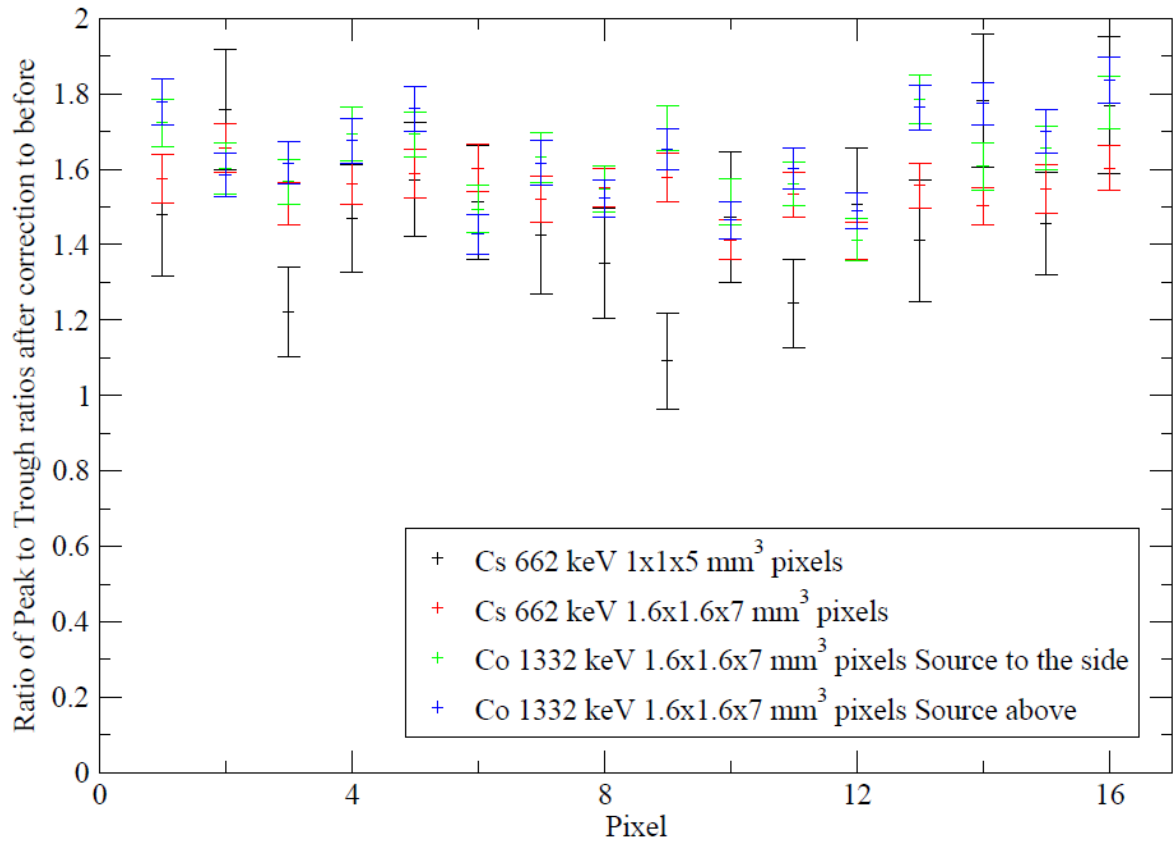


Figure 37 – Ratio of the peak to trough ratio after correction to before - shown for 16 pixels for a ^{137}Cs source (662 keV gamma-rays) and a ^{60}Co source (1332 keV gamma-rays). The Caesium source analysis is performed for both detectors with the source situated above the detectors. The Cobalt analysis is performed with the larger detector and with the source both to the right-hand side of the detector and above. Pixel maps for this data showing the peak to trough ratio in each pixel before and after correction are seen in Appendix C.

4.6 Comparison of Efficiency Increase in Individual Pixels Compared to Efficiency Increase within the Entire Detector

The improvements seen in Sections 4.1, 4.2, 4.4 and 4.5 showed the increase in efficiency and improvement in energy resolution as a ratio of the values before and after corrections. Table 6 shows the efficiency increase, energy resolution improvement (FWHM decrease) and peak to trough ratio averaged across the 16 pixels together with those calculated for the entire detector. The values presented were calculated as a ratio of the value (efficiency, FWHM and peak to trough) after correction to before.

	Average Efficiency Increase (Pixels)	Total Efficiency Increase (Detector)	Average Energy Resolution Increase (Pixels)	Total Energy Resolution Increase (Detector)	Average Peak to Trough Ratio Increase (Pixels)	Total Peak to Trough Ratio Increase (Detector)
^{137}Cs Above $1 \times 1 \times 5$ mm^3 pixel detector	1.08 ± 0.04	1.32 ± 0.04	0.93 ± 0.03	0.66 ± 0.01	1.47 ± 0.15	1.88 ± 0.05
^{137}Cs Above $1.6 \times 1.6 \times 7$ mm^3 pixel detector	1.21 ± 0.02	1.49 ± 0.01	0.97 ± 0.01	0.78 ± 0.01	1.54 ± 0.06	2.08 ± 0.02
^{60}Co Side $1.6 \times 1.6 \times 7$ mm^3 pixel detector	1.50 ± 0.02	2.14 ± 0.02	1.01 ± 0.01	0.75 ± 0.01	1.62 ± 0.06	2.33 ± 0.02
^{60}Co Above $1.6 \times 1.6 \times 7$ mm^3 pixel detector	1.44 ± 0.02	2.01 ± 0.03	0.97 ± 0.01	0.74 ± 0.01	1.64 ± 0.06	2.40 ± 0.02

Table 6 - Table showing the ratios of efficiency and energy resolution after correction to the initial values. The average improvement for individual pixels is shown in addition to the measured values for the entire detectors. Measurements were performed using ^{137}Cs 662 keV and ^{60}Co 1332 keV sources with both detector sizes.

The first column in Table 6 shows the average efficiency increase for the pixels due to the correction process. Column 2 shows the measured efficiency increase for the detector. These values are substantially different, differing by as much as 50% for the larger pixel detector when measuring with a ^{60}Co source; and showing nearly 30% differences for the 662 keV ^{137}Cs gamma-ray source in both detectors. This is because ‘gain matching’ (calibration) is not included in the single pixel analysis. The third and fourth columns show the averaged improvement in energy resolution across the pixels and the total improvement in energy resolution respectively. Once again the improvement is significantly greater when examining the total detector. However, unlike with the efficiency, the single pixels exhibit virtually no improvement while the detector exhibits significant improvements of 20% or more. The

difference between these values suggests that most of the improvement seen is not a result of the straightening of the peak itself, but rather of the earlier step of aligning the gains of the pixels. Finally, the fifth and sixth columns show the improvement in the ‘peak to trough’ ratio and suggest that while the ‘gain matching’ has a significant effect, the process of ‘straightening’ the photopeaks is equally important.

4.7 Confirmation of the Absence of a Dependence upon the Source Location of the Energy Resolution and Efficiency Improvements

In order to confirm that the location of the source produces no positional dependence, a plot was made to show the energy resolution and efficiency improvements for the two different source locations. The pixels have been arranged to match their physical layout, as illustrated in Figure 38.

1	5	9	15
3	7	11	13
2	6	10	16
4	8	12	14

Figure 38 - Location of pixels within the detector.

Accordingly, in Figure 39, the pixels have been laid out (from left to right) in the order:

4	8	12	14		2	6	10	16		3	7	11	13		1	5	9	15
---	---	----	----	--	---	---	----	----	--	---	---	----	----	--	---	---	---	----

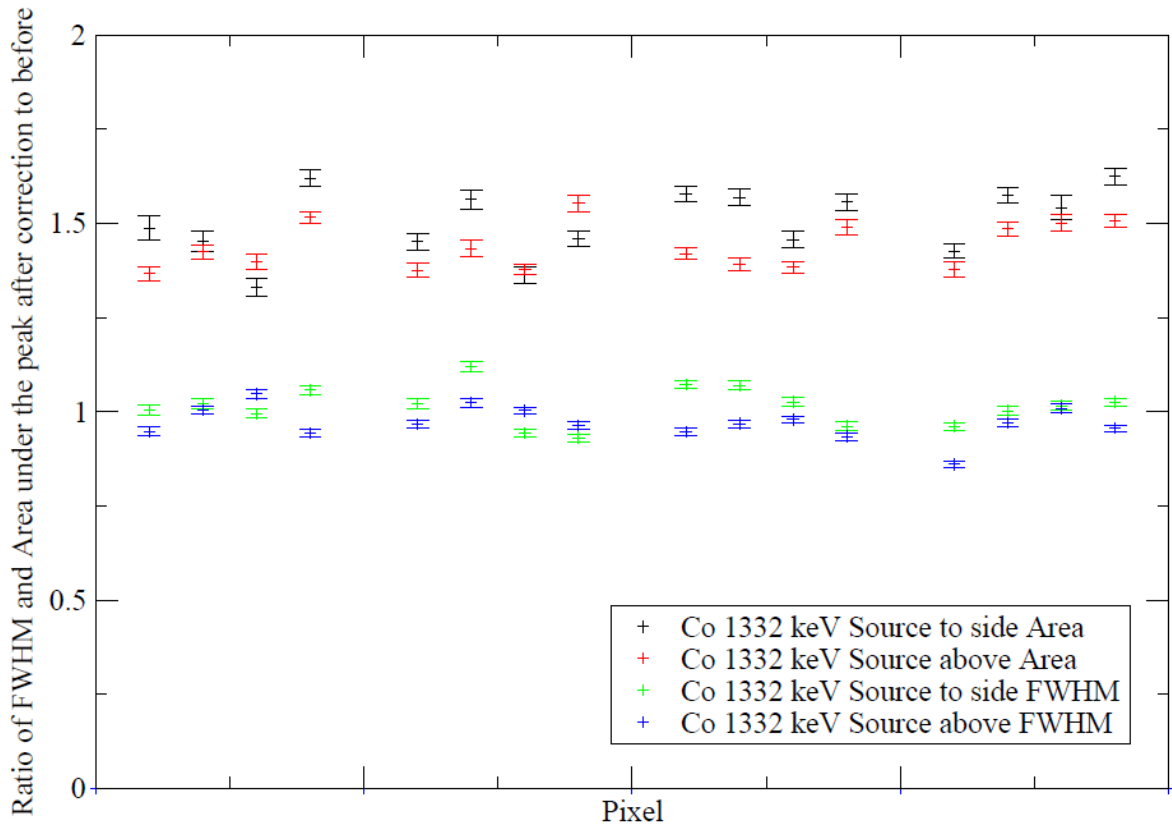


Figure 39 - Ratio of the area under the peak and the Full-Width Half Maximum of the peak after correction to before. The analysis was performed for a ^{60}Co source (1332 keV gamma) situated to the right-hand side of the detector and with the source situated above the detector. Ratios less than 1 indicate a decrease in FWHM after correction and thus an improvement in energy resolution.

If the source location was important then the improvement for measurements where the source was situated to the RHS of the detector would be greater to the right hand side of each group of four pixels. It is apparent that this is not the case, either for the efficiency or for the energy resolution. The values for the measurement with the source to the side are in agreement with those where the source was above the detectors.

4.8 Dependence of the Energy Resolution and Efficiency Improvements as a Function of Source Energy

Analysis was performed to confirm the presence of any energy dependence in the polynomial correction applied to remove the low energy tail. Since the source data were taken on different occasions, the amplifier gains and other settings were not always fixed. Hence the present analysis focuses on the enhancement due to the straightening of the peak line-shapes. A series of measurements were analysed. These included three different measurements using ^{60}Co (all of which used the 1332 keV peak and one of which also involved the 1173 keV peak), one measurement was performed using ^{152}Eu , four measurements using ^{22}Na (using different noise rejection techniques) and six measurements using ^{137}Cs .

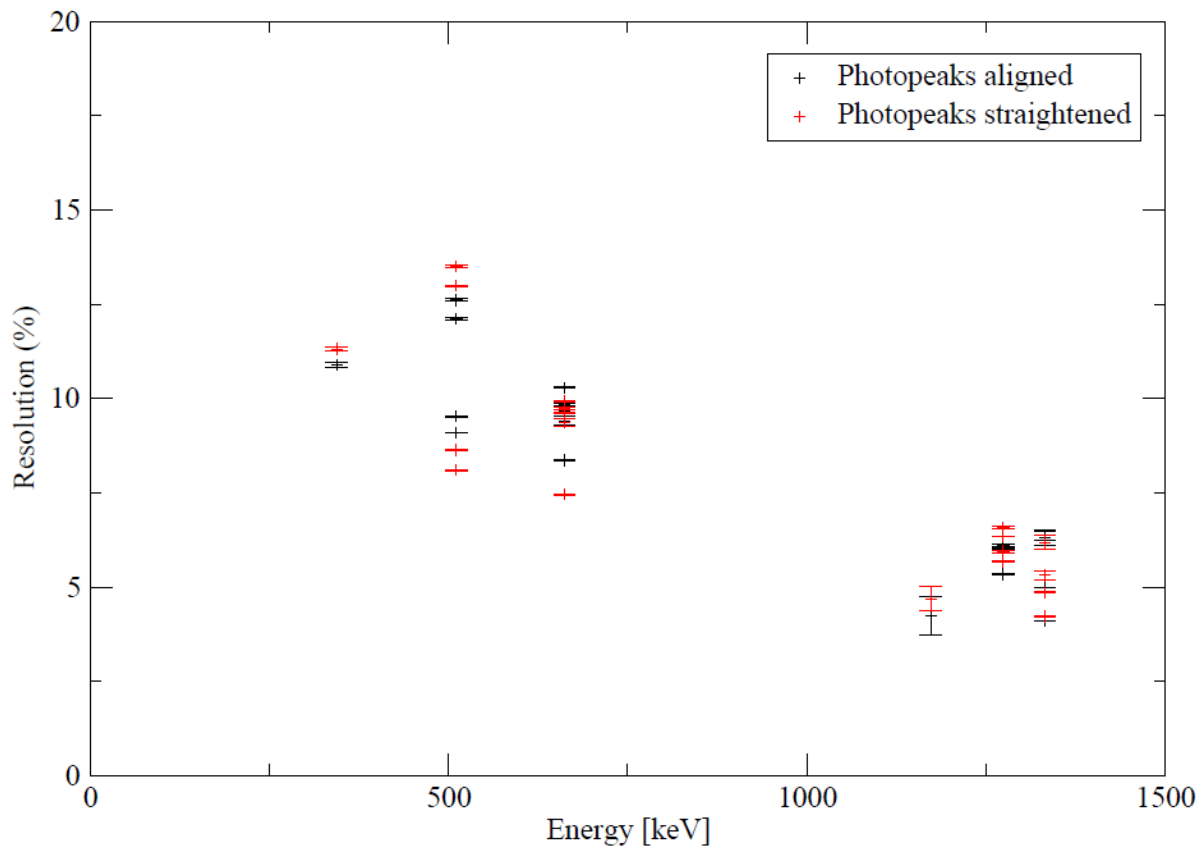


Figure 40 - Plot of detector energy resolution (%) against Source energy (keV) both after alignment and after the photopeaks were straightened. Measurements are shown for 344.27 keV (^{152}Eu), 511 keV (^{22}Na), 662 keV (^{137}Cs), 1173 keV (^{60}Co), 1274 keV (^{22}Na) and 1332 keV (^{60}Co). Measurements were taken for all data points with sources both to the side and above the detectors.

Figure 40 shows the percentage energy resolution ($\Delta E / E$) of the larger detector as a function of the source energy. The figure suggests that the energy resolution of this detector is around 10% at 662 keV. However, the statistical error bars present do not completely describe the uncertainties in the points, suggesting a large (as much as 7% at 511 keV) systematic error. Figure 41 shows the ratio of FWHM after the photopeaks have been straightened to after alignment for the 12 measurements (15 photopeaks).

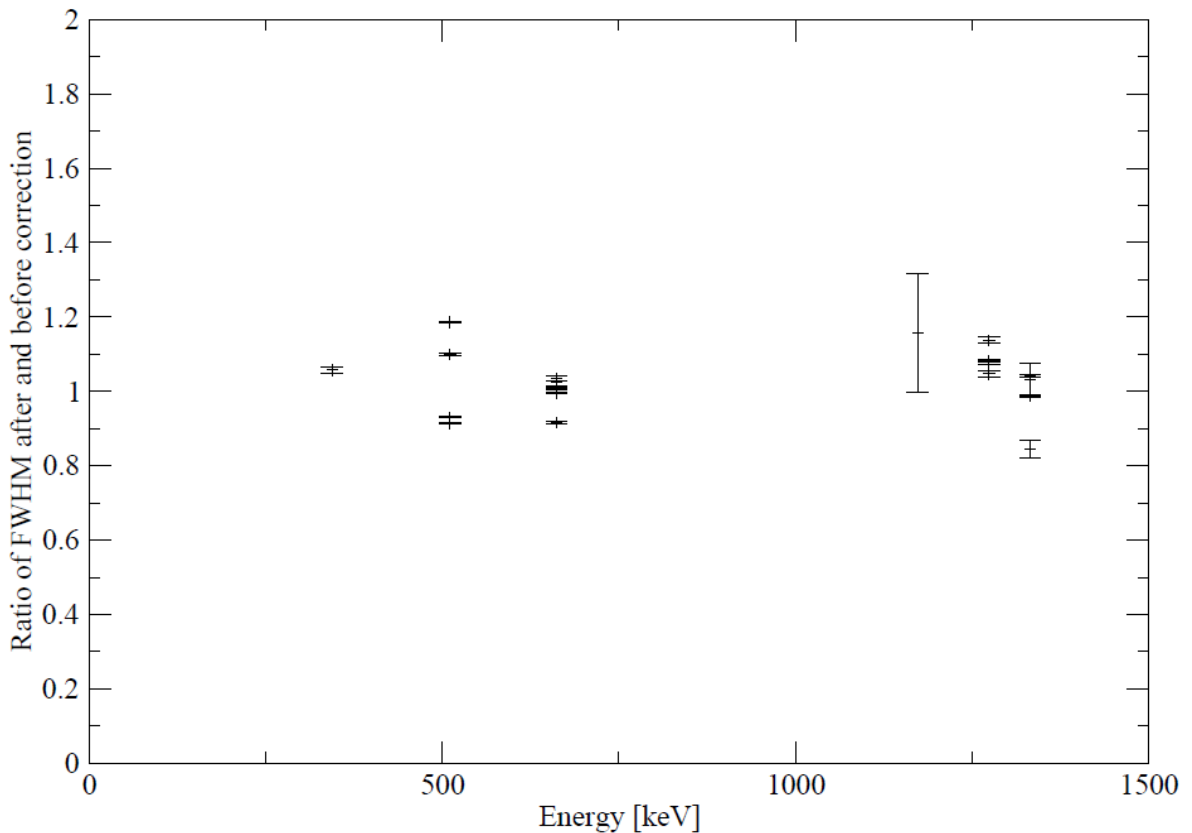


Figure 41 - Ratio of the FWHM after peak straightening to after alignment. Measurements are shown for 344.27 keV (^{152}Eu), 511 keV (^{22}Na), 662 keV (^{137}Cs), 1173 keV (^{60}Co), 1274 keV (^{22}Na) and 1332 keV (^{60}Co). Measurements were taken for all data points with sources both to the side and above the detectors.

Despite three ^{60}Co source measurements being analysed, it was only possible to accurately fit the 1173 keV peak with one. Even in the case where this analysis was possible, the error was large. Nevertheless, it is apparent that the FWHM improvement changes very little with energy. It is also clear from the measurements that the error bars do not fully account for the uncertainties in this analysis, again indicating that the errors have a further systematic contribution.

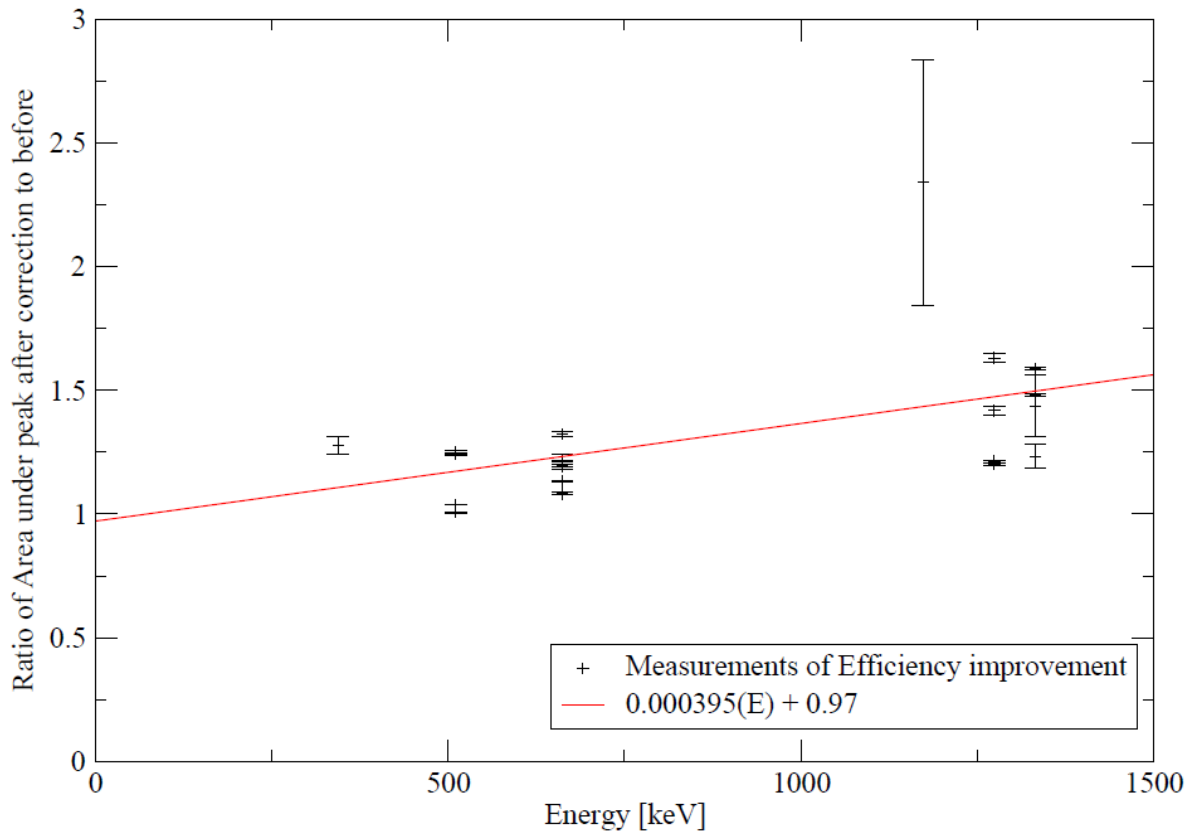


Figure 42 - Ratio of the area under the peak after peak straightening to after alignment. Measurements are shown for 344.27 keV (^{152}Eu), 511 keV (^{22}Na), 662 keV (^{137}Cs), 1173 keV (^{60}Co), 1274 keV (^{22}Na) and 1332 keV (^{60}Co). Measurements were taken for all data points with sources both to the side and above the detectors. The trend line is based upon a weighted fit, the weightings for each data point being the reciprocal of the errors squared. A trend is shown suggesting that the improvement in the area under the peak is indeed energy dependent and that this improvement increases at around 40% per MeV. Ratios greater than 1 indicate an increase in the area under the peak after correction and thus an increase in efficiency.

Figure 42 shows the ratio of area under the photopeak after the gains were aligned. It is apparent that the ratio increases with source energy (around 40% per MeV).

4.9 Conclusion

In conclusion, the improvements seen in the energy resolution and also in the efficiency are dominated by the relative improvement due to the alignment of the photopeaks. This is verified by the fact that individual pixel improvements are less than those for the entire detector. However, this is not the only component; significant efficiency gains can result from the process of straightening the photopeaks and, as seen when comparing different sources, this improvement appears to increase with energy. The energy dependence of this improvement in efficiency is likely to be a result of the apparent increase in curvature of the photopeaks with energy (as seen in Figure 28). Overall, the alignment process contributed around a 35% increase in efficiency in the larger detector, and the straightening process (which was energy dependent) a subsequent 50% increase at 1332 keV and 8% at 662 keV. The smaller detector exhibited a 43% increase due to alignment and between 30% and 100% increases due to the straightening at 1332 keV but the efficiency apparently decreased by 8% at 662 keV. However, these latter results suffered from relatively poor statistics compared to the measurements performed with the larger detector.

The energy resolution was not significantly improved by the straightening of the peak. It is probable that the dominance of events close to the complete collection line limits the effect which events lying within the energy tail can have upon the FWHM. While the energy resolution was not improved by the straightening process, the improvement due to the alignment process ranged from 15% to 28% in both detectors, and the change in the energy resolution due to the straightening of the detectors varied from a 16.5% improvement to a 29% deterioration in the smaller detector but only from a 8% improvement to a 4% deterioration in the larger detector. Finally, the improvements in energy resolution were found not to exhibit any strong energy dependence, while those in efficiency exhibited a dependence of around a 40% improvement per MeV.

5. Signal Sharing between Pixels

In Section 3, it was suggested that the component of the spectrum to the left of the line of complete collection on the cathode (the solid line in Figure 43) could be due to incomplete charge collection on the anode, caused by sharing of signal between pixels.

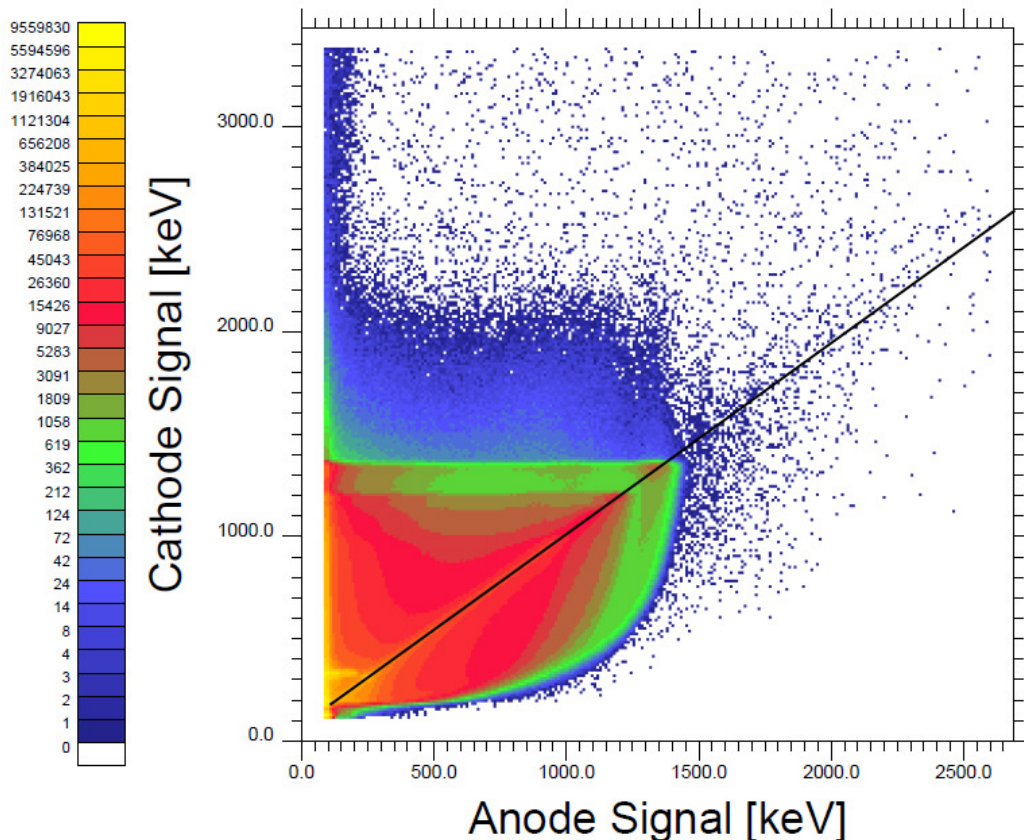


Figure 43 – CZT spectrum where proposed signal sharing can be seen to the left of the line of maximum collection on the cathode (as indicated by the solid line) – the spectrum corresponds to a ^{60}Co source located to the side of the $1.6 \times 1.6 \times 7 \text{ mm}^3$ pixel detector. Note the vertical pile-up present in this spectrum due to high detector counting rate.

If this suggestion is correct, then, for an event where only a single, central, pixel is active, the corresponding spectrum should exhibit no such component to the left of the line of complete collection; that is to say, a multiplicity one event occurring within a central pixel should not exhibit this feature.

In order to demonstrate this, spectra were produced for three pixels; situated centrally (pixel 6), upon one side of the detector (pixel 5) and at a corner (pixel 4); the locations of these pixels are as shown in Figure 38. The spectra for each pixel can be seen in Figure 44, Figure 45 and Figure 46, respectively.

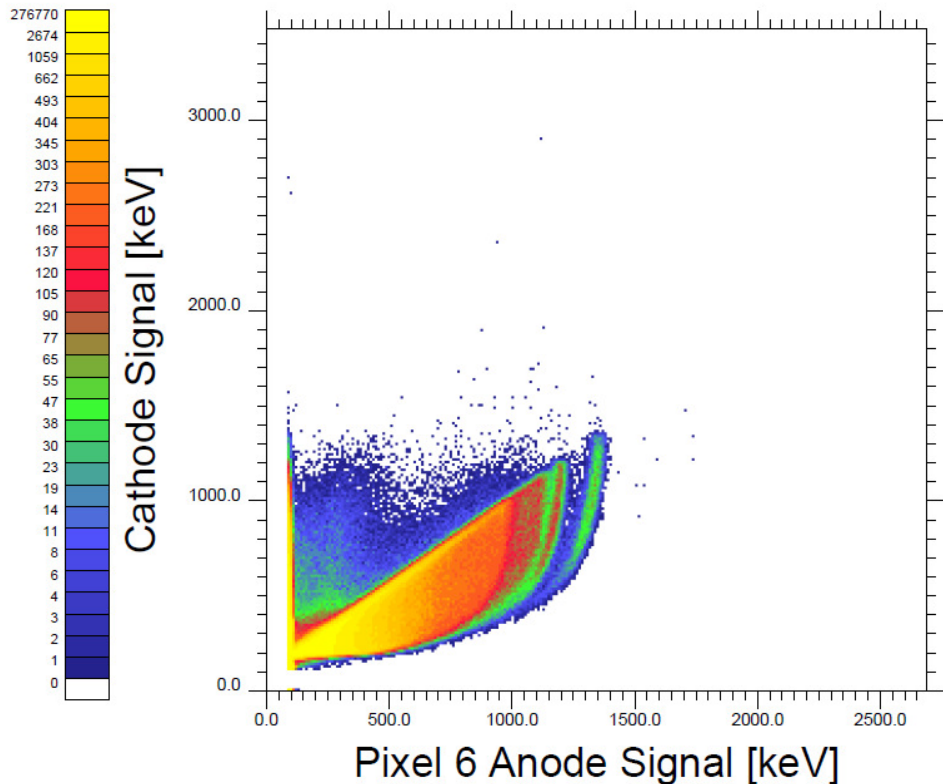


Figure 44 - Spectrum for ^{60}Co source located to the side of the $1.6 \times 1.6 \times 7 \text{ mm}^3$ pixel detector for multiplicity 1 events - within a central pixel (pixel 6). Events lying above the diagonal of complete collection are reduced, in addition, the single pixel and single event nature of this spectrum leads to significantly improved resolution of the two photopeaks.

Figure 44 shows the spectrum produced for a central pixel; as expected, the additional component to the left of the line in Figure 43 is almost completely eliminated and this is mirrored in the other central pixels. However, this is not the case for pixels which are situated near the edge of the detector.

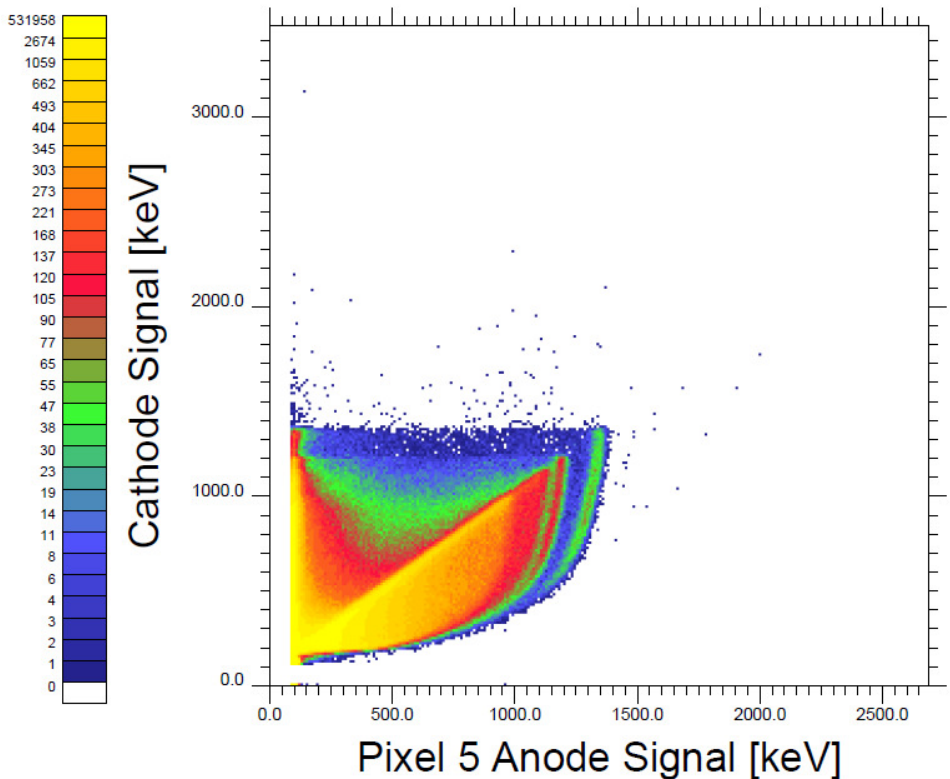


Figure 45 - Spectrum for ^{60}Co source located to the side of the $1.6 \times 1.6 \times 7 \text{ mm}^3$ pixel detector for multiplicity 1 events - within a pixel situated on the side of the detector (pixel 5). While the two photopeaks remain clear, the events above the diagonal of compete collection have increased.

For those pixels which lie at the side of the detector such as that seen in Figure 45, the component is still present. This is believed to be due to events occurring near the cathode (hence the large cathode signal), the electrons from which will then drift as a charge distribution to the anode. As the charge distribution moves, it also spreads out, which, in the case of pixels at the edge of the detector, can lead to charge being ‘lost’ to the anode. If the distribution drifts into another pixel, then this second pixel’s anode will collect the signal and hence such events are removed from this analysis as they are no longer seen to be multiplicity one events. This effect should then be more pronounced for the event where the pixel borders two faces of the detector (i.e. a corner pixel).

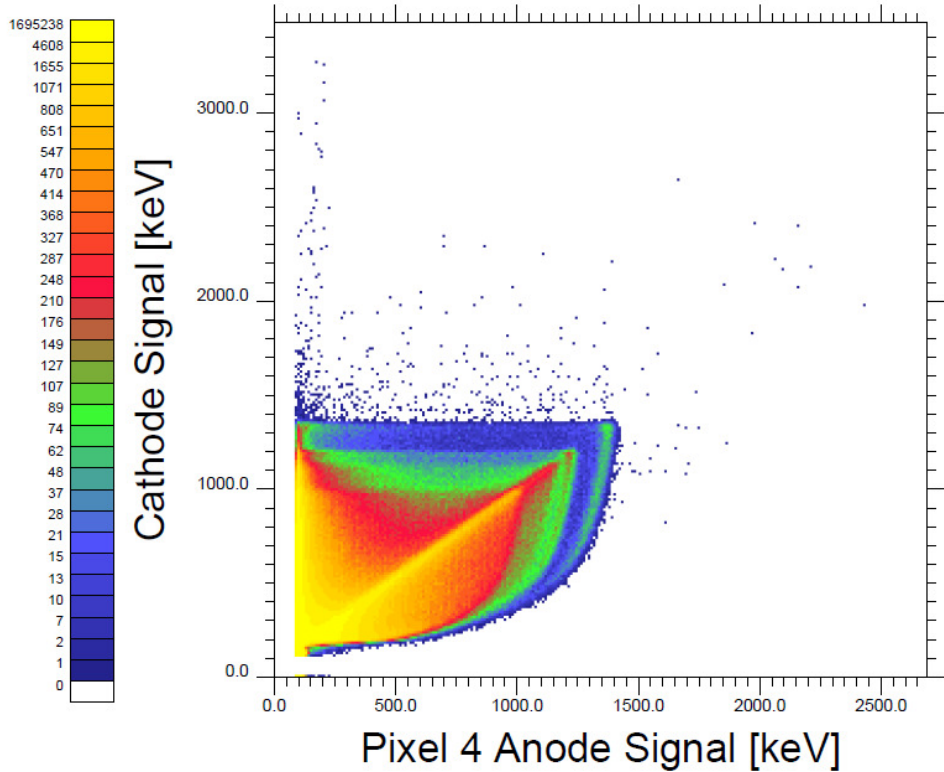


Figure 46 - Spectrum for ^{60}Co source located to the side of the $1.6 \times 1.6 \times 7 \text{ mm}^3$ pixel detector - within a pixel situated on the corner of the detector (pixel 4). The events above the diagonal of complete collection have increased substantially over pixel 6, and even over pixel 5.

In Figure 46, which shows the spectrum for a corner-located pixel, it is clear that the additional component is even more pronounced, indicating that charge distribution dispersal is an important feature of the behaviour of the detector.

5.1 The Effect of Signal Sharing

Figure 44 clearly shows that for multiplicity 1 events, the central pixel strongly suppresses the additional component which lies to the left of the maximum cathode collection line. The pixels near the sides, however, and especially those at the corners, substantially demonstrate this feature. The reduction of this component could have a marked effect on the relative intensity of the peak to background ratio in the low energy part of the spectrum, in particular for the pixels around the edge of the detector. In order to explore this, one-dimensional spectra were created within a window, placed on the energy deposited on the cathode, of

1065.6 ± 133.2 keV. A two-dimensional spectrum for pixel 6 (the central pixel) is shown in Figure 47 which illustrates this energy cut. The corresponding one-dimensional spectra are plotted in Figure 48.

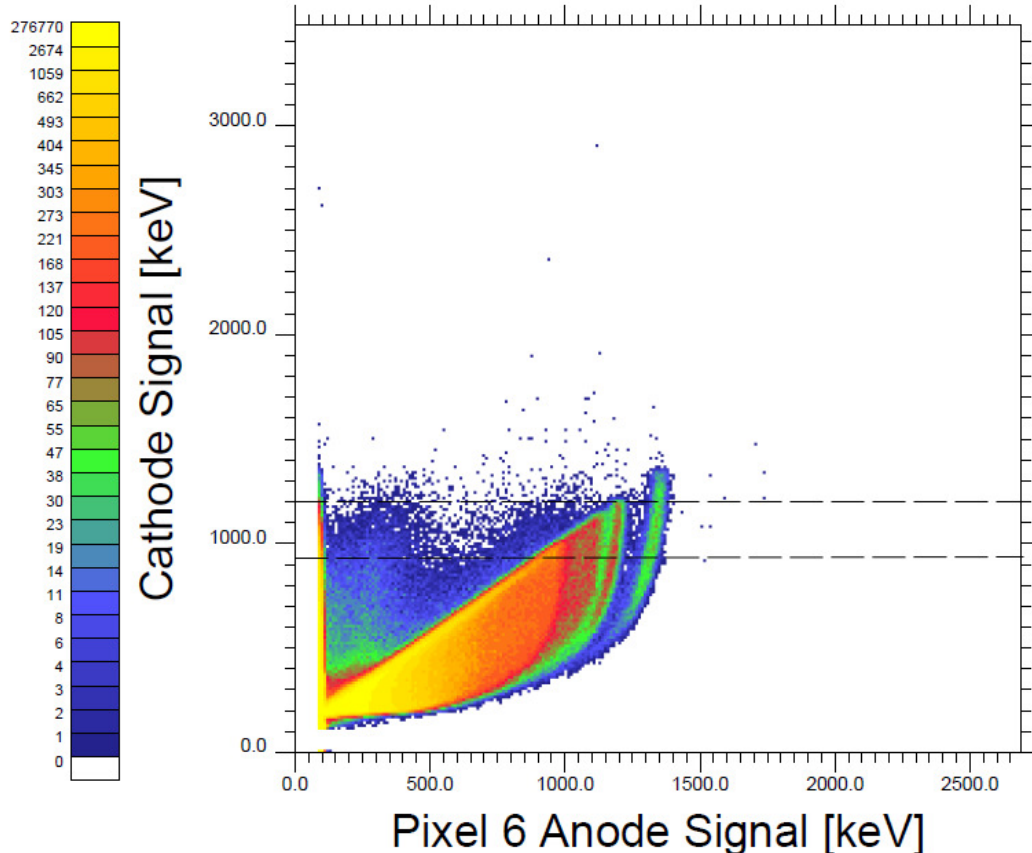


Figure 47 – Two-dimensional spectrum of multiplicity 1 events measured in the central pixel (pixel 6) plotted against the cathode energy of the large ($1.6 \times 1.6 \times 7$ mm 3 pixel) detector showing the cathode energy window of 1065.6 ± 133.2 keV used to produce the spectra in Figure 48.

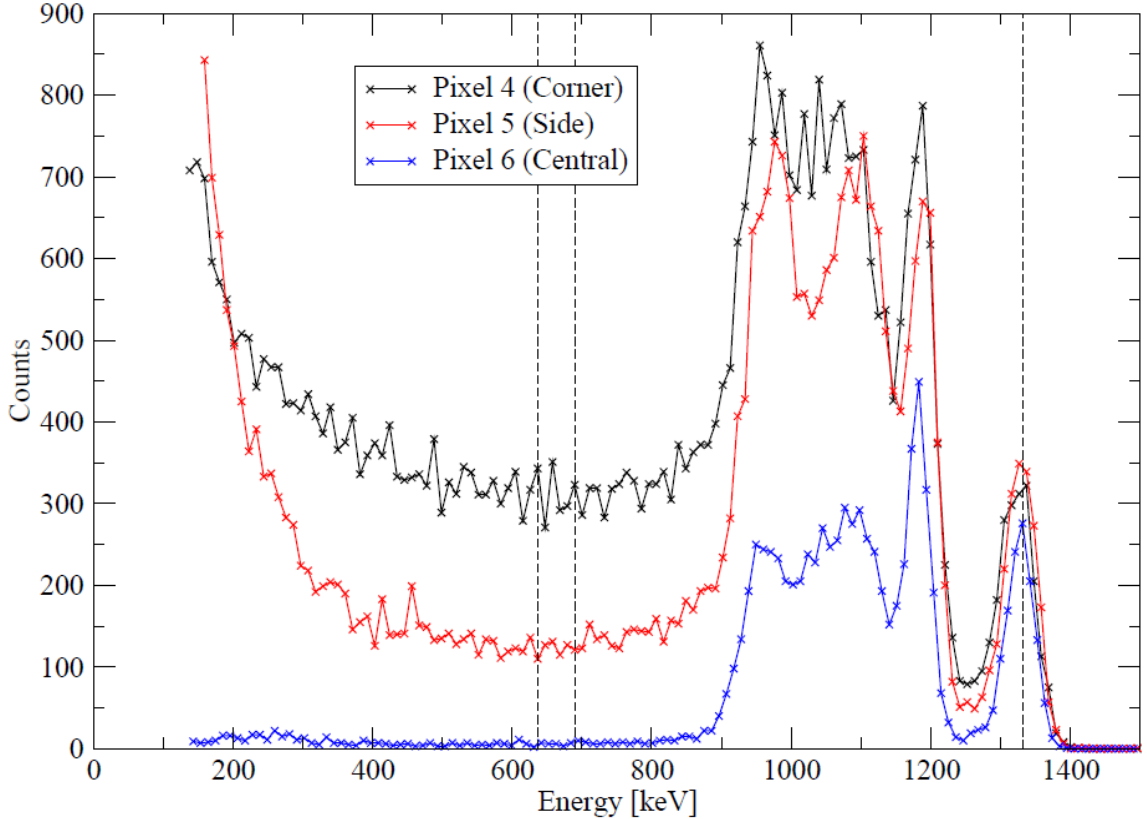


Figure 48 – One-dimensional spectra of energy deposited in pixels 4, 5 and 6, for multiplicity 1 events, within a cathode energy range of 1065.6 ± 133.2 keV for the larger ($1.6 \times 1.6 \times 7$ mm 3) pixel detector.

Ratios were taken of the size of the intensity of the component of interest (averaged between 637 and 690 keV) against the intensity of the 1332 keV photopeak. An example of the spectra is seen in Figure 48, for the larger detector. Dashed lines mark the extent of the averaging region and also the photopeak. It is apparent that the ratio for the corner pixels is approximately unity, while the ratio of the central pixel is extremely large.

Measurement using ^{60}Co Source 1332 keV Peak	Intensity ratio for detector of pixel size $1 \times 1 \times 5$ mm 3	Intensity ratio for detector of pixel size $1.6 \times 1.6 \times 7$ mm 3
Corner pixel (4)	$1:1.33 \pm 0.20$	$1:1.15 \pm 0.03$
Side pixel (5)	$1:0.82 \pm 0.20$	$1:0.51 \pm 0.03$
Central pixel (6)	$1:1.17 \pm 0.24$	$1:0.09 \pm 0.07$

Table 7 – Change in the ratio of photopeak intensity to component intensity with the source located to the side of the detector. The ratio changes as signal sharing is suppressed for events where only one pixel is triggered.

Table 7 shows the ratio of peak intensity to component intensity for multiplicity one events with the source located to the side. In the larger detector, the ratio is almost doubled when moving from a corner pixel to a side pixel and is increased by a factor of 10 when moving to the central pixels. This indicates that corner pixels exhibit far greater loss of signal out of the detector than side pixels (a factor of two), but both pixels lose substantial amounts of charge when compared to the central pixels. It can be argued, that the larger pixel size greatly increases the chance of collecting an event in a single pixel, and, where the possibility of loss outside the detector is removed, this effect becomes dominant. However, in the smaller detector, the change in ratio is minimal, indeed the ratios are almost consistent with unity. Observation of the spectra reveals that for the larger detector, the majority of full energy signals lie near the cathode, while for the smaller detector, events are distributed more evenly. This can be seen in Figure 49.

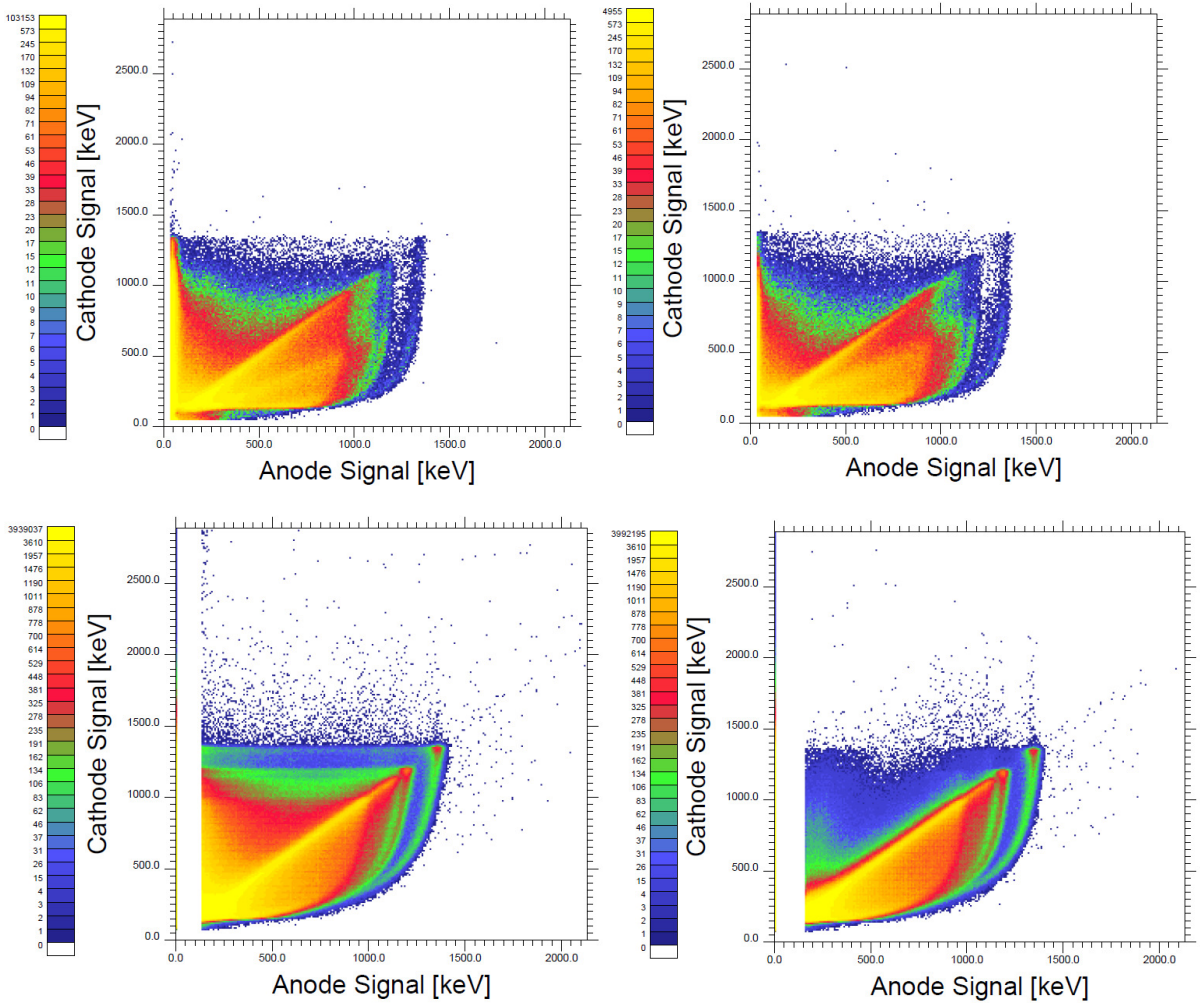


Figure 49 – Sample spectra from corner and central pixels (left and right respectively) in the small and large detectors (top and bottom respectively). It is apparent that the central pixels have reduced signal above the line of complete collection, but that while this reduction is very large in the larger detector, it is minimal in the small detector. All four measurements were performed with the ^{60}Co source located to the side of the detectors.

This focus of events near the cathode in the larger detectors greatly emphasises the ratio of peak to shared signal. In the smaller detector where this concentration is not present, the ratio is more even.

A second study was performed to examine the same ratio for those pixels when both they and another pixel were active. This measurement would allow events where a particle interacted in two pixels, and also where the dispersed charge distribution or x-ray fluorescence triggered a second pixel, to contribute to the background component.

Measurement using ^{60}Co Source 1332 keV Peak	Intensity ratio for detector of pixel size $1\times 1\times 5 \text{ mm}^3$	Intensity ratio for detector of size $1.6\times 1.6\times 7 \text{ mm}^3$
Corner pixel (4)	$1:6.94\pm 0.12$	$1:2.31\pm 0.025$
Side pixel (5)	$1:5.85\pm 0.11$	$1:1.88\pm 0.023$
Central pixel (6)	$1:8.50\pm 0.14$	$1:1.94\pm 0.025$

Table 8 – Change in the ratio of peak intensity to component intensity as signal sharing between pixels is suppressed for events where two pixels are triggered.

Table 8 shows the ratio of the peak intensity to the component intensity for events where two pixels are triggered. As a result, movement from the corner pixels to the central pixels will remove the element of the component that is composed of shared charge distributions, but not the element which is due to events being shared between multiple pixels. In the smaller detector, central detectors do apparently see an increased component relative to corner pixels, but the effect is small compared to the dominance of shared events. However, the large detector shows a reduction in component intensity in the central pixel relative to the corner. This suggests that sharing of events is central to the increased component in the central pixels when compared to the side pixels, but that some other effect is dominant in the corner pixels. The component is significantly smaller in the larger detector, and the relative change is also smaller suggesting that multi-site events are less frequent in larger-pixel arrays.

The above analysis confirms that the sharing of signal between pixels, and the loss of signal outside the detector, is the source of the component of the spectrum observed in Figure 43; and, at least for central pixels, that the sharing of events should constitute the component in its entirety. In order to confirm this, a spectrum was plotted showing the signal collected on the cathode against the signal on a centrally located pixel anode for events where two pixels were ‘active’ (see Figure 50).

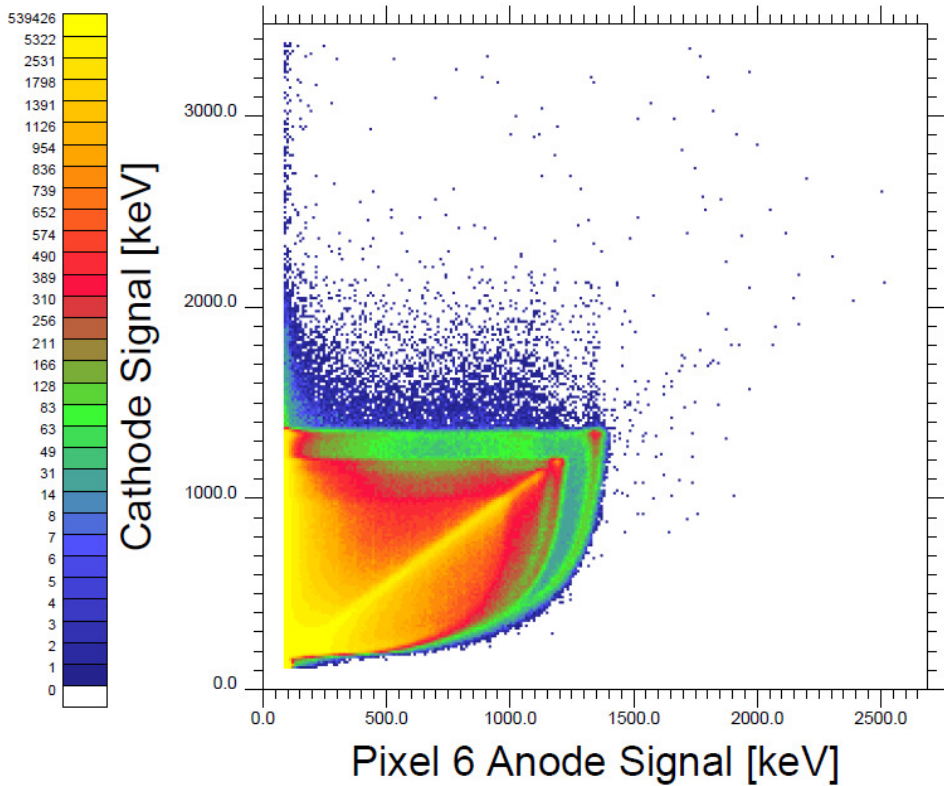


Figure 50 - Spectrum for central pixel of a $1.6 \times 1.6 \times 7 \text{ mm}^3$ pixel detector with a ^{60}Co source, located to the side of the detector, where only two pixels (one of which is the central pixel) are triggered.

The additional component situated to the left of the highest energy peak (at the complete collection line for the cathode) would then be caused almost exclusively by sharing of the signal between pixels. This is revealed when plotting the anode signal for pixel 6 against the anode signal for the second active pixel, as seen in Figure 51.

In Figure 51, any event where complete collection is found (within the whole detector) will be represented by a diagonal line whose ends lie at the total energy of the event on both axes. In the event that this line was bowed, and not a straight line, then this would be indicative of charge loss.⁹¹ There is some indication of charge loss within the diagonal representing the 1173 keV photopeak and the Compton scatter line from the 1332 keV photopeak. This suggests that in events where a gamma-ray undergoes a Compton scatter, there is some loss of energy to adjacent pixels, most likely in the form of x-ray fluorescence or charge carriers being collected on adjacent pixels.

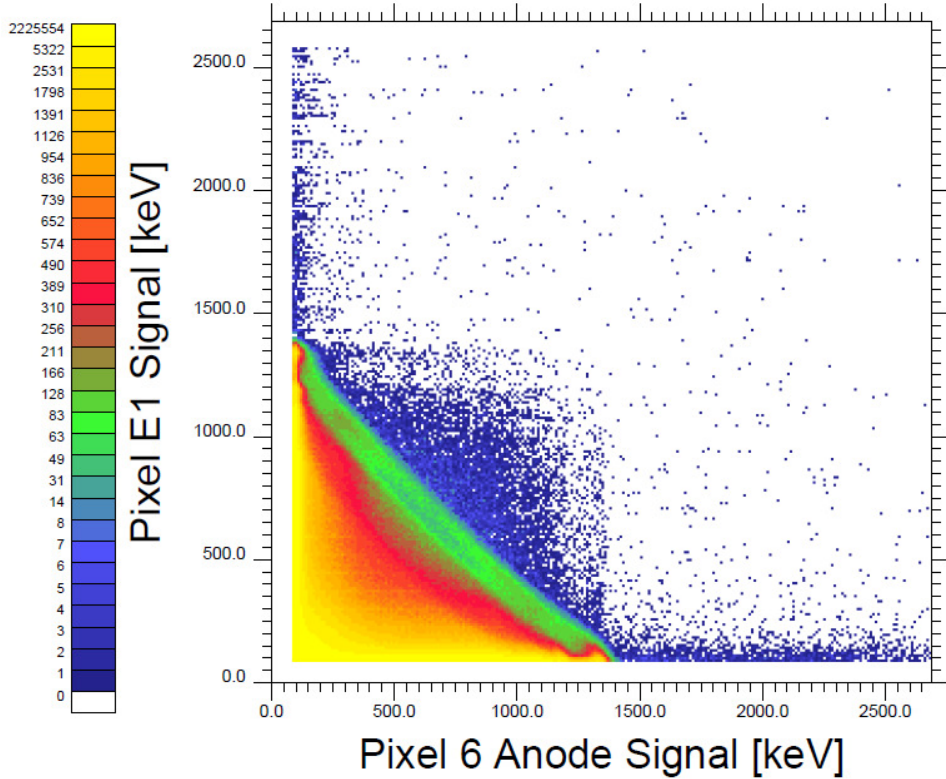


Figure 51 - Plot of signal in the central pixel against signal in the second active pixel for a $1.6 \times 1.6 \times 7 \text{ mm}^3$ pixel detector with a ^{60}Co source located to the side of the detector. Events which are completely collected between the two pixels lie within a diagonal line of that energy. Events which lie below these diagonals are due to incomplete collection, either due to loss of energy outside the detector, or loss to adjacent pixels which are not triggered. Those events which lie above the diagonal suggest events where two independent gamma-ray's were collected, to some extent, upon the two pixels, these events will also contribute to the spectrum within the diagonals.

The complete collection line for the 1332 keV peak of the ^{60}Co source lies on a diagonal of two values whose sum is 1332 keV. By integrating the number of events which lie along this line (within a gate of ± 50 keV) and the events which lie along the cathode value at 1332 keV ± 50 keV in Figure 50, it is possible to confirm if the two numbers are in agreement, and thus, if the component is indeed primarily formed by events whose signal is shared between pixels.

5.2 Recombining the Signals

As was shown in Section 5.1, events shared between two pixels can be seen to be correlated in energy. It should be possible to recombine these events in order to increase the efficiency of the detector. Furthermore, by recombining these events they can be removed from the single pixel event spectra, reducing the additional background component. An example of this recombination is presented in Figure 52.

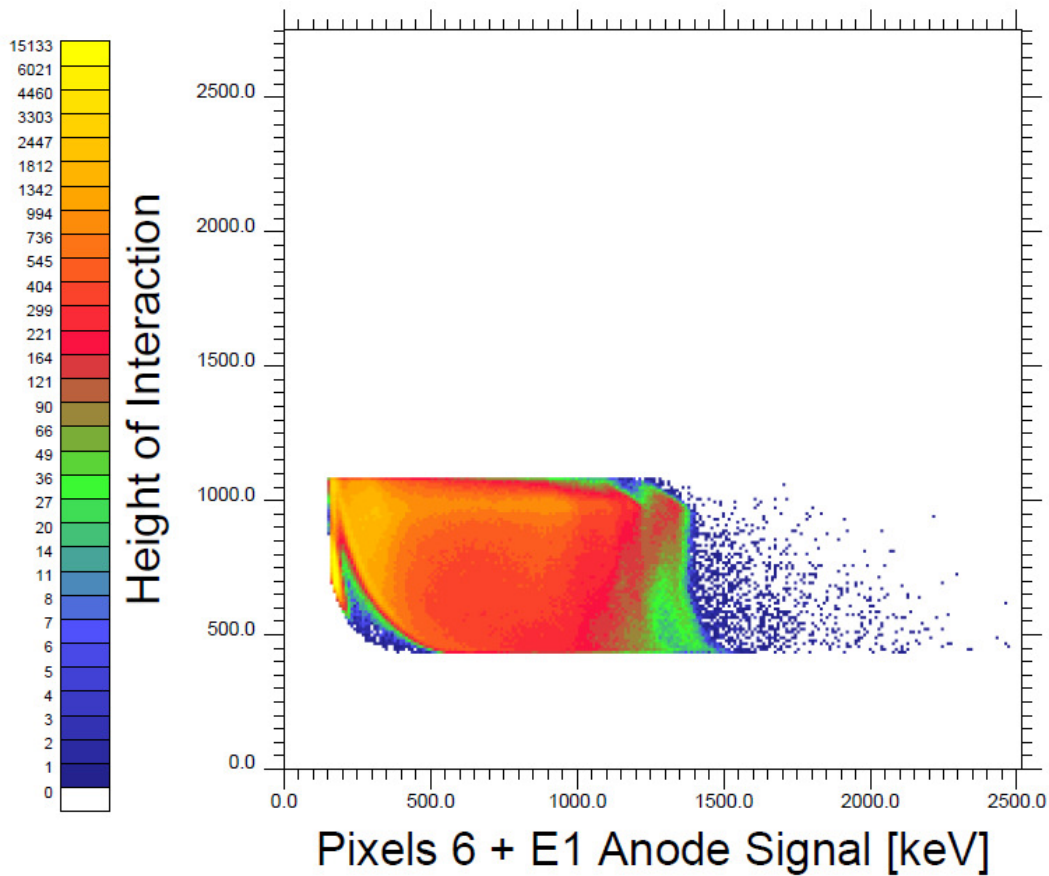


Figure 52 - Example of spectra of multiplicity two events where pixel 6 and one other pixel (E1) were active. The measurement was taken using a $1.6 \times 1.6 \times 7 \text{ mm}^3$ pixel detector and a ^{60}Co source located to the side of the detector. A threshold of 70 keV was used to select active pixels. The diagonal line of complete collection is seen, along with events which are apparently still due to sharing/loss of signal to adjacent pixels. In addition, the 1332 keV photopeak is seen to be constructed of 2 components. In addition, there are also components of events where two separate gamma-rays have been collected, seen at anode signals of greater than 1332 keV and of pile-up of signals upon the cathode (seen at cathode signals of greater than 1332 keV).

Figure 52 shows the recombination of pixel 6 and another pixel when only two pixels were triggered. The correction process outlined in Section 3 has been applied to the data.

Events were sorted by energy such that E1 was the pixel with the most deposited energy (or if pixel 6 met that condition, then E1 was the pixel with the second largest energy deposition). The spectrum in Figure 52 shows the recombined events for any event where only two pixels (one of which was pixel 6) were active, and an energy of greater than 70 keV was deposited within each. The energy resolution of the photo-peak is reduced relative to that seen in Figure 43.

The reduced energy resolution is due to the combination of one of the following possibilities:

- x-ray's fluoresced from the incident pixel have not been recaptured within the two pixels, reducing the photopeak energy;
- two pixels are associated with a single event, but both have mismatched energy calibrations;
- two gamma rays interact independently within the two pixels;
- two pixels are associated with a single event, but one or both lose energy on the anode by charge distribution dispersal, either outside the detector or into adjacent pixels where the energy collected is below the threshold;
- one pixel is triggered by a real event, the second by noise, the tail of which can still be seen in the spectrum.

The energy resolution for the recombined events in Figure 52 is substantially larger than $\sqrt{2}$ greater than the energy resolution for single events, suggesting that the other factors dominate. The issues with noise can be reduced by increasing the threshold energy. The data in Figure 52 shows the analysis with a threshold of 70 keV and Figure 53 with a threshold of 205 keV. There is a substantial improvement in the energy resolution of the 1332 keV photopeak in this latter spectrum, however this is counter-balanced by a significant reduction in efficiency.

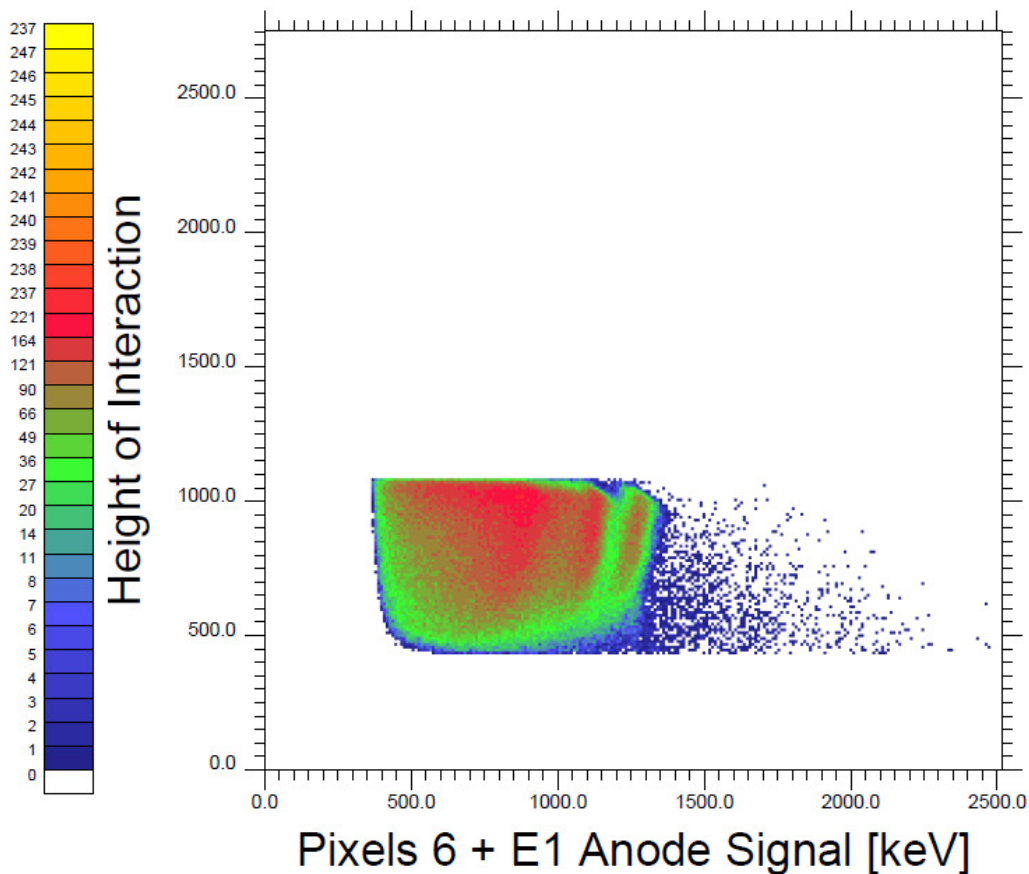


Figure 53 - Multiplicity 2 events where pixel 6 and one other pixel (E1) were active. The measurement was taken using a $1.6 \times 1.6 \times 7$ mm³ pixel detector and a ^{60}Co source located to the side of the detector. A threshold of 205 keV was used. The number of events which are incompletely collected upon the two pixels is reduced, but still significant, however, the 1332 keV photopeak is now comprised of one component, and the energy resolution is greatly improved

Further increases in the threshold reduce the efficiency even more, while improving the energy resolution of the summed peak. Figure 54 shows a spectrum plotted for two pixels exceeding 345 keV. There is still some element of the component due to signal sharing, in this case due to events split over several pixels (only 2 of which have energy deposition over the threshold), or where significant energy is lost out of the detector due to charge carrier dispersion.

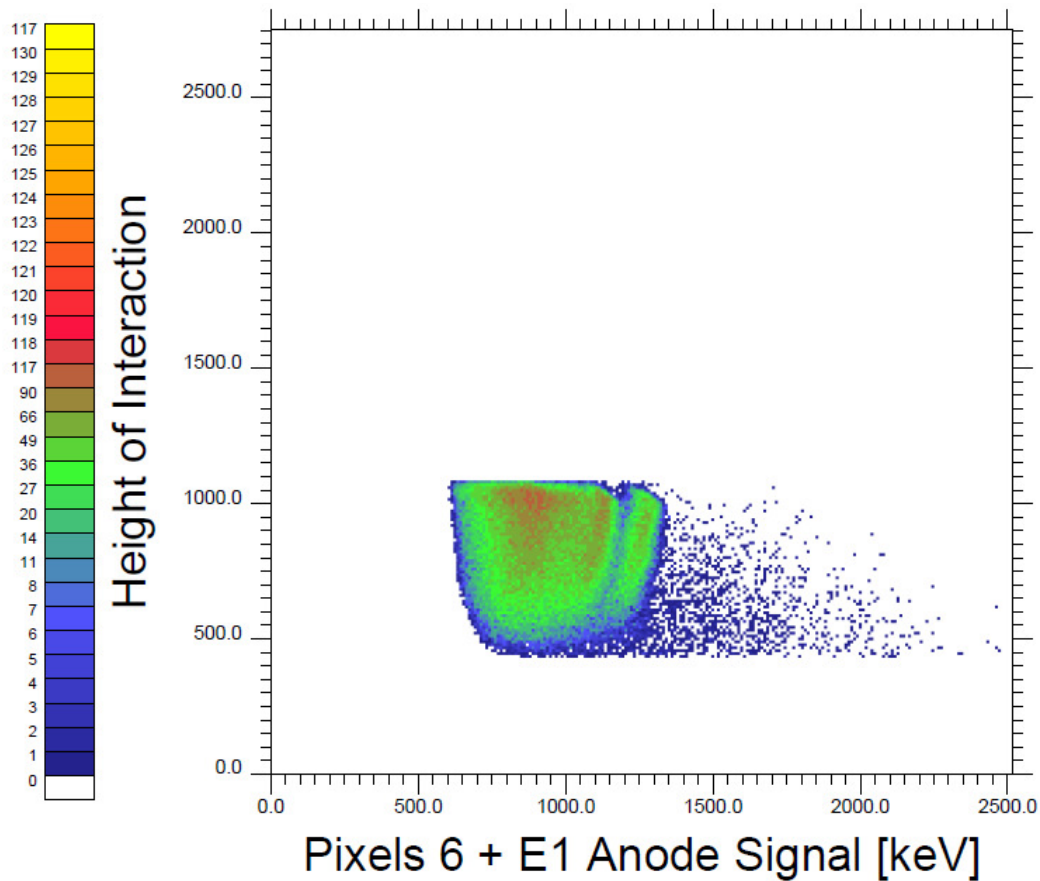


Figure 54 - Multiplicity 2 events where pixel 6 and one other pixel (E1) were active. The measurement was taken using a $1.6 \times 1.6 \times 7$ mm³ pixel detector and a ^{60}Co source located to the side of the detector. A threshold of 345 keV was used. The incompletely collected events are again reduced, with some further gain in energy resolution to the photopeaks. However, the efficiency of the peaks is greatly reduced.

The energy resolution and efficiency of the recombined photopeak (events within a cathode signal window of 1267 ± 79.5 keV) are shown in Table 9.

Threshold (keV)	Area (counts)	FWHM (keV)
Multiplicity 1	1605 ± 41	42.7 ± 0.8
70	50002 ± 313	89.1 ± 0.4
105	38674 ± 338	105.7 ± 0.7
140	27097 ± 301	105.5 ± 0.9
175	20597 ± 211	82.8 ± 0.8
205	18475 ± 184	76.2 ± 0.7
345	12025 ± 130	67.5 ± 0.7
485	6473 ± 94	64.3 ± 0.8
625	2494 ± 56	63.4 ± 1.2

Table 9 - Table showing the area under the ^{60}Co 1332 keV photopeak and the FWHM of the section of the peak that lies within a window on the Cathode energy of 1267 ± 79.5 keV while increasing the threshold energy on the pixel anodes. All the values are calculated for multiplicity two events where pixel 6 and one other pixel are active, except for the multiplicity one value, which is calculated for events within pixel 6. All are software threshold values and are applied after hardware thresholds.

Table 9 shows that the energy resolution of the peaks improves as the threshold increases; however the efficiency decreases substantially. The decrease in energy resolution indicates that $\sigma(E)$ must be a strong function of threshold energy. A multiplicity one value is given (threshold at 0 keV) to demonstrate the achieved energy resolution for multiplicity one events within the measurement. The apparently lower energy resolution at 70 keV (where the software threshold lies below the hardware threshold already applied) is due to the intensity of events where one pixel fully collects an event while a second pixel measures some electronic noise. The dominance of this effect means that the multiplicity two events contribute little to the FWHM measurement. The constraining limit on the energy resolution of $\sigma_{M2} = \sqrt{2}\sigma_{M1}$ is almost reached at a threshold energy of 485 keV.

As has been seen, the ability to reduce the component to the left of the full charge collection line due to shared events, (see Table 7) is important in background reduction, and particularly important in low count-rate experiments. In addition, it is important to note that the current pixel size allows complete photo-peak collection within a pixel, since the range of a 1 MeV

electron is \sim 1 mm; a fact that is not the case with proposed 200 micron pixel size detectors. For small pixel sizes, it is essential that events can be recombined within the detectors with good energy resolution and efficiency.

It is apparent that the removal of the outer edge pixels from calculations will substantially remove the background due to charge carrier loss, and, accordingly, limit the contribution to the left of the line of complete collection to multiplicity two or greater events. In addition, these removed pixels may be used as a veto to eliminate alpha-particle and other extrinsic events arising in the detector environment, or in the passivation material on the detector surface.

6. Compton Camera Techniques

The use of gamma-ray detectors outside of fundamental research has become an increasingly important area of study in recent years,^{92,93} in particular the use of detectors as gamma or ‘Compton Cameras’. Accordingly, work was performed here to study the possibility of using a pair of pixelated CZT detectors (or even a single pixelated detector) to predict the location of a source. This ability has practical applications within the bounds of neutrino-less double-beta decay searches, as it allows background sources to be located and removed, as well as in industrial, space and security environments.

As described in Section 5, the events which lie to the left of the complete charge collection line on the cathode are due to the sharing of the charge deposited between pixels. The observation of events shared between pixels suggested that a gamma-ray whose complete energy was deposited on the cathode, but was shared between pixels, could be tracked through the detector. In order to expand the detector system (and this tracking potential) to larger scale devices, it is necessary to examine this process in events where a gamma-ray also splits the energy deposition between two detectors. Assuming that the interaction within one of the detectors was first a Compton scatter for a particular incident energy, the energy deposition in that detector will be a function of the angle through which the gamma-ray is scattered. Thus, with two interactions it is possible to establish a cone of vectors along which the gamma-ray was incident, as seen in Figure 55.

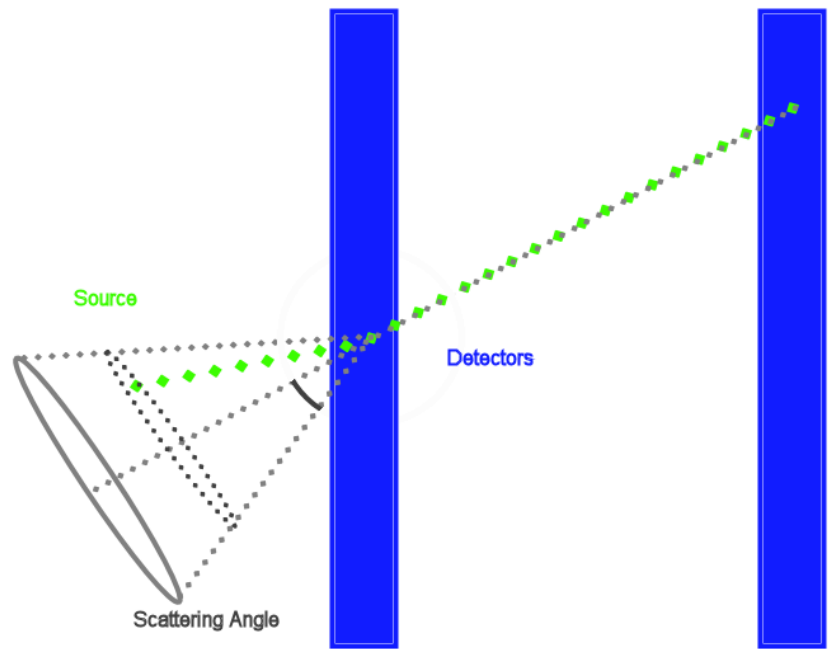


Figure 55 – The energy deposited during the Compton scatter in the first detector is a function of the angle through which the gamma-ray scattered. By establishing a vector from the point of the scatter to the point of deposition in the second detector, it is possible to find a cone of vectors along which the gamma-ray must have travelled prior to the scatter.

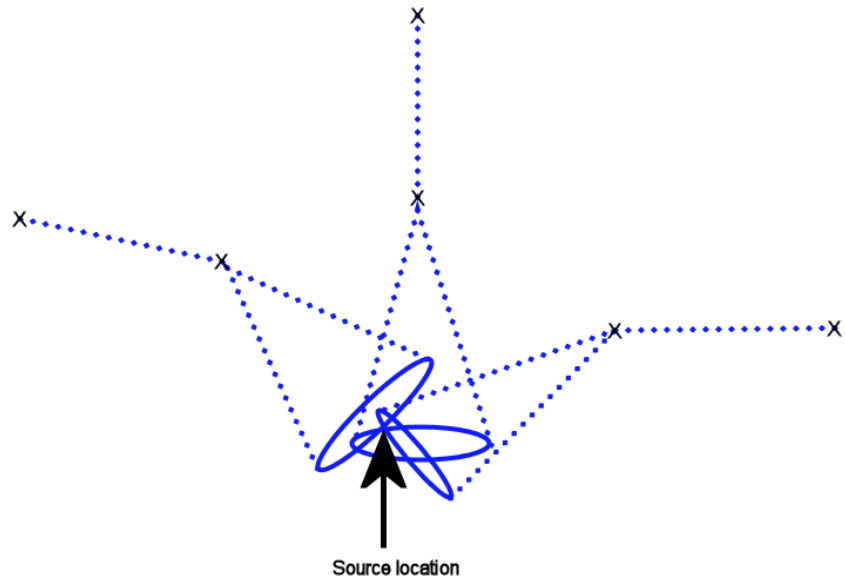


Figure 56 – By examining events in multiple pairs of detectors, it is possible to find cones along which the gamma-rays must have travelled within several planes. The source is located as indicated at the crossing point of the 3 cones created from interactions in detectors situated at each of the points marked X.

By expanding this method to multiple events shared between several pairs of detectors in different locations, a number of these cones can be found (as shown in Figure 56), the intersection of which corresponds to the location of the source.

This method of locating a source is the so-called ‘Compton Camera’ technique.⁹⁴ The method was originally proposed as a method in nuclear medicine imaging where it could be used to locate sources inside the human body (and thus could be used as an alternative to Positron-Emission-Tomography or PET). The technique can be used not only to precisely locate sources (such as finding localised background sources in a laboratory environment), but also to study fluid flow (by adding gamma emitters to the liquid, and studying the location of the sources as time progresses, it is possible to observe areas of lower viscosity) and to check bags or bottles at airports for radioactive materials.

Central to the camera’s operation is the fact that the energy deposited during the scatter is a function of the angle through which the gamma-ray is scattered. The energy given to the electron from which the gamma-ray scatters (and thus the energy deposited in the first detector) is given by equation 6.1. The remaining energy, given by equation 6.2, is carried by the photon and deposited in the second detector.

$$E_s(\theta) = E_{\text{gamma}} - \frac{E_{\text{gamma}}}{1 + \frac{E_{\text{gamma}}}{mc^2}(1 - \cos(\theta))} \quad (6.1)$$

$$E(\theta) = \frac{E_{\text{gamma}}}{1 + \frac{E_{\text{gamma}}}{mc^2}(1 - \cos(\theta))} \quad (6.2)$$

Here $E_s(\theta)$ is the energy deposited in the first detector (during the scatter), $E(\theta)$ is the energy deposited in the second detector (the energy carried away by the gamma-ray after the scatter), E_{gamma} is the energy of the original gamma-ray, m is the mass of the electron, c is the speed of light and θ is the angle through which the gamma-ray Compton scattered.

The probability of a gamma-ray scattering through a given angle θ is defined by the Klein-Nishina (K-N) distribution.^{95,96,97,98} This distribution, given in Equation 6.3,⁹⁶ shows the probability of scatter through a given angle as a function of the angle θ , a factor α and a constant r_0 .

$$\frac{d\sigma_c}{d\Omega} = r_0^2 \left[\frac{1}{1 + \alpha(1 - \cos\theta)} \right]^3 \left[\frac{1 + \cos^2\theta}{2} \right] \left[1 + \frac{\alpha^2(1 - \cos\theta)^2}{(1 + \cos^2\theta)[1 + \alpha(1 - \cos\theta)]} \right] \quad (6.3)$$

$$r_0 = \frac{e^2}{4\pi\epsilon_0 mc^2} = 2.818 \text{ fm} \quad (6.4)$$

$$\alpha = \frac{E_{gamma}}{mc^2} \quad (6.5)$$

Here r_0 is a function of the electron's charge (e), the mass of the electron (m) and the speed of light (c) while α is a function of the incident gamma-ray energy (E_{gamma}), the mass of the electron (m) and the speed of light (c) (thus for a gamma-ray energy of $E_{gamma} = 511 \text{ keV}$, α will have a value of $\alpha = 1$).

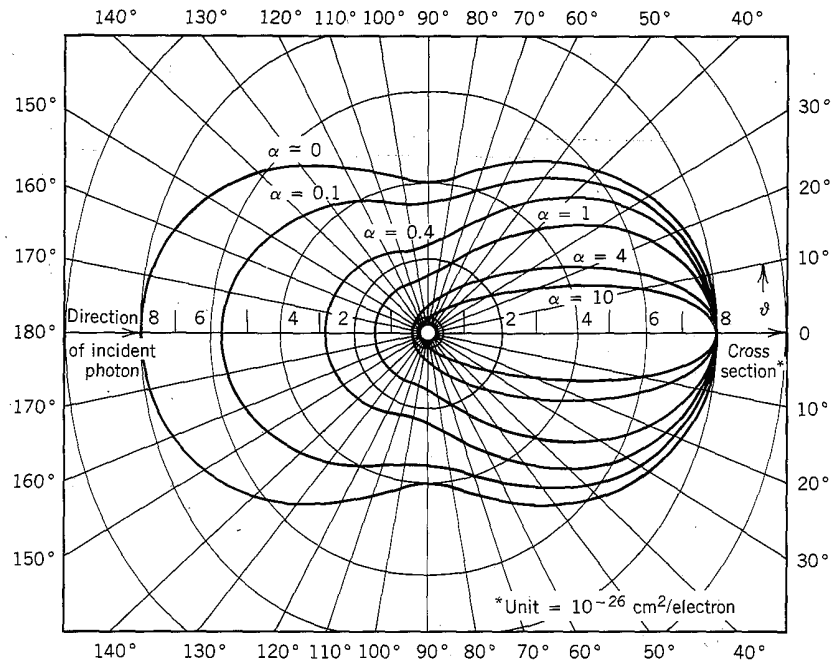


Figure 57 - Intensity of scattered radiation as a function of scattering angle for Compton scattering at various incident energies α ($E_{gamma}/511$), as predicted by Equation 6.3.⁹⁹

The distribution produced by the Klein-Nishina formula (as seen in Figure 57) reveals that for low energy gamma-rays ($\alpha \rightarrow 0$) the distribution is symmetric about the axis perpendicular to the 0° . However, as the energy of the gamma-ray increases, the intensity of scattered radiation becomes more forward focused and so called ‘back-scatter’, where a photon is scattered back to return along the path from which it entered, is significantly reduced. This means that for

gamma-ray energies even as low as 662 keV the probability of backscatter is strongly suppressed,^{xv} and the angle through which the photon will scatter will be forward focused.

By utilising this information it is possible to draw several conclusions concerning the energy deposited in a pair of detectors. In most situations, a path from the source through the two detectors would involve either a small angle scatter in one detector, or a large angle scatter in the other detector. By comparing the most probable energies deposited in the two detectors with the calculated energies from the Compton scatter formula, it is then possible to find the angle through which the photon must have scattered. The method used is outlined in Section 6.1.

6.1 Pixelated CZT Detectors as a Compton Camera

It is known that a pair of detectors can be used as a Compton Camera, whose precision in pinpointing a cone of vectors, along which a source must lie, is a function of the precision with which the interactions within the detectors can be located, and thus of the size of the detector. For this reason, a pair of pixelated detectors whose positional precision is better than in conventional systems (but whose efficiency is large compared to a single pixel sized detector) can be used to greatly improve the accuracy of this cone. As outlined in Section 6, by examining the energy deposited in one detector (for an event that also interacted in a second detector), it is possible to calculate the angle through which the photon must have scattered in the first detector. This can then be combined with the location of the two interactions (which provide a vector for the post-scatter path) to give a ‘cone’ of vectors for the pre-scatter path (See Figure 55).

An array of three detectors was installed on master boards as seen in Figure 58. For this work, measurements were taken with the detectors in the configuration shown in Figure 59. The detectors were mounted on the master boards onto 18 pin connectors which provided voltage input and readout to the cathode, a ground channel and 16-channel readout from the

^{xv} At $\alpha = 1$ or $E_{\text{gamma}} = 511 \text{ keV}$, the ratio of gamma-rays scattering through 50° to gamma-rays scattering through 0° is around 37%, while the ratio of gamma-rays scattering through 180° to those scattering through 0° is around 19%.

anode. Two such boards were mounted, one situated vertically above the other in an inverted configuration (such that the detector was mounted with the cathode face downwards).

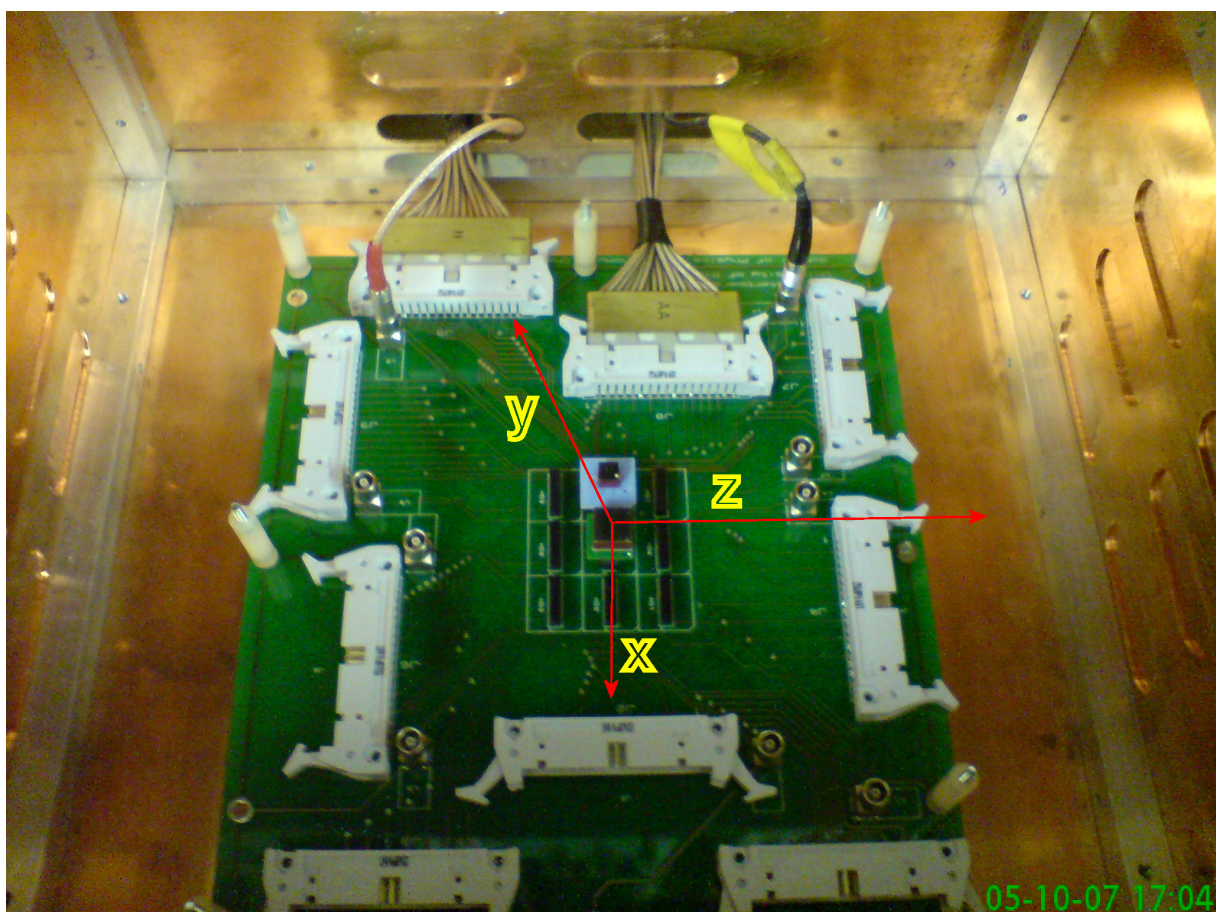


Figure 58 - Photo of lower master board showing a small detector in position 8 (top middle) and the larger detector in position 5 (central).

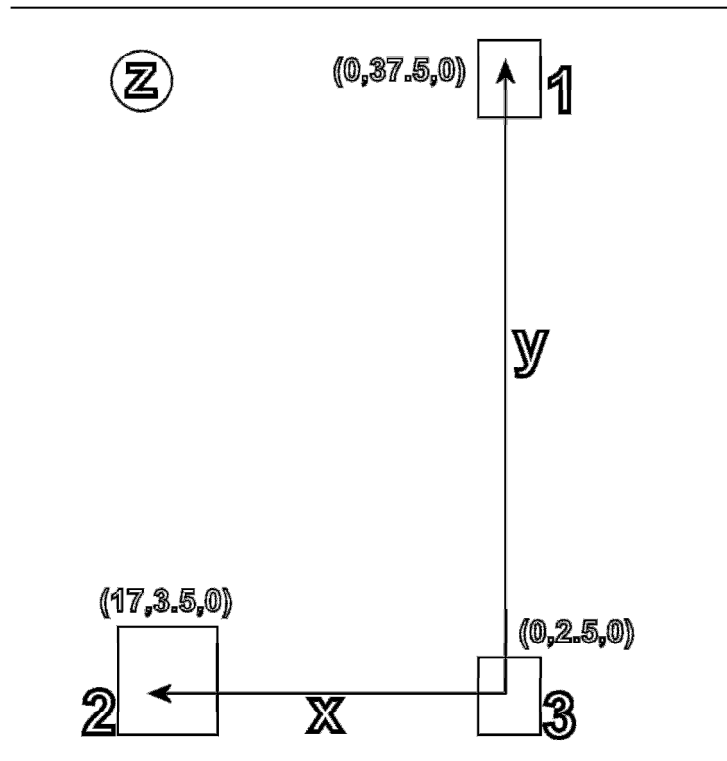


Figure 59 - Diagram showing relative location of detectors in the Compton Camera measurements. Detectors one and three are $4 \times 5 \times 4 \text{ mm}^3$ and detector two is $6.4 \times 7 \times 6.4 \text{ mm}^3$. The centre of detector three's base was chosen as the origin, meaning that the detectors are centred at $(0,37.5,0)$, $(17,3.5,0)$ and $(0,2.5,0)$ respectively. All units are given in mm. The z-axis is into the plane of the paper.

In order to examine the potential of a system composed of pixelated CZT detectors, the three detectors were installed, calibrated and corrected for the depth dependence (as described in Section 3). A measurement was then taken using the 662 keV gamma-rays from a ^{137}Cs source. A spectrum was created for events where two detectors were triggered with a single pixel active in each; the energy in the first detector was then plotted against the energy in the second. An example of such a plot is shown in Figure 60, for detectors two and three.

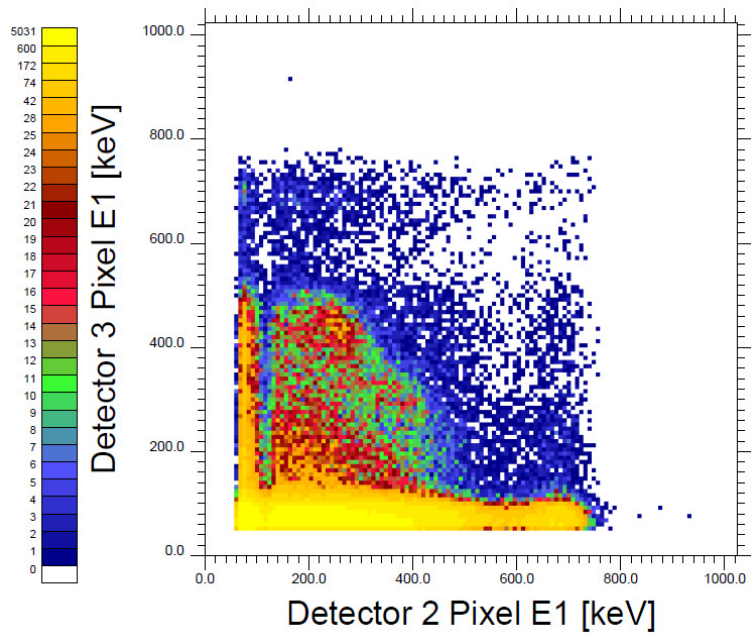


Figure 60 – Signal sharing between detectors two and three where both detectors only see one pixel active from a ^{137}Cs 662 keV gamma-ray source.

In this analysis, detector three was a $4 \times 4 \times 5 \text{ mm}^3$ detector lying $27.8 \pm 0.6 \text{ mm}$ from the source, while detector two was a $6.4 \times 6.4 \times 7 \text{ mm}^3$ detector lying $22 \pm 0.6 \text{ mm}$ diagonally from the source.^{xvi} All the detectors were divided into 16 pixels. Figure 60 reveals several features of interest: A diagonal line, running from 662 keV on each axis, indicates events that are fully collected and shared between the two detectors. At 662 keV on both axes lie events where a gamma ray was collected within one detector along with electrical noise or a second gamma-ray in the other detector. At around 500 keV on the two axes, the Compton edges of the two photopeaks can be seen showing events where a gamma-ray entered a detector and scattered out. A window of width $\pm 85 \text{ keV}$ was placed around the diagonal line where the two gamma-ray energies sum to 662 keV and is plotted in Figure 61. Note that no cut has been made to remove the low energy noise.

^{xvi} That is to say the Detectors were located as in Figure 59 with the source lying 22 mm out of the plane.

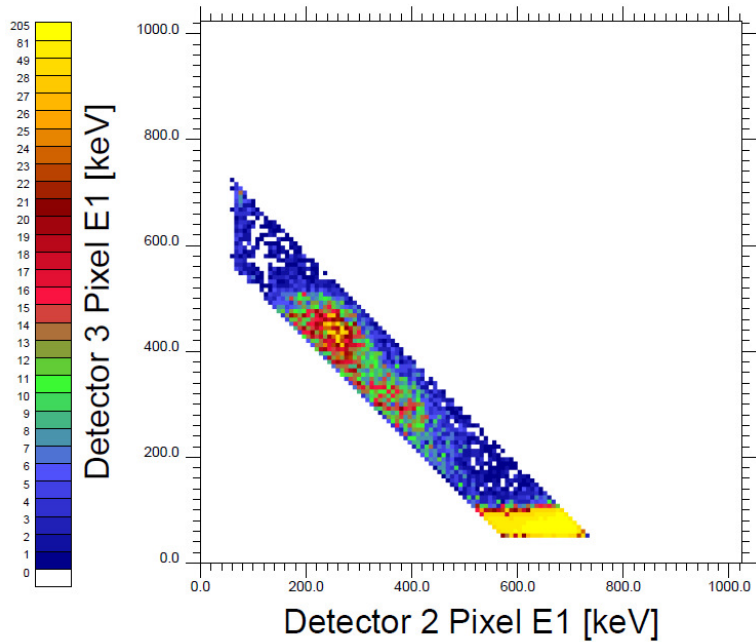


Figure 61 - Signal sharing between detectors two and three where both detectors only have one pixel active from a ^{137}Cs 662 keV gamma-ray. A 170 keV gate has been taken around the full gamma energy of 662 keV.

This process can also be performed with pixels within a single detector, but with a great reduction in angular precision. However, the efficiency is greatly increased as the surrounding detector provides a 4π coverage.

An example analysis for coincident events within a single pixelated detector is shown in Figure 62 and Figure 63. The energy deposited in one pixel is plotted against that deposited in a second pixel (this analysis only uses events where two pixels were active). The features present in Figure 60 are also found in this spectrum. The diagonal line indicating events where a 662 keV gamma ray was shared between the two pixels is clear and a sum energy window of 662 ± 85 keV has been placed around the data, as shown in Figure 63.

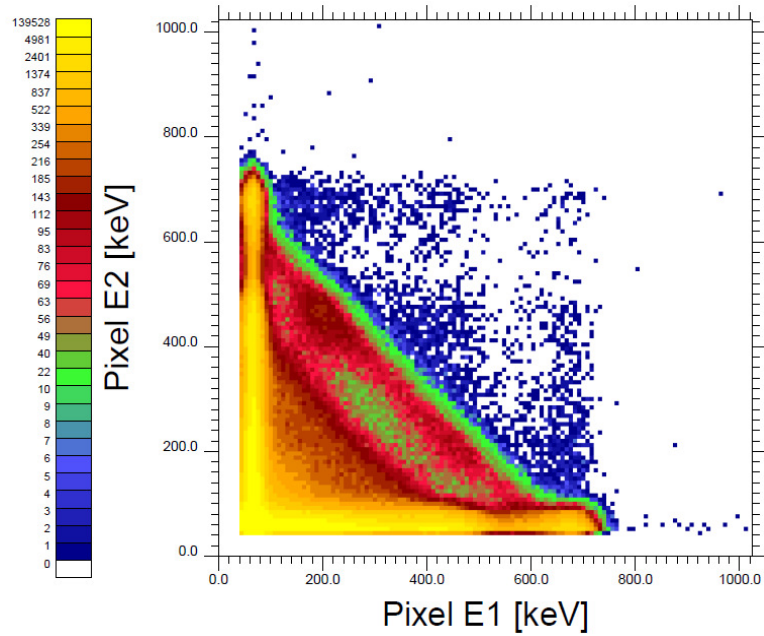


Figure 62 - Signal sharing between two pixels in detector one with a ^{137}Cs 662 keV source.

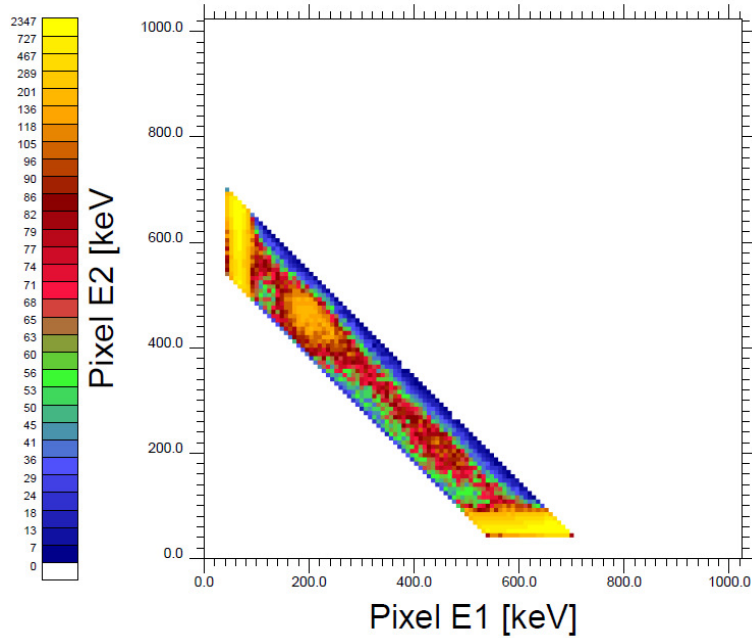


Figure 63 - Signal sharing between two pixels in detector one with a 170 keV gate around the 662 keV gamma line from a ^{137}Cs gamma source.

The following discussion focuses primarily on events in which the gamma-ray energy was shared between two detectors. A projection of the spectrum in Figure 60 was taken onto the x and y-axes to give the energy deposition in an individual detector for two co-incident events.

These energy spectra are then composed of events from four main sources:

- 1) energy deposition in the detector due to Compton scatter within the detector;
- 2) energy deposition in the detector having Compton scattered in the other detector;
- 3) random coincidences of separate gamma-rays – this should lead to a roughly even distribution of energy in the detectors;
- 4) energy deposition in one detector while the second detector is triggered due to electronic noise.

Due to the nature of the projection, a peak in one projection should have a corresponding peak in the other, such that their energies sum to 662 keV. As argued in Section 6, the most intense peak pair should be the one that corresponds to the most likely energy deposition. This pairing should always favour low angle scatters (once $\alpha \geq 1$). Using the Compton formula to calculate the angle which must be scattered through to produce the energies in the two detectors, it is possible to deduce in which order the matched pair of energy peaks were deposited, this will be termed the preferred route. The peaks for the alternative route do not always lie underneath the peaks for the preferred route and thus can be used (if sufficiently high statistics are available) to provide a second measure of the source location. The simplest application of this logic is that the detector with the lowest energy high intensity peak is the detector in which the gamma-ray is most likely to have first interacted. Thus, this detector is typically nearer the source.

The Klein-Nishina formula shows that the probability of near 180° scatters is small; similarly a 170° scatter is significantly less likely than a 10° scatter. Thus, if the source lies such that a gamma-ray could have scattered through 10° in detector one, or through 170° in detector two, the ratio of the intensity of the two pairs of peaks will be quite large. However, if the two paths both involve a near 90 degree scatter, the ratio will be close to unity. For an event where the source lies between the two detectors but out of the plane, and thus the angle of scatter for both routes is roughly equivalent, the relative intensities will be very similar.

These arguments can all be used to provide a simple analysis of the projections. In the example shown in Figure 64, the black histogram shows the original data and the red line

shows a fit to the data. This fit is made of a background component (blue) and a two peak Gaussian fit (green).

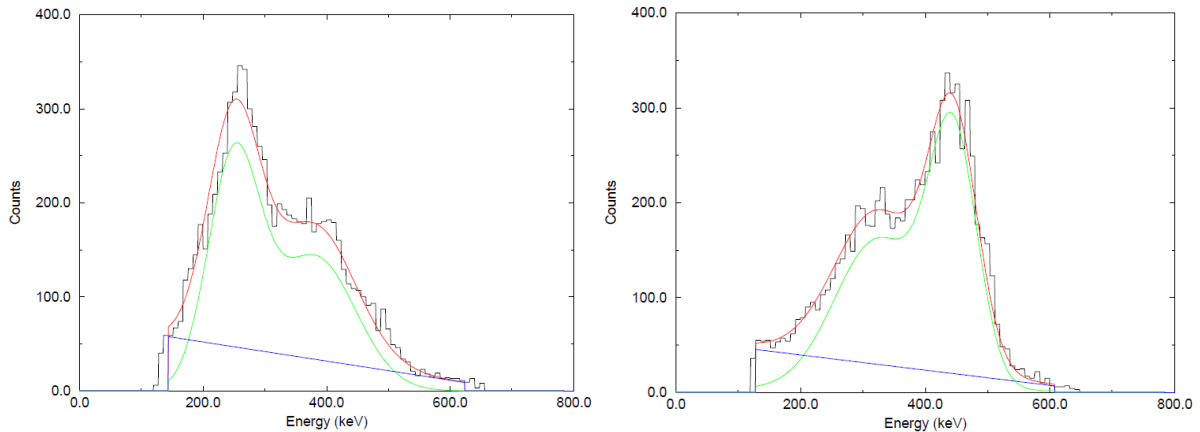


Figure 64 - Energy collected in detector two (left) and three (right) from events extending into the window shown in Figure 61 - showing the original data in black, the fitted function in green, the background in blue and the function and background in red. The peaks in detector two lie at 251.6 ± 2.2 keV and 379.9 ± 5.4 keV while the peaks in detector three lie at 326.2 ± 7.2 keV and 446.2 ± 2.1 keV.

Figure 64 shows the projections (after the low level noise has been removed) of Figure 61. The more intense pair of peaks is seen at around 252 keV in detector two and 446 keV in detector three. By following the arguments described above, it can be argued that detector two lies closer to the source; as a low angle scatter within detector two is favoured. Likewise, the high angle scatter required to deposit 446 keV in detector three is unlikely and so it is more likely that the deposition of 446 keV is due to the gamma-ray interacting photo-electrically in detector three, after Compton scattering within detector two.

By extending this system to three detectors, the source can be located unambiguously where the three cones intersect, as seen in Figure 56. This method was used to locate the source in a series of measurements with different energy sources in different places, specifically five measurements using ^{137}Cs and four measurements using ^{60}Co sources. The source locations are given in Appendix A

Since for any source location there will be two paths to interact in the two detectors, each projection should have two peaks present which can be fitted with Gaussian line-shapes. A location for the source was calculated from the method outlined above and this was then used,

along with the relative locations of the sources and the Compton scatter equation, to calculate the energies for the six peaks (two for each detector). By comparing the measured peak energies with those calculated, the source location was adjusted until the difference was minimised.^{xvii} With the detector locations used (see Figure 59) the source could be located in all dimensions. However, if the source lay out of the plane, only the distance from the detectors could be found, rather than the side of the plane defined by the three detectors. A MathCAD worksheet which employed equations 6.1 and 6.2 was also used to confirm this analysis, and is described in Appendix B.

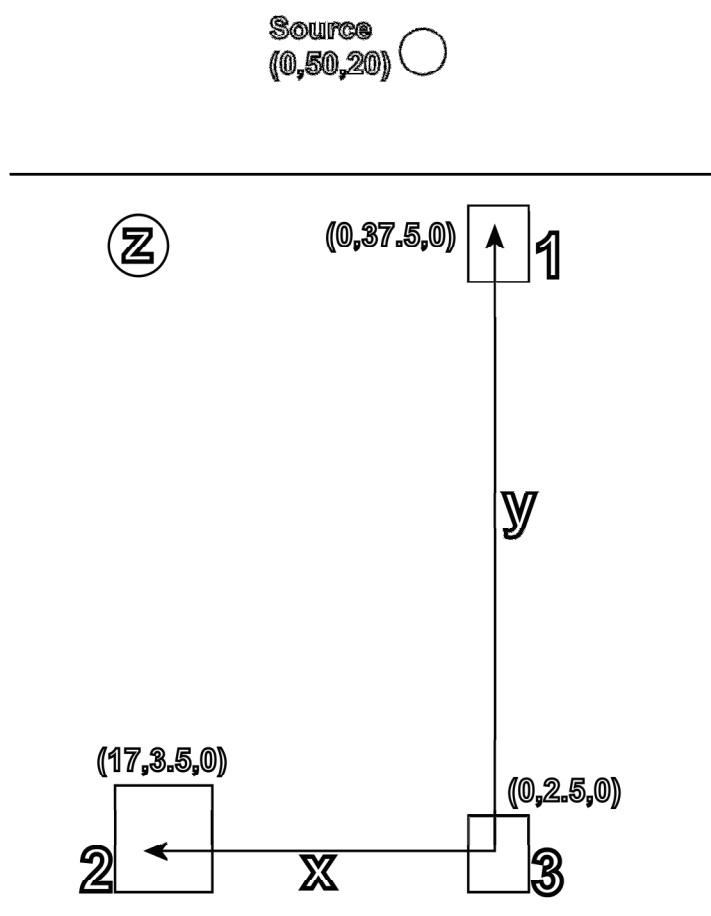


Figure 65 - Diagram showing layout of the detectors and source. The detectors are centred at $(x,y,z) = (0,37.5,0)$, $(17,3.5,0)$ and $(0,2.5,0)$. The source was located at $(5,50,20)$. All units are given in mm. The z-axis is into the paper.

^{xvii} This method produced a single value representative of how close the fitted peaks were to the real ones. The formalism for its calculation is described as the ‘Sum of the residuals’.

An example of a comparison of the simulation and the real data is presented in Figure 66. For this particular measurement, the source was placed on top of the upper board, slightly out of the plane of the detectors. The configuration is shown in Figure 65. However, an examination of the spectrum, suggests that the source lay roughly equidistant from all three detectors. This could only be attained by the source lying significantly out of the plane. Since it was known that the source was placed on the upper board, this led to the conclusion that the source lay nearer detector one (i.e. at a higher vertical elevation), between detectors two and three in the horizontal plane and out of the plane by some undetermined distance.

Using this method the source location could be predicted. This was then used as the starting point in the fitting routine which minimized the average, and summed, differences by moving the source location. The result is shown below in Table 10. Note that the actual location of the sources were not accurately noted during measurement, thus the values given for the expected source location are an estimate with an expected uncertainty of ± 5 mm.

	Position along horizontal axis of detector plane (mm)	Position along vertical axis of detector plane (mm)	Position out of detector plane (mm)
Measured location of detector 1	0 ± 0.5	37.5 ± 0.5	0 ± 0.5
Measured location of detector 2	17 ± 0.5	3.5 ± 0.5	0 ± 0.5
Measured location of detector 3	0	2.5	0
Actual source location	0 ± 5	50 ± 5	-20 ± 5
Fitted location of source	$-3.5^{+1.6}_{-0}$	$53.1^{+0.6}_{-0}$	$-17.5^{+0.2}_{-0}$

Table 10 - Table showing the detector locations along with the expected and fitted location of the source. Detector three's location is defined as the origin for all other points. The fit is a good match for the actual source location.

This fit is in agreement with the actual source location to within the given errors. The errors were calculated by performing the fitting routine with peak values adjusted to include the observed error in the centroid (recalculating the fit using the peak values of 'centroid \pm

error'). The fit is invariant in some cases, which suggests that small changes in centroid value do not move the source location. For instance, in the example given in Table 10, the fitted location in the x-axis was found to be at a minimum of -3.5 mm in the horizontal plane; the recalculated fit where the centroids were modified to account for the error led to a maximum deviation of +1.6mm. Adjusting the centroid in the other direction also moved the fitted position in the positive direction.

In order to corroborate the above analysis, a simulation using C++ was written. In this simulation a source location was selected, along with a grid of points in the two detectors, to calculate the two vectors along which the photon could travel. The angle between them was then determined to be the angle of the Compton scatter; from this angle the energy deposited in the first detector (i.e. during the scatter) was determined. The remaining energy of the photon was then deposited in the second detector. This particular simulation did not include the Klein-Nishina distribution, thus all scattering paths between the two detectors were equally probable. Accordingly, peaks that are strongly suppressed and thus invisible in real data can be seen clearly in the simulation. The source code for this program is given in Appendix D. The results have been plotted against the measured data, shown in Figure 66.

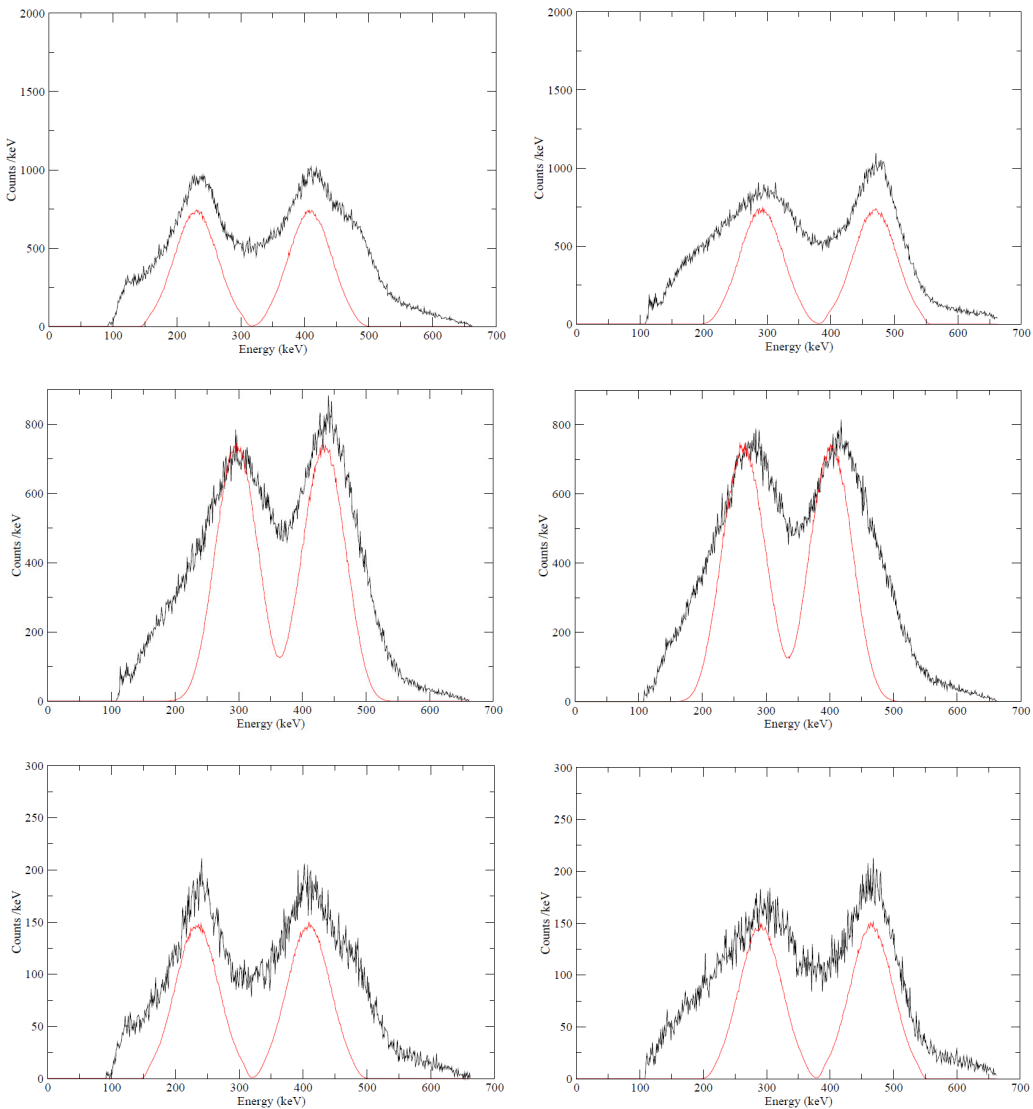


Figure 66 - Energy collected in detector one (left) and detector two (right) from events shared between detectors one and two (top), in detector two (left) and detector three (right) from events shared between detectors two and three (middle) and in detector one (left) and detector three (right) from events shared between detectors one and three (bottom). Events shown are those extending into the 170 keV window around the 1332 keV gamma line from a Co-60 gamma source. Black shows the real data, red shows the simulated fit folded with a 40 keV energy resolution. Note that the lack of the Klein-Nishina formula in the simulation means that the intensities of the simulated peaks are identical.

The result of this analysis for the five ^{137}Cs measurements and 4 ^{60}Co measurements are given in Table 11. The fitted source locations are given along with two tests of quality of the fit: The ‘Sum of the residuals’ is the sum of the difference between the fitted peak energies and the peak energies calculated from the Compton equation.

$$\text{'Sum of the residuals'} = \sum_{i=1}^4 |E_{\text{calc}}_i - E_{\text{measured}}_i|$$

E_{calc}_i is the calculated energy deposited in the detector, determined with the Compton scatter equation from the fitted location. Since there are four available peaks (two per detector) there are four values. E_{measured}_i is the measured energy deposited in the detector; again, since there are four peaks, there are four values.

The ‘Fit vs. the Prediction’ is the square root of the sum of the differences between the fitted source locations and the actual source locations squared

$$\text{'Fit vs. Prediction'} = [(x_{\text{fit}} - x_{\text{pred}})^2 + (y_{\text{fit}} - y_{\text{pred}})^2 + (z_{\text{fit}} - z_{\text{pred}})^2]^{1/2}$$

x_{fit} – The fitted position of the source in the x dimension.

x_{pred} – The actual position of the source in the x dimension.

As in Table 10, the errors in Table 11 indicate that some points are largely insensitive to the uncertainties in the ‘Compton Peak’ Centroids.

<i>Measurement</i>	Source (Energy)	X (Horizontal in plane of detectors) (mm)	Y (Vertical in plane of detectors) (mm)	Z (Horizontal out of plane of detectors) (mm)	Sum of the residuals (keV)	Fit vs. Prediction (mm)
Det.1		0 ± 0.5	37.5 ± 0.5	0 ± 0.5		
Det.2		17 ± 0.5	3.5 ± 0.5	0 ± 0.5		
Det.3		0	2.5	0		
3	^{137}Cs (662 keV)	$4.0_{-7.3}^{+0.0}$	$12.9_{-0.2}^{+1.9}$	$78_{-0}^{+5.9}$	$7.3_{-3.5}^{+7.8}$	$30.8_{-0}^{+5.8}$
4	^{137}Cs (662 keV)	$-5.5_{-0.6}^{+0.4}$	$53.1_{-0}^{+0.2}$	$15.7_{-0.2}^{+0.4}$	$72.5_{-1.7}^{+7.8}$	$16.6_{-0.3}^{+0.5}$
5	^{137}Cs (662 keV)	$-3.5_{-0}^{+1.6}$	$53.1_{-0}^{+0.6}$	$-17.5_{-0}^{+0.2}$	$44.3_{-6.6}^{+8.5}$	$4.2_{-0}^{+1.1}$
6	^{137}Cs (662 keV)	$27.1_{-0}^{+5.4}$	$12.1_{-0}^{+6.7}$	$-1_{-0.7}^{+0}$	$21.5_{-2.7}^{+8}$	12.3_{-0}^{+8}
7	^{137}Cs (662 keV)	17.3_{-0}^{+0}	48.3_{-0}^{+0}	0.1_{-0}^{+0}	$66.3_{-1.4}^{+1.4}$	7.5_{-0}^{+0}
8	^{60}Co (1332 keV + 1173 keV)	$5.2_{-0.8}^{+1}$	$-24.5_{-0.9}^{+0}$	$195.5_{-0.5}^{+4.5}$	$11.9_{-1.2}^{+1.3}$	$15.2_{-0}^{+0.6}$
9&10	^{60}Co (1332 keV + 1173 keV)	$-3.5_{-0}^{+0.3}$	52.5_{-0}^{+0}	5.8_{-0}^{+0}	$171.7_{-1.1}^{+2.5}$	$9_{-0}^{+0.3}$
11	^{60}Co (1332 keV + 1173 keV)	$13.9_{-1.9}^{+0}$	0_{-0}^{+0}	$62.6_{-0.1}^{+0}$	$95.7_{-0}^{+1.5}$	$15.4_{-1.1}^{+0}$
12	^{60}Co (1332 keV + 1173 keV)	$-2.9_{-1.1}^{+0}$	$54.2_{-0}^{+0.4}$	$21.3_{-0.1}^{+0.7}$	$17.7_{-0.6}^{+2.6}$	$9_{-0}^{+1.1}$

Table 11 - Table showing the calculated source locations for a series of measurements. Locations were fitted by using a predicted location (noted in Appendix A) and finding the local minimum of the average of the differences given as the ‘Sum of the residuals’. The ‘Sum of the residuals’ measure is given by the average of the differences between the real peak energies and the peak energies, as predicted by the Compton scatter equation, when the source is in the fitted location. As a result, this is a measure of the accuracy of the fitted location. Finally, the fit vs. the prediction is the sum of the difference between the fitted location and the initially estimated location. As such it is an estimate of how close the fitted location lay in relation to the estimated location of the source. The detectors are located by their positions in the boards. Detector three was designated as the origin and the other source locations were measured from that point.

The two tests allow a comparison between the predicted location of the source and the actual location (given by the ‘Fit vs. Prediction’ test) and a comparison of the calculated and measured peak energies (given by the ‘Sum of the residuals’ test). The values given by these tests represent real world values as shown in the examples below.

The ‘Fit vs. Prediction’ test gives a measure of the accuracy of the three measured values to the predictions. The largest error shown by any of the measurements ($30.8+5.8$) squared is equal to the sum of the three squared differences between measurement and prediction. Thus the difference in any individual value (if all three dimensional values are equally accurate) is given as:

$$\sqrt{\frac{(30.843 + 5.778)^2}{3}} = 21.1\text{mm}$$

The ‘Sum of the residuals’ test similarly gives the difference between the measured peak centroids and those produced by the fit. Since six peaks are used, this value is the sum of these six differences, suggesting that for a value of 100 keV, the fitted peaks are within 17 keV of the measured peak centroids.

Only one measurement has a value of the ‘Sum of the residuals’ which is greater than 100; measurements 9&10, which used the ^{60}Co source and proved more difficult to fit. The initial fitting located the source substantially out-of-the-plane and away from the known location. The difficulty arose from the apparent presence of three peaks in the spectra rather than two. However, more detailed analysis revealed that this arose from the spreading of the peak when the source is located near to the detector. In this scenario, the finite size of both detectors and sources must be taken into account, and, when this is done, the peaks spread substantially, even with quite small source sizes. It is this feature that leads to large values of the ‘Sum of the residuals’, as the large full-width half maximum of the peak makes calculation of the centroid extremely difficult.

In order to confirm the understanding of the Compton scatter process within this particular detector arrangement, a Geant4 simulation was developed using Geant4.9.2. This simulation included two detectors with dimensions of $6.4\text{ mm} \times 6.4\text{ mm} \times 6.4\text{ mm}$. The simulated source was configured to produce photons travelling within a specified volume, but randomly

distributed. Simulations consisting of a million events were performed. However, due to the inclusion of detailed cross-sections of interactions and angular distributions the calculations were significantly slower and less efficient than the C++ calculation described earlier. For 10^6 gamma-rays there were only $\sim 10^3$ events where the complete energy of a 662 keV gamma was collected. Events where the complete energy had been deposited in the two detectors were then analysed. The energy deposited in each detector segment was summed and the energy histogrammed. The code used in these simulations is given in Appendix E.

The detectors were pixelated within the simulation, which allowed simulation of not only events where photons were completely collected in a single detector, but also where they underwent Compton scatter within the detector. In addition, the nature of the simulation allowed an additional level of precision in the analysis, by providing the actual interaction position.

A simulation of the configuration of the source and detectors in the positions outlined in Table 12 and Figure 67 was then performed, similar to the detector arrangement shown in Table 11. This example simulation was chosen to give the greatest distinction in energy deposited within each detector, and does not conform to any of the real measurements.

	X (cm)	Y (cm)	Z (cm)
Source	0	0	-32.64
Detector 1	-4.22	23	-28.58
Detector 2	12.78	-18	-28.58

Table 12 - Table showing the location of the source and detectors in the Geant4 simulation

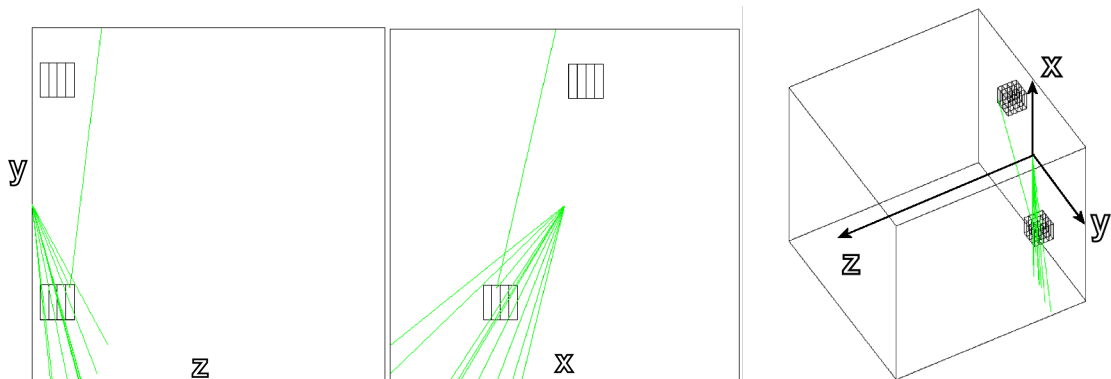


Figure 67 - Diagram showing the relative location of the detectors to the source and each other for the Geant4 simulation. The detectors and source are located as outlined in Table 12.

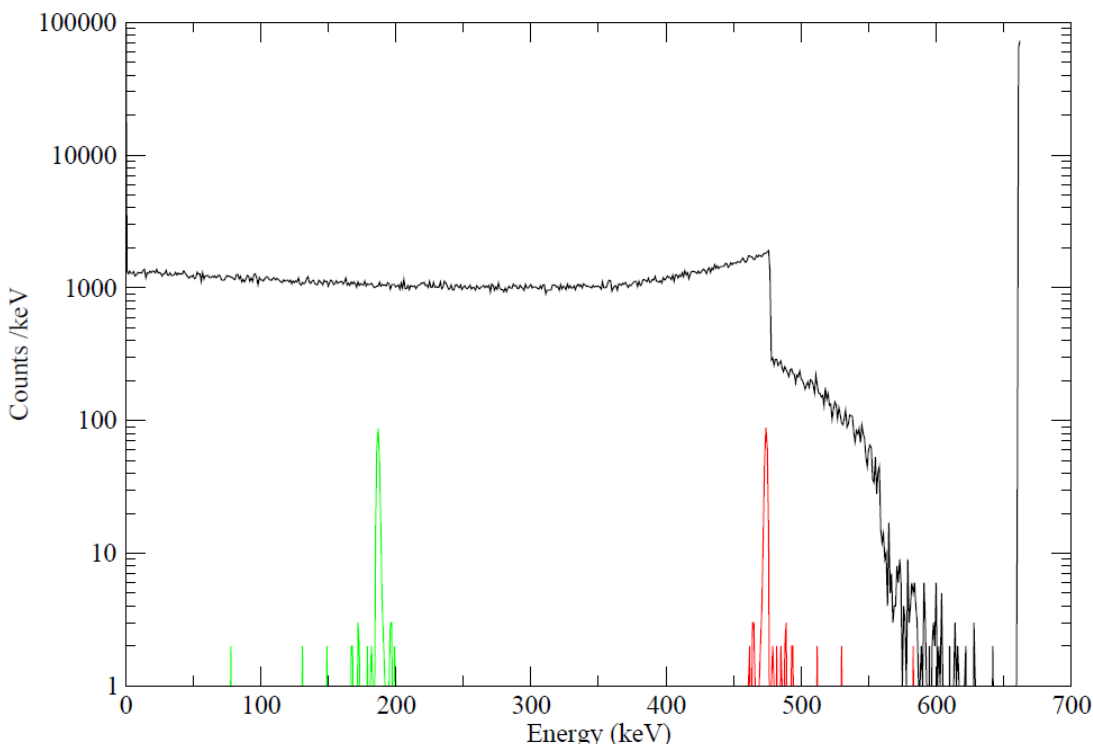


Figure 68 - Geant4 simulation of events where a 662 keV gamma-ray interacts in a single detector (black) and where the gamma-ray scatters in the first detector (red) and then interacts in the second detector (green) depositing its full energy in the two detectors. The single detector spectrum shows the photopeak and Compton edge clearly, while the double detector spectrum shows the symmetrical nature of such plots. The detectors and source locations are given in Table 12 and Figure 67.

The output from this simulation is plotted in Figure 68, showing events where the gamma ray (662 keV) deposited energy within a single detector (black line) or was fully collected with the energy shared between two detectors (red and green lines). The single detector spectrum,

shown in black, shows the photopeak at 662 keV and the Compton edge at 470 keV. The red line shows energy deposited in the second detector while the green line shows energy deposited in the first. From this it can be seen that a large angle scatter is required in detector two for the photon to then enter detector one (shown in Figure 67). This is clear from the large energy deposition in detector two and the small probability relative to single detector interactions.

This spectrum was then modified by folding the spectrum with the detector energy resolution. This is required as Geant4 models the physical interactions and records the energy deposition and location; it does not model the detector's energy response. The energy resolution folded spectrum is shown in Figure 69. Once again, the black line shows events that deposited in the first detector, the red line shows events which interact and deposit fully on the two detectors and shows the deposition in the first detector and the green line shows the deposition in the second detector.

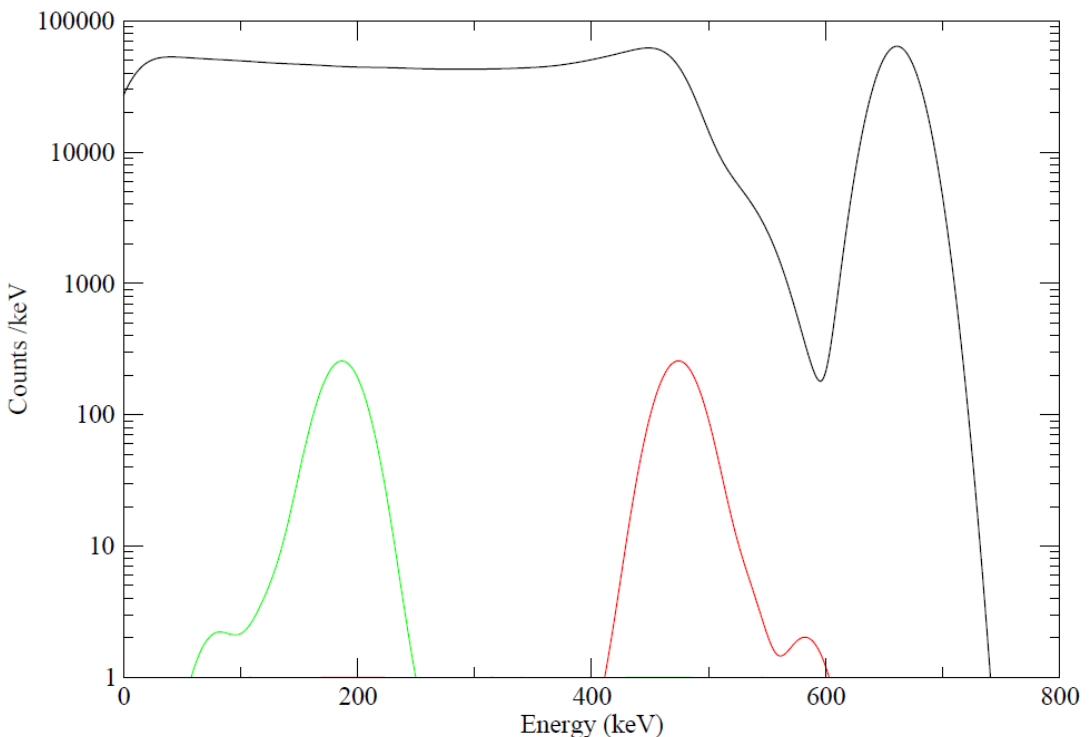


Figure 69 – Geant4 simulation of a 662 keV gamma-ray showing events where the gamma-ray interacts only in a single detector (black) showing the photopeak and Compton edge, and events where the gamma-ray scatters in the first detector (red) and then interacts in the second detector (green) depositing its full energy in the two detectors. An energy resolution of 40 keV has been convoluted with the simulations. The detector and source locations are given in Table 12 and Figure 67.

A simulation of ‘measurement 3’, as described in Table 11, is shown in Figure 70, the simulation is compared to the measurement itself as calculated with a 170 keV gate. It is apparent that the size of the gate reduces the energy resolution of the peaks substantially, however, the fit is accurate in peak energy and indicates the relative intensities of the two peaks for each detector.

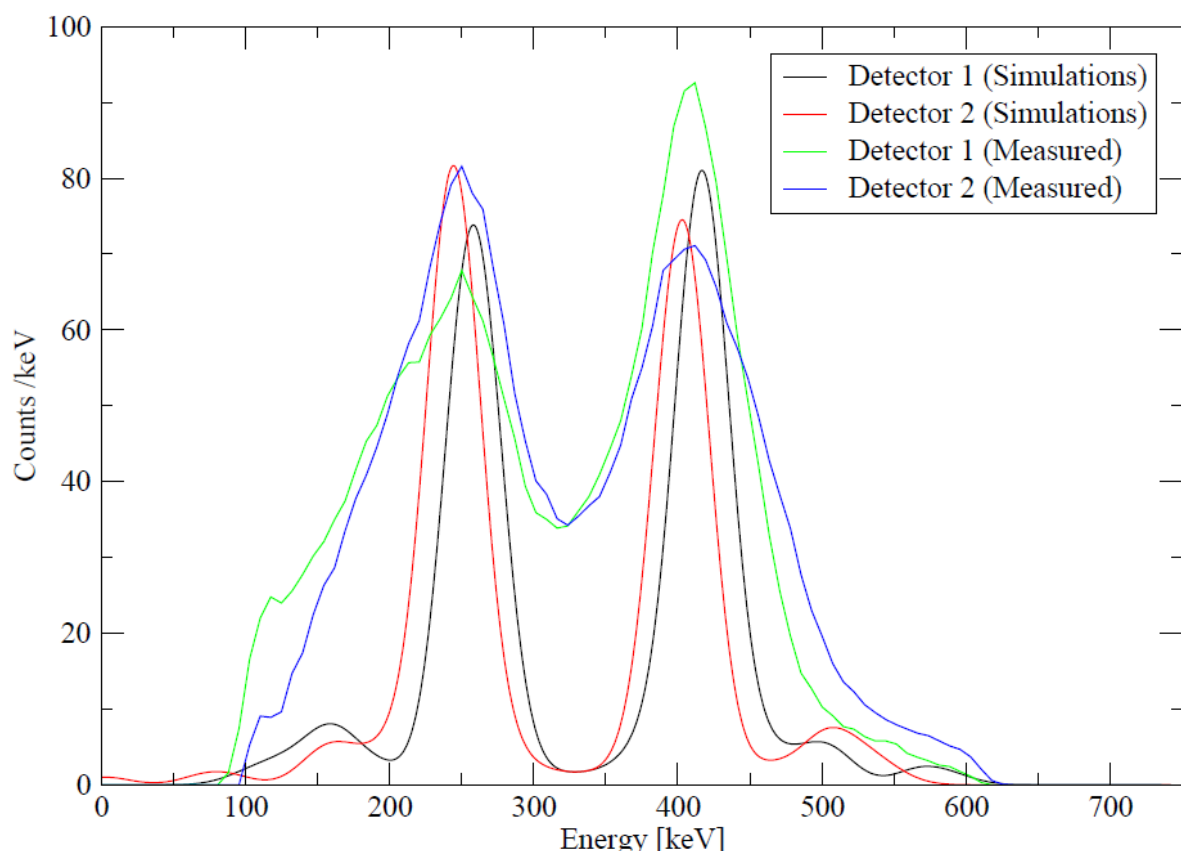


Figure 70 - Simulations of measurement 3, from Table 11, compared to the measurement with a gate of 170 keV. The peaks are seen to lie at the same energies in both simulation and measurement although significant reduction in energy resolution is seen in the measurements.

6.2 Pixelation and Improvement to Scattering Angle Calculations

The analysis presented in Section 6.1 shows that the precision of the source fit is directly dictated by the precision of the determination of the Compton scattering peak centroids. Since this calculation requires the interaction positions to be known, then the precision of these positions will also strongly govern the quality of the fit. In the above calculations (Table 11), the centre of the detector was used as the point of interaction, but it is possible, if the calculation of the angle is performed for each individual event, to use the actual interaction position as calculated via pulse shape analysis, as demonstrated by the AGATA collaboration,¹⁰⁰ and by using the cathode signal to calculate a depth of interaction. Accordingly, a series of simulations were run to examine how the angular resolution increases under such circumstances. The detectors modelled in this step were $6.4 \times 6.4 \times 7 \text{ mm}^3$ and were subdivided into sixteen $1.6 \times 1.6 \times 7 \text{ mm}^3$ pixels.

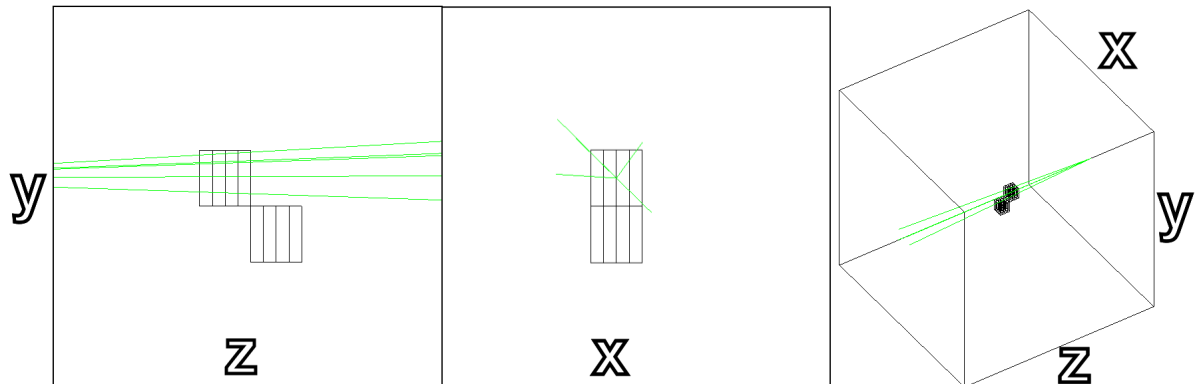


Figure 71 - Diagram showing location of two detectors relative to one another. Photons enter from the left, aimed to hit the upper detector. The second detector is situated at the lower edge of the first detector (situated 6.4 mm downstream (z) and 7 mm vertically displaced (y)).

The first simulation, shown in Figure 71, was performed with a 662 keV gamma-ray source situated at the location $(x,y,z)=(0,0,-64.6)$ with detector one at $(0,0,-10)$. The source was configured to aim photons throughout the entire solid angle of the detector. Detector two was then placed at $(0, -7, -3.6)$ - one detector thickness further along the beam axis and offset vertically (in the direction of the height of the pixels) by 7mm (as shown in Figure 71).

For events where the entire 662 keV was deposited in the two detectors, the angle between the vector from the source to the first interaction point and the vector from the first interaction point to the second was calculated. In addition the angle was calculated assuming that the interactions happened in the centre of the pixels in which they interacted. Finally the angle, assuming that the interaction happened in the centre of the detectors, was also calculated. These are plotted against the energy deposited in detector one in Figure 72.

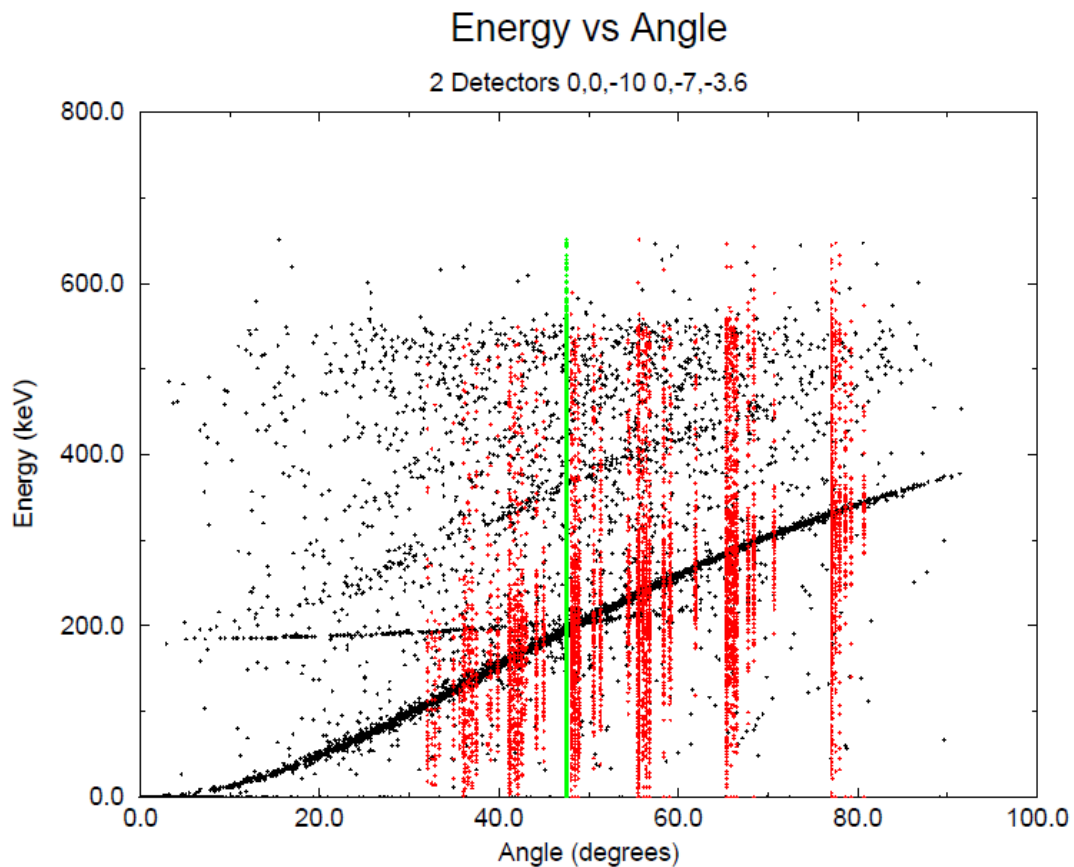


Figure 72 - Plot showing the actual angles between interaction points in black, the angles measured by using the centre of pixels as interactions points in red and the angle measured when using the centre of the detectors as the interaction points in green. This plot matches the setup shown in Figure 71. The angles shown are the angle of scatter within detector 1.

The angle calculated using the centre of the detectors corresponds to the green line in Figure 72; the angle is always seen to be 45.76° . Similarly, the angle calculated using the centre of the pixels is seen in red, this shows a relatively well defined description of the angle/energy dependence as seen with the actual angles, but there is a significant degradation in the

description of the angular dependence of the simulated data. Much of this is due to the angle being calculated in the same plane as the pixel depth, which gives a substantial variation in the angle.

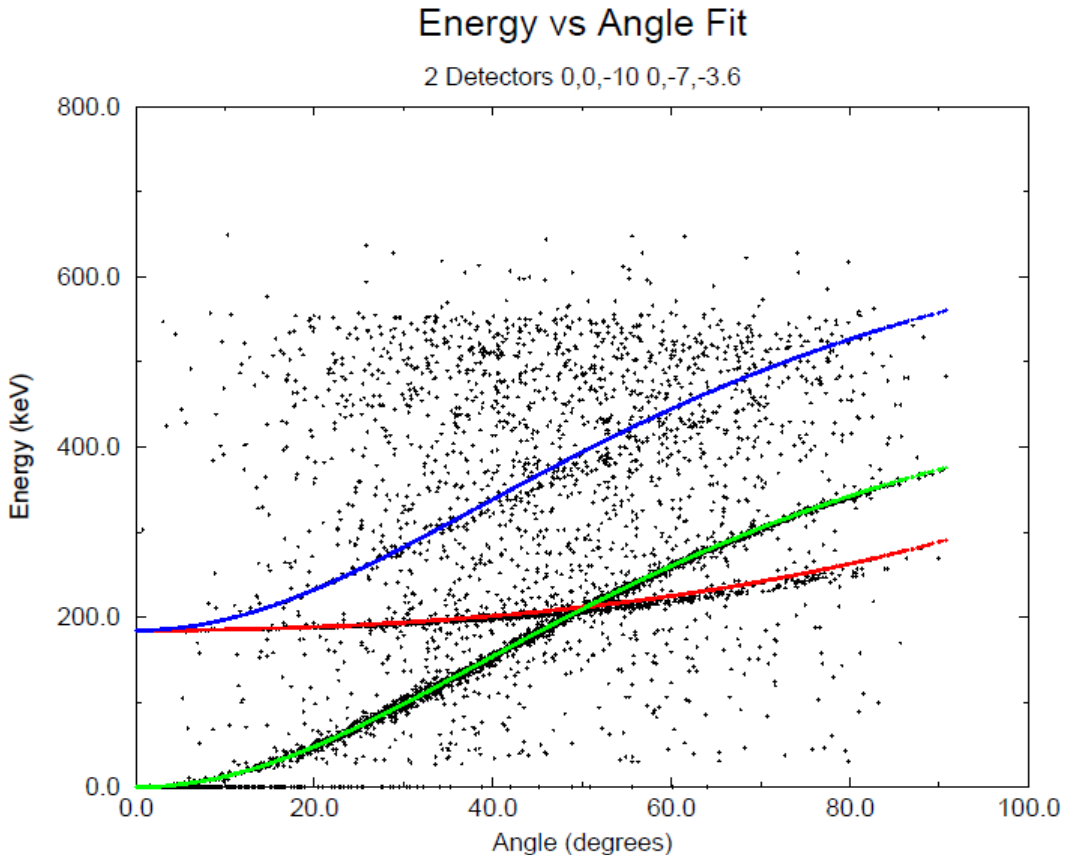


Figure 73 - Plot showing the curves for three types of interactions overlaid on the plot for the simulated interactions. The green curve shows events where the photon has scattered through some angle in detector one and deposited the remnant in detector two. The red curve indicates events where a photon has passed through detector one and undergone a $(180 - \text{angle})^\circ$ scatter in detector two to return to the first. Finally the blue line shows events where the photon scattered in detector one to enter detector two before undergoing a near 180° scatter to return to detector one. This plot matches the setup described in Figure 71. The angles shown are the angle of scatter within detector 1.

Interestingly, the actual angles appear to follow three loci, which are shown in Figure 73. The green line shows events where the photon has scattered in detector one, depositing energy proportional to the angle of scatter, and then deposited the remnant in detector two. The red line indicates events where a photon has passed through detector one and undergone a near 180° scatter in detector two, before depositing the remnant in detector one. Finally the blue

line shows events where the photon scattered in detector one, underwent a near 180° scatter in detector two and then deposited the remnant in detector one. These paths are shown in Figure 74.

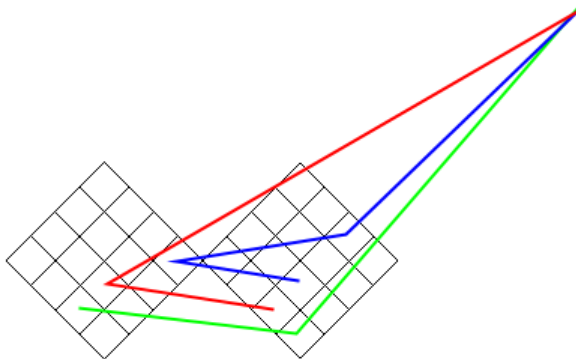


Figure 74 - Diagram showing the paths of photons described by the three loci seen in Figure 73.

The blue line does not match the actual values – the indication is that slightly more energy is lost in the second detector than can be accounted for by simply considering a 180° scatter. This is a result of the way that the angle is calculated. The angle is calculated as the angle between the two vectors defined by:

- the path from the source to the final interaction within detector one;
- the path from the final interaction within detector one to the final interaction in detector two.

In most cases this is not a problem. In the first case – of an interaction in detector one scattering to deposit the residue in detector two - the only source of uncertainty is if the photon interacts twice within detector one or undergoes a second scatter in detector two. In the second case, the angle calculated approximates to $180 - \theta$ (the source is located sufficiently far away as to produce the angle at that vertex of the triangle close to 0) where θ is the angle scattered through in detector two.

However, when a photon scatters within detector one, then again in detector two before returning to detector one, the angle calculated is the angle between the two vectors:

- from the source to the final deposition position within detector one;
- from the final deposition point in the first detector to the interaction position in detector two.

Thus, the angle calculated is not really the angle scattered, but rather, if θ_1 is the angle scattered through in the interaction in detector one and θ_2 is the angle scattered through in the interaction in detector two, then the angle measured $\theta_c = \theta_1 + (180 - \theta_2)$ (once again assuming that the source is located sufficiently distant for the angle of emission not to have changed). If the source were located closer (such that x defined the angular error introduced) then the three equations would expand to:

- In the case where the photon scatters in detector one before depositing in detector two.
 - $\theta_c = \theta_1$
- In the case where the photon scatters in detector two before depositing in detector one.
 - $\theta_c = x + (180 - \theta_2)$
- In the case where the photon scatters in detector one, scatters again in detector two and depositing within detector one.
 - $\theta_c = x + \theta_1 + (180 - \theta_2)$

These effects account for those events which apparently occur at random energies and angles; although these events may also be due to multiple interactions within a single detector affecting the energy deposition within that pixel.

A second simulation was performed, again with the 662 keV source situated at (0, 0, -64.6) and detector one situated at (0, 0, -10), however, the second detector was now located at (-6.4, 0, -3.6); which is one detector thickness along the beam axis and offset horizontally (in the pixelated plane) by one detector thickness. This layout is shown in Figure 75.

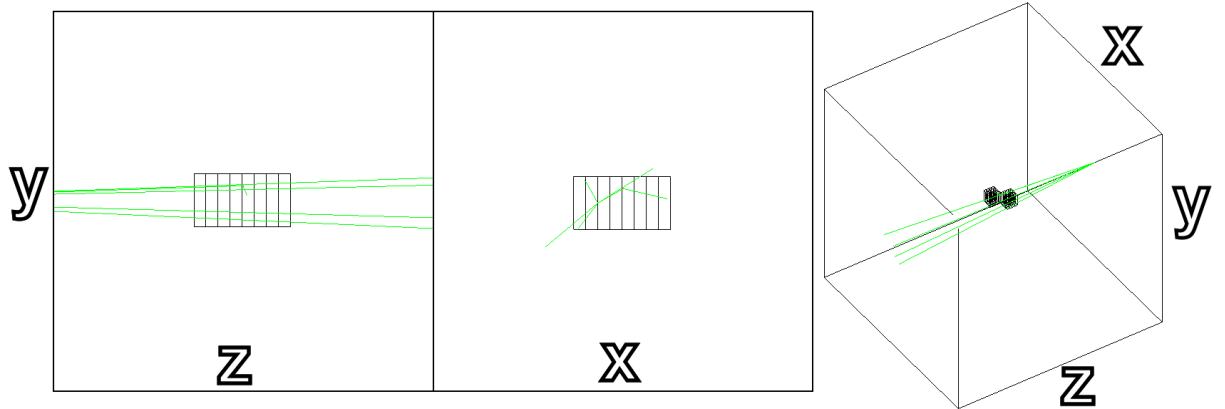


Figure 75 - Diagram showing location of two detectors relative to one another. Photons enter from the left, aimed to hit the nearer detector. The second detector is situated at the side edge of the first detector (situated 6.4 mm downstream (z) and 6.4 mm horizontally displaced (x)).

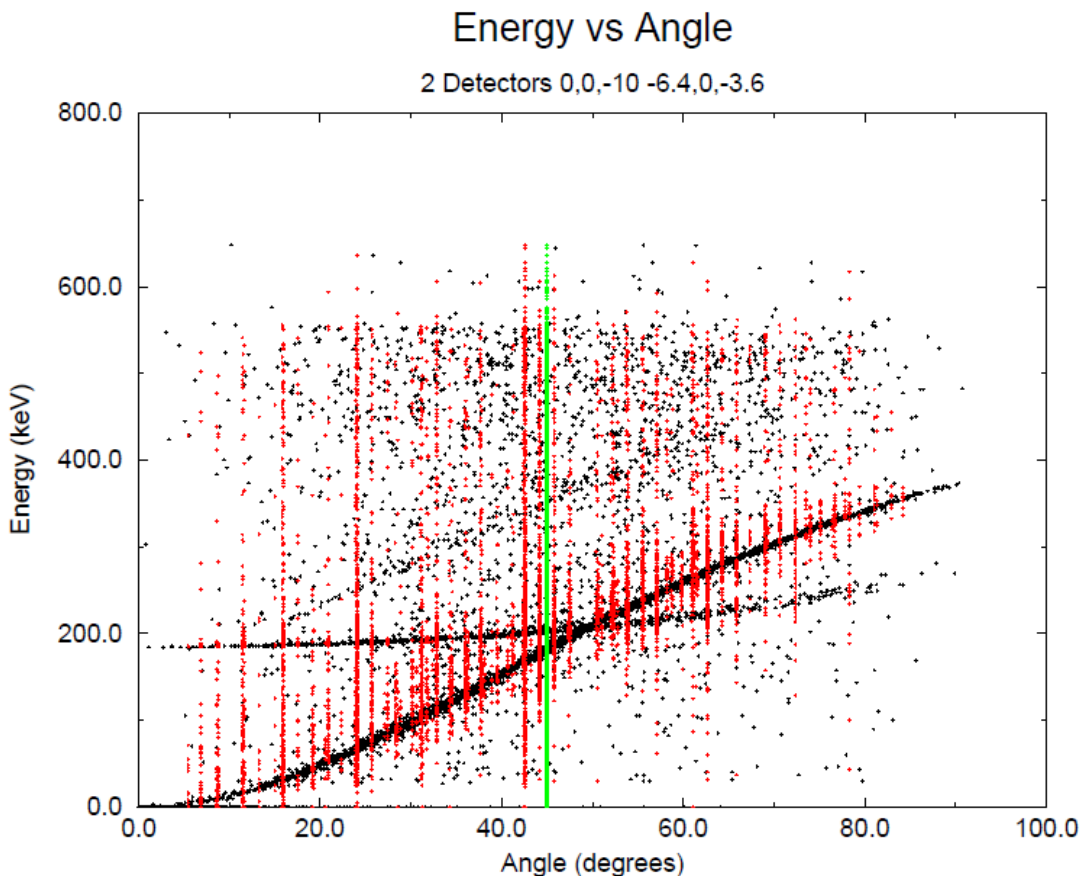


Figure 76 - Plot of energy against angle showing the real angle calculated from the interaction positions in black, the angle assuming the interactions occurred in the centre of the pixels in red and the angle assuming the interactions occurred in the centre of the detectors in green. This plot matches the setup described in Figure 75. The angles shown are the angle of scatter within detector 1.

The plot of energy versus angle is seen in Figure 76. The angle, assuming the interactions occurred in the centre of the pixels, is closer to the actual angular dependence than in Figure 72. This is due to a reduced range of angles available for an interaction within the same pixels. Once again, the angle calculated from assuming the interaction in the centre of the detectors possesses none of the detail that the pixelated picture provides.

The three loci described for the previous setup in Figure 73 are still present and are shown for this setup in Figure 76. The Green line shows the angle of scatter that can be calculated by using the centre of the detectors as the interaction point, it is apparent that moving to a pixelated system for the interaction points provides a far greater angular resolution with accordingly reduced angular error. This could be quantified by arguing that, for a single detector, the error in the angle would be equivalent to the maximum extent of the real angles subtended by the detector. Thus in Figure 76, the calculated angle from the entire detector would be $45^\circ \pm 45^\circ$, while the error in the pixels would be no greater than 7° . It is clear that the ideal situation would be to calculate the exact location by techniques such as pulse shape analysis and depth analysis to provide the ‘true’ location and accordingly attain a near zero error in the angle.

7. Efficiency Calculations and Measurements

Geant4 has been shown to be extremely useful in performing simulations of the response of CZT and other such materials. While the simulations presented both in Section 3 and Section 6 used Geant4, none of them required accurate cross-sections, only that the ratios of cross-sections behaved appropriately. In order to confirm that Geant4 is capable of making accurate estimates of cross-sections at low energies (important given that the package was written for high energy experiments at CERN); comparisons were made with experimental measurements.

The Geant4 simulation initially presented in Section 6 was for a pair of $6.4 \times 6.4 \times 6.4 \text{ mm}^3$ detectors. This simulation was modified to simulate a single detector $6.4 \times 6.4 \times 6.4 \text{ mm}^3$ detector. Gamma rays of energies 1332 and 662 keV were directed at the detector (3.5×10^6 events /energy). These events were used to calculate the intrinsic peak efficiency.

Two values were measured; firstly the efficiency of the entire detector – this is the number of photons which interacted in the detector and deposited their entire energy (across several pixels or otherwise). Secondly, the value described as ‘16 pixels’ is the number of photons which interacted and deposited their energy exclusively within one of the 16 pixels.

	Efficiency (%)
662 keV (Entire detector)	2.41 ± 0.25
662 keV (16 Pixels)	1.45 ± 0.16
1332 keV (Entire detector)	0.63 ± 0.07
1332 keV (16 Pixels)	0.24 ± 0.03

Table 13 - Table of results of efficiency simulations of a $6.4 \times 6.4 \times 6.4 \text{ mm}^3$ detector. Entire detector indicates events where the photon deposited its energy within the detector, possibly across several pixels. ‘16 pixels’ indicates events where the photon deposited its energy within a single pixel.

A series of measurements were made with the CZT detectors described at the end of Section 2.4. These consisted of measurements with three sources; a ^{60}Co source, a ^{137}Cs source and a

^{22}Na source; i.e. gamma-ray energies of 511, 662, 1173, 1274 and 1332 keV. The Cobalt and Caesium sources were situated 22 mm from the centre of the large detector while the Sodium source was located at a distance of 29.5 mm. In all other respects the 3 sources were all located in the same positions.

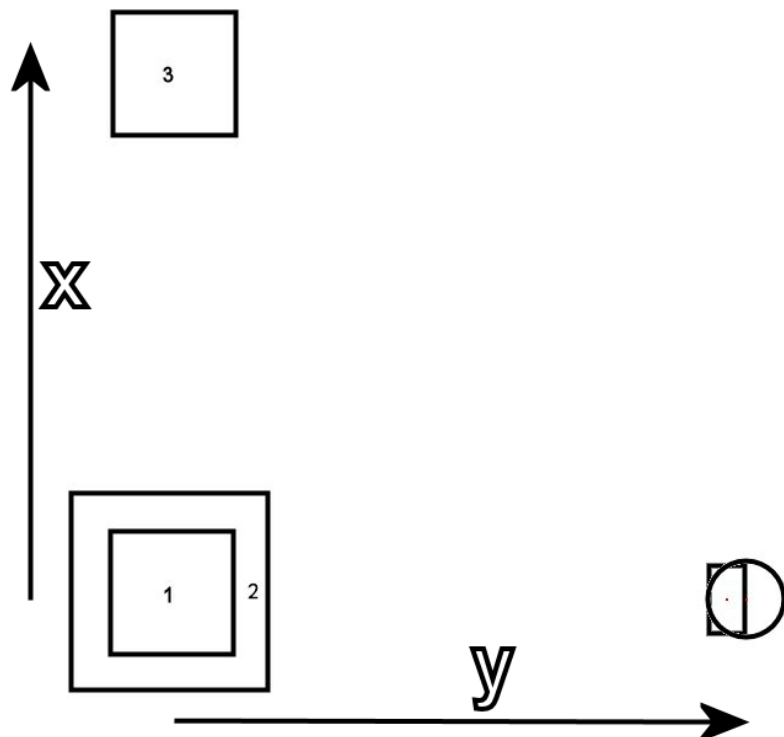


Figure 77 – Scale diagram showing the relative locations of the three detectors to the sources in the efficiency measurements. The detectors lie at (0,37.5,0), (0,3.5,0) and 17,2.5,0) respectively. The circular ^{22}Na source lies at (0,29.5,-2.5) and the rectangular ^{137}Cs and ^{60}Co sources both lie at (0,22,-2.5). All measurements are in mm and the z-axis is into the plane of the paper.

The solid angle for each of the three detectors was then calculated by taking the area of the plane which faced the source. The efficiencies calculated were the peak efficiencies. The lower energy gamma-ray from the ^{60}Co (1173 keV) was not used due to the low statistics resulting from a low activity source and the fact that it was not clearly resolved from Compton scattering contributions. In addition, the low statistics for the 1332 keV gamma-ray, compared with other contributions, meant that the peak could not be unambiguously

identified in the two small detectors. The values of the efficiencies determined from the measurements are shown in Figure 78.

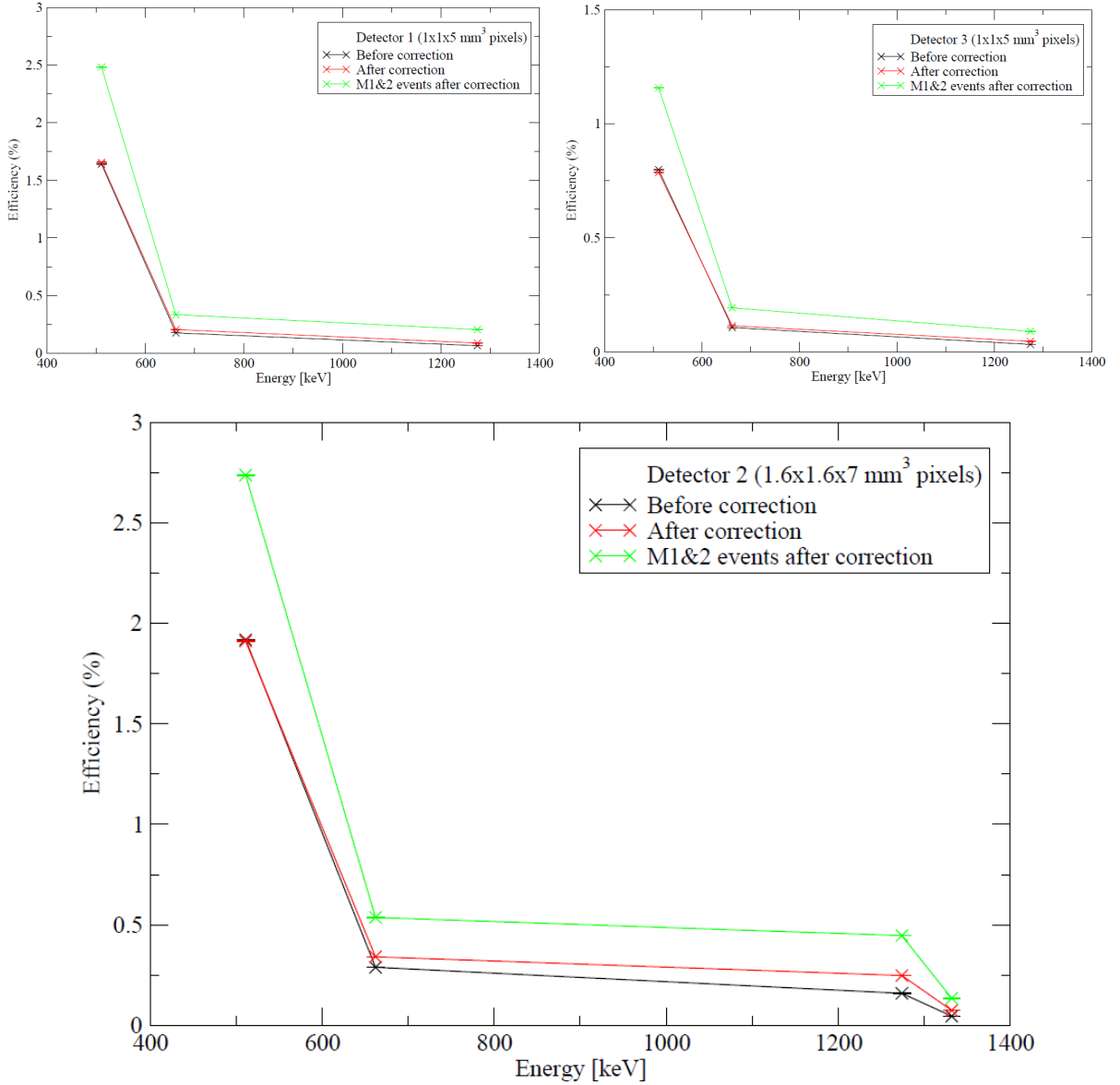


Figure 78 – Plots of efficiency values in the three detectors. ‘Before correction’ indicates the efficiency measured before the peaks were aligned, ‘flattened’ and ‘straightened’ as described in Section 3. ‘After correction’ indicates the efficiency measurement after those processes. ‘M1&2 events’ indicates where the efficiency after correction has been combined with the recovered efficiency due to multiplicity two events.

These are the intrinsic peak efficiency values for individual pixels (except for the efficiency including multiplicity two events, which are the intrinsic peak efficiency values for individual

and two pixel events), however, these efficiencies are measured for all 16 pixels at the same time.

Table 14 shows the ratio of efficiencies for multiplicity one and multiplicity two events to multiplicity one events for the three detectors. This ratio should increase with energy as the probability of the photon being completely collected within a single pixel decreases as photon energy increases. Accordingly, the probability of the photon being collected in two pixels increases. This effect should be less marked in the larger detector (detector two) as the larger pixels should be more likely to collect the photon completely. The table also shows the expected ratio of events completely collected in the entire detector to those collected in a single pixel based on a Geant4 simulation at 662 keV and 1332 keV.

	Detector 1 ($1 \times 1 \times 5 \text{ mm}^3$) pixels	Detector 2 ($1.6 \times 1.6 \times 7 \text{ mm}^3$) pixels	Detector 3 ($1 \times 1 \times 5 \text{ mm}^3$) pixels	Geant4 Simulation ($1.6 \times 1.6 \times 6.4 \text{ mm}^3$) pixels
511 keV	1.50 ± 0.00	1.43 ± 0.00	1.47 ± 0.00	N/A
662 keV	1.63 ± 0.01	1.57 ± 0.00	1.69 ± 0.00	1.66
1274 keV	2.32 ± 0.02	1.80 ± 0.00	1.95 ± 0.00	N/A
1332 keV	N/A	1.81 ± 0.00	N/A	2.66

Table 14 – Table showing the ratio of the efficiency for multiplicity one and two events against the efficiency for multiplicity one events only. In addition a Geant4 prediction is given of the ratio of events of any multiplicity to events of multiplicity one within a 16 pixel $6.4 \times 6.4 \times 6.4 \text{ mm}^3$ detector.

It is noticeable that the ratio for the larger detector is generally lower, not only than the two smaller detectors, but also than the Geant4 simulation. It was expected that the large detector would collect more photons in single pixels than the smaller detectors. The discrepancy between the real ratio and the Geant4 ratio suggests that more events are being collected in multiplicity three and above interactions in the large detector than in the small detectors. It is possible that the greater size of the detector means that photons have a greater chance of interacting several times within the detector and thus being fully collected; this is not seen in the small detectors as their size is insufficient for a photon to scatter many times without leaving the detector material.

Further experimental data with the sources located on the cathode face of detector two were used to calculate values of intrinsic peak efficiency which are compared with Geant4 simulations for a $6.4 \times 6.4 \times 6.4$ mm³ detector in Figure 79. The simulation was expanded to include gamma-ray energies from 50 keV up to 1500 keV including 511, 662, 1274, and 1332 keV.

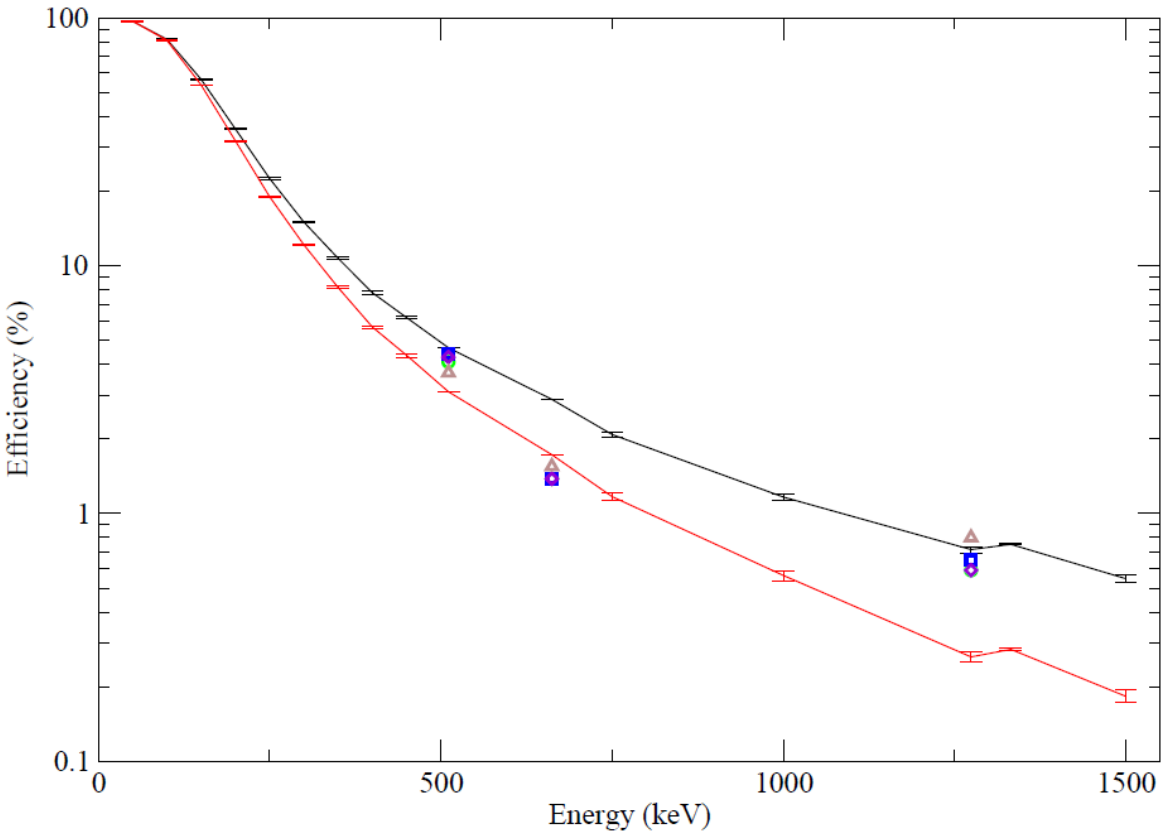


Figure 79 - Measured efficiency against Geant4 simulations for a $6.4 \times 6.4 \times 6.4$ mm³ detector. The red line shows the efficiency for the 16 pixels, while the black line shows the efficiency for the entire detector. The green circle denotes the efficiency for the initial data, the blue square the efficiency for the data after the peaks were aligned (as in Section 3), the purple diamond the efficiency after the spectrum was ‘flattened’ and the brown triangle shows the efficiency for the vertically straightened data.

Statistical error bars are given in both Figure 79 and Figure 80 for the simulations and experimentally determined efficiencies; where they are not visible the error is less than 1% of the value. The largest systematic errors (not included in the error bars) are likely to be the calculation of the solid angle, and the precision of the source activity measurement. In both

cases all four values of the efficiency calculated at each energy value will have the same error, and this error will also be consistent across both sodium energies.

As the new measurements fitted the simulation more closely, but not perfectly, a new series of simulations were run with both the $4 \times 4 \times 5 \text{ mm}^3$ and the $6.4 \times 6.4 \times 7 \text{ mm}^3$ detectors simulated. These simulations were performed for a range of energies from 50 keV to 1500 keV and are shown in Figure 80. The 662 keV gamma-rays from the ^{137}Cs still appears to have a lower efficiency than both the 511 keV annihilation peak and the 1274 keV photo peak from the ^{22}Na .

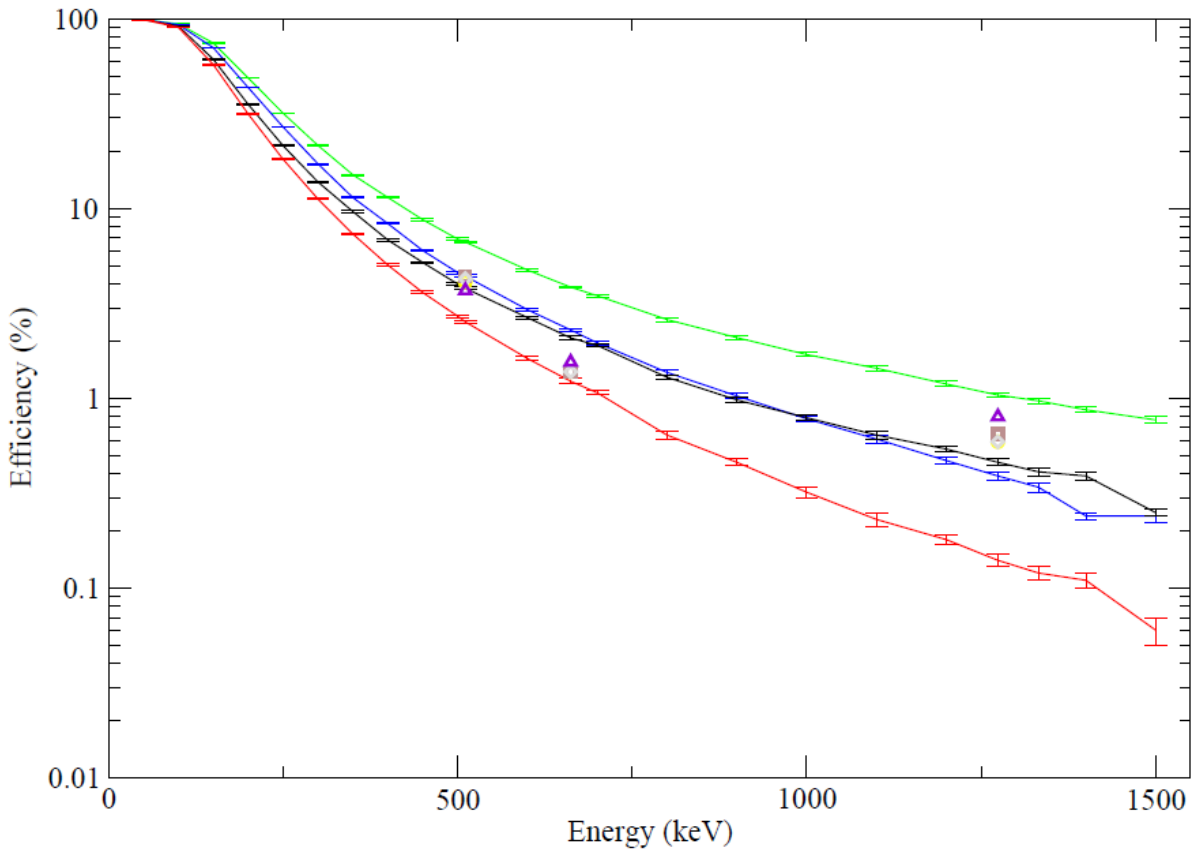


Figure 80 - Efficiency plot for the newer simulations, the green line denotes simulations for the entire large detector, the blue line is the simulations for the single pixels of the large detector. The black line is the entire small detector and the red line is the pixels of the small detector. The single markers show the calculated efficiencies within the large detector. The yellow circle shows the initial measurement, the brown square shows the measurement after the photopeaks were ‘aligned’, the grey diamond shows the efficiency after the spectra were ‘flattened’ and, finally, the purple triangle shows the efficiency after the peaks were ‘straightened’. These points should lie around the same values as the blue line.

Despite the apparently reduced efficiency in the real measurements at 662 keV, all the data points lie within a reasonable distance (1% or 2% at the extreme) of the simulated efficiency for the combined efficiency within the individual pixels (blue line). The fact that these data points lie close to the results from the Geant4 simulations (which, it should be remembered, do not take into account trapping of holes or induction of signal resulting in poor energy resolution), suggests that the energy tail of the photopeaks plays a relatively minor role in efficiency of the detectors (as seen in Section 4).

These efficiency measurements confirm that Geant4 is capable of simulating CZT detectors accurately, as well as demonstrating the suitability of the simulation package at low energies (keV to MeV scale). In addition, the efficiency calculations outlined in this Section are essential information for future analysis work using these detectors.

Conclusion

Neutrino-less double-beta decay is seen by many as a golden test for the Majorana nature of the neutrino. Experimental evidence for such a decay would provide important information about the neutrino mass, as well as forcing a re-examination of the ‘standard model’ of particle physics. However, the large half-life values associated with double-beta decay dictates that any experiment must have significant background reduction techniques applied. Accordingly, an ideal experiment would use an intrinsic detector system such as Cadmium-Zinc-Telluride. CZT is of great interest to researchers both as a result of the ability to operate at room temperatures and the presence of nine double-beta-decaying isotopes.

CZT is, however, well known to experience poor energy resolution as a result of relatively poor hole mobility. This results in a low energy tail on the anode and a distributed cathode signal. However, these two effects are a function of the depth within the material where the event took place. In addition, this effect can be minimised by the ‘small pixel effect’ by segmenting the anode into pixels. This segmentation does not completely remove the presence of the energy tail and this must be removed by other means.

The low energy tail has been shown to be modelled by the Shockley-Ramo theorem; however, these simulations are heavily constrained by both processor time and calculation limits. An alternative has been used in this work, to model the curvature of the energy tail empirically, and thus to calculate a ‘correction’ to the curvature.

The ‘corrected’ spectra have been shown to exhibit substantially increased events within the photopeaks and an increase in the relative intensity of signals within the photopeak and the tail. However, the Full-Width Half-Maximum is found to be unchanged as a result of the dominance of events within the photopeak. The result of this work has been to show that, across the three tests, the ‘correction’ can be shown to provide an improvement in energy resolution and efficiency as great as that seen due to gain matching.

It has also been shown that the signal collected within two pixels can be re-combined to further increase the efficiency of events; however, a significant loss in energy resolution is found as a result of this process. This recombination can be expanded to include events shared between detectors, and hence to the use of multiple detectors (or even multiple pixels in a single detector) as a Compton Camera. It has been shown in this work that, for a source located at most 200 mm away from the detectors in any given dimension, the location can be fixed to a precision of no worse than 21.1 mm in each dimension (and often better).

During this work, the centres of the detectors were used to calculate the source locations. However, there is no reason other than processing time not to use the centre of the pixels triggered or even (if depth information can be extracted from the cathode signal and lateral position information from pulse shape analysis in adjacent pixels) the calculated position of interaction. It has been shown that the improvement of the interaction location used (from centre of detector to centre of pixel and then to calculated interaction location), provides substantial improvements in a plot of the angle scattered through as a function of the energy deposited.

Finally, the efficiency of the three detectors was calculated and compared to Geant4 simulations. It was found that the calculated efficiencies matched the simulated values to a precision of 1%. This suggested that significant systematic errors were present, but that the simulation package presented reasonable conformity to the real measurements.

Outlook and Future Work

The development of pixelated CZT detectors has many applications, from use as a Compton Camera in security applications to fundamental science research. However, various challenges must be overcome, especially in neutrino-less double-beta decay searches. Primary among these is a further improvement in the precision knowledge of interaction location within the pixels. It has been shown by Unsworth et al¹⁰⁰ that it is possible to use induced signal in adjacent pixels to indicate the location within the pixel. Furthermore, it was argued within this work that the signal induced upon the cathode may be used as an indicator of depth of interaction. However, no correlation between cathode signal and depth of interaction has been

established during this work, indeed evidence has suggested that the relationship may not be as simple as desired, as discussed in Sections 2.4 and 3.3 and seen in Figure 13.

Figure 13 shows that the response of the two detectors is drastically different, suggesting that the large detector does not show a linear depth/cathode signal relationship. This would ideally be tested, either by the use of a collimated source to provide measurements at varying detector height, or by use of a varying energy source to provide variable implantation depths. An experiment fitting the second description has been preliminarily setup in the department in Birmingham, but no measurements have yet been performed.

Finally, experiments such as those outlined here should be performed on the ‘ideal’ sized pixels of 200 μ m. Verification of the performance of these detectors is essential if experiments such as COBRA are to succeed.

Appendices

Appendix A – Measurements and Source Locations

9	8	7
6	5	4
3	2	1

Table 15 - Table showing the connector locations on the Masterboard.

Measurements performed in November 2008 using 2 detectors: The larger detector was mounted in channel 5, the smaller detector was mounted in channel 8.

- R3 – ^{60}Co source located to the right hand side of the detectors.
- R4 – Co source located above the detectors.
- R6 – ^{137}Cs source located to the right hand side of the detectors.
- R7 – ^{152}Eu source located to the right hand side of the detectors with a large gain setting.
- R8 – ^{152}Eu source located to the right hand side of the detectors with a small gain setting.

Measurements performed in January 2009 using 3 detectors: The larger detector was mounted in channel 5 in the lower board and smaller detectors were mounted in channel 8 of the lower board and channel 5 of the upper board.

- R3 – ^{137}Cs source located on the lower board to the left of the detectors.
- R4 – ^{137}Cs source located on top of the upper board ‘below’ detectors 2 and 3.
- R5 – ^{137}Cs source located on top of the upper board to the right of the detectors.
- R6 – ^{137}Cs source located on the lower board ‘above’ the detectors.
- R7 – ^{137}Cs source located on top of the upper board vertically above detectors 2 and 3.
- R8 – ^{60}Co source located on the bottom of the chamber to the left of the detectors.
- R9 – ^{60}Co source located on top of the upper board ‘below’ detectors 2 and 3. Detector 3 was not working.
- R10 – ^{60}Co source located on top of the upper board ‘below’ detectors 2 and 3.

- R11 – ^{60}Co source located on the lower board to the right of the detectors.
- R12 – ^{60}Co source located on top of the upper board to the left of the detectors.

Measurements performed in November 2009 using 3 detectors: The larger detector was mounted in channel 8 in the lower board and the smaller detectors were mounted in channel 5 of the lower board and channel 5 of the upper board.

- R4 – ^{137}Cs source located on the lower board pressed against the right side of channel 4's mounting.
- R5 – ^{60}Co source located on the lower board pressed against the right side of channel 4's mounting.
- R6 – ^{60}Co source located on the lower board pressed against the right side of channel 4's mounting.
- R7 – ^{22}Na source located on the lower board pressed against the right side of channel 4's mounting.

Measurements performed in January 2010 using 1 large detector mounted in channel 5 of the lower board.

- R9 – ^{137}Cs source located on top of the detector.
- R10 – ^{22}Na source located on top of the detector.

Appendix B – MathCAD Analysis

The energy of the source and the detector and source locations (in two dimensions) are given. In this example, the energy is fixed at 1333 keV, the detectors at 0,30 17,0 and 0,0 and the source at $33 \pm 3,37$.

The equations to calculate the energy deposited during a scatter and the energy remaining with the particle are included along with the equation to calculate the angle between; the source to first detector vector and the first detector to second detector vector. Note that, in this instance, the system is limited to two dimensions – however, this can be (and was) easily expanded to three. Finally, this angle is used to calculate the energies deposited within the two detectors; which are compared to the measured values to give a ‘difference’.

$$\begin{aligned}
i &= 0..20 & E\gamma &:= 1333 \\
d1_0 &= 0 & d1_1 &= 30 & d2_0 &= 17 & d2_1 &= 0 & d3_0 &= 0 & d3_1 &= 0 \\
S_{0,i} &:= -33 + \frac{(i-10)\cdot 1}{3} & S_{1,i} &:= 37 + \frac{(i-10)\cdot 0}{4} \\
E(\theta) &:= \frac{E\gamma}{1 + \frac{E\gamma}{511} \cdot (1 - \cos(|\theta|))} & Ed(\theta) &:= E\gamma - \frac{E\gamma}{1 + \frac{E\gamma}{511} \cdot (1 - \cos(|\theta|))} \\
\theta dp(S, d1, d2, i) &:= \arccos \left[\frac{(S_{0,i} - d1_0)}{\left[(S_{0,i} - d1_0)^2 + (S_{1,i} - d1_1)^2 \right]^{0.5}} \cdot \frac{(d1_0 - d2_0)}{\left[(d1_0 - d2_0)^2 + (d1_1 - d2_1)^2 \right]^{0.5}} + \frac{(S_{1,i} - d1_1)}{\left[(S_{0,i} - d1_0)^2 + (S_{1,i} - d1_1)^2 \right]^{0.5}} \cdot \frac{(d1_1 - d2_1)}{\left[(d1_0 - d2_0)^2 + (d1_1 - d2_1)^2 \right]^{0.5}} \right] \\
\text{S-d1-d2 system: } & \theta S1_d1_d2 := \theta dp(S, d1, d2, i) & E2a_i &:= E(\theta S1_d1_d2) & E1a_i &:= Ed(\theta S1_d1_d2) & \text{diff}_{0,i} &:= E1a_i - 1600 & \text{diff}_{1,i} &:= E2a_i - 1152 \\
\text{S-d2-d1 system: } & \theta S1_d2_d1 := \theta dp(S, d2, d1, i) & E1b_i &:= E(\theta S1_d2_d1) & E2b_i &:= Ed(\theta S1_d2_d1) & \text{diff}_{2,i} &:= E1b_i - 512 & \text{diff}_{3,i} &:= E2b_i - 2192 \\
\text{S-d1-d3 system: } & \theta S1_d1_d3 := \theta dp(S, d1, d3, i) & E3a_i &:= E(\theta S1_d1_d3) & E1c_i &:= Ed(\theta S1_d1_d3) & \text{diff}_{4,i} &:= E1c_i - 1906 & \text{diff}_{5,i} &:= E3a_i - 865 \\
\text{S-d3-d1 system: } & \theta S1_d3_d1 := \theta dp(S, d3, d1, i) & E1d_i &:= E(\theta S1_d3_d1) & E3b_i &:= Ed(\theta S1_d3_d1) & \text{diff}_{6,i} &:= E1d_i - 569 & \text{diff}_{7,i} &:= E3b_i - 2146 \\
\text{S-d2-d3 system: } & \theta S1_d2_d3 := \theta dp(S, d2, d3, i) & E3c_i &:= E(\theta S1_d2_d3) & E2c_i &:= Ed(\theta S1_d2_d3) & \text{diff}_{8,i} &:= E2c_i - 2202 & \text{diff}_{9,i} &:= E3c_i - 521 \\
\text{S-d3-d2 system: } & \theta S1_d3_d2 := \theta dp(S, d3, d2, i) & E2d_i &:= E(\theta S1_d3_d2) & E3d_i &:= Ed(\theta S1_d3_d2) & \text{diff}_{10,i} &:= E2d_i - 1354 & \text{diff}_{11,i} &:= E3d_i - 1400
\end{aligned}$$

Figure 81 - MathCAD sheet showing the detector locations, variable source location and the resulting energies deposited for scatters within the three detectors.

The location of the source relative to the three detectors is plotted. Note that the source has a spread in the x-axis.

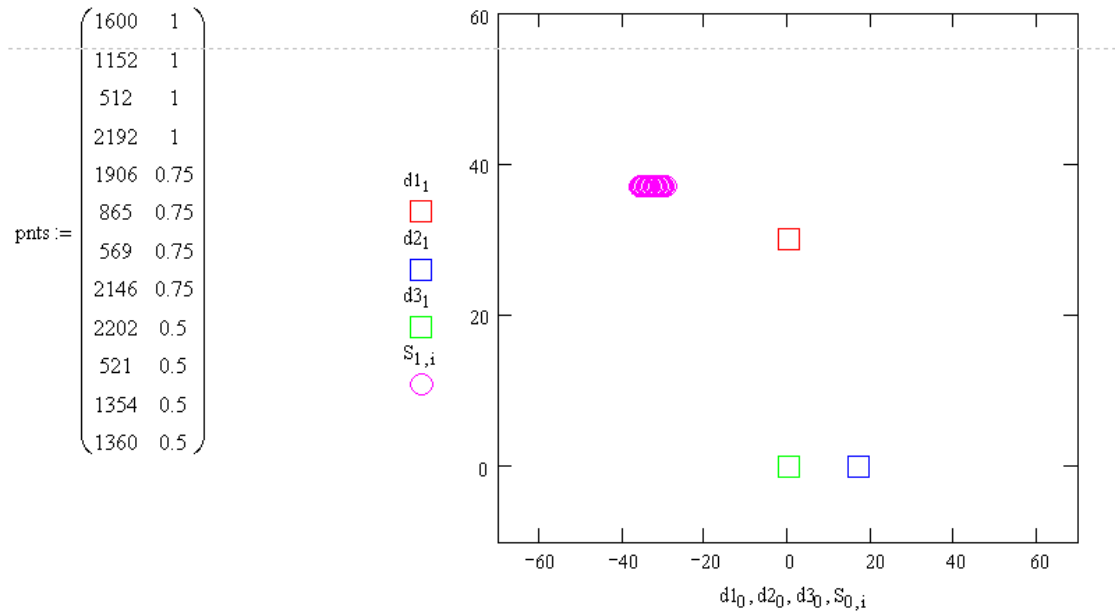


Figure 82 –Two-dimensional plot of the detector and source positions in the simulation. Also shown is the table of data-points for the peak centroids in the measured data, with a value of 1 associated to the detector 1 and 2 pairing, 0.75 to the detector 1 and 3 pairing and 0.5 to the detector 2 and 3 pairing.

The measured channels ($2 \times$ energy) for the peaks are plotted as ‘X’ on Figure 83. In addition the fitted peaks are shown with a spread of energies due to the variability in the detectors location.

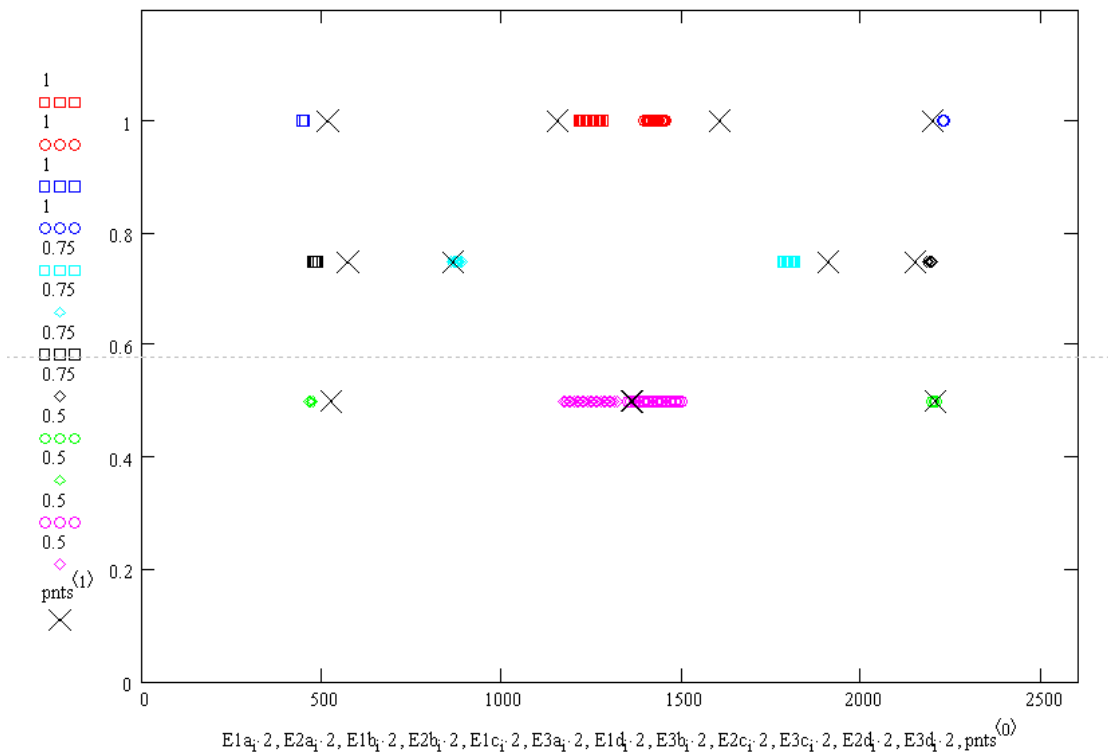


Figure 83 - Plot showing the real peak locations (marked as X) and the peak locations with the current fitted source location. Y-axis values of 1 relate to the detector 1 and 2 pairing, 0.75 to the detector 1 and 3 pairing and 0.5 to the detector 2 and 3 pairing.

Finally, the sum of the differences between the fitted and real peaks was plotted against the x-axis component of the source location. Thus, we can see how a change in the source location will improve the fit.

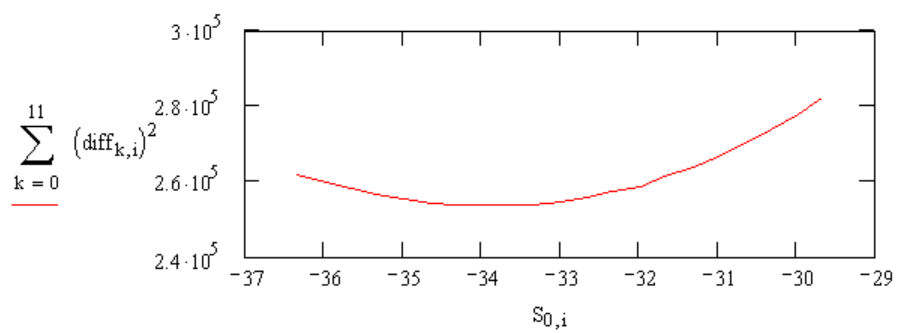


Figure 84 - Sum of the squared difference between the fitted and the measured peak locations, as a function of the source location.

Appendix C – Pixel maps for improvements

As in Figure 39 these pixel maps show the area under the peak, FWHM in keV and Peak to Trough ratios prior and post correction, laid out in the order the pixels appear in the real detectors, with the bottom row on the far left, and the top row on the far right:

4	8	12	14		2	6	10	16		3	7	11	13		1	5	9	15
---	---	----	----	--	---	---	----	----	--	---	---	----	----	--	---	---	---	----

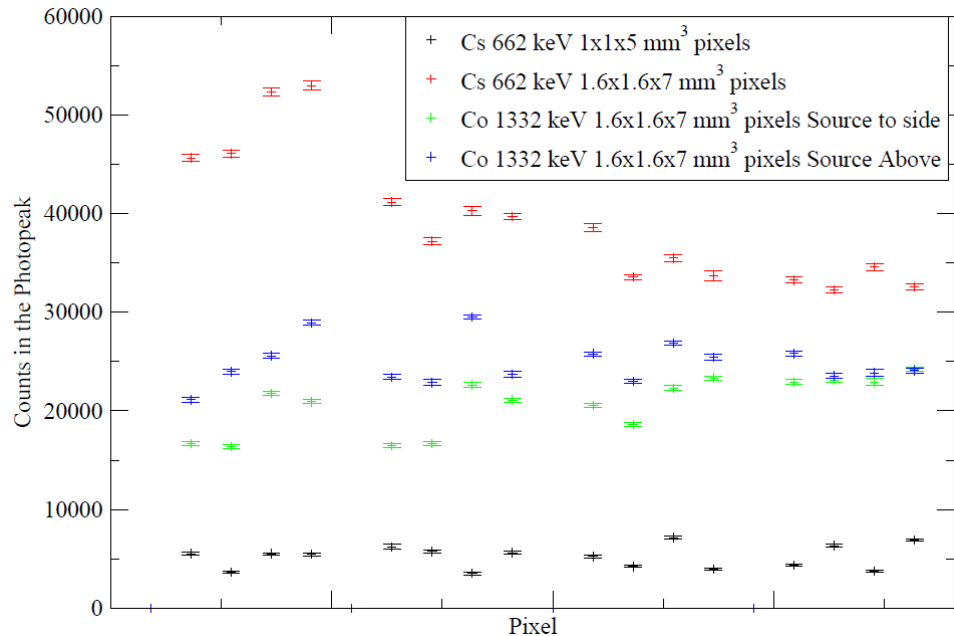


Figure 85 - Pixel map showing the area in the photopeak prior to 'correction'.

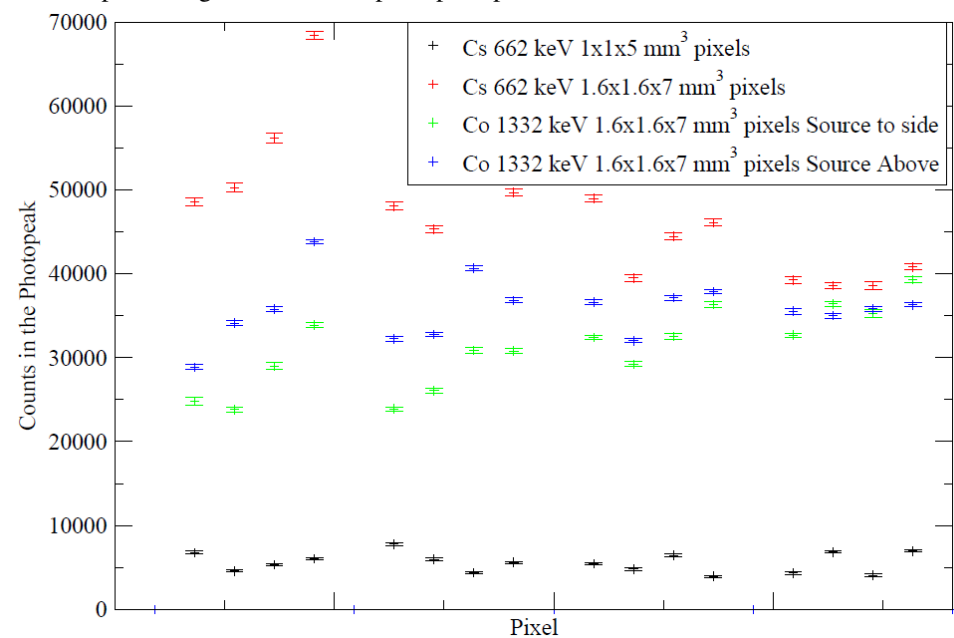


Figure 86 - Pixel map showing the area in the photopeak after 'correction'.

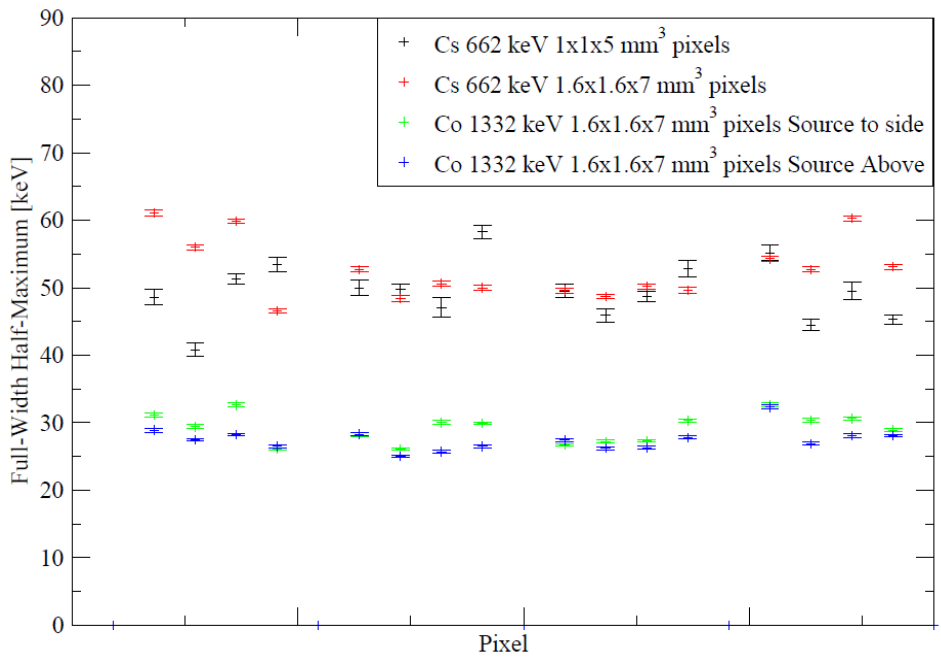


Figure 87 - Pixel map showing the FWHM in keV prior to 'correction'.

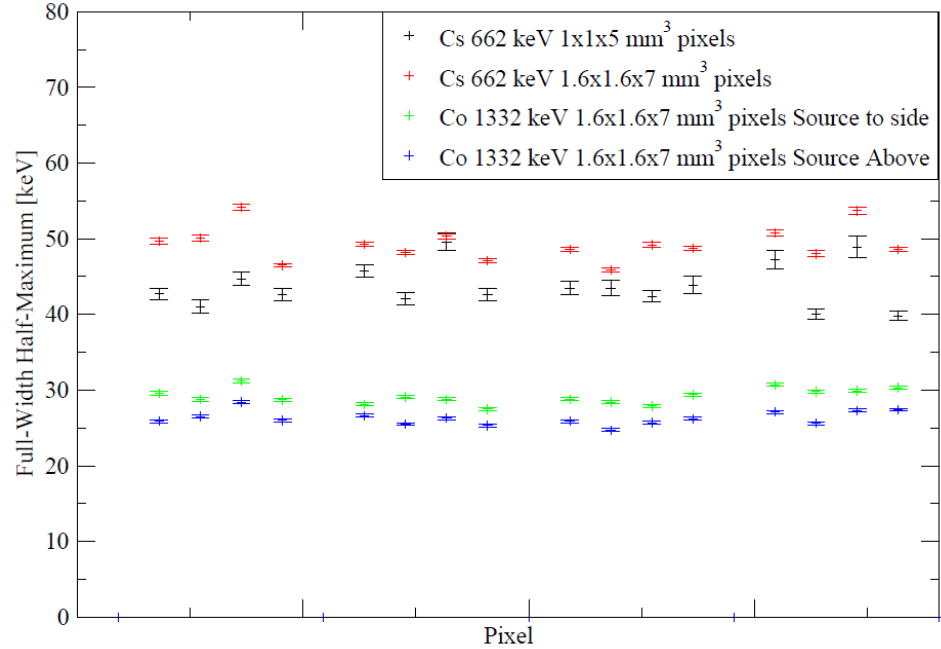


Figure 88 - Pixel map showing the FWHM in keV after 'correction'.

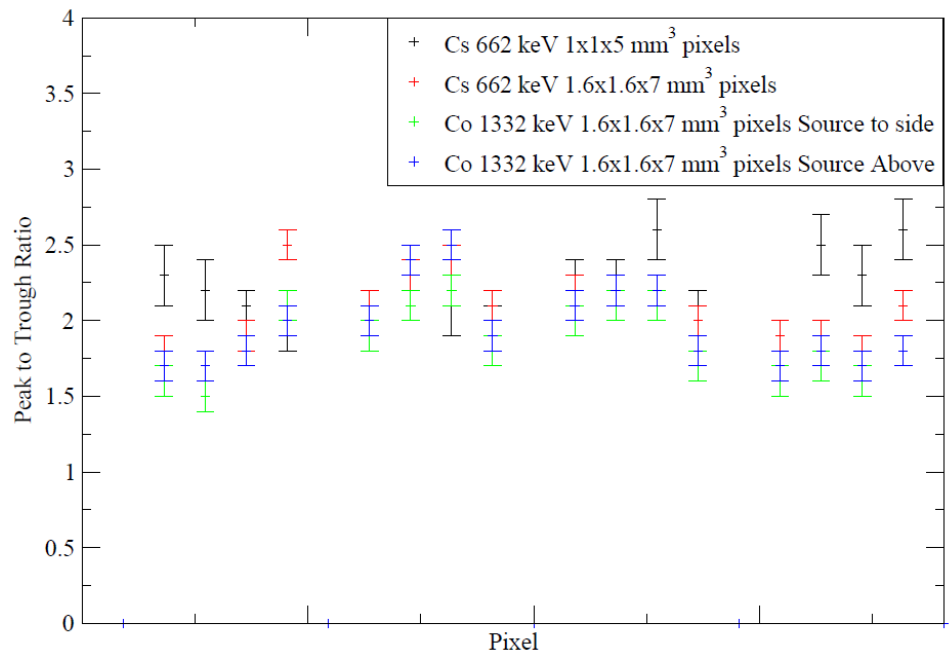


Figure 89 - Pixel map showing the Peak to Trough ratio prior to 'correction'.

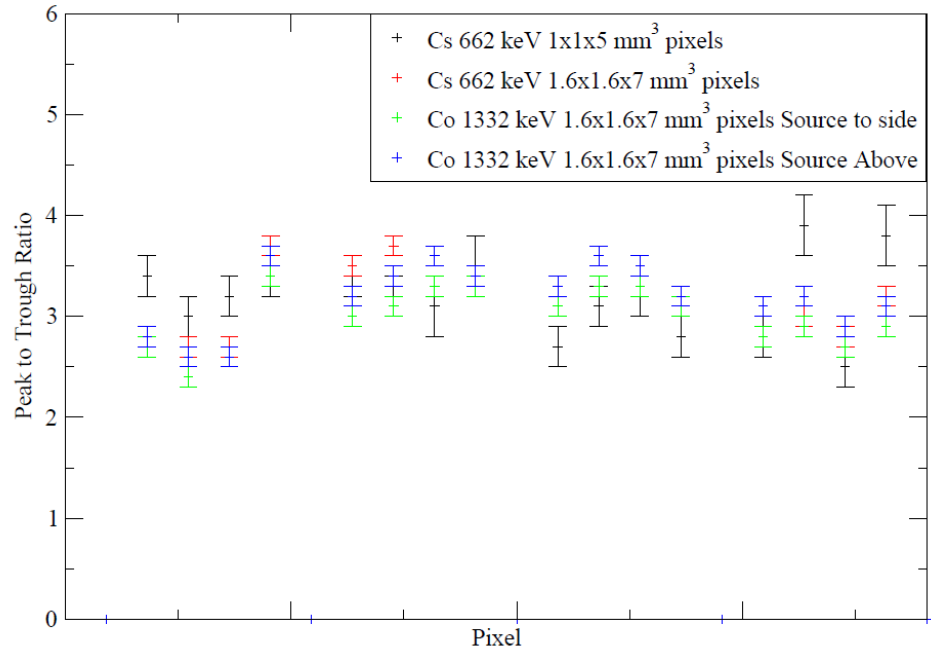


Figure 90 - Pixel map showing the Peak to Trough ratio after 'correction'.

Appendix D – C++ Simulation of Compton Scattering

This simulation scans across the three dimensions of the two detectors and calculates the angle through which the photon must scatter to interact in both locations. The energy deposited in the first detector is then taken to be the energy deposited during the Compton scatter correspondent with that angle. No cross-sections were included and the energy deposited in the second detector was simply the remaining energy after the Compton scatter.

```
//  
// S. Spencer - Modified 18th May 2010  
//  
// This program uses sweeps across Detectors to force interactions  
// in 2 Detectors and outputs the energy that such an interaction  
// would deposit  
#include <iostream.h>  
#include <fstream.h>  
#include <cmath>  
#include <stdlib.h>  
#include <string.h>  
main()  
{  
    fstream out;  
    time_t seed;  
    int steplim;  
    int particles;  
    float d[4][4],xsize[4],ysize[4],zsize[4];  
    float pi=3.141592654;  
    int i,j,a,b;  
    char *filename;  
    char *file;  
    int randx,randy,randz,rand2x,rand2y,rand2z;  
    float scatterx,scattery,scatterz,depositx,deposity,depositz;  
    float minscatterx,minscattery,minscatterz,mindepositx  
        ,mindeposity,mindepositz;  
    float maxscatterx,maxscattery,maxscatterz,maxdepositx  
        ,maxdeposity,maxdepositz;  
    float thetax1,thetax2,thetax3;  
    float minthetafor,minthetaback,maxthetafor,maxthetaback  
        ,mintheta,maxtheta;  
    float sx,sy,sz,d1x,d1y,d1z,d2x,d2y,d2z;  
    float thetaparts[6],theta1,theta2,theta3,theta;  
    double totsig,ang,cs,cs2,sig1,r0,alpha,sig2,sig3,sig4,sig;  
    double probtheta1,probtheta2,storetheta1,storetheta2;  
    float Escatter1,Esource,Edeposit1,Escatter2,Edeposit2;  
    int step,countscatter1[10001],countdeposit1[10001];  
    int countscatter2[10001],countdeposit2[10001];  
    float randEs1,randEd1,randEs2,randEd2,sigma,FWHM;  
    float meanscatter1,meandeposit1,meanscatter2,meandeposit2;  
    float probEs1,probEd1,probEs2,probEd2,r1,r2;  
    int z,y,x,p,q,r,lim;  
    double range;  
    double sigr1,sigr2,totsig1,totsig2,rang1,range2;  
    float mintheta1,mintheta2,maxtheta1,maxtheta2;  
    for (step=0;step<=9999;step++)
```

```

{
    countscatter1[step]=0;
    countdeposit1[step]=0;
    countscatter2[step]=0;
    countdeposit2[step]=0;
}

// We initialise the seed for the random number
seed=time(NULL);
srand(seed);
d[0][0]=3.0;
d[0][1]=-6.3;
d[0][2]=51.5;
d[0][3]=0;
sx=d[0][0];
sy=d[0][1];
sz=d[0][2];
d[1][0]=0;
d[1][1]=-38.5;
d[1][2]=0;
d[1][3]=1;
d[2][0]=17;
d[2][1]=0;
d[2][2]=0;
d[2][3]=0;
d[3][0]=0;
d[3][1]=0;
d[3][2]=0;
d[3][3]=0;
xsize[1]=4;
ysize[1]=2.5;
zsize[1]=4;
xsize[2]=6.4;
ysize[2]=3.2;
zsize[2]=6.4;
xsize[3]=4;
ysize[3]=2.5;
zsize[3]=4;
cout << "First Detector (1-3): ";
cin >> i;
cout << endl << "Second Detector (1-3): ";
cin >> j;
cout << endl << "Source Energy (keV): ";
cin >> Esource;
cout << endl << "Name of output file (.csv): ";
cin >> file;
strcat(file,".csv");
cout << endl << "Filename is "<<file<<endl;
out.open(file,ios::out);
particles=0;
r0=2.8179402894E-12;
alpha=Esource/511;
totsig1=0;
totsig2=0;
ang=0;
double n1x,n1y,n1z,n2x,n2y,n2z;
n1x=0.;
n1y=0.;
n1z=0.;
```

```

n2x=0.;
n2y=0.;
n2z=0.;
steplim=5;
mintheta1=999;
maxtheta1=0;
mintheta2=999;
maxtheta2=0;
for (n1x=0;n1x<=steplim;n1x++)
{
    cout << endl << n1x;
    for (n1y=0;n1y<=steplim;n1y++)
    {
        for (n1z=0;n1z<=steplim;n1z++)
        {
            for (n2x=0;n2x<=steplim;n2x++)
            {
                for (n2y=0;n2y<=steplim;n2y++)
                {
                    for (n2z=0;n2z<=steplim;n2z++)
                    {

d1x=((d[i][0]-(xsize[i]/2))+((n1x/steplim)*(xsize[i])));
d1y=((d[i][1]-(ysize[i]))+((n1y/steplim)*(ysize[i]*2)));
d1z=((d[i][2]-(zsize[i]/2))+((n1z/steplim)*(zsize[i])));
d2x=((d[j][0]-(xsize[j]/2))+((n2x/steplim)*(xsize[j])));
d2y=((d[j][1]-(ysize[j]))+((n2y/steplim)*(ysize[j]*2)));
d2z=((d[j][2]-(zsize[j]/2))+((n2z/steplim)*(zsize[j])));
range1=sqrt(pow(d1x-sx,2)+pow(d1y-sy,2)+pow(d1z-sz,2));
range2=sqrt(pow(d2x-sx,2)+pow(d2y-sy,2)+pow(d2z-sz,2));
thetaparts[1]=(sx-d1x)/(sqrt(pow((sx-d1x),2)+pow((sy-d1y),2)
    +pow((sz-d1z),2)));
thetaparts[2]=(d1x-d2x)/(sqrt(pow((d1x-d2x),2)+pow((d1y-d2y),2)
    +pow((d1z-d2z),2)));
thetaparts[3]=(sy-d1y)/(sqrt(pow((sx-d1x),2)+pow((sy-d1y),2)
    +pow((sz-d1z),2)));
thetaparts[4]=(d1y-d2y)/(sqrt(pow((d1x-d2x),2)+pow((d1y-d2y),2)
    +pow((d1z-d2z),2)));
thetaparts[5]=(sz-d1z)/(sqrt(pow((sx-d1x),2)+pow((sy-d1y),2)
    +pow((sz-d1z),2)));
thetaparts[6]=(d1z-d2z)/(sqrt(pow((d1x-d2x),2)+pow((d1y-d2y),2)
    +pow((d1z-d2z),2)));

thetax1=thetaparts[1]*thetaparts[2];
thetax2=thetaparts[3]*thetaparts[4];
thetax3=thetaparts[5]*thetaparts[6];
thetal=acos(thetax1+thetax2+thetax3);
if (thetal<mintheta1)
{
    mintheta1=thetal;
}
if (thetal>maxtheta1)
{
    maxtheta1=thetal;
}
thetaparts[1]=(sx-d2x)/(sqrt(pow((sx-d2x),2)+pow((sy-d2y),2)
    +pow((sz-d2z),2)));
thetaparts[3]=(sy-d2y)/(sqrt(pow((sx-d2x),2)+pow((sy-d2y),2)
    +pow((sz-d2z),2)));
thetaparts[5]=(sz-d2z)/(sqrt(pow((sx-d2x),2)+pow((sy-d2y),2)
    +pow((sz-d2z),2)));

```

```

        +pow((sz-d2z),2)));
thetaparts[2]=(d2x-d1x)/(sqrt(pow((d2x-d1x),2)+pow((d2y-d1y),2)
        +pow((d2z-d1z),2)));
thetaparts[4]=(d2y-d1y)/(sqrt(pow((d2x-d1x),2)+pow((d2y-d1y),2)
        +pow((d2z-d1z),2)));
thetaparts[6]=(d2z-d1z)/(sqrt(pow((d2x-d1x),2)+pow((d2y-d1y),2)
        +pow((d2z-d1z),2)));

thetax1=thetaparts[1]*thetaparts[2];
thetax2=thetaparts[3]*thetaparts[4];
thetax3=thetaparts[5]*thetaparts[6];
theta2=acos(thetax1+thetax2+thetax3);
if (theta2<mintheta2)
{
    mintheta2=theta2;
}
if (theta2>maxtheta2)
{
    maxtheta2=theta2;
}
cs=cos(theta1);
cs2=pow(cs,2);
sig1=pow(r0,2)/(pow((1+alpha*(1-cs)),3));
sig2=(1+cs2)/2;
sig3=pow(alpha,2)*pow((1-cs),2);
sig4=(1+cs2)*(1+alpha*(1-cs));
sigrl=sig1*sig2*(1+sig3/sig4)*(1/sin(theta1))*(1*pow(range1,2));
totsig1=totsig1+sigrl;
cs=cos(theta2);
cs2=pow(cs,2);
sig1=pow(r0,2)/(pow((1+alpha*(1-cs)),3));
sig2=(1+cs2)/2;
sig3=pow(alpha,2)*pow((1-cs),2);
sig4=(1+cs2)*(1+alpha*(1-cs));
sigr2=sig1*sig2*(1+sig3/sig4)*(1/sin(theta2))*(1*pow(range2,2));
totsig2=totsig2+sigr2;
}
}
}
}
}
}
for (randx=0;randx<=steplim;randx++)
{
    cout << endl << randx;
    for (randy=0;randy<=steplim;randy++)
    {
        for (randz=0;randz<=steplim;randz++)
        {
            for (rand2x=0;rand2x<=steplim;rand2x++)
            {
                for (rand2y=0;rand2y<=steplim;rand2y++)
                {
                    for (rand2z=0;rand2z<=steplim;rand2z++)
                    {
scatterx=((d[i][0]-(xsize[i]/2))+((randx/steplim)*(xsize[i])));
scattery=((d[i][1]-(ysize[i]))+((randy/steplim)*(ysize[i]*2)));
scatterz=((d[i][2]-(zsize[i]/2))+((randz/steplim)*(zsize[i])));
depositx=((d[j][0]-(xsize[j]/2))+((rand2x/steplim)*(xsize[j])));

```

```

deposity=((d[j][1]-(ysize[j]))+((rand2y/steplim)*(ysize[j]*2)));
depositz=((d[j][2]-(zsize[j]/2))+((rand2z/steplim)*(zsize[j])));
sx=d[0][0];
sy=d[0][1];
sz=d[0][2];
d1x=scatterx;
d1y=scattery;
d1z=scatterz;
d2x=depositx;
d2y=deposity;
d2z=depositz;
thetaparts[1]=(sx-d1x)/(sqrt(pow((sx-d1x),2)+pow((sy-d1y),2)
+pow((sz-d1z),2)));
thetaparts[2]=(d1x-d2x)/(sqrt(pow((d1x-d2x),2)+pow((d1y-d2y),2)
+pow((d1z-d2z),2)));
thetaparts[3]=(sy-d1y)/(sqrt(pow((sx-d1x),2)+pow((sy-d1y),2)
+pow((sz-d1z),2)));
thetaparts[4]=(d1y-d2y)/(sqrt(pow((d1x-d2x),2)+pow((d1y-d2y),2)
+pow((d1z-d2z),2)));
thetaparts[5]=(sz-d1z)/(sqrt(pow((sx-d1x),2)+pow((sy-d1y),2)
+pow((sz-d1z),2)));
thetaparts[6]=(d1z-d2z)/(sqrt(pow((d1x-d2x),2)+pow((d1y-d2y),2)
+pow((d1z-d2z),2)));

theta1=thetaparts[1]*thetaparts[2];
theta2=thetaparts[3]*thetaparts[4];
theta3=thetaparts[5]*thetaparts[6];
theta=acos(theta1+theta2+theta3);
if (theta<0)
{
    theta=theta+pi;
}

Escatter1=Esource/(1+((Esource/511)*(1-cos(theta))));
Edeposit1=(Esource-Escatter1);
r1=sqrt(pow((scatterx-sx),2)+pow((scattery-sy),2)+pow((scatterz-sz),2));
storetheta1=theta;
a=i;
b=j;
scatterx=((d[b][0]-(xsize[b]/2))+((randx/steplim)*(xsize[b])));
scattery=((d[b][1]-(ysize[b]))+((randy/steplim)*(ysize[b]*2)));
scatterz=((d[b][2]-(zsize[b]/2))+((randz/steplim)*(zsize[b])));
depositx=((d[a][0]-(xsize[a]/2))+((rand2x/steplim)*(xsize[a])));
deposity=((d[a][1]-(ysize[a]))+((rand2y/steplim)*(ysize[a]*2)));
depositz=((d[a][2]-(zsize[a]/2))+((rand2z/steplim)*(zsize[a])));
sx=d[0][0];
sy=d[0][1];
sz=d[0][2];
d1x=scatterx;
d1y=scattery;
d1z=scatterz;
d2x=depositx;
d2y=deposity;
d2z=depositz;
thetaparts[1]=(sx-d1x)/(sqrt(pow((sx-d1x),2)+pow((sy-d1y),2)
+pow((sz-d1z),2)));
thetaparts[2]=(d1x-d2x)/(sqrt(pow((d1x-d2x),2)+pow((d1y-d2y),2)
+pow((d1z-d2z),2)));
thetaparts[3]=(sy-d1y)/(sqrt(pow((sx-d1x),2)+pow((sy-d1y),2),

```

```

        +pow((sz-d1z),2)));
thetaparts[4]=(d1y-d2y)/(sqrt(pow((d1x-d2x),2)+pow((d1y-d2y),2)
        +pow((d1z-d2z),2)));
thetaparts[5]=(sz-d1z)/(sqrt(pow((sx-d1x),2)+pow((sy-d1y),2)
        +pow((sz-d1z),2)));
thetaparts[6]=(d1z-d2z)/(sqrt(pow((d1x-d2x),2)+pow((d1y-d2y),2)
        +pow((d1z-d2z),2)));

theta1=thetaparts[1]*thetaparts[2];
theta2=thetaparts[3]*thetaparts[4];
theta3=thetaparts[5]*thetaparts[6];
theta=acos(theta1+theta2+theta3);
if (theta<0)
{
    theta=pi+theta;
}
Escatter2=Esource/(1+((Esource/511)*(1-cos(theta))));
Edeposit2=(Esource-Escatter2);
r2=sqrt(pow((scatterx-sx),2)+pow((scattery-sy),2)+pow((scatterz-sz),2));
storetheta2=theta;
cs=cos(storetheta1);
cs2=pow(cs,2);
sig1=pow(r0,2)/(pow((1+alpha*(1-cs)),3));
sig2=(1+cs2)/2;
sig3=pow(alpha,2)*pow((1-cs),2);
sig4=(1+cs2)*(1+alpha*(1-cs));
sig=sig1*sig2*(1+(sig3/sig4))*(1/sin(storetheta1))*(1*(pow(r1,2)));
//cout << storetheta1 << "\t" << sin(storetheta1) << endl;
probtheta1=sig/totsig1;

cs=cos(storetheta2);
cs2=pow(cs,2);
sig1=pow(r0,2)/(pow((1+alpha*(1-cs)),3));
sig2=(1+cs2)/2;
sig3=pow(alpha,2)*pow((1-cs),2);
sig4=(1+cs2)*(1+alpha*(1-cs));

sig=sig1*sig2*(1+(sig3/sig4))*(1/sin(storetheta2))*(1*pow(r2,2));
//cout << storetheta2 << "\t" << sin(storetheta2) << endl;
probtheta2=sig/totsig2;

FWHM=80;
sigma=FWHM/(2*(sqrt(2*log(2))));

meanscatter1 = ((meanscatter1*particles)+Escatter1)/(particles+1);
meandeposit1 = ((meandeposit1*particles)+Edeposit1)/(particles+1);
meanscatter2 = ((meanscatter2*particles)+Escatter2)/(particles+1);
meandeposit2 = ((meandeposit2*particles)+Edeposit2)/(particles+1);
randEs1=((rand()/32767.)*160)-80;
randEd1=((rand()/32767.)*160)-80;
randEs2=((rand()/32767.)*160)-80;
randEd2=((rand()/32767.)*160)-80;

probEs1=(1/(sigma*(sqrt(2*pi))))*(exp(-1*(pow(((Escatter1+randEs1)
        -meanscatter1),2)/(2*pow(sigma,2)))));
probEd1=(1/(sigma*(sqrt(2*pi))))*(exp(-1*(pow(((Edeposit1+randEd1)
        -meandeposit1),2)/(2*pow(sigma,2)))));
probEs2=(1/(sigma*(sqrt(2*pi))))*(exp(-1*(pow(((Escatter2+randEs2)
        -meanscatter2),2)/(2*pow(sigma,2)))));
probEd2=(1/(sigma*(sqrt(2*pi))))*(exp(-1*(pow(((Edeposit2+randEd2)

```

```

-meandeposit2),2)/(2*pow(sigma,2))));

Escatter1=(Escatter1+randEs1);
Edeposit1=(Edeposit1+randEd1);
Escatter2=(Escatter2+randEs2);
Edeposit2=(Edeposit2+randEd2);
for (step=0;step<=Esource;step++)
{
    if ((Escatter1>=step)&&(Escatter1<step+1))
    {
        countscatter1[step]=countscatter1[step]+int(1000*pow(steplim,6)
            *probtheta1*probEs1);
    }
    if ((Edeposit1>=step)&&(Edeposit1<step+1))
    {
        countdeposit1[step]=countdeposit1[step]+int(1000*pow(steplim,6)
            *probtheta1*probEd1);
    }
    if ((Escatter2>=step)&&(Escatter2<step+1))
    {
        countscatter2[step]=countscatter2[step]+int(1000*pow(steplim,6)
            *probtheta2*probEs2);
    }
    if ((Edeposit2>=step)&&(Edeposit2<step+1))
    {
        countdeposit2[step]=countdeposit2[step]+int(1000*pow(steplim,6)
            *probtheta2*probEd2);
    }
}
}
}
}
}

out << "Energy" << "\t" << j << "\t" << i << "\t"
    << "deposit during scatter " << i;
out << "\t" << "deposit at end of track " << j << "\t"
    << "deposit during scatter";
out << j << "\t";
out << "deposit at end of track" << i << endl;

for (step=0;step<=Esource;step++)
{
    out << step << "\t";
    out << countscatter1[step]+countdeposit2[step];
    out << "\t" << countdeposit1[step]+countscatter2[step] << "\t";
    out << countdeposit1[step] << "\t" << countscatter1[step]
        << "\t";
    out << countdeposit2[step] << "\t" << countscatter2[step]
        << endl;
}
cout << "mintheta1 " << mintheta1 << " maxtheta1 " << maxtheta1
    << endl;
cout << "mintheta2 " << mintheta2 << " maxtheta2 " << maxtheta2
    << endl;
}

```

Appendix E – Geant4 Simulation of Compton Scattering

The Geant4 simulation used was a modified version of example N02 as distributed with Geant4.9.2p01. The modified files are given below along with some additional comments to indicate the major changes.

The bulk of these changes were implemented to stop Geant4 writing to the display (and so speed up the program). In addition, much of the information was written out to a file that could be analysed afterwards. Finally, ExN02DetectorConstruction.cc was modified to ‘create’ the two detectors and allow their dimensions and other parameters to be modified. ExN02PrimaryGeneratorAction.cc was also modified to change the default beam of particles from a pencil beam to a broad beam which was incident upon the entire face of the detector.

In addition to the source code for the Geant4 simulation, an example of an output file, copies of the visualisation file and an analysis program are also given.

ExN02DetectorConstruction.cc

```
//  
// Code modified by S. Spencer 7th May 2010  
//  
// *****  
// * License and Disclaimer  
// *  
// * The Geant4 software is copyright of the Copyright Holders of *  
// * the Geant4 Collaboration. It is provided under the terms and *  
// * conditions of the Geant4 Software License, included in the file *  
// * LICENSE and available at http://cern.ch/geant4/license . These *  
// * include a list of copyright holders.  
// *  
// * Neither the authors of this software system, nor their employing *  
// * institutes, nor the agencies providing financial support for this *  
// * work make any representation or warranty, express or implied, *  
// * regarding this software system or assume any liability for its *  
// * use. Please see the license in the file LICENSE and URL above *  
// * for the full disclaimer and the limitation of liability.  
// *  
// * This code implementation is the result of the scientific and *  
// * technical work of the GEANT4 collaboration.  
// * By using, copying, modifying or distributing the software (or *  
// * any work based on the software) you agree to acknowledge its *  
// * use in resulting scientific publications, and indicate your *  
// * acceptance of all terms of the Geant4 Software license.  
// *****  
//  
//  
// $Id: ExN02DetectorConstruction.cc,v 1.21 2008/09/22 16:41:20 maire Exp $  
// GEANT4 tag $Name: geant4-09-02 $  
//  
  
#include "ExN02DetectorConstruction.hh"  
#include "ExN02DetectorMessenger.hh"  
#include "ExN02ChamberParameterisation.hh"  
#include "ExN02MagneticField.hh"  
#include "ExN02TrackerSD.hh"  
  
#include "G4Material.hh"  
#include "G4Box.hh"  
#include "G4LogicalVolume.hh"  
#include "G4PVPlacement.hh"  
#include "G4PVPParameterised.hh"  
#include "G4SDManager.hh"  
#include "G4GeometryTolerance.hh"  
#include "G4GeometryManager.hh"  
  
#include "G4UserLimits.hh"  
  
#include "G4VisAttributes.hh"  
#include "G4Colour.hh"  
  
#include "G4ios.hh"  
  
//....ooo00000ooo.....ooo000000ooo.....ooo00000ooo.....ooo00000ooo
```

```

ExN02DetectorConstruction::ExN02DetectorConstruction()
:solidWorld(0), logicWorld(0), physiWorld(0),
:solidTarget(0), logicTarget(0), physiTarget(0),
:solidTracker(0), logicTracker(0), physiTracker(0),
:solidChamber(0), logicChamber(0), physiChamber(0),
:TargetMater(0), ChamberMater(0), chamberParam(0),
:stepLimit(0), fpMagField(0),
:fWorldLength(0.), fTargetLength(0.), fTrackerLength(0.),
:NbOfChambers(0), ChamberWidth(0.), ChamberSpacing(0.)
{
    fpMagField = new ExN02MagneticField();
    DetectorMessenger = new ExN02DetectorMessenger(this);
}

//....ooo00000ooo.....ooo00000ooo.....ooo00000ooo.....ooo00000ooo

ExN02DetectorConstruction::~ExN02DetectorConstruction()
{
    delete fpMagField;
    delete stepLimit;
    delete chamberParam;
    delete DetectorMessenger;
}

//....ooo00000ooo.....ooo00000ooo.....ooo00000ooo.....ooo00000ooo

G4VPhysicalVolume* ExN02DetectorConstruction::Construct()
{
//----- Material definition -----
    G4double a, z;
    G4double density, temperature, pressure;
    G4int nel;

    //Air
    G4Element* N = new G4Element("Nitrogen", "N", z=7., a= 14.01*g/mole);
    G4Element* O = new G4Element("Oxygen" , "O", z=8., a= 16.00*g/mole);

    G4Material* Air = new G4Material("Air", density= 1.29*mg/cm3, nel=2);
    Air->AddElement(N, 70*perCent);
    Air->AddElement(O, 30*perCent);

    //Lead
    G4Material* Pb =
        new G4Material("Lead", z=82., a= 207.19*g/mole, density= 11.35*g/cm3);

    //Xenon gas
    G4Material* Xenon =
        new G4Material("XenonGas", z=54., a=131.29*g/mole, density= 5.458*mg/cm3,
                      kStateGas, temperature= 293.15*kelvin, pressure= 1*atmosphere);

    //Germanium - Added to allow simulation of germanium Detectors
    G4Material* Ge = new G4Material("Germanium", z=32., a=72.59*g/mole,
                                    density=5.323*g/cm3);

    //CZT - Added to allow simulation of CZT Detectors
    G4Element* Cd = new G4Element("Cadmium" , "Cd", z=48., a=112.41*g/mole);
    G4Element* Zn = new G4Element("Zinc"      , "Zn", z=30., a=65.38*g/mole);
}

```

```

G4Element* Te = new G4Element("Tellurium", "Te", z=52., a=127.60*g/mole);
G4Material* CZT = new G4Material("CZT", density=5.8*g/cm3, nel=3);
CZT->AddElement(Cd, 48*perCent);
CZT->AddElement(Zn, 02*perCent);
CZT->AddElement(Se, 50*perCent);

// Print all the materials defined.
G4cout << G4endl << "The materials defined are : " << G4endl << G4endl;
G4cout << *(G4Material::GetMaterialTable()) << G4endl;

//----- Sizes of the principal geometrical components (solids) -----
// Section modified to suit experimental layout
NbOfChambers = 4;
ChamberWidth = 1.50*mm;
ChamberSpacing = 1.60*mm;

fTrackerLength = (NbOfChambers)*ChamberSpacing; // Full length of Tracker
fTargetLength = 0.0001 * mm; // Full length of Target

TargetMater = Air;
ChamberMater = CZT;

fWorldLength= 20.2 *(fTargetLength+fTrackerLength);

G4double targetSize = 0.5*fTargetLength; //Half length of the Target
G4double trackerSize = 0.5*fTrackerLength; //Half length of the Tracker

//----- Definitions of Solids, Logical Volumes, Physical Volumes -----
//-----
// World
//-----

G4double HalfWorldLength = 0.5*fWorldLength;

G4GeometryManager::GetInstance()->SetWorldMaximumExtent(fWorldLength);
G4cout << "Computed tolerance = "
      << G4GeometryTolerance::GetInstance()->GetSurfaceTolerance()/mm
      << " mm" << G4endl;

solidWorld= new G4Box("world",HalfWorldLength,HalfWorldLength,
                      HalfWorldLength);
logicWorld= new G4LogicalVolume( solidWorld, Air, "World", 0, 0, 0);

// Must place the World Physical volume unrotated at (0,0,0).
//
physiWorld = new G4PVPlacement(0, // no rotation
                               G4ThreeVector(), // at (0,0,0)
                               logicWorld, // its logical volume
                               "World", // its name
                               0, // its mother volume
                               false, // no boolean operations
                               0); // copy number

//-----
// Detectors
//-----
// Existing Detectors removed and replaced

```

```

G4double D1X=0; // Defines central location of Detector 1
G4double D1Y=0;
G4double D1Z=-10;

G4double D2X=-6.4; // Defines central location of Detector 2
G4double D2Y=0;
G4double D2Z=-3.6;

G4int D3X=0; // Defines location of Detector 3
G4int D3Y=0;
G4int D3Z=0;

G4double Height=3.5; // Defines Detector height - remember to divide by 2

G4cout << "D1 is located at " << D1X << " " << D1Y << " " << D1Z
      << G4endl << "D2 is located at " << D2X << " " << D2Y
      << " " << D2Z << G4endl;

// Position pixels around Detector location
G4ThreeVector positionChamber11 = G4ThreeVector(D1X-2.4,D1Y,D1Z-2.4);
G4ThreeVector positionChamber12 = G4ThreeVector(D1X-2.4,D1Y,D1Z-0.8);
G4ThreeVector positionChamber13 = G4ThreeVector(D1X-2.4,D1Y,D1Z+0.8);
G4ThreeVector positionChamber14 = G4ThreeVector(D1X-2.4,D1Y,D1Z+2.4);
G4ThreeVector positionChamber15 = G4ThreeVector(D1X-0.8,D1Y,D1Z-2.4);
G4ThreeVector positionChamber16 = G4ThreeVector(D1X-0.8,D1Y,D1Z-0.8);
G4ThreeVector positionChamber17 = G4ThreeVector(D1X-0.8,D1Y,D1Z+0.8);
G4ThreeVector positionChamber18 = G4ThreeVector(D1X-0.8,D1Y,D1Z+2.4);
G4ThreeVector positionChamber19 = G4ThreeVector(D1X+0.8,D1Y,D1Z-2.4);
G4ThreeVector positionChamber110= G4ThreeVector(D1X+0.8,D1Y,D1Z-0.8);
G4ThreeVector positionChamber111= G4ThreeVector(D1X+0.8,D1Y,D1Z+0.8);
G4ThreeVector positionChamber112= G4ThreeVector(D1X+0.8,D1Y,D1Z+2.4);
G4ThreeVector positionChamber113= G4ThreeVector(D1X+2.4,D1Y,D1Z-2.4);
G4ThreeVector positionChamber114= G4ThreeVector(D1X+2.4,D1Y,D1Z-0.8);
G4ThreeVector positionChamber115= G4ThreeVector(D1X+2.4,D1Y,D1Z+0.8);
G4ThreeVector positionChamber116= G4ThreeVector(D1X+2.4,D1Y,D1Z+2.4);

G4ThreeVector positionChamber21 = G4ThreeVector(D2X-2.4,D2Y,D2Z-2.4);
G4ThreeVector positionChamber22 = G4ThreeVector(D2X-2.4,D2Y,D2Z-0.8);
G4ThreeVector positionChamber23 = G4ThreeVector(D2X-2.4,D2Y,D2Z+0.8);
G4ThreeVector positionChamber24 = G4ThreeVector(D2X-2.4,D2Y,D2Z+2.4);
G4ThreeVector positionChamber25 = G4ThreeVector(D2X-0.8,D2Y,D2Z-2.4);
G4ThreeVector positionChamber26 = G4ThreeVector(D2X-0.8,D2Y,D2Z-0.8);
G4ThreeVector positionChamber27 = G4ThreeVector(D2X-0.8,D2Y,D2Z+0.8);
G4ThreeVector positionChamber28 = G4ThreeVector(D2X-0.8,D2Y,D2Z+2.4);
G4ThreeVector positionChamber29 = G4ThreeVector(D2X+0.8,D2Y,D2Z-2.4);
G4ThreeVector positionChamber210= G4ThreeVector(D2X+0.8,D2Y,D2Z-0.8);
G4ThreeVector positionChamber211= G4ThreeVector(D2X+0.8,D2Y,D2Z+0.8);
G4ThreeVector positionChamber212= G4ThreeVector(D2X+0.8,D2Y,D2Z+2.4);
G4ThreeVector positionChamber213= G4ThreeVector(D2X+2.4,D2Y,D2Z-2.4);
G4ThreeVector positionChamber214= G4ThreeVector(D2X+2.4,D2Y,D2Z-0.8);
G4ThreeVector positionChamber215= G4ThreeVector(D2X+2.4,D2Y,D2Z+0.8);
G4ThreeVector positionChamber216= G4ThreeVector(D2X+2.4,D2Y,D2Z+2.4);

// Defines size of pixel chambers
G4Box* solidChamber11 = new G4Box("chamber11",0.8*mm,Height,0.8*mm);
G4Box* solidChamber12 = new G4Box("chamber12",0.8*mm,Height,0.8*mm);
G4Box* solidChamber13 = new G4Box("chamber13",0.8*mm,Height,0.8*mm);

```

```

G4Box* solidChamber14 = new G4Box("chamber14", 0.8*mm, Height, 0.8*mm);
G4Box* solidChamber15 = new G4Box("chamber15", 0.8*mm, Height, 0.8*mm);
G4Box* solidChamber16 = new G4Box("chamber16", 0.8*mm, Height, 0.8*mm);
G4Box* solidChamber17 = new G4Box("chamber17", 0.8*mm, Height, 0.8*mm);
G4Box* solidChamber18 = new G4Box("chamber18", 0.8*mm, Height, 0.8*mm);
G4Box* solidChamber19 = new G4Box("chamber19", 0.8*mm, Height, 0.8*mm);
G4Box* solidChamber110= new G4Box("chamber110", 0.8*mm, Height, 0.8*mm);
G4Box* solidChamber111= new G4Box("chamber111", 0.8*mm, Height, 0.8*mm);
G4Box* solidChamber112= new G4Box("chamber112", 0.8*mm, Height, 0.8*mm);
G4Box* solidChamber113= new G4Box("chamber113", 0.8*mm, Height, 0.8*mm);
G4Box* solidChamber114= new G4Box("chamber114", 0.8*mm, Height, 0.8*mm);
G4Box* solidChamber115= new G4Box("chamber115", 0.8*mm, Height, 0.8*mm);
G4Box* solidChamber116= new G4Box("chamber116", 0.8*mm, Height, 0.8*mm);

G4Box* solidChamber21 = new G4Box("chamber21", 0.8*mm, Height, 0.8*mm);
G4Box* solidChamber22 = new G4Box("chamber22", 0.8*mm, Height, 0.8*mm);
G4Box* solidChamber23 = new G4Box("chamber23", 0.8*mm, Height, 0.8*mm);
G4Box* solidChamber24 = new G4Box("chamber24", 0.8*mm, Height, 0.8*mm);
G4Box* solidChamber25 = new G4Box("chamber25", 0.8*mm, Height, 0.8*mm);
G4Box* solidChamber26 = new G4Box("chamber26", 0.8*mm, Height, 0.8*mm);
G4Box* solidChamber27 = new G4Box("chamber27", 0.8*mm, Height, 0.8*mm);
G4Box* solidChamber28 = new G4Box("chamber28", 0.8*mm, Height, 0.8*mm);
G4Box* solidChamber29 = new G4Box("chamber29", 0.8*mm, Height, 0.8*mm);
G4Box* solidChamber210= new G4Box("chamber210", 0.8*mm, Height, 0.8*mm);
G4Box* solidChamber211= new G4Box("chamber211", 0.8*mm, Height, 0.8*mm);
G4Box* solidChamber212= new G4Box("chamber212", 0.8*mm, Height, 0.8*mm);
G4Box* solidChamber213= new G4Box("chamber213", 0.8*mm, Height, 0.8*mm);
G4Box* solidChamber214= new G4Box("chamber214", 0.8*mm, Height, 0.8*mm);
G4Box* solidChamber215= new G4Box("chamber215", 0.8*mm, Height, 0.8*mm);
G4Box* solidChamber216= new G4Box("chamber216", 0.8*mm, Height, 0.8*mm);

// Defines chamber name
G4LogicalVolume* logicChamber11 = new G4LogicalVolume(solidChamber11,
                                                       ChamberMater,"1 1",0,0,0);
G4LogicalVolume* logicChamber12 = new G4LogicalVolume(solidChamber12,
                                                       ChamberMater,"1 2",0,0,0);
G4LogicalVolume* logicChamber13 = new G4LogicalVolume(solidChamber13,
                                                       ChamberMater,"1 3",0,0,0);
G4LogicalVolume* logicChamber14 = new G4LogicalVolume(solidChamber14,
                                                       ChamberMater,"1 4",0,0,0);
G4LogicalVolume* logicChamber15 = new G4LogicalVolume(solidChamber15,
                                                       ChamberMater,"1 5",0,0,0);
G4LogicalVolume* logicChamber16 = new G4LogicalVolume(solidChamber16,
                                                       ChamberMater,"1 6",0,0,0);
G4LogicalVolume* logicChamber17 = new G4LogicalVolume(solidChamber17,
                                                       ChamberMater,"1 7",0,0,0);
G4LogicalVolume* logicChamber18 = new G4LogicalVolume(solidChamber18,
                                                       ChamberMater,"1 8",0,0,0);
G4LogicalVolume* logicChamber19 = new G4LogicalVolume(solidChamber19,
                                                       ChamberMater,"1 9",0,0,0);
G4LogicalVolume* logicChamber110= new G4LogicalVolume(solidChamber110,
                                                       ChamberMater,"1 10",0,0,0);
G4LogicalVolume* logicChamber111= new G4LogicalVolume(solidChamber111,
                                                       ChamberMater,"1 11",0,0,0);
G4LogicalVolume* logicChamber112= new G4LogicalVolume(solidChamber112,
                                                       ChamberMater,"1 12",0,0,0);
G4LogicalVolume* logicChamber113= new G4LogicalVolume(solidChamber113,
                                                       ChamberMater,"1 13",0,0,0);
G4LogicalVolume* logicChamber114= new G4LogicalVolume(solidChamber114,
                                                       ChamberMater,"1 14",0,0,0);

```

```

ChamberMater,"1 14",0,0,0);
G4LogicalVolume* logicChamber115= new G4LogicalVolume(solidChamber115,
ChamberMater,"1 15",0,0,0);
G4LogicalVolume* logicChamber116= new G4LogicalVolume(solidChamber116,
ChamberMater,"1 16",0,0,0);

G4LogicalVolume* logicChamber21 = new G4LogicalVolume(solidChamber21,
ChamberMater,"2 1",0,0,0);
G4LogicalVolume* logicChamber22 = new G4LogicalVolume(solidChamber22,
ChamberMater,"2 2",0,0,0);
G4LogicalVolume* logicChamber23 = new G4LogicalVolume(solidChamber23,
ChamberMater,"2 3",0,0,0);
G4LogicalVolume* logicChamber24 = new G4LogicalVolume(solidChamber24,
ChamberMater,"2 4",0,0,0);
G4LogicalVolume* logicChamber25 = new G4LogicalVolume(solidChamber25,
ChamberMater,"2 5",0,0,0);
G4LogicalVolume* logicChamber26 = new G4LogicalVolume(solidChamber26,
ChamberMater,"2 6",0,0,0);
G4LogicalVolume* logicChamber27 = new G4LogicalVolume(solidChamber27,
ChamberMater,"2 7",0,0,0);
G4LogicalVolume* logicChamber28 = new G4LogicalVolume(solidChamber28,
ChamberMater,"2 8",0,0,0);
G4LogicalVolume* logicChamber29 = new G4LogicalVolume(solidChamber29,
ChamberMater,"2 9",0,0,0);
G4LogicalVolume* logicChamber210= new G4LogicalVolume(solidChamber210,
ChamberMater,"2 10",0,0,0);
G4LogicalVolume* logicChamber211= new G4LogicalVolume(solidChamber211,
ChamberMater,"2 11",0,0,0);
G4LogicalVolume* logicChamber212= new G4LogicalVolume(solidChamber212,
ChamberMater,"2 12",0,0,0);
G4LogicalVolume* logicChamber213= new G4LogicalVolume(solidChamber213,
ChamberMater,"2 13",0,0,0);
G4LogicalVolume* logicChamber214= new G4LogicalVolume(solidChamber214,
ChamberMater,"2 14",0,0,0);
G4LogicalVolume* logicChamber215= new G4LogicalVolume(solidChamber215,
ChamberMater,"2 15",0,0,0);
G4LogicalVolume* logicChamber216= new G4LogicalVolume(solidChamber216,
ChamberMater,"2 16",0,0,0);

// Place chambers in location
G4VPhysicalVolume* physiChamber11 = new G4PVPlacement(0,
positionChamber11,logicChamber11,"1 1",logicWorld,false,0);
G4VPhysicalVolume* physiChamber12 = new G4PVPlacement(0,
positionChamber12,logicChamber12,"1 2",logicWorld,false,0);
G4VPhysicalVolume* physiChamber13 = new G4PVPlacement(0,
positionChamber13,logicChamber13,"1 3",logicWorld,false,0);
G4VPhysicalVolume* physiChamber14 = new G4PVPlacement(0,
positionChamber14,logicChamber14,"1 4",logicWorld,false,0);
G4VPhysicalVolume* physiChamber15 = new G4PVPlacement(0,
positionChamber15,logicChamber15,"1 5",logicWorld,false,0);
G4VPhysicalVolume* physiChamber16 = new G4PVPlacement(0,
positionChamber16,logicChamber16,"1 6",logicWorld,false,0);
G4VPhysicalVolume* physiChamber17 = new G4PVPlacement(0,
positionChamber17,logicChamber17,"1 7",logicWorld,false,0);
G4VPhysicalVolume* physiChamber18 = new G4PVPlacement(0,
positionChamber18,logicChamber18,"1 8",logicWorld,false,0);
G4VPhysicalVolume* physiChamber19 = new G4PVPlacement(0,
positionChamber19,logicChamber19,"1 9",logicWorld,false,0);
G4VPhysicalVolume* physiChamber110= new G4PVPlacement(0,

```

```

        positionChamber110,logicChamber110,"1 10",logicWorld,false,0);
G4VPhysicalVolume* physiChamber111= new G4PVPlacement(0,
    positionChamber111,logicChamber111,"1 11",logicWorld,false,0);
G4VPhysicalVolume* physiChamber112= new G4PVPlacement(0,
    positionChamber112,logicChamber112,"1 12",logicWorld,false,0);
G4VPhysicalVolume* physiChamber113= new G4PVPlacement(0,
    positionChamber113,logicChamber113,"1 13",logicWorld,false,0);
G4VPhysicalVolume* physiChamber114= new G4PVPlacement(0,
    positionChamber114,logicChamber114,"1 14",logicWorld,false,0);
G4VPhysicalVolume* physiChamber115= new G4PVPlacement(0,
    positionChamber115,logicChamber115,"1 15",logicWorld,false,0);
G4VPhysicalVolume* physiChamber116= new G4PVPlacement(0,
    positionChamber116,logicChamber116,"1 16",logicWorld,false,0);

G4VPhysicalVolume* physiChamber21 = new G4PVPlacement(0,
    positionChamber21,logicChamber21,"2 1",logicWorld,false,0);
G4VPhysicalVolume* physiChamber22 = new G4PVPlacement(0,
    positionChamber22,logicChamber22,"2 2",logicWorld,false,0);
G4VPhysicalVolume* physiChamber23 = new G4PVPlacement(0,
    positionChamber23,logicChamber23,"2 3",logicWorld,false,0);
G4VPhysicalVolume* physiChamber24 = new G4PVPlacement(0,
    positionChamber24,logicChamber24,"2 4",logicWorld,false,0);
G4VPhysicalVolume* physiChamber25 = new G4PVPlacement(0,
    positionChamber25,logicChamber25,"2 5",logicWorld,false,0);
G4VPhysicalVolume* physiChamber26 = new G4PVPlacement(0,
    positionChamber26,logicChamber26,"2 6",logicWorld,false,0);
G4VPhysicalVolume* physiChamber27 = new G4PVPlacement(0,
    positionChamber27,logicChamber27,"2 7",logicWorld,false,0);
G4VPhysicalVolume* physiChamber28 = new G4PVPlacement(0,
    positionChamber28,logicChamber28,"2 8",logicWorld,false,0);
G4VPhysicalVolume* physiChamber29 = new G4PVPlacement(0,
    positionChamber29,logicChamber29,"2 9",logicWorld,false,0);
G4VPhysicalVolume* physiChamber210= new G4PVPlacement(0,
    positionChamber210,logicChamber210,"2 10",logicWorld,false,0);
G4VPhysicalVolume* physiChamber211= new G4PVPlacement(0,
    positionChamber211,logicChamber211,"2 11",logicWorld,false,0);
G4VPhysicalVolume* physiChamber212= new G4PVPlacement(0,
    positionChamber212,logicChamber212,"2 12",logicWorld,false,0);
G4VPhysicalVolume* physiChamber213= new G4PVPlacement(0,
    positionChamber213,logicChamber213,"2 13",logicWorld,false,0);
G4VPhysicalVolume* physiChamber214= new G4PVPlacement(0,
    positionChamber214,logicChamber214,"2 14",logicWorld,false,0);
G4VPhysicalVolume* physiChamber215= new G4PVPlacement(0,
    positionChamber215,logicChamber215,"2 15",logicWorld,false,0);
G4VPhysicalVolume* physiChamber216= new G4PVPlacement(0,
    positionChamber216,logicChamber216,"2 16",logicWorld,false,0);

G4cout << "There are " << NbOfChambers
<< " chambers in the tracker region. "
<< "The chambers are " << ChamberWidth/mm << " mm of "
<< ChamberMater->GetName() <<"\n The distance between chamber is "
<< ChamberSpacing/cm << " cm" << G4endl;

//-----
// Sensitive Detectors
//-----
G4cout << "Sensitive Detector" << G4endl;

```

```

G4SDManager* SDman = G4SDManager::GetSDMpointer();
G4String trackerChamberSDname = "ExN02/TrackerChamberSD";

ExN02TrackerSD* aTrackerSD = new ExN02TrackerSD( trackerChamberSDname );

SDman->AddNewDetector( aTrackerSD );

logicWorld->SetSensitiveDetector( aTrackerSD );

logicChamber11->SetSensitiveDetector( aTrackerSD );
logicChamber12->SetSensitiveDetector( aTrackerSD );
logicChamber13->SetSensitiveDetector( aTrackerSD );
logicChamber14->SetSensitiveDetector( aTrackerSD );
logicChamber15->SetSensitiveDetector( aTrackerSD );
logicChamber16->SetSensitiveDetector( aTrackerSD );
logicChamber17->SetSensitiveDetector( aTrackerSD );
logicChamber18->SetSensitiveDetector( aTrackerSD );
logicChamber19->SetSensitiveDetector( aTrackerSD );
logicChamber110->SetSensitiveDetector( aTrackerSD );
logicChamber111->SetSensitiveDetector( aTrackerSD );
logicChamber112->SetSensitiveDetector( aTrackerSD );
logicChamber113->SetSensitiveDetector( aTrackerSD );
logicChamber114->SetSensitiveDetector( aTrackerSD );
logicChamber115->SetSensitiveDetector( aTrackerSD );
logicChamber116->SetSensitiveDetector( aTrackerSD );

G4cout << "Sensitive Detectors Initialized" << G4endl;
//----- Visualization attributes -----
G4cout << "Visualization" << G4endl;
G4VisAttributes* BoxVisAtt= new G4VisAttributes(G4Colour(1.0,1.0,1.0));

G4VisAttributes* ChamberVisAtt = new G4VisAttributes(G4Colour(0.0,
                           0.0,0.0));
logicWorld->SetVisAttributes(ChamberVisAtt);

logicChamber11->SetVisAttributes(ChamberVisAtt);
logicChamber12->SetVisAttributes(ChamberVisAtt);
logicChamber13->SetVisAttributes(ChamberVisAtt);
logicChamber14->SetVisAttributes(ChamberVisAtt);
logicChamber15->SetVisAttributes(ChamberVisAtt);
logicChamber16->SetVisAttributes(ChamberVisAtt);
logicChamber17->SetVisAttributes(ChamberVisAtt);
logicChamber18->SetVisAttributes(ChamberVisAtt);
logicChamber19->SetVisAttributes(ChamberVisAtt);
logicChamber110->SetVisAttributes(ChamberVisAtt);
logicChamber111->SetVisAttributes(ChamberVisAtt);
logicChamber112->SetVisAttributes(ChamberVisAtt);
logicChamber113->SetVisAttributes(ChamberVisAtt);
logicChamber114->SetVisAttributes(ChamberVisAtt);
logicChamber115->SetVisAttributes(ChamberVisAtt);
logicChamber116->SetVisAttributes(ChamberVisAtt);
logicChamber21->SetVisAttributes(ChamberVisAtt);
logicChamber22->SetVisAttributes(ChamberVisAtt);
logicChamber23->SetVisAttributes(ChamberVisAtt);
logicChamber24->SetVisAttributes(ChamberVisAtt);
logicChamber25->SetVisAttributes(ChamberVisAtt);
logicChamber26->SetVisAttributes(ChamberVisAtt);
logicChamber27->SetVisAttributes(ChamberVisAtt);

```

```

logicChamber28->SetVisAttributes(ChamberVisAtt);
logicChamber29->SetVisAttributes(ChamberVisAtt);
logicChamber210->SetVisAttributes(ChamberVisAtt);
logicChamber211->SetVisAttributes(ChamberVisAtt);
logicChamber212->SetVisAttributses(ChamberVisAtt);
logicChamber213->SetVisAttributes(ChamberVisAtt);
logicChamber214->SetVisAttributes(ChamberVisAtt);
logicChamber215->SetVisAttributes(ChamberVisAtt);
logicChamber216->SetVisAttributes(ChamberVisAtt);

    return physiWorld;
}

//....ooo00000ooo.....ooo00000ooo.....ooo00000ooo.....ooo00000ooo

void ExN02DetectorConstruction::setTargetMaterial(G4String materialName)
{
    // search the material by its name
    G4Material* pttoMaterial = G4Material::GetMaterial(materialName);
    if (pttoMaterial)
        {TargetMater = pttoMaterial;
        logicTarget->SetMaterial(pttoMaterial);
        G4cout << "\n----> The target is " << fTargetLength/cm << " cm of "
            << materialName << G4endl;
        }
}

//....ooo00000ooo.....ooo00000ooo.....ooo00000ooo.....ooo00000ooo

void ExN02DetectorConstruction::setChamberMaterial(G4String materialName)
{
    // search the material by its name
    G4Material* pttoMaterial = G4Material::GetMaterial(materialName);
    if (pttoMaterial)
        {ChamberMater = pttoMaterial;
        logicChamber->SetMaterial(pttoMaterial);
        G4cout << "\n----> The chambers are " << ChamberWidth/cm << " cm of "
            << materialName << G4endl;
        }
}

//....ooo00000ooo.....ooo00000ooo.....ooo00000ooo.....ooo00000ooo

void ExN02DetectorConstruction::SetMagField(G4double fieldValue)
{
    fpMagField->SetFieldValue(fieldValue);
}

//....ooo00000ooo.....ooo00000ooo.....ooo00000ooo.....ooo00000ooo

void ExN02DetectorConstruction::SetMaxStep(G4double maxStep)
{
    if ((stepLimit)&&(maxStep>0.)) stepLimit->SetMaxAllowedStep(maxStep);
}

```

ExN02EventAction.cc

```
//  
// Code modified by S. Spencer 21st October 2009  
//  
// *****  
// * License and Disclaimer  
// *  
// * The Geant4 software is copyright of the Copyright Holders of *  
// * the Geant4 Collaboration. It is provided under the terms and *  
// * conditions of the Geant4 Software License, included in the file *  
// * LICENSE and available at http://cern.ch/geant4/license . These *  
// * include a list of copyright holders.  
// *  
// * Neither the authors of this software system, nor their employing *  
// * institutes, nor the agencies providing financial support for this *  
// * work make any representation or warranty, express or implied, *  
// * regarding this software system or assume any liability for its *  
// * use. Please see the license in the file LICENSE and URL above *  
// * for the full disclaimer and the limitation of liability.  
// *  
// * This code implementation is the result of the scientific and *  
// * technical work of the GEANT4 collaboration.  
// * By using, copying, modifying or distributing the software (or *  
// * any work based on the software) you agree to acknowledge its *  
// * use in resulting scientific publications, and indicate your *  
// * acceptance of all terms of the Geant4 Software license.  
// *****  
//  
//  
// $Id: ExN02EventAction.cc,v 1.11 2006/06/29 17:48:05 gunter Exp $  
// GEANT4 tag $Name: geant4-09-02 $  
//  
  
#include "ExN02EventAction.hh"  
  
#include "G4Event.hh"  
#include "G4EventManager.hh"  
#include "G4TrajectoryContainer.hh"  
#include "G4Trajectory.hh"  
#include "G4ios.hh"  
#include <fstream> // Included to allow filestream support  
#include <iostream>  
//....ooo00000ooo.....ooo000000ooo.....ooo00000ooo.....ooo00000ooo  
  
ExN02EventAction::ExN02EventAction()  
{ }  
  
//....ooo00000ooo.....ooo000000ooo.....ooo00000ooo.....ooo00000ooo  
  
ExN02EventAction::~ExN02EventAction()  
{ }  
  
//....ooo00000ooo.....ooo000000ooo.....ooo00000ooo.....ooo00000ooo  
  
void ExN02EventAction::BeginOfEventAction(const G4Event* evt)  
{  
// Modified to remove print to screen
```

```

G4int event_id = evt->GetEventID();
out.open ("output.csv",std::ios::out|std::ios::app);
out << " BOE " << evt->GetEventID() << G4endl;
out.close();
}

//....ooo00000ooo.....ooo00000ooo.....ooo00000ooo.....ooo00000ooo

void ExN02EventAction::EndOfEventAction(const G4Event* evt)
{
    G4int event_id = evt->GetEventID();

    // get number of stored trajectories
    //
    G4TrajectoryContainer* trajectoryContainer =
                                evt->GetTrajectoryContainer();
    G4int n_trajectories = 0;
    if (trajectoryContainer) n_trajectories = trajectoryContainer->entries();

    // periodic printing
    //
    // Modified to remove print to screen

    out.open ("output.csv",std::ios::out|std::ios::app);
    out << " EOE " << evt->GetEventID() << G4endl << G4endl;
    out.close();

    if (event_id < 100 || event_id%100 == 0) {
    }
}

```

ExN02PrimaryGeneratorAction.cc

```
//  
// Code modified by S. Spencer 28th April 2010  
//  
// *****  
// * License and Disclaimer  
// *  
// * The Geant4 software is copyright of the Copyright Holders of *  
// * the Geant4 Collaboration. It is provided under the terms and *  
// * conditions of the Geant4 Software License, included in the file *  
// * LICENSE and available at http://cern.ch/geant4/license . These *  
// * include a list of copyright holders.  
// *  
// * Neither the authors of this software system, nor their employing *  
// * institutes, nor the agencies providing financial support for this *  
// * work make any representation or warranty, express or implied, *  
// * regarding this software system or assume any liability for its *  
// * use. Please see the license in the file LICENSE and URL above *  
// * for the full disclaimer and the limitation of liability.  
// *  
// * This code implementation is the result of the scientific and *  
// * technical work of the GEANT4 collaboration.  
// * By using, copying, modifying or distributing the software (or *  
// * any work based on the software) you agree to acknowledge its *  
// * use in resulting scientific publications, and indicate your *  
// * acceptance of all terms of the Geant4 Software license.  
// *****  
//  
//  
// $Id: ExN02PrimaryGeneratorAction.cc,v 1.7 2006/06/29 17:48:13 gunter Exp  
$  
// GEANT4 tag $Name: geant4-09-02 $  
//  
  
#include "ExN02PrimaryGeneratorAction.hh"  
#include "ExN02DetectorConstruction.hh"  
  
#include "G4Event.hh"  
#include "G4ParticleGun.hh"  
#include "G4ParticleTable.hh"  
#include "G4ParticleDefinition.hh"  
#include "globals.hh"  
#include "randomize.hh" // Added to allow random numbers  
//....ooo00000ooo.....ooo00000ooo.....ooo00000ooo.....ooo00000ooo  
  
ExN02PrimaryGeneratorAction::ExN02PrimaryGeneratorAction(  
                                         ExN02DetectorConstruction* myDC):myDetector(myDC)  
{  
    G4int n_particle = 1;  
    particleGun = new G4ParticleGun(n_particle);  
  
    // default particle  
  
    G4ParticleTable* particleTable = G4ParticleTable::GetParticleTable();  
    G4ParticleDefinition* particle = particleTable->FindParticle("proton");  
  
    particleGun->SetParticleDefinition(particle);
```

```

particleGun->SetParticleMomentumDirection(G4ThreeVector(0.,0.,1.));
particleGun->SetParticleEnergy(0.6*MeV);
}

//....ooo00000ooo.....oooo00000ooo.....ooo00000ooo.....ooo00000ooo

ExN02PrimaryGeneratorAction::~ExN02PrimaryGeneratorAction()
{
    delete particleGun;
}

//....ooo00000ooo.....oooo00000ooo.....ooo00000ooo.....ooo00000ooo

void ExN02PrimaryGeneratorAction::GeneratePrimaries(G4Event* anEvent)
{
    G4double position = -0.5*(myDetector->GetWorldFullLength());
    particleGun->SetParticlePosition(G4ThreeVector(0.*cm,0.*cm,position));
    G4double zTheta = 1; // Modified to provide fixed z direction

    // x and y components to allow the particlegun vector to exclusively
    // enter the Detector.

    // For 4,4,5 Detector
    // G4double ux = (-0.197395559*0.2) + (0.2
    //                         *0.394791119*G4UniformRand());
    // G4double uy = (0.1397*-0.336674819*0.814285714) + (0.1397
    //                         *0.673349638*0.814285714*G4UniformRand());
    // G4double uz = zTheta;

    // For 6,4,6,4,7 Detector
    G4double ux = (0.184615384*-0.336674819) + (0.184615384
    *0.673349638*G4UniformRand());
    G4double uy = (0.181102362*-0.336674819) + (0.181102362
    *0.673349638*G4UniformRand());
    G4double uz = zTheta;

    particleGun ->SetParticleMomentumDirection(G4ThreeVector(ux,uy,uz));

    particleGun->GeneratePrimaryVertex(anEvent);
}

```

ExN02RunAction.cc

```
//  
// Code modified by S. Spencer 21st October 2009  
//  
// *****  
// * License and Disclaimer  
// *  
// * The Geant4 software is copyright of the Copyright Holders of *  
// * the Geant4 Collaboration. It is provided under the terms and *  
// * conditions of the Geant4 Software License, included in the file *  
// * LICENSE and available at http://cern.ch/geant4/license . These *  
// * include a list of copyright holders.  
// *  
// * Neither the authors of this software system, nor their employing *  
// * institutes, nor the agencies providing financial support for this *  
// * work make any representation or warranty, express or implied, *  
// * regarding this software system or assume any liability for its *  
// * use. Please see the license in the file LICENSE and URL above *  
// * for the full disclaimer and the limitation of liability.  
// *  
// * This code implementation is the result of the scientific and *  
// * technical work of the GEANT4 collaboration.  
// * By using, copying, modifying or distributing the software (or *  
// * any work based on the software) you agree to acknowledge its *  
// * use in resulting scientific publications, and indicate your *  
// * acceptance of all terms of the Geant4 Software license.  
// *****  
//  
//  
// $Id: ExN02RunAction.cc,v 1.9 2006/06/29 17:48:16 gunter Exp $  
// GEANT4 tag $Name: geant4-09-02 $  
//  
  
#include "ExN02RunAction.hh"  
  
#include "G4Run.hh"  
  
//....ooo00000ooo.....ooo000000ooo.....ooo00000ooo.....ooo00000ooo  
  
ExN02RunAction::ExN02RunAction()  
{ }  
  
//....ooo00000ooo.....ooo000000ooo.....ooo00000ooo.....ooo00000ooo  
  
ExN02RunAction::~ExN02RunAction()  
{ }  
  
//....ooo00000ooo.....ooo000000ooo.....ooo00000ooo.....ooo00000ooo  
  
void ExN02RunAction::BeginOfRunAction(const G4Run* aRun)  
// Print to screen removed  
{ }  
  
//....ooo00000ooo.....ooo000000ooo.....ooo00000ooo.....ooo00000ooo  
  
void ExN02RunAction::EndOfRunAction(const G4Run*)  
{ }
```

ExN02SteppingVerbose.cc

```
//  
// Code modified by S. Spencer 21st October 2009  
//  
// *****  
// * License and Disclaimer  
// *  
// * The Geant4 software is copyright of the Copyright Holders of *  
// * the Geant4 Collaboration. It is provided under the terms and *  
// * conditions of the Geant4 Software License, included in the file *  
// * LICENSE and available at http://cern.ch/geant4/license . These *  
// * include a list of copyright holders.  
// *  
// * Neither the authors of this software system, nor their employing *  
// * institutes, nor the agencies providing financial support for this *  
// * work make any representation or warranty, express or implied, *  
// * regarding this software system or assume any liability for its *  
// * use. Please see the license in the file LICENSE and URL above *  
// * for the full disclaimer and the limitation of liability.  
// *  
// * This code implementation is the result of the scientific and *  
// * technical work of the GEANT4 collaboration.  
// * By using, copying, modifying or distributing the software (or *  
// * any work based on the software) you agree to acknowledge its *  
// * use in resulting scientific publications, and indicate your *  
// * acceptance of all terms of the Geant4 Software license.  
// *****  
//  
//  
// $Id: ExN02SteppingVerbose.cc,v 1.12 2006/06/29 17:48:21 gunter Exp $  
// GEANT4 tag $Name: geant4-09-02 $  
//  
  
#include "ExN02SteppingVerbose.hh"  
  
#include "G4SteppingManager.hh"  
#include "G4UnitsTable.hh"  
#include <iostream> // Included to allow file streams  
#include <fstream>  
  
//....ooo00000ooo.....ooo000000ooo.....ooo00000ooo.....ooo00000ooo  
  
ExN02SteppingVerbose::ExN02SteppingVerbose()  
{ }  
  
//....ooo00000ooo.....ooo000000ooo.....ooo00000ooo.....ooo00000ooo  
  
ExN02SteppingVerbose::~ExN02SteppingVerbose()  
{ }  
  
//....ooo00000ooo.....ooo000000ooo.....ooo00000ooo.....ooo00000ooo  
  
void ExN02SteppingVerbose::StepInfo()  
{  
    CopyState();  
  
    G4int prec = G4cout.precision(3);
```

```

// Modified to print to file not screen
out.open ("output.csv",std::ios::out|std::ios::app);

if( verboseLevel >= 1 ){
    if( verboseLevel >= 4 ) VerboseTrack();
    if( verboseLevel >= 3 ){
        out << std::setw( 5 ) << "#Step#" << " "
            << std::setw( 6 ) << "X" << " "
            << std::setw( 6 ) << "Y" << " "
            << std::setw( 6 ) << "Z" << " "
            << std::setw( 9 ) << "KineE" << " "
            << std::setw( 9 ) << "dEStep" << " "
            << std::setw(10) << "StepLeng"
            << std::setw(10) << "TrakLeng"
            << std::setw(10) << "Volume" << " "
            << std::setw(10) << "Process" << G4endl;
    }
}

out << fTrack->GetCurrentStepNumber() << "\t"
    << std::setw(6) << fTrack->GetPosition().x() << "\t"
    << std::setw(6) << fTrack->GetPosition().y() << "\t"
    << std::setw(6) << fTrack->GetPosition().z() << "\t"
    << std::setw(6) << fTrack->GetKineticEnergy() << "\t"
    << std::setw(6) << fStep->GetTotalEnergyDeposit() << "\t"
    << std::setw(6) << fStep->GetStepLength() << "\t"
    << std::setw(6) << fTrack->GetTrackLength() << "\t";

if( fTrack->GetNextVolume() != 0 ) {
    out << std::setw(10) << fTrack->GetVolume()->GetName() << "\t";
} else {
    out << std::setw(10) << "OutOfWorld" << "\t";
}

if(fStep->GetPostStepPoint()->GetProcessDefinedStep() != NULL) {
    out << " "
        << std::setw(10) << fStep->GetPostStepPoint()
            ->GetProcessDefinedStep()->GetProcessName() << "\t";
} else {
    out << "    UserLimit" << "\t";
}
out << "eol" << G4endl;
out.close();

if( verboseLevel == 2 ){
    G4int tN2ndariesTot = fN2ndariesAtRestDoIt +
                            fN2ndariesAlongStepDoIt +
                            fN2ndariesPostStepDoIt;
    if(tN2ndariesTot>0){
        for(size_t lp1=(*fSecondary).size()-tN2ndariesTot;
            lp1<(*fSecondary).size(); lp1++){}}

    }
}

}
}

```

```

//....ooo00000ooo.....ooo00000ooo.....ooo00000ooo.....ooo00000ooo

void ExN02SteppingVerbose::TrackingStarted()
{
    CopyState();
    G4int prec = G4cout.precision(3);
    if( verboseLevel > 0 ){

        // Modified to print to file not screen
        out.open ("output.csv",std::ios::out|std::ios::app);

        out << " Track" << "\t" << fTrack->GetTrackID() << "\t"
            << "Parent" << "\t" << fTrack->GetParentID() << "\t" "eol" << G4endl;
        out << std::setw( 6 ) << " Step#" << "\t"
            << std::setw( 6 ) << "X" << "\t"
            << std::setw( 6 ) << "Y" << "\t"
            << std::setw( 6 ) << "Z" << "\t"
            << std::setw( 9 ) << "KineE" << "\t"
            << std::setw( 9 ) << "dEStep" << "\t"
            << std::setw(10) << "StepLeng" << "\t"
            << std::setw(10) << "TrakLeng" << "\t"
            << std::setw(10) << "Volume" << "\t"
            << std::setw(10) << "Process" << "\t" << "eol" << G4endl;

        out << fTrack->GetCurrentStepNumber()
            << std::setw(6) << "\t" << fTrack->GetPosition().x()
            << std::setw(6) << "\t" << fTrack->GetPosition().y()
            << std::setw(6) << "\t" << fTrack->GetPosition().z()
            << std::setw(6) << "\t" << fTrack->GetKineticEnergy()
            << std::setw(6) << "\t" << fStep->GetTotalEnergyDeposit()
            << std::setw(6) << "\t" << fStep->GetStepLength()
            << std::setw(6) << "\t" << fTrack->GetTrackLength();

        if(fTrack->GetNextVolume()){
            out << "\t" << std::setw(10) << fTrack->GetVolume()->GetName();
        } else {
            out << "\t" << std::setw(10) << "OutOfWorld";
        }
        out << "\t" << " initStep" << "\t" << "eol" << G4endl;
        out.close();
    }
}

```

ExN02EventAction.hh

```
//  
// Code modified by S. Spencer 21st October 2009  
//  
//  
// ****  
// * License and Disclaimer  
// *  
// * The Geant4 software is copyright of the Copyright Holders of *  
// * the Geant4 Collaboration. It is provided under the terms and *  
// * conditions of the Geant4 Software License, included in the file *  
// * LICENSE and available at http://cern.ch/geant4/license . These *  
// * include a list of copyright holders.  
// *  
// * Neither the authors of this software system, nor their employing *  
// * institutes, nor the agencies providing financial support for this *  
// * work make any representation or warranty, express or implied,  
// * regarding this software system or assume any liability for its *  
// * use. Please see the license in the file LICENSE and URL above *  
// * for the full disclaimer and the limitation of liability.  
// *  
// * This code implementation is the result of the scientific and *  
// * technical work of the GEANT4 collaboration.  
// * By using, copying, modifying or distributing the software (or *  
// * any work based on the software) you agree to acknowledge its *  
// * use in resulting scientific publications, and indicate your *  
// * acceptance of all terms of the Geant4 Software license.  
// ****  
//  
//  
// $Id: ExN02EventAction.hh,v 1.8 2006/06/29 17:47:35 gunter Exp $  
// GEANT4 tag $Name: geant4-09-02 $  
//  
  
#ifndef ExN02EventAction_h  
#define ExN02EventAction_h 1  
  
#include "G4UserEventAction.hh"  
#include <fstream> // Include filestream headers  
#include <iostream>  
  
class G4Event;  
  
//....ooo00000ooo.....ooo00000ooo.....ooo00000ooo.....ooo00000ooo  
  
class ExN02EventAction : public G4UserEventAction  
{  
public:  
    ExN02EventAction();  
    ~ExN02EventAction();  
  
public:  
    void BeginOfEventAction(const G4Event*);  
    void EndOfEventAction(const G4Event*);  
    std::ofstream out; // Allow use of output file streams  
};  
#endif
```

ExN02SteppingVerbose.hh

```
//  
// Code modified by S. Spencer 21st October 2009  
//  
// *****  
// * License and Disclaimer  
// *  
// * The Geant4 software is copyright of the Copyright Holders of *  
// * the Geant4 Collaboration. It is provided under the terms and *  
// * conditions of the Geant4 Software License, included in the file *  
// * LICENSE and available at http://cern.ch/geant4/license . These *  
// * include a list of copyright holders.  
// *  
// * Neither the authors of this software system, nor their employing *  
// * institutes, nor the agencies providing financial support for this *  
// * work make any representation or warranty, express or implied,  
// * regarding this software system or assume any liability for its *  
// * use. Please see the license in the file LICENSE and URL above *  
// * for the full disclaimer and the limitation of liability.  
// *  
// * This code implementation is the result of the scientific and *  
// * technical work of the GEANT4 collaboration.  
// * By using, copying, modifying or distributing the software (or *  
// * any work based on the software) you agree to acknowledge its *  
// * use in resulting scientific publications, and indicate your *  
// * acceptance of all terms of the Geant4 Software license.  
// *****  
//  
//  
// $Id: ExN02SteppingVerbose.hh,v 1.8 2006/06/29 17:47:50 gunter Exp $  
// GEANT4 tag $Name: geant4-09-02 $  
//  
// This class manages the verbose outputs in G4SteppingManager.  
// It inherits from G4SteppingVerbose.  
// It shows how to extract informations during the tracking  
// of a particle.  
  
class ExN02SteppingVerbose;  
  
#ifndef ExN02SteppingVerbose_h  
#define ExN02SteppingVerbose_h 1  
  
#include "G4SteppingVerbose.hh"  
#include <fstream> // Allow filestreams  
#include <iostream>  
//....ooo00000ooo.....ooo000000ooo.....ooo00000ooo.....ooo00000ooo  
  
class ExN02SteppingVerbose : public G4SteppingVerbose  
{  
public:  
  
    ExN02SteppingVerbose();  
    ~ExN02SteppingVerbose();  
    void StepInfo();  
    void TrackingStarted();  
    std::ofstream out; // Allow output filestream  
};  
#endif
```

Below is an example of an event from the output file from Geant4 – as the particle/photon moves through the system, it is tracked and wherever it interacts, the location and type of interaction are noted. ‘BOE’ and ‘EOE’ indicate the beginning and end of the event respectively, ‘eol’ indicates the end of a line. Other information is in the columns as given.

BOE 0										
Track	1	Parent	0	eol						
Step#	X	Y	Z	KinE	dEStep	StepLeng	TrakLeng	Volume	Process	eol
0	0.00	0.00	-64.64	0.66	0.00	0.00	0.00	World	initStep	eol
1	1.30	-1.91	-13.20	0.66	0.00	51.49	51.49	World	Transportation	eol
2	1.34	-1.97	-11.60	0.66	0.00	1.60	53.09	1 9	Transportation	eol
3	1.38	-2.03	-10.00	0.66	0.00	1.60	54.70	1 10	Transportation	eol
4	1.42	-2.08	-8.40	0.66	0.00	1.60	56.30	1 11	Transportation	eol
5	1.46	-2.14	-6.80	0.66	0.00	1.60	57.90	1 12	Transportation	eol
6	3.26	-4.79	64.64	0.66	0.00	71.51	129.41	OutOfWorld	Transportation	eol
EOE 0										

Table 16 - example of output file from Geant4 simulation measured using a 662 keV photon within a $1.6 \times 1.6 \times 7$ mm³ detector.

A macro was used to demonstrate that the program was operating correctly, by showing the detector from a series of angles and running for 100 events at each angle.

vis.mac

```
/vis/open OGLSWin32 600x600-0+0
/vis/drawVolume
/vis/viewer/set/viewpointThetaPhi 0 0 deg
/vis/viewer/zoom 1.4
/vis/scene/add/trajectories
/vis/scene/add/hits
/vis/scene/endOfEventAction accumulate
/vis/viewer/set/background 1 1 1
/control/verbose 2
/run/verbose 2
/tracking/verbose 1
/gun/particle gamma
/gun/energy 662 keV
/random/setSeeds 1169508480 575684672
/run/beamOn 100
/vis/viewer/set/viewpointThetaPhi 180 90 deg
/run/beamOn 100
/vis/viewer/set/viewpointThetaPhi 90 180 deg
/run/beamOn 100
```

Measurements were performed with macro files such as the one given below. The seed numbers are chosen at random, and the macrofile runs Geant4 for 100,000 events.

Example macro file

```
/control/verbose 2
/run/verbose 2
/tracking/verbose 1
/gun/particle gamma
/gun/energy 662 keV
/random/setSeeds 1406264192 915493696
/run/beamOn 100000
```

The final program analyses the output files produced by Geant4 and decodes the information stored within it to calculate the number of events which interact in both detectors and deposit the entire photon energy within them.

Counter.cc

```
// Counter.cc, formerly procsingpixcomp.cc, as of 05 May 2010
// The program reads in files from output.csv (or an alternative
// given in the first command line argument), it reads in events 0 to
// 100,000 (or those given by the start and finish limits given in the
// second and third arguments). A fourth argument will stop the program
// printing verbosely.
#include <iostream>
#include <fstream>
#include <cmath>
#include <iomanip>
#include <cstdlib>
using namespace std;

// Initialise the Program with the arguments (of number argc-1) to
// the array argv[].
int main(int argc, char* argv[])
{
    // This information is only printed if there are less than 4 arguments
    // at the command line.
    if (argc < 5)
    {
        cout << "This Program sorts events in file output.csv from 0-100,000"
            << endl;
        cout << "Events of interest are re-written to print.csv" << endl;
        cout << "Counters determine the energy deposited in either of"
            "the Detectors" << endl;
        cout << "this information is then binned into plot.csv." << endl;
        cout << "In addition hits in individual pixels over"
            "(Total energy-10) keV" << endl;
        cout << "is also stored, and then printed as numbers into plot.csv."
            << endl;
        cout << "The program has 4 available arguments at comandline:"
            << endl;
        cout << "1. The name of the input file with extension" << endl;
        cout << "2. The initial event" << endl;
        cout << "3. The final event" << endl;
        cout << "4. If the 4th argument is set (any value) then this"
            "information is not shown" << endl;
        cout << "Program start" << endl << endl;
    }

    // Create a character array called file to read in a filename from the
    // 1st argument, if none is found use "output.csv" as default.
    const char* file;
    if (argc >= 2)
    {
        file = argv[1];
    }
}
```

```

    }
else
{
    file = "output.csv";
}
cout << "The Input filename is " << file << endl;

// Create integer start and end events and read these in from the 2nd
// and 3rd arguments, if none found use the defaults of 0 and 100,000.
int startevent, endevent;
if (argc >= 3)
{
    startevent = atoi(argv[2]);
}
else
{
    startevent = 0;
}
if (argc >= 4)
{
    endevent = atoi(argv[3]);
}
else
{
    endevent = 100000;
}
cout << "Running from event " << startevent << " to " << endevent
    << endl;

// Initialise variables.
char track[50];
char process[500][50];
int stepper;
int i;
int eventwritecounter = 0;
int end;
int point;
int invert;
int number;
double total;
double digit[10];
int exponent;
int Detector1hit;
int Detector2hit;
int event = 0;
int step;
int maxstep;
double x[500];
double y[500];
double z[500];
double kE[500];
double dE[500];
double steplength[500];
double tracklength[500];
int Detectorhit[50000];
int pixelhit[500];
int tracknum[500];
int parentnum[500];
double energyleft;

```

```

double Detector1deposit;
double Detector2deposit;
double totalenergy;
int energyhitter1[5000];
int energyhitter2[5000];
int energysteplimit;
int d1p1hit = 0;
int d1p2hit = 0;
int d1p3hit = 0;
int d1p4hit = 0;
int d1p5hit = 0;
int d1p6hit = 0;
int d1p7hit = 0;
int d1p8hit = 0;
int d1p9hit = 0;
int d1p10hit = 0;
int d1p11hit = 0;
int d1p12hit = 0;
int d1p13hit = 0;
int d1p14hit = 0;
int d1p15hit = 0;
int d1p16hit = 0;
int d2p1hit = 0;
int d2p2hit = 0;
int d2p3hit = 0;
int d2p4hit = 0;
int d2p5hit = 0;
int d2p6hit = 0;
int d2p7hit = 0;
int d2p8hit = 0;
int d2p9hit = 0;
int d2p10hit = 0;
int d2p11hit = 0;
int d2p12hit = 0;
int d2p13hit = 0;
int d2p14hit = 0;
int d2p15hit = 0;
int d2p16hit = 0;
double d1p1deposit = 0;
double d1p2deposit = 0;
double d1p3deposit = 0;
double d1p4deposit = 0;
double d1p5deposit = 0;
double d1p6deposit = 0;
double d1p7deposit = 0;
double d1p8deposit = 0;
double d1p9deposit = 0;
double d1p10deposit = 0;
double d1p11deposit = 0;
double d1p12deposit = 0;
double d1p13deposit = 0;
double d1p14deposit = 0;
double d1p15deposit = 0;
double d1p16deposit = 0;
double d2p1deposit = 0;
double d2p2deposit = 0;
double d2p3deposit = 0;
double d2p4deposit = 0;
double d2p5deposit = 0;

```

```

double d2p6deposit = 0;
double d2p7deposit = 0;
double d2p8deposit = 0;
double d2p9deposit = 0;
double d2p10deposit = 0;
double d2p11deposit = 0;
double d2p12deposit = 0;
double d2p13deposit = 0;
double d2p14deposit = 0;
double d2p15deposit = 0;
double d2p16deposit = 0;
int Detector = 0;
int d1point = 0;
int d2point = 0;

// Initialise the energy array for the 2 Detectors to be 0 at all values.
for (step = 0; step <= 5000; step++)
{
    energyhitter1[step] = 0;
    energyhitter2[step] = 0;
}

// Open files and check that the input file exists, if not then return
// to commandline.
fstream input, output, output2;
input.open(file, ios::in);
if (!input)
{
    cout << "File " << file << " not found. " << endl
        << "Returning to Prompt";
    return 0;
}
output.open("print.csv", ios::out);
output2.open("plot.csv", ios::out);

// Run through unwanted events.
cout << "Skipping " << startevent << " events" << endl;
while (event < startevent)
{
    input >> track;
    if ((track[0] == 'E') && (track[1] == 'O')
        && (track[2] == 'E'))
    {
        event++;
        input >> track;
        if ((event % 100000) == 0)
        {
            cout << event << endl;
        }
    }
}
// Running through unwanted events
cout << "Events skipped - starting run" << endl;

// Main body of program,
while (!input.eof())
{
    number = 0;
    input >> track;
}

```

```

// As we progress through the event the tracknumber and parentnumber
// stay the same
    if (step >= 1)
    {
        tracknum[step] = tracknum[step-1];
        parentnum[step] = parentnum[step-1];
    }

// If the line begins with Track then set the various values to be 0
    if (((track[0]) == 84) && ((track[1]) == 114)
        && ((track[2]) == 97))
    {
        if (((track[3]) == 99) && ((track[4]) == 107))
        {
            input >> tracknum[step];
            input >> track;
            input >> parentnum[step];
            input >> track;
            x[step] = 0;
            y[step] = 0;
            z[step] = 0;
            kE[step] = 0;
            dE[step] = 0;
            steplength[step] = 0;
            tracklength[step] = 0;
            Detectorhit[step] = 0;
            pixelhit[step] = 0;
        }
    }

// If the line begins with Step# then set the various values to be 0
    if (((track[0]) == 83) && ((track[1]) = 116) && ((track[2]) ==
101))
    {
        if (((track[3]) == 112) && ((track[4]) == 35))
        {
            input >> track;
            x[step] = 0;
            y[step] = 0;
            z[step] = 0;
            kE[step] = 0;
            dE[step] = 0;
            steplength[step] = 0;
            tracklength[step] = 0;
            Detectorhit[step] = 0;
            pixelhit[step] = 0;
        }
    }

// Write the numbers into arrays of "hits"

```

```

if (step == -1)
{
    if ((Detector1hit > 0) && (Detector2hit > 0)
        && (energyleft <= (0.05)))
    {

// Store events where energy in pixels meet the requirements
        int range = 10;
        if ((1000*d1p1deposit) >
            ((totalenergy*1000) - range))
        {
            d1p1hit++;
        }
        if ((1000*d1p2deposit) >
            ((totalenergy*1000) - range))
        {
            d1p2hit++;
        }
        if ((1000*d1p3deposit) >
            ((totalenergy*1000) - range))
        {
            d1p3hit++;
        }
        if ((1000*d1p4deposit) >
            ((totalenergy*1000) - range))
        {
            d1p4hit++;
        }
        if ((1000*d1p5deposit) >
            ((totalenergy*1000) - range))
        {
            d1p5hit++;
        }
        if ((1000*d1p6deposit) >
            ((totalenergy*1000) - range))
        {
            d1p6hit++;
        }
        if ((1000*d1p7deposit) >
            ((totalenergy*1000) - range))
        {
            d1p7hit++;
        }
        if ((1000*d1p8deposit) >
            ((totalenergy*1000) - range))
        {
            d1p8hit++;
        }
        if ((1000*d1p9deposit) >
            ((totalenergy*1000) - range))
        {
            d1p9hit++;
        }
        if ((1000*d1p10deposit) >
            ((totalenergy*1000) - range))
        {
            d1p10hit++;
        }
        if ((1000*d1p11deposit) >

```

```

((totalenergy*1000) - range))
{
    d1p11hit++;
}
if ((1000*d1p12deposit) >
    ((totalenergy*1000) - range))
{
    d1p12hit++;
}
if ((1000*d1p13deposit) >
    ((totalenergy*1000) - range))
{
    d1p13hit++;
}
if ((1000*d1p14deposit) >
    ((totalenergy*1000) - range))
{
    d1p14hit++;
}
if ((1000*d1p15deposit) >
    ((totalenergy*1000) - range))
{
    d1p15hit++;
}
if ((1000*d1p16deposit) >
    ((totalenergy*1000) - range))
{
    d1p16hit++;
}
if ((1000*d2p1deposit) >
    ((totalenergy*1000) - range))
{
    d2p1hit++;
}
if ((1000*d2p2deposit) >
    ((totalenergy*1000) - range))
{
    d2p2hit++;
}
if ((1000*d2p3deposit) >
    ((totalenergy*1000) - range))
{
    d2p3hit++;
}
if ((1000*d2p4deposit) >
    ((totalenergy*1000) - range))
{
    d2p4hit++;
}
if ((1000*d2p5deposit) >
    ((totalenergy*1000) - range))
{
    d2p5hit++;
}
if ((1000*d2p6deposit) >
    ((totalenergy*1000) - range))
{
    d2p6hit++;
}

```

```

        if ((1000*d2p7deposit) >
            ((totalenergy*1000) - range))
    {
        d2p7hit++;
    }
    if ((1000*d2p8deposit) >
        ((totalenergy*1000) - range))
    {
        d2p8hit++;
    }
    if ((1000*d2p9deposit) >
        ((totalenergy*1000) - range))
    {
        d2p9hit++;
    }
    if ((1000*d2p10deposit) >
        ((totalenergy*1000) - range))
    {
        d2p10hit++;
    }
    if ((1000*d2p11deposit) >
        ((totalenergy*1000) - range))
    {
        d2p11hit++;
    }
    if ((1000*d2p12deposit) >
        ((totalenergy*1000) - range))
    {
        d2p12hit++;
    }
    if ((1000*d2p13deposit) >
        ((totalenergy*1000) - range))
    {
        d2p13hit++;
    }
    if ((1000*d2p14deposit) >
        ((totalenergy*1000) - range))
    {
        d2p14hit++;
    }
    if ((1000*d2p15deposit) >
        ((totalenergy*1000) - range))
    {
        d2p15hit++;
    }
    if ((1000*d2p16deposit) >
        ((totalenergy*1000) - range))
    {
        d2p16hit++;
    }

// If all the values are 0 then add 2 to step
for (step = 2;step <= (maxstep - 1);step++)
{
    if ((x[step] == 0) && (y[step] == 0)
        && (z[step] == 0)
        && (kE[step] == 0)
        && (dE[step] == 0))
    {

```

```

        if (((steplength[step] == 0)
            && (tracklength[step] == 0)
            && (Detectorhit[step] == 0)
            && (pixelhit[step] == 0)))
    {
        step++;
        step++;
    }
}

// Multiply our full energy value and the energies deposited in the
// 2 Detectors by 1000 (MeV to keV) then histogram them and increase
// the number of stored events.
energysteplimit = int(totalenergy * 1000);
Detector1deposit = Detector1deposit * 1000;
Detector2deposit = Detector2deposit * 1000;
for (step = 0; step <= (energysteplimit + 1); step++)
{
    if ((Detector1deposit >= step)
        && (Detector1deposit < step + 1))
    {
        energyhitter1[step]++;
    }
    if ((Detector2deposit >= step)
        && (Detector2deposit < step + 1))
    {
        energyhitter2[step]++;
    }
}
eventwritecounter++;

}// Matches output requirements
step = -1;
}//Matches writing numbers into array of "hits"

// Determine if the contents of track are a number
if (((track[0] >= 48) && (track[0] <= 57))
    || ((track[0] >= 45)
        && (track[0] <= 46)))
{
    number = 1;
    i = 0;
    invert = 0;
    point = 0;
    end = 0;
    exponent = 0;

// We run to the end of the number and find if it is negative, and
// where the DP lies.
    while (int(end == 0))
    {
        if (int(track[0]) == 45)
        {
            invert = 1;
        }
        if (int(track[i]) == 46)
        {
            point = i;

```

```

        }
        if (int(track[i]) == 0)
        {
            end = i;
        }
        if (int(track[i]) == 101)
        {
            exponent = i;
        }
        i++;
    }
    if (point == 0)
    {
        point = end;
    }
    if (invert == 0) // If the number is +ve
    {

// We now make the digit array values equal their real values
        i = 0;
        while (i != point)
        {
            digit[i] = (double(track[i]) - 48)
                        * pow(10., (point - ((i) + 1)));
            i++;
        }
        i++;
        while (i < end)
        {
            digit[i] = (double(track[i]) - 48)
                        * pow(10., (point - (i)));
            i++;
        }
        while (i <= 10)
        {
            digit[i] = 0;
            i++;
        }
        total = 0;
        for (i = 0;i < point;i++)
        {
            total = total + digit[i];
        }
        for (i = int(point) + 1;i <= 10;i++)
        {
            total = total + digit[i];
        }

// This section deals with exponents!
        if ((exponent > 0) &&
            (int(track[exponent+1]) == 45))
        {
            total = 0;
        }
    }//Matches invert==0
    if (invert == 1) // If the number is -ve
    {

// We now make the digit array values equal their real values

```

```

        digit[0] = 0;
        i = 1;
        while (i != point)
        {
            digit[i] = (double(track[i]) - 48)
                        * pow(10., (point - ((i) + 1)));
            i++;
        }
        i++;
        while (i < end)
        {
            digit[i] = (double(track[i]) - 48)
                        * pow(10., (point - (i)));
            i++;
        }
        while (i <= 10)
        {
            digit[i] = 0;
            i++;
        }
        total = 0;
        for (i = 0;i < point;i++)
        {
            total = total + digit[i];
        }
        for (i = int(point) + 1;i <= 10;i++)
        {
            total = total + digit[i];
        }
        total = total * -1;
        if ((exponent > 0) &&
            (int(track[exponent+1]) == 45))
        {
            total = 0;
        }
    } // Matches invert==1
} // Matches if track is a number

// Beginning of event action
if ((track[0] == 'B') && (track[1] == 'O')
    && (track[2] == 'E'))
{
    input >> track;
    stepper = 0;
    Detector1hit = 0;
    Detector2hit = 0;
    Detector1deposit = 0;
    Detector2deposit = 0;
    step = 0;
    maxstep = 0;
    d1p1deposit = 0;
    d1p2deposit = 0;
    d1p3deposit = 0;
    d1p4deposit = 0;
    d1p5deposit = 0;
    d1p6deposit = 0;
    d1p7deposit = 0;
    d1p8deposit = 0;
    d1p9deposit = 0;
}

```

```

d1p10deposit = 0;
d1p11deposit = 0;
d1p12deposit = 0;
d1p13deposit = 0;
d1p14deposit = 0;
d1p15deposit = 0;
d1p16deposit = 0;
d2p1deposit = 0;
d2p2deposit = 0;
d2p3deposit = 0;
d2p4deposit = 0;
d2p5deposit = 0;
d2p6deposit = 0;
d2p7deposit = 0;
d2p8deposit = 0;
d2p9deposit = 0;
d2p10deposit = 0;
d2p11deposit = 0;
d2p12deposit = 0;
d2p13deposit = 0;
d2p14deposit = 0;
d2p15deposit = 0;
d2p16deposit = 0;
d1point = 0;
d2point = 0;
    // Beginning of event action

// End of line action
    else if ((track[0] == 'e') && (track[1] == 'o')
              && (track[2] == 'l'))
    {
        stepper = 0;
        step++;
        maxstep++;
    }

// End of event action
    else if ((track[0] == 'E') && (track[1] == 'O')
              && (track[2] == 'E'))
    {
        step = -1;
        input >> track;
        event++;
        if (event > endevent)
        {
            break;
        }
        if (Detector1hit > 0)
        {
        }
        if (Detector2hit > 0)
        {
        }
        if ((Detector1hit) && (Detector2hit > 0)
              && (energyleft <= 0.05))
        {
            float d1x[16], d1y[16], d1z[16]
            float d2x[16], d2y[16], d2z[16];
            float d1xfix = 0;

```

```

float d1yfix = 0;
float d1zfix = -10;
float d2xfix = 0;
float d2yfix = -7;
float d2zfix = -3.6;
d1x[1] = d1xfix - 2.4;
d1x[2] = d1xfix - 2.4;
d1x[3] = d1xfix - 2.4;
d1x[4] = d1xfix - 2.4;
d1x[5] = d1xfix - 0.8;
d1x[6] = d1xfix - 0.8;
d1x[7] = d1xfix - 0.8;
d1x[8] = d1xfix - 0.8;
d1x[9] = d1xfix + 0.8;
d1x[10] = d1xfix + 0.8;
d1x[11] = d1xfix + 0.8;
d1x[12] = d1xfix + 0.8;
d1x[13] = d1xfix + 2.4;
d1x[14] = d1xfix + 2.4;
d1x[15] = d1xfix + 2.4;
d1x[16] = d1xfix + 2.4;
d2x[1] = d2xfix - 2.4;
d2x[2] = d2xfix - 2.4;
d2x[3] = d2xfix - 2.4;
d2x[4] = d2xfix - 2.4;
d2x[5] = d2xfix - 0.8;
d2x[6] = d2xfix - 0.8;
d2x[7] = d2xfix - 0.8;
d2x[8] = d2xfix - 0.8;
d2x[9] = d2xfix + 0.8;
d2x[10] = d2xfix + 0.8;
d2x[11] = d2xfix + 0.8;
d2x[12] = d2xfix + 0.8;
d2x[13] = d2xfix + 2.4;
d2x[14] = d2xfix + 2.4;
d2x[15] = d2xfix + 2.4;
d2x[16] = d2xfix + 2.4;
for (i = 1;i <= 16;i++)
{
    d1y[i] = d1yfix;
    d2y[i] = d2yfix;
}
d1z[1] = d1zfix - 2.4;
d1z[2] = d1zfix - 0.8;
d1z[3] = d1zfix + 0.8;
d1z[4] = d1zfix + 2.4;
d1z[5] = d1zfix - 2.4;
d1z[6] = d1zfix - 0.8;
d1z[7] = d1zfix + 0.8;
d1z[8] = d1zfix + 2.4;
d1z[9] = d1zfix - 2.4;
d1z[10] = d1zfix - 0.8;
d1z[11] = d1zfix + 0.8;
d1z[12] = d1zfix + 2.4;
d1z[13] = d1zfix - 2.4;
d1z[14] = d1zfix - 0.8;
d1z[15] = d1zfix + 0.8;
d1z[16] = d1zfix + 2.4;
d2z[1] = d2zfix - 2.4;

```

```

d2z[2] = d2zfix - 0.8;
d2z[3] = d2zfix + 0.8;
d2z[4] = d2zfix + 2.4;
d2z[5] = d2zfix - 2.4;
d2z[6] = d2zfix - 0.8;
d2z[7] = d2zfix + 0.8;
d2z[8] = d2zfix + 2.4;
d2z[9] = d2zfix - 2.4;
d2z[10] = d2zfix - 0.8;
d2z[11] = d2zfix + 0.8;
d2z[12] = d2zfix + 2.4;
d2z[13] = d2zfix - 2.4;
d2z[14] = d2zfix - 0.8;
d2z[15] = d2zfix + 0.8;
d2z[16] = d2zfix + 2.4;
double sdx = (0 - x[d1point]);
double sdy = (0 - y[d1point]);
double sdz = (-64.64101 - z[d1point]);
double ddx = (x[d1point] - x[d2point]);
double ddy = (y[d1point] - y[d2point]);
double ddz = (z[d1point] - z[d2point]);
double pt1 = sdx / (pow((pow(sdx, 2))
                         + (pow(sdy, 2)) + (pow(sdz, 2)), 0.5));
double pt2 = ddx / (pow((pow(ddx, 2))
                         + (pow(ddy, 2)) + (pow(ddz, 2)), 0.5));
double pt3 = sdy / (pow((pow(sdx, 2))
                         + (pow(sdy, 2)) + (pow(sdz, 2)), 0.5));
double pt4 = ddy / (pow((pow(ddx, 2))
                         + (pow(ddy, 2)) + (pow(ddz, 2)), 0.5));
double pt5 = sdz / (pow((pow(sdx, 2))
                         + (pow(sdy, 2)) + (pow(sdz, 2)), 0.5));
double pt6 = ddz / (pow((pow(ddx, 2))
                         + (pow(ddy, 2)) + (pow(ddz, 2)), 0.5));
double angle = ((pt1 * pt2) + (pt3 * pt4)
                + (pt5 * pt6));

cout << x[d1point] << "\t" << y[d1point]
    << "\t" << z[d1point] << "\t" << x[d2point]
    << "\t" << y[d2point] << "\t" << z[d2point]
    << "\t" << pixelhit[d1point] << "\t"
    << pixelhit[d2point] << "\t"
    << Detector1deposit << "\t"
    << Detector2deposit << "\t" << angle
    << "\t";
output << x[d1point] << "\t" << y[d1point]
    << "\t" << z[d1point] << "\t" << x[d2point]
    << "\t" << y[d2point] << "\t" << z[d2point]
    << "\t" << pixelhit[d1point] << "\t"
    << pixelhit[d2point] << "\t"
    << Detector1deposit << "\t"
    << Detector2deposit << "\t" << angle
    << "\t";
sdx = (0 - d1x[pixelhit[d1point]]);
sdy = (0 - d1y[pixelhit[d1point]]);
sdz = (-64.64101 - d1z[pixelhit[d1point]]);
ddx = (d1x[pixelhit[d1point]]
        - d2x[pixelhit[d2point]]);
ddy = (d1y[pixelhit[d1point]]
        - d2y[pixelhit[d2point]]);

```

```

ddz = (d1z[pixelhit[d1point]]
       - d2z[pixelhit[d2point]]));
pt1 = sdx / (pow((pow(sdx, 2)) + (pow(sdy, 2))
                  + (pow(sdz, 2)), 0.5));
pt2 = ddx / (pow((pow(ddx, 2)) + (pow(ddy, 2))
                  + (pow(ddz, 2)), 0.5));
pt3 = sdy / (pow((pow(sdx, 2)) + (pow(sdy, 2))
                  + (pow(sdz, 2)), 0.5));
pt4 = ddy / (pow((pow(ddx, 2)) + (pow(ddy, 2))
                  + (pow(ddz, 2)), 0.5));
pt5 = sdz / (pow((pow(sdx, 2)) + (pow(sdy, 2))
                  + (pow(sdz, 2)), 0.5));
pt6 = ddz / (pow((pow(ddx, 2)) + (pow(ddy, 2))
                  + (pow(ddz, 2)), 0.5));
angle = ((pt1 * pt2) + (pt3 * pt4) + (pt5 * pt6));
cout << d1x[pixelhit[d1point]] << "\t"
     << d1y[pixelhit[d1point]] << "\t"
     << d1z[pixelhit[d1point]] << "\t"
     << d2x[pixelhit[d1point]] << "\t"
     << d2y[pixelhit[d1point]] << "\t"
     << d2z[pixelhit[d1point]] << "\t"
     << Detector1deposit << "\t"
     << Detector2deposit << "\t" << angle << endl;
output << d1x[pixelhit[d1point]] << "\t"
       << d1y[pixelhit[d1point]] << "\t"
       << d1z[pixelhit[d1point]] << "\t"
       << d2x[pixelhit[d1point]] << "\t"
       << d2y[pixelhit[d1point]] << "\t"
       << d2z[pixelhit[d1point]] << "\t"
       << Detector1deposit << "\t"
       << Detector2deposit << "\t" << angle
       << endl;
}
stepper = 0;
}// End of event action
else
{
// Print out values for x->tracklength, and store to arrays
    if ((stepper >= 0) && (stepper <= 7))
    {
        if (number == 1)
        {
            if (stepper == 1)
            {
                x[step] = total;
            }
            if (stepper == 2)
            {
                y[step] = total;
            }
            if (stepper == 3)
            {
                z[step] = total;
            }
            if (stepper == 4)
            {
                kE[step] = total;
            }
        }
    }
}

```

```

        if (stepper == 5)
        {
            dE[step] = total;
        }
        if (stepper == 6)
        {
            steplength[step] = total;
        }
        if (stepper == 7)
        {
            tracklength[step] = total;
        }
    }

// We dont need to store in 0 values if track is not a number as we
// only ever look for dE which we look at in it's own section. However,
// note that this is not done for editing. We may need to add a section
// below that uses the tracklength or some such for angle work! Mostly
// this section exists for print to screen.

} // Matches stepper=1 to 7
// Set initial energy of event
if ((step == 2) && (stepper == 4))
{
    energyleft = kE[step];
    totalenergy = kE[step];
}
// Find total energy at this step.
if ((step > 3) && (stepper == 5) && (number == 1))
{
    energyleft = energyleft - dE[step];
}
// Now looking at the Detector value under volume
if (stepper == 8)
{
    Detector = 0;
    int Detectorj = int(track[0]) - 48;
    int Detectork = int(track[1]) - 48;
    if (Detectorj > 16)
    {
        Detectorj = 0;
    }
    if (Detectork > 16)
    {
        Detectork = 0;
    }
    if (Detectork > -1)
    {
        Detector = (10 * Detectorj) + Detectork;
    }
    else
    {
        Detector = Detectorj;
    }
    if (Detector != 0)
    {
        Detectorhit[step] = Detector;
    }
    if (Detector == 0)
    {

```

```

        Detectorhit[step] = 0;
    }
//if(Detector==0){cout << track << "\t";}
else
{
    //cout << "Detect " << Detector << "\t";
    if (Detector == 1)
    {
        Detector1hit++;
        Detector1deposit = Detector1deposit
                           + dE[step];
        d1point = step;
    }
    if (Detector == 2)
    {
        Detector2hit++;
        Detector2deposit = Detector2deposit
                           + dE[step];
        d2point = step;
    }
}
}// Matches stepper=8
// Now looking at the Pixel value under volume
if (stepper == 9)
{
    int pixel = 0;
    int pixelj = int(track[0]) - 48;
    int pixelk = int(track[1]) - 48;
    if (pixelj > 16)
    {
        pixelj = 0;
    }
    if (pixelk > 16)
    {
        pixelk = 0;
    }
    if (pixelk > -1)
    {
        pixel = (10 * pixelj) + pixelk;
    }
    else
    {
        pixel = pixelj;
    }
    if (pixel != 0)
    {
        pixelhit[step] = pixel;
    }
    if (pixel == 0)
    {
        pixelhit[step] = 0;
    }
    if (pixel != 0)
    {
        if (Detector == 1)
        {
            if (pixel == 1)
            {
                d1p1deposit = d1p1deposit

```

```

                + dE[step];
}
if (pixel == 2)
{
    d1p2deposit = d1p2deposit
        + dE[step];
}
if (pixel == 3)
{
    d1p3deposit = d1p3deposit
        + dE[step];
}
if (pixel == 4)
{
    d1p4deposit = d1p4deposit
        + dE[step];
}
if (pixel == 5)
{
    d1p5deposit = d1p5deposit
        + dE[step];
}
if (pixel == 6)
{
    d1p6deposit = d1p6deposit
        + dE[step];
}
if (pixel == 7)
{
    d1p7deposit = d1p7deposit
        + dE[step];
}
if (pixel == 8)
{
    d1p8deposit = d1p8deposit
        + dE[step];
}
if (pixel == 9)
{
    d1p9deposit = d1p9deposit
        + dE[step];
}
if (pixel == 10)
{
    d1p10deposit = d1p10deposit
        + dE[step];
}
if (pixel == 11)
{
    d1p11deposit = d1p11deposit
        + dE[step];
}
if (pixel == 12)
{
    d1p12deposit = d1p12deposit
        + dE[step];
}
if (pixel == 13)
{

```

```

        d1p13deposit = d1p13deposit
                      + dE[step];
    }
    if (pixel == 14)
    {
        d1p14deposit = d1p14deposit
                      + dE[step];
    }
    if (pixel == 15)
    {
        d1p15deposit = d1p15deposit
                      + dE[step];
    }
    if (pixel == 16)
    {
        d1p16deposit = d1p16deposit
                      + dE[step];
    }
} // Detector1
if (Detector == 2)
{
    if (pixel == 1)
    {
        d2p1deposit = d2p1deposit
                      + dE[step];
    }
    if (pixel == 2)
    {
        d2p2deposit = d2p2deposit
                      + dE[step];
    }
    if (pixel == 3)
    {
        d2p3deposit = d2p3deposit
                      + dE[step];
    }
    if (pixel == 4)
    {
        d2p4deposit = d2p4deposit
                      + dE[step];
    }
    if (pixel == 5)
    {
        d2p5deposit = d2p5deposit
                      + dE[step];
    }
    if (pixel == 6)
    {
        d2p6deposit = d2p6deposit
                      + dE[step];
    }
    if (pixel == 7)
    {
        d2p7deposit = d2p7deposit
                      + dE[step];
    }
    if (pixel == 8)
    {
        d2p8deposit = d2p8deposit

```

```

                                + dE[step];
}
if (pixel == 9)
{
    d2p9deposit = d2p9deposit
        + dE[step];
}
if (pixel == 10)
{
    d2p10deposit = d2p10deposit
        + dE[step];
}
if (pixel == 11)
{
    d2p11deposit = d2p11deposit
        + dE[step];
}
if (pixel == 12)
{
    d2p12deposit = d2p12deposit
        + dE[step];
}
if (pixel == 13)
{
    d2p13deposit = d2p13deposit
        + dE[step];
}
if (pixel == 14)
{
    d2p14deposit = d2p14deposit
        + dE[step];
}
if (pixel == 15)
{
    d2p15deposit = d2p15deposit
        + dE[step];
}
if (pixel == 16)
{
    d2p16deposit = d2p16deposit
        + dE[step];
}
}
// Detector2
}//Pixel!=0
}// Matchers stepper=9
stepper++;
}// Matches else

// Stepper=11 is for the final column, but there is only an 11 if
// 9 (location of event) is in a Detector and thus 9 is split into 9/10.
// Confusing, but this information is useless except for printing
// to screen.
if (stepper == 11)
{
    for (i = 0;i <= 20;i++)
    {
        process[step][i] = track[i];
    }
}

```

```

} // Matches "while input!eof"

// Now all data is sorted, write the values out to output2 (plot.csv).
cout << endl << "All data processed" << endl << endl;;
cout << eventwritecounter << " events met the criteria " << endl;
for (step = 0; step <= (energysteplimit + 1); step++)
{
    output2 << endl << step << "\t";
    output2 << energyhitter1[step] << "\t" << energyhitter2[step];
    output2 << "\t" << d1p1hit << "\t" << d1p2hit << "\t"
        << d1p3hit << "\t" << d1p4hit << "\t" << d1p5hit;
    output2 << "\t" << d1p6hit << "\t" << d1p7hit << "\t"
        << d1p8hit << "\t" << d1p9hit << "\t" << d1p10hit;
    output2 << "\t" << d1p11hit << "\t" << d1p12hit << "\t"
        << d1p13hit << "\t" << d1p14hit << "\t" << d1p15hit;
    output2 << "\t" << d1p16hit << "\t" << d2p1hit << "\t"
        << d2p2hit << "\t" << d2p3hit << "\t" << d2p4hit;
    output2 << "\t" << d2p5hit << "\t" << d2p6hit << "\t"
        << d2p7hit << "\t" << d2p8hit << "\t" << d2p9hit;
    output2 << "\t" << d2p10hit << "\t" << d2p11hit << "\t"
        << d2p12hit << "\t" << d2p13hit << "\t" << d2p14hit;
    output2 << "\t" << d2p15hit << "\t" << d2p16hit;
}
cout << "All event information written to plot.csv - D1, D2, D1P,
D2P" << endl;
// Close all files and end Program.
input.close();
output.close();
output2.close();
cout << "Program Completed" << endl;
} // Matches main

```

Additional Bibliography

Journal Articles

- Abbas M. – J Phys D 39 (2006) p3952.
- Allen J. – Phys Rev 61 (1942) p692.
- Amrani R. et al. – Nucl Instr Meth A 458 (2001) p772.
- Avignone F. et al. – New J Phys 7 (2005) p6.
- Bayley D. S. & Crane H. R. – Phys Rev 12 (1937) p604.
- Bloxham T. et al. – Phys Rev C 76 (2007) p025501.
- Budjáš D. et al. – J Inst 4 (2009) p10007.
- Buskulic. D. et al. – Phys Lett B 349 (1995) p585.
- Crane H. R. & Halpern J. – Phys Rev 53 (1938) p789.
- Crane H. R. – Phys Rev 55 (1939) p501.
- Crane H. R. – Rev Mod Phys 20 (1948) p278.
- Dawson J. V. et al. – arXiv:0901.0996v1.
- Ejiri H. – J Phys Soc Japan 74 (2005) p2101.
- Elliot S. R. & Engel J. – J Phys G: Nucl Part Phys 30 (2004) p183.
- Elliot S. R. et al. – arXiv:0807.1741v1.
- Gironi L. – arXiv:0911.1061v1.
- Goessling C. et al. – Phys Rev C 72 (2005) p064328.
- Gryziński M. – Phys Rev 115 (1959) p1087.
- Gürler O. & Yalçın S. – Annals Nucl Energy 32 (2005) p1918.
- Jenkins J. H. et al. – arXiv:0808.3283v1.
- Jenkins J. H. & Fischbach E. – arXiv:0808.3156v1.
- Kiel H. et al. – Nucl Phys A 723 (2003) p499.
- Klapdor-Kleingrothaus H. V. – arXiv:hep-ph/0302248v1.
- Klapdor-Kleingrothaus H. V. – Phys Scripta T127 (2006) p40.
- Korzhov M. – Physics World 21 (2008) p29.
- Lee J. H. & Lee C. S. – J Korean Phys Soc 49 (2006) p97.
- Li D. et al. – J Nucl Sci Tech 33 (1996) p736.

- Loeb L. B. – Phys Rev 34 (1929) p1212.
- Münstermann D. & Zuber K. – J Phys G: Nucl Part Phys 29 (2003) pB1.
- Nakamura K. et al. – J Phys G 37 (2010) p075021 – section retrieved from <http://pdg.lbl.gov/2010/reviews/rpp2010-rev-neutrinoless-double-beta-decay.pdf>.
- Pontecorvo B. – Rep Prog Phys 11 (1947) p32.
- Ramachers Y. & Stewart D. Y. – J Inst 2 (2007) p12003.
- Rutherford E. – Philosophical Magazine 6 (1911) p21.
- Saleh Yousef M. et al. – Nucl Phys B 188 (2009) p56.
- Sato G. et al. – IEEE Transaction on Nuclear Science 49 (2002) p1258.
- Schmitz N. – arXiv:hep-ex/0211041v1.
- Serbini S. et al. – J Nucl Medicine 20 (1979) p882.
- Stewart D. Y. & Ramachers Y. – J Inst 3 (2008) p01007.
- Szeles C. – Phys Stat Sol (b) 3 (2004) p783.
- Valle J. W. F. – arXiv:hep-ex/0608101v1.
- Verger L. et al. – Nucl Inst Meth A 571 (2007) p33.
- Weinheimer C. – Nucl Phys B 118 (2003) p279.
- Wilson J. R. – J Phys: Conference Series 120 (2008) p052048.
- Zuber K. – Acta Physica Polonica B 37 (2006) p1905.
- Zuber K. – Phys Rev D 56 (1997) p1816.
- Zuber K. – Phys Lett B 519 (2001) p1.
- Zuber K. – Phys Lett B 571 (2003) p148.
- Zuber K. – Nucl Phys B 138 (2005) p236.
- Zuber K. – Prog Part Nucl Phys 57 (2006) p235.
- Zuber K. – J Phys Conference Series 203 (2010) p012070.

Conference Proceedings

- Gong H. et al. – ICSICT-2006 - 2006 8th International Conference on Solid-State and Integrated Circuit Technology Proceedings p959 – retrieved from <http://ieeexplore.ieee.org/stamp/stamp.jsp?tp=&arnumber=4098290>.
- Philips B. F. et al. - Nuclear Science Symposium Conference Record, 2003 IEEE p3380 – retrieved from <http://ieeexplore.ieee.org/stamp/stamp.jsp?tp=&arnumber=1352630>.

Zhang F. et al. - Nuclear Science Symposium Conference Record (NSS/MIC), 2009 IEEE p2012 – retrieved from <http://ieeexplore.ieee.org/stamp/stamp.jsp?tp=&arnumber=5402137>.

Websites

Smith D. – Student Lecture Series for MiniBooNE – retrieved from
<http://physicsx.pr.erau.edu/Office/oscillations.pdf> on 21/12/2010.

Kearns E. – Atmospheric Neutrinos – summary for Super-Kamiokande – retrieved from
hep.bu.edu/~superk/atmnu/ on 21/12/2010.

Presentations

Cernak P. – The COBRA Experiment: Progress Report – retrieved from
http://www.uni-tuebingen.de/ilias-dbd/PMN08/src/Melos-Talks/cermak_COBRA.pdf

Dawson J. – The COBRA Double Beta Decay Experiment – retrieved from
<http://Irt2006.in2p3.fr/talks/lrtjd.pdf>

Engel J. – Effective Operator for Double-Beta Decay – retrieved from
http://www.int.washington.edu/talks/WorkShops/int_08_3/People/Engel_J/Engel.pdf

Falk E. – Neutrinos: The Ghost Particles (Presented at Birmingham 7th October 2009)

Wilson J. – The COBRA Experiment – retrieved from
<http://lss.fnal.gov/conf/C0606131/3.8Wilson.pdf>

Books

Yoshio Nishina: Father of Modern Physics in Japan – Dong-Won Kim – Taylor and Francis Group (2007).

Nuclear Physics: Principles and Applications – John Lilley – Wiley (2005).

Quantum Physics: of Atoms, Molecules, Solids, Nuclei, and Particles – Robert Eisberg & Robert Resnick – Wiley (1985) 2nd Edition.

Seventy Years of Double Beta Decay – Hans Volker Klapdor-Kleingrothaus – World Scientific Publishing (2010).

References

-
- ¹ Rutherford E. – Philosophical Magazine 21 (1911) p669.
 - ² Bohr N. – Philosophical Magazine 26 (1913) p1.
 - ³ Bohr N. – Philosophical Magazine 26 (1913) p476.
 - ⁴ Bohr N. – Philosophical Magazine 26 (1913) p857.
 - ⁵ Rutherford E. – Philosophical magazine 37 (1919) p537.
 - ⁶ Rutherford E. – Proc Roy Soc A 97 (1920) p374.
 - ⁷ Chadwick J. – Letter to Rutherford, 14 January 1914 – Cambridge University Library.
 - ⁸ Ellis C. D. & Wooster W. A. – Proc Roy Soc A 117 (1927) p109.
 - ⁹ Chadwick J. – Nature 129 (1932) p312.
 - ¹⁰ Chadwick J. – Proc Roy Soc A 136 (1932) p692.
 - ¹¹ Leipunski A. I. – Proc Camb Phil Soc 32 (1936) p301.
 - ¹² Csikai J. & Szalay. S – Proc Intern Congr Nucl Phys Paris (1958) – ‘The electron neutrino angular correlation in the beta decay of He6’ published by Dunod (1959) p840.
 - ¹³ Krane K. S. – Introducing Nuclear Physics – Wiley (1988) – p273.
 - ¹⁴ Krane K. S. – Introducing Nuclear Physics – Wiley (1988) – Figure 9.1.
 - ¹⁵ Pauli W. – Letter to ‘Physikalisches Institut’ Zurich, 4th December 1930.
 - ¹⁶ Klapdor-Kleingrothaus H. V. – Sixty Years of Double-beta Decay – World Scientific Publishing (2001) – p101.
 - ¹⁷ Fermi E. – Zeits f Physik 88 (1934) p161.
 - ¹⁸ Cowan C. L. & Reines F. – Science 124 (1956) p103.
 - ¹⁹ Reines F. & Cowan C. L. – Phys Rev Lett 117 (1960) p159.
 - ²⁰ Street J. C. & Stevenson E. C. – Phys Rev 52 (1937) p1003.
 - ²¹ Danby G. – Phys Rev Lett 9 (1962) p36.
 - ²² Perl R. et al – Phys Rev Lett 35 (1975) p1489.
 - ²³ Abrams D. S. et al – Phys Rev Lett 63 (1989) p2173.
 - ²⁴ Abreu G. et al – Phys Lett B 241 (1990) p435.
 - ²⁵ Adeva B. et al – Phys Lett B 238 (1990) p122.
 - ²⁶ Akrawy M. Z. et al – Phys Lett B 240 (1990) p497.
 - ²⁷ Decamp D. et al – Phys Lett B 235 (1990) p399.

-
- ²⁸ Holzschuh E. – Rep Prog Phys 55 (1992) p1035.
- ²⁹ Kodama K. – Phys Rev Lett B 504 (2001) p218.
- ³⁰ Goepert-Mayer M. – Phys Rev 48 (1935) p512.
- ³¹ Davis R. et al – Phys Rev Lett 20 (1968) p1205 .
- ³² Krane K. S. – Introducing Nuclear Physics – Wiley (1988) – Figure 3.18.
- ³³ Majorana E. – Nuovo Cimento 14 (1937) p17.
- ³⁴ Furry W. H – Physical Review 56 (1939) p1184.
- ³⁵ Zuber K. – J Phys G 31 (2005) p1471.
- ³⁶ Boehm F. & Vogel P. – Physics of Massive Neutrinos – Cambridge University Press 2nd Edition (1992) – p182.
- ³⁷ <http://www.sns.ias.edu/~jnb/> – retrieved 29/09/08.
- ³⁸ Bethe H. A. & Critchfield C. L. – Phys Rev 54 (1938) p248.
- ³⁹ <http://en.wikipedia.org/wiki/Image:FusionintheSun.svg> – retrieved 15/09/2008.
- ⁴⁰ Lande K. et al in Hampel W. (Ed.) Proc 4th Int. Solar Neutrino Conference, MPIK, Heidelberg, 1997.
- ⁴¹ Bahcall J. N. & Pinsonneault M. H. – Rev Mod Phys 67 (1995) p781.
- ⁴² Davis R. – Int J Mod Phys A18 (2003) p3089.
- ⁴³ Assamagan K. et al – Phys Rev D 53 (1996) p6065.
- ⁴⁴ Bilenky S.M. – J Phys A 40 (2007) p6707.
- ⁴⁵ Zuber K. – Physics Reports 305 (1998) p295.
- ⁴⁶ Mohapatra R. N. – Ann Rev Nucl Part Sci 56 (2006) p569.
- ⁴⁷ Heeger K. – Invited talk at SEESAW25: International Conference on the Seesaw Mechanism and Neutrino Mass, Paris, France, 10-11 June 2004 - <http://arxiv.org/abs/hep-ex/0412032v2> – retrieved 07/07/10.
- ⁴⁸ Avignone F. et al – Rev Mod Phys 80 (2008) p481.
- ⁴⁹ Roulet E. – Lectures given at the V Latin-American Symposium of High Energy Physics, Lima, Peru, July 2004 - <http://arxiv.org/abs/astro-ph/0412639v1> – retrieved 07/07/10.
- ⁵⁰ <http://www.sno.phy.queensu.ca/> – retrieved 25/09/08.
- ⁵¹ <http://www-numi.fnal.gov/> – retrieved 25/09/08.
- ⁵² Belesev A. I. – Phys Lett B 350 (1995) p263.
- ⁵³ Daum M. – Phys Rev D 20 (1979) p2692.
- ⁵⁴ Buskulic S. – Phys Lett B 349 (1995) p585.

-
- ⁵⁵ Elliot S. R. and Vogel P. – Ann Rev Nucl Part Sci 52 (2002) p115.
- ⁵⁶ Zuber K. – Eur Phys J C 33 (2004) p817.
- ⁵⁷ Barabash A. – NEMO 3 double-beta decay experiment: latest results – arXiv:0807.2336v2 – retrieved 25/09/08.
- ⁵⁸ http://www.mpi-hd.mpg.de/gerda/reportsLNGS/proposal_21sept.pdf – retrieved 07/09/2010.
- ⁵⁹ Journal of Physics Conference series 110 (2008) ‘The GERmanium Detector Array, GERDA’ – http://iopscience.iop.org/1742-6596/110/8/082010/pdf/jpcconf8_110_082010.pdf – retrieved 07/09/2010.
- ⁶⁰ <http://majorana.pnl.gov/> – retrieved 12/07/2010.
- ⁶¹ <http://crio.mib.infn.it/wigmi/pages/cuore.php> – retrieved 12/07/2010.
- ⁶² Gorla P. – Journal of Low Temperature Physics 151 (2008) p607.
- ⁶³ <http://nemo.in2p3.fr/nemow3/> – retrieved 12/07/2010.
- ⁶⁴ <http://cobra.physik.uni-dortmund.de/> – retrieved 28/05/2010.
- ⁶⁵ Apyan A. et al – Physics Review D 77 (2008) 037901.
- ⁶⁶ Klapdor-Kleingrothaus H. V. – Sixty Years of Double-beta Decay – World Scientific Publishing – 1st Edition (2001) p14.
- ⁶⁷ Zuber K. – Contemporary Physics 45 (2004) p491.
- ⁶⁸ Streetman B. G. – Solid State electronic Devices – Prentice Hall 5th edition (2000).
- ⁶⁹ Knoll G. F. – Radiation Detection and Measurement – Wiley (2000) 3rd Edition – Chapter 13 p483.
- ⁷⁰ Krane K. S. – Introducing Nuclear Physics – Wiley (1988) – p225.
- ⁷¹ Krane K. S. – Introducing Nuclear Physics – Wiley (1988) – p217.
- ⁷² Krane K. S. – Introducing Nuclear Physics – Wiley (1988) – p224.
- ⁷³ Zuber K. – Progress in Particle and Nuclear Physics 57 (2006) p235.
- ⁷⁴ Knoll G. F. – Radiation Detection and Measurement – Wiley 3rd Edition (2000) – p357.
- ⁷⁵ Zumbiehl A. et al – Nucl Instr Meth Phys Res A 469 (2001) p227.
- ⁷⁶ Knoll G. F. – Radiation Detection and Measurement – Wiley 3rd Edition (2000) – Chapter 13 p 486.
- ⁷⁷ Lachish U. – CdTe and CdZnTe Crystal Growth and Production of Gamma Radiation Detectors – <http://urila.tripod.com/crystal.htm> - retrieved 23 Sep 2010.
- ⁷⁸ Knoll G. F. – Radiation Detection and Measurement – Wiley 3rd Edition (2000) – p152.

-
- ⁷⁹ He Z. - Nucl Instr Meth Phys Res A 463 (2001) p250.
- ⁸⁰ Jackson J. D. – Classical Electrodynamics 2nd Ed Wiley (New York) 1975 p68.
- ⁸¹ Un-published - Spencer S. - M.Sc. Project – 2007.
- ⁸² Thesis – Bloxham T. – The simulation and use of Cadmium Zinc Telluride Detectors as part of the search for neutrino-less double-beta decay.
- ⁸³ <http://www.evproducts.com/electronics.html> retrieved 29/09/08 at 13:53.
- ⁸⁴ Bloxham T. & Freer M. – Nucl. Instr. Meth. Phys. Res. A 572 (2007) p722.
- ⁸⁵ <http://atom.kaeri.re.kr/cgi-bin/nuclide?nuc=Bi-214> – retrieved 13/01/2011.
- ⁸⁶ <http://www.geant4.org/geant4/> - retrieved 29/09/2008.
- ⁸⁷ POISON Version 0.9.2 COBRA GEANT4 Monte Carlo User Manual – H. Kiel October 30, 2007.
- ⁸⁸ Determination of the Half Lives of Rare Decays of Cd, Te and Zn Isotopes for the COBRA Experiment – Doctoral Thesis – retrieved from <https://eldorado.tu-dortmund.de/bitstream/2003/21509/2/diss-20050523.ps> - 5th October 2010.
- ⁸⁹ Tretyak V. I. & Zdesenko Y. G. - Atomic Data and Nuclear Data Tables 61 (1995) p43.
- ⁹⁰ Tretyak V. I. & Zdesenko Y. G. – Atomic Data and Nuclear Data Tables 80 (2002) p83.
- ⁹¹ Rigby S. V. et al. - Nuclear Science Symposium Conference Record, 2006. IEEE. – <http://ieeexplore.ieee.org/stamp/stamp.jsp?tp=&arnumber=4179818> – retrieved 04 Oct 2010.
- ⁹² An Evaluation of Hospital Radiation Detectors for Use in Screening Potentially Contaminated Individuals - <http://www.bt.cdc.gov/radiation/pdf/hospitalinstruments.pdf> - retrieved 15/7/2010.
- ⁹³ Detecting nuclear and radiological materials - <http://royalsociety.org/WorkArea/DownloadAsset.aspx?id=5509> – retrieved 15/7/2010.
- ⁹⁴ Todd R. W., Nightingale J. M. & Everett D. B. – Nature 251 (1974) p132.
- ⁹⁵ Nishina Y. - Zeitschrift für Physik 52 (1929) p869.
- ⁹⁶ Klein O. & Nishina Y. – Nature 122 (1928) p398.
- ⁹⁷ Nishina Y. – Nature 122 (1928) p843.
- ⁹⁸ Nishina Y. – Nature 123 (1929) p349.
- ⁹⁹ Krane K. S. – Introducing Nuclear Physics – Wiley (1988) – figure 7.7.
- ¹⁰⁰ Unsworth C. et al – Nucl Instr Meth Phys Res A 604 (2009) p67.